Microfabricated inserts for sensitivity enhancement in MAS NMR

Zur Erlangung des akademischen Grades eines

DOKTORS DER INGENIEURWISSENSCHAFTEN (Dr.-Ing.)

von der KIT-Fakultät für Maschinenbau des
Karlsruher Instituts für Technologie (KIT)
genehmigte

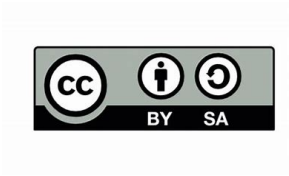
DISSERTATION

von

M.Sc. Shyamsundar Adhikari

Tag der mündlichen Prüfung: 17. April 2023

Referent: Prof. Dr. Jan G. Korvink
Korreferentin: Prof. Dr. Gisela Guthausen



This document is licensed under a Creative Commons Attribution-ShareAlike 4.0 International License (CC BY-SA 4.0): https://creativecommons.org/licenses/by-sa/4.0/deed.en

Karlsruher Institut für Technologie
Institut für Mikrostrukturtechnik
Hermann-von-Helmholtz Platz 1
76344 Eggenstein-Leopoldshafen

Abstract

This thesis reports on the development and stabilization of the fabrication process of NMR micro-detectors as a part of the effort to address the gap in accessibility to miniaturized detectors for the NMR community.

The magic angle coil spinning (MACS) approach in NMR has combined the advantages offered by a micro-coil detector and magic angle spinning (MAS) to bring about considerable improvements in sensitivity and resolution in solid-state NMR experiments. The MACS strategy features co-rotation of the sample and the micro-detector while the latter is inductively coupled to the pick-up coil in the MAS probehead. The micro-detector used for this technique was conceived as handwound micro-solenoid with its ends soldered to an off the shelf capacitors to form a micro-resonator circuit tuned to the Larmor frequency of interest. This manual fabrication of the MACS detectors is not only cumbersome but also makes these devices imprecise and prone to imbalance. Moreover, the wireless inductive coupling arrangement mandates adequate electrical performance from these devices to avoid signal losses. Another drawback of the MACS technique is the sample heating due to induced eddy currents in the spinning micro-detector.

On the other hand, utilization of MEMS fabrication techniques delivers photolithographic accuracies as well as scalability and reproducibility for these devices. Implementing the capacitor on-chip to go with the automated wirebonding process for the micro-coil would eliminate the issues associated with the manual hand fabrication method. Therefore, with this backdrop, this thesis reports on the development of microfabricated MACS devices that are fine tuned not only for their electrical performance but also provides excellent thermal performance with reduced induced eddy currents. Furthermore, the goal was also to produce devices that are reproducible, robust and easy to handle so as to seamlessly facilitate NMR measurements. Therefore, this thesis tackles the challenges associated with having a suitable design for the on-chip capacitor connected to the micro-coil as well as finer aspects of microfabrication techniques employed to manufacture the MACS detectors. These devices are also extensively characterized using standard benchmarking protocols and the feasibility of adopting these devices for metabolomic studies is also investigated.

Another major focus of this thesis is to explore the concept for the non-resonant variant of MACS detector with broadband performance across the frequency spectrum. This would overcome the limitations associated with tuned MACS devices which originate from the requirement to tune them to the target Larmor frequency to have the best NMR sensitivity. Wideband characteristics render the devices flexible with respect to either magnetic field strength and/or nuclei of interest and would also bring in added benefits for cross-polarization (CP) and heteronuclear experiments.

The broadband functionality is conceptualized by integrating the micro-coil as a part of Lenz lens arrangement instead of an on-chip capacitor. Three different designs are introduced and analyzed analytically as well as using FEM simulations. In order to implement these geometries, innovative micro-manufacturing approaches have been established keeping in focus the objective of high volume fabrication.

Thus, the major outcome of this work is an established wafer scale fabrication process to deliver micro-detectors that are cost effective and at the same time that drastically boost NMR sensitivity for mass- and volume-limited samples and offer part per billion spectral resolution for NMR metabolomics.

Zusammenfassung

Das Ziel dieser Arbeit ist die Entwicklung und Stabilisierung des Herstellungsprozesses von NMR Mikro-detektoren als Teil der Bemühungen, die Lücke in der Zugänglichkeit von miniaturisierten Detektoren für die NMR-Gemeinschaft zu schließen.

Der Ansatz des Magic Angle Coil Spinning (MACS) in der NMR hat die Vorteile eines Mikrospulendetektors und des Magic Angle Spinning (MAS) kombiniert, um die Empfindlichkeit und Auflösung bei Festkörper-NMR-Experimenten erheblich zu verbessern. Bei der MACS-Strategie werden die Probe und der Mikrodetektor gemeinsam rotiert, während der Mikrodetektor mit der Aufnahmespule im MAS-Probenkopf induktiv gekoppelt ist. Der für diese Technik verwendete Mikrodetektor wurde als handgewickeltes Mikro-Solenoid konzipiert, dessen Enden an einen handelsüblichen Kondensator gelötet wurden, um einen Mikroresonator zu bilden, der auf die gewünschte Larmor-Frequenz abgestimmt ist. Diese manuelle Herstellung der MACS-Detektoren ist nicht nur mühsam, sondern macht diese Bauteile auch ungenau und anfällig für Unwucht. Außerdem erfordert die drahtlose induktive Kopplung eine angemessene elektrische Leistung dieser Sensoren, um Signalverluste zu vermeiden. Ein weiterer Nachteil der MACS-Technik ist die Erwärmung der Probe aufgrund der induzierten Wirbelströme in dem sich drehenden Mikrodetektor.

Andererseits bietet die Verwendung von MEMS-Fertigungstechniken photolithographische Genauigkeit sowie Skalierbarkeit und Reproduzierbarkeit für diese Detektoren. Die Implementierung des Kondensators auf dem Chip zusammen mit dem automatisierten Drahtbondverfahren für die Mikrospule würde die Probleme beseitigen, die mit der manuellen Herstellung von Hand verbunden sind. Vor diesem Hintergrund berichtet diese Arbeit über die Entwicklung von mikrogefertigten MACS-Bauelementen, die nicht nur hinsichtlich ihrer elektrischen Leistung abgestimmt sind, sondern auch eine hervorragende thermische Leistung mit reduzierten induzierten Wirbelströmen aufweisen. Darüber hinaus war es das Ziel, MACS-Sensoren herzustellen, die reproduzierbar, robust und einfach zu handhaben sind, um NMR-Messungen nahtlos zu ermöglichen. Daher befasst sich diese Arbeit mit den Herausforderungen, die mit einem geeigneten Design für den mit der Mikrospule verbundenen On-Chip-Kondensator, sowie mit feineren Aspekten der Mikrofabrikationstechniken, die zur Herstellung der MACS-Detektoren eingesetzt werden. Diese mikro-Detektoren werden auch von Standard-Benchmarking-Protokollen umfassend charakterisiert, und es wird auch untersucht, ob diese Bauteile für metabolomische Studien eingesetzt werden können.

Ein weiterer Schwerpunkt dieser Arbeit ist die Erforschung des Konzepts einer nichtresonanten Variante des MACS-Detektors mit breitbandiger Leistung über das Frequenzspektrum. Dies würde die Einschränkungen überwinden, die mit abgestimmten MACS-Detektoren verbunden sind, die aus der Anforderung resultieren, sie auf die Ziel-Larmor-Frequenz abzu-

stimmen, um die beste NMR-Empfindlichkeit zu erreichen. Die breitbandigen Eigenschaften machen die Bauteile flexibel in Bezug auf die Magnetfeldstärke und/oder die interessierenden Kerne und würden auch zusätzliche Vorteile für Kreuzpolarisation (CP) und heteronukleare Experimente bringen.

Die breitbandige Funktionalität wird durch die Integration der Mikrospule als Teil der Lenz-Linsenanordnung anstelle eines On-Chip-Kondensators konzipiert. Drei verschiedene Designs werden vorgestellt und sowohl analytisch als auch mit FEM-Simulationen analysiert. Um diese Geometrien zu implementieren, wurden innovative Ansätze für die Mikrofertigung entwickelt, wobei das Ziel der Herstellung in hohen Stückzahlen im Vordergrund steht.

Somit ist das bedeutendste Ergebnis dieser Arbeit ein etablierter Herstellungsprozess auf Wafer-Ebene zur Erzeugung günstiger Mikrodetektoren, die NMR-Empfindlichkeit für massen- und volumenbegrenzte Proben drastisch erhöhen und pro Milliarde (ppb) Auflösung für NMR Experimente liefern.

Nomenclature

Abbreviations

$2D$	Two Dimensional
$3D$	Three Dimensional
LC	An electric circuit consisting of an inductor and a capacitor
ppb	Part per billion
ppm	Part per million
COSY	Correlation Spectroscopy
CP	Cross Polarization
DNP	Dynamic nuclear polarisation
DSLL	Double solenoid Lenz lens
emf	Electromotive force
FEM	Finite element method
FID	Free induction decay
FOM	Figure of merit
FWHM	Peak width at its half-height
HF	High frequency
HH	Helmholtz
HMQC	Heteronuclear multiple-quantum correlation spectroscopy
LF	Low frequency
LL	Lenz lens
LOD	Limit of detection
MACS	Magic angle coil spinning
MAS	Magic angle spinning
MEMS	Micro electro-mechanical system
MRI	Magnetic resonance imaging
nLOD	normalised limit of detection
NMR	Nuclear magnetic resonance
PVD	Physical vapour deposition
RF	Radio frequency
SNR	Signal to noise ratio
SSLL	Single solenoid Lenz lens
TR	Relaxation time

Constants

ϵ_0	Vacuum permittivity
μ_0	Vacuum permeability
h	Planck constant
k_b	Boltzmann constant

Symbols

δ	Skin depth
ϵ_r	Relative permittivity
γ	Gyromagnetic ratio
λ	Wavelength
μ_r	Relative magnetic permeability
ρ	Specific electrical resistance
σ	Standard deviation
$\tau_{\pi/2}$	90° pulse duration
$\vec{\mu}$	Magnetic moment
$\vec{\omega_0}$	Larmor frequency
$\vec{\vec{\chi}}$	Magnetic susceptibility
$\vec{B_0}$	Static magnetic field
$\vec{B_1}$	RF magnetic field
$\vec{I}$	Nuclear spin
$\vec{M_0}$	Net magnetisation
$\vec{S}$	Spin angular momentum
m	Magnetic quantum number
Q	Quality factor
S_{ij}	S-parameter
T	Temperature
T_1	Longitudinal (spin-lattice) relaxation time constant
T_2	Spin-spin relaxation time constant

Contents

Abstract i

Zusammenfassung iii

Nomenclature v

1 Introduction 1
- 1.1 Motivation . . . 2
- 1.2 Organisation . . . 2
- 1.3 Publication . . . 3
  - 1.3.1 In the scope of this thesis . . . 3
  - 1.3.2 Side projects . . . 3
  - 1.3.3 Conference contributions . . . 4
  - 1.3.4 Book Chapter . . . 4

2 Starting point 7
- 2.1 Nuclear spin interactions . . . 8
- 2.2 Solid state NMR . . . 9
- 2.3 MAS NMR . . . 11
  - 2.3.1 Sensitivity issues with state of the art MAS technology . . . 15
  - 2.3.2 Sensitivity enhancement techniques for solid state NMR . . . 15
- 2.4 Micro-coils in NMR . . . 19
  - 2.4.1 NMR Figures of merit . . . 19
  - 2.4.2 Micro-coil topologies . . . 21
  - 2.4.3 Micro-coils in solid-state NMR . . . 22
- 2.5 MACS NMR . . . 23
  - 2.5.1 Inductively coupled micro-coils . . . 24
  - 2.5.2 Effect of frequency offset of MACS inserts . . . 27
  - 2.5.3 Effect of Q factor of the micro-resonator . . . 28
- 2.6 Microfabricated MACS detectors . . . 29
- 2.7 Discussion . . . 31

3 MEMS capacitors for MACS 35
- 3.1 RF MEMS components in micro-NMR . . . 35
- 3.2 On chip capacitors for MACS . . . 37

3.3 Simulations . . . 38
3.3.1 Evaluation of the Q-factor . . . 39
3.3.2 Induced eddy currents in the capacitor . . . 40
3.4 Fabrication . . . 45
3.4.1 Interdigitated capacitors . . . 45
3.4.2 Parallel plate capacitors . . . 47
3.4.3 Failure mode effects and Analysis . . . 50
3.5 Characterization . . . 51
3.5.1 Electrical characterization . . . 51
3.5.2 Thermal characterization . . . 53
3.6 Discussion . . . 55

4 Microfabricated MACS inserts **59**
4.1 Simulations . . . 60
4.1.1 B_1 field simulation . . . 60
4.1.2 B_0 field simulation . . . 61
4.2 Fabrication . . . 64
4.2.1 HAR SU-8 lithography . . . 65
4.2.2 Wirebonded micro-coils . . . 68
4.2.3 Back end processing . . . 68
4.2.4 FMEA . . . 69
4.3 Characterization . . . 73
4.3.1 Electrical and thermal characterization . . . 73
4.3.2 Resonance splitting due to inductive coupling . . . 76
4.3.3 NMR characterization . . . 79
4.4 Yield, risk, failure and reliability analysis . . . 94
4.4.1 Yield . . . 94
4.4.2 Risk analysis . . . 95
4.4.3 Reliability and failure analysis . . . 95
4.4.4 Process capability index (Cpk) . . . 96
4.5 Discussion . . . 98

5 Broadband MACS inserts **101**
5.1 Lenz lens inserts in NMR . . . 102
5.2 Theoretical formulations . . . 103
5.3 Design and simulation of broadband MACS inserts . . . 105
5.3.1 Single solenoid Lenz lens inserts (SSLL) . . . 106
5.3.2 Double solenoid Lenz lens inserts (DSLL) . . . 108
5.3.3 Helmholtz Lenz lens inserts (HHLL) . . . 109
5.3.4 Conclusion . . . 111
5.4 Fabrication of broadband MACS inserts . . . 111
5.4.1 Fabrication of SSLL and DSLL inserts . . . 114

5.4.2 Fabrication of HHLL inserts . . . 118
5.4.3 Conclusion . . . 120
5.5 Characterization . . . 120
5.5.1 Electrical characterization . . . 120
5.5.2 NMR characterization . . . 121
5.6 Discussion . . . 124

6 Conclusion and outlook **129**
6.1 Conclusion . . . 129
6.2 Outlook . . . 131

Appendix **135**
A1 Zebrafish husbandry and embryo culture . . . 135
A2 Larmor frequency of some common isotopes at 11.74 T . . . 135
A3 Magic angle spinning probe calibration . . . 136
A4 Sample preparation for NMR experiments . . . 136
A5 Calculation of proton concentration in a solution . . . 137
A6 Instructions for liquid sample filling . . . 137
A7 Fabrication process parameters . . . 139
A8 Electrical characterisation of micro-coils . . . 141
A9 Automated stage . . . 143
A10 Calibration of Z probes . . . 145
A11 Background signal from SU-8 . . . 145
A12 Process capability index . . . 146
A13 Matlab code to generate the bondhead trajectory for a 850 µm coil . . . 147
A14 Matlab code to generate the bondhead trajectory for a DSLL coil . . . 153
A15 Wire bonder parameters for copper wire . . . 159

Bibliography **163**

Publications **185**

Acknowledgment **188**

List of Figures

2.1 Schematic representation of the MAS configuration 13
2.2 Filling factors associated with MAS and MACS setup 15
2.3 Schematic of MACS arrangement 23
2.4 Topology of a LC resonator inductively coupled to a primary coil 25
2.5 Relative sensitivity gain from MACS with respect to the deviation from the Larmor frequency at various Q factors. 28
2.6 Sensitivity loss in inductively coupled coils as compared to tethered coils as a function of Q factor 30
2.7 First reported microfabricated MACS detector 31

3.1 Illustration of a microfabricated MACS insert 38
3.2 Q-factor comparison between interdigitated and parallel plate capacitors at various electrode thicknesses 39
3.3 Eddy current formations in the capacitor. 41
3.4 Simulation of the trajectory of induced eddy currents in capacitor structures 44
3.5 Simulated current densities and specific power dissipation in a parallel plate capacitor structure due to induced eddy currents 44
3.6 Process flow steps to fabricate the parallel plate capacitor 46
3.7 Experimental plan for grinding the SU-8 dielectric layer 47
3.8 Various stages in the fabrication of parallel plate capacitor 48
3.9 Fabricated interdigitated and parallel plate capacitor 49
3.10 Fabrication issues during grinding and polishing process 50
3.11 Delamination of contact pads during wirebonding 51
3.12 Frequency dependent measured capacitances of the interdigitated and parallel plate capacitor 52
3.13 Frequency dependent measured phase angle of the interdigitated and parallel plate capacitor 53
3.14 Q-factor values of the interdigitated and parallel plate capacitor derived from measured phase angle 54
3.15 In-situ temperature calibration and measurement using ethylene glycol . . . 55
3.16 Measured temperature increase due to induced eddy currents in the capacitors. 56

4.1 B_1 field simulation of MACS detectors 61
4.2 B_0 field simulation study to evaluate the effect of material susceptibilities . . 62
4.3 B_0 field perturbation along the direction transverse to the applied magnetic field 62

4.4 B_0 field simulation study to evaluate the effect of material susceptibilities under magic angle condition . . . 63
4.5 Process flow steps to fabricate the micro-coil of the MACS resonator . . . 64
4.6 Experimental plan for fabrication of SU-8 pillars . . . 65
4.7 Optimized post exposure bake cycle for HAR SU-8 structures . . . 66
4.8 Various stages in the fabrication of the micro-coil . . . 67
4.9 Schematic of a capacitor . . . 69
4.10 Negative effects of SU-8 residues on contact pads . . . 70
4.11 Proposal to iron out the obstacle of SU-8 residues on the contact pads . . . 71
4.12 Experimental plan to optimize the thickness of the sacrificial layer . . . 72
4.13 Effect of using an AZ sacrificial layer between contact pads and SU-8 resist 72
4.14 Process issues during encapsulation . . . 73
4.15 Warping of substrates due to internal stress during encapsulation process . . 73
4.16 Electrical characterization of a micro-coil . . . 74
4.17 Electrical and thermal characterization of the MACS device . . . 74
4.18 Changes to the reflection curve upon the introduction of a tuned MACS resonator inside the MAS probe . . . 76
4.19 Changes to the reflection curve observed upon the introduction of various MACS resonators having resonant frequencies from 460 MHz to 540 MHz into the MAS probe. . . . 77
4.20 Tuning and matching the reflection curve of the inductively coupled system back to 500 MHz . . . 78
4.21 Handling liquid samples and packaging the MAS rotor . . . 79
4.22 Solid state sample handling for MACS inserts . . . 80
4.23 Comparison of the nutation spectrum for MAS and MACS coils . . . 81
4.24 $\pi/2$-pulse length at different excitation power levels . . . 82
4.25 Evaluation of the sensitivity enhancement achieved with a MACS insert . . . 83
4.26 NMR spectrum of 500 mM sucrose obtained from a MACS insert . . . 84
4.27 ^{1}H-^{1}H COSY spectrum of 340 mM uniformly ^{13}C-labeled glucose . . . 86
4.28 ^{1}H-^{1}H COSY spectrum of L-Alanine . . . 87
4.29 Schematic of a cross polarization (CP) technique in NMR . . . 88
4.30 CP experiment on 2-^{13}C-labeled glycine . . . 88
4.31 2D HMQC NMR spectrum of 340 mM ^{13}C labeled glucose solution . . . 89
4.32 2D HMQC NMR spectrum of 1 mM natural abundance glucose solution . . . 90
4.33 ^{1}H MAS NMR spectrum of a single Zebrafish embryo . . . 92
4.34 ^{1}H-^{1}H COSY NMR spectrum of a single Zebrafish embryo under MAS condition 93

5.1 Topology of the broadband MACS insert inductively coupled to a MAS probe coil . . . 104
5.2 FEM simulation model of an SSLL insert inductively coupled to a primary coil 106
5.3 B_1 field enhancement observed with SSLL inserts using 2D maps . . . 106

5.4 Simulated B_1 field enhancement observed in the sample region with and without an SSLL insert at various frequencies . . . 107
5.5 Simulated B_1 field obtained in the sample region with an SSLL insert when the diameter of the flux collector is less than 2.5 mm . . . 107
5.6 FEM simulation model of DSLL insert inductively coupled to a primary coil . 108
5.7 B_1 field enhancement observed with DSLL inserts with 2D field maps . . . 109
5.8 Simulated B_1 field enhancement observed in the sample region with and without a DSLL insert at various frequencies . . . 109
5.9 Simulated B_1 field enhancement obtained in the sample region with a HHLL insert . . . 110
5.10 Optimization of the stacked HHLL insert . . . 110
5.11 Experimental plan for dicing using a tunable ultrafast laser . . . 112
5.12 Separation of SU-8 blocks from the substrate using laser ablation . . . 113
5.13 Visual inspection of the substrate after laser ablation . . . 113
5.14 Description of process flow for the fabrication of single solenoid Lenz lens inserts . . . 114
5.15 Partial pre-dicing of the substrate with a laser . . . 115
5.16 Visual inspection of the pre-diced substrate after laser ablation . . . 115
5.17 Various stages in the fabrication of the SSLL inserts . . . 116
5.18 Various stages in the fabrication of the DSLL inserts . . . 117
5.19 SSLL and DSLL inserts . . . 118
5.20 Electroplated electrodes of HHLL inserts . . . 118
5.21 Fabricated HHLL inserts . . . 119
5.22 S_{11} measurements of the DSLL outer coil . . . 121
5.23 Nutation spectrum for SSLL insert . . . 122
5.24 Evaluation of the sensitivity enhancement achieved with a SSLL insert . . . 123
5.25 Nutation spectrum for DSLL insert . . . 124
5.26 Evaluation of the sensitivity enhancement achieved with a DSLL insert . . . 125

A.1 Magic angle probe calibration . . . 136
A.2 Electrical characterization of 550 µm micro-coil . . . 141
A.3 Electrical characterization of 850 µm micro-coil . . . 142
A.4 Electrical characterization of 2550 µm micro-coil . . . 142
A.5 Automated stage for wafer level RF characterization . . . 143
A.6 S-parameter measurements of the MACS detector . . . 144
A.7 Mapping of the characterized MACS coils on the wafer . . . 144
A.8 Calibration of the Z-probe . . . 145
A.9 Background signal from SU-8 . . . 146
A.10 Cpk values for gold electroplating thickness . . . 146
A.11 Cpk values for dielectric thickness . . . 147
A.12 Cpk values for SU-8 pillar height . . . 147

List of Tables

3.1 Desired parameters for MACS detectors 45
3.2 Table of capacitor characteristics 57

4.1 Relative permeability of various materials in the MACS device 61
4.2 Risk analysis 96
4.3 Cpk values for gold electroplating thickness 97
4.4 Cpk values for dielectric thickness after the grinding process 97
4.5 Cpk values for SU-8 pillar height after HAR SU-8 fabrication 97
4.6 Comparison of various MACS detectors for a 4 mm MAS system 98

A.1 Larmor frequency of some common isotopes at 11.74 T 135
A.2 Wirebonder parameters 160

1 Introduction

Amongst the standard set of analytical instruments available, a non-destructive method that would furnish in-depth information from a bare minimum quantity of sample would be the ultimate goal. Alas, such a scenario still remains a distant Utopia. The consequences of not having a universal analytical method allude to the stark reality that the investigators must often rely on their expertise to select the right analytical techniques for their applications and be prepared to work under the constraints of these respective methods.

One of the common methods among these battery of analytical tools is Nuclear magnetic resonance (NMR). It has evolved into a mainstream choice among analytical chemists, structural biologists, medical professionals, quality engineers, material scientists, ever since first successful experiments were conducted by Felix Bloch and colleagues on water at Stanford [1] and independently by Edward Purcell and colleagues on paraffin wax at Harvard [2]. The underlying principle of NMR is based on the perturbation of nuclear spins of active isotopes in a strong constant magnetic field by a weak alternating magnetic field and observing the electromagnetic response of these spins. The frequency response of these nuclear spins are unique and thus serve as fingerprints to reveal the structure of the molecules containing those nuclei.

The underlying reason for widespread adoption of the NMR technique is because of the capability to generate information on structure of the molecules as well as on intermolecular and intramolecular dynamics in a non-destructive manner, since the sample irradiation is done with non-ionizing beams. Moreover, the experimental versatility offered by this technique, in that analysis of broad range of measures such as temperature, flow etc. can be done on solid-, liquid- and gaseous-state specimens under various physical conditions (pressure, temperature, concentration), has made it an invaluable tool.

However, when it comes to minimum required sample for an analysis, NMR is at a significant disadvantage as compared to other common techniques such as mass spectroscopy (MS), X-ray computed tomography (X-ray CT), and infrared spectroscopy (IS) [3]. The low intrinsic sensitivity of NMR technique is due to the low population difference between the two transitional energy states at room temperature. In particular, the low intrinsic sensitivity of the NMR approach is palpable when access to the amount of sample available is restricted. Reduction in sample amount leads to further decrease in the discernible signal from the NMR experiment and this has resulted in the demand for highly sensitive NMR detection methods. This has lead to extensive exploration into NMR methodologies and has been diversified to touch every aspect surrounding NMR whether in direction of instrumentation or acquisition techniques or sample manipulation.

1.1 Motivation

The low intrinsic sensitivity of NMR is a major drawback when studying mass- and volume-limited samples. Furthermore, in the case of solid-state NMR, the demand for sample rotation during magic angle spinning (MAS) further deteriorates the signal-to noise ratio (SNR) due the reduced fraction of volume occupied by the sample inside the detector. The SNR of an NMR experiment [4] for microscopic samples significantly depends on the geometry of the receiver coil, as well on the excitation efficiency (B_1/i). Hence, the application of micro-coils [5–8] has become widespread among NMR practitioners when there is a need to access the reduced number of spins on offer as the sample volume decreases. Consequently, the micro-coil has also made waves in solid-state NMR with the advent of the "piggyback" micro-MAS [9] and magic angle coil spinning technique (MACS) [10], which offers improved SNR as a result of the increase in the fraction of sample volume in the detector.

However, one negative aspect concerned with these techniques is their penetration in the NMR community. Apart from a select few research groups and laboratories, these techniques, although quite promising, have not been adopted across the board. A straightforward yet significant reason which is hindering the progress is due to the cumbersome and tedious nature of constructing these micro-resonators used in these techniques.

Therefore, the main contribution of this thesis is to build on the approach [11] to materialize these miniaturized micro-resonators with the help of advanced micromanufacturing methods and at the same time maintain the excellent NMR performance furnished by these handmade detectors. The developments reported in this thesis aim to take the production of the micro-resonators away from the 'hands' of the NMR spectroscopist, and thereby facilitate high-throughput, high sensitive magic angle spinning NMR experiments.

1.2 Organisation

The thesis is organized into six chapters. The content of chapters are coordinated as follows:

The current chapter (Chapter 1) contains an introduction and the motivation of the topic of the thesis, including a list of objectives.

Chapter 2 provides an introduction on the essentials of NMR and solid-state NMR. The general introduction into NMR is condensed so as to focus more on the solid-state section. Following the introduction into theory, the chapter evolves into an introduction on micro-coils and the MACS technique.

Chapter 3 is dedicated to the various design requirements and fabrication of on-chip capacitors for microfabricated resonators. The chapter also delves into different characterization methods to evaluate the suitability of the on-chip capacitors for the MACS approach.

In Chapter 4, fabrication process of the MACS micro-detector is presented. This is followed by complete characterization of the aforementioned NMR detectors electrically. The NMR performance of these detectors for various samples are also discussed. The devices are also compared to other detectors reported in literature.

In Chapter 5, a novel type of broadband micro-detector for the MACS approach is introduced. The chapter mainly deals with the design and fabrication of these detectors as well as the feasibility of integrating these broadband inserts with the MACS technique.

The results of this thesis are summarized in Chapter 6. A discussion on the the scope and future advancements of the micro-resonators as well as the broadband micro-detectors is initiated.

1.3 Publication

1.3.1 In the scope of this thesis

The results obtained during the course of this thesis are detailed in two publications:

Capacitor re-design overcomes the rotation rate limit of MACS resonators[SA1]:
Journal: Concepts in Magnetic Resonance Part B: Magnetic Resonance Engineering 2018-Wiley
Authorship: Lead author
Content: In this paper, limitations of the tuning capacitor as a part of the MACS detector is explored. The performance of the on-chip capacitors are compared with that of the commercial capacitors. A comprehensive analysis of the advantages and disadvantages of having a capacitor on-chip is discussed.
Contributions: Conceptualization, Microfabrication, data collection, formal analysis, investigation, validation, writing.

Inductively coupled magic angle spinning microresonators benchmarked for high-resolution single embryo metabolomic profiling[SA2]:
Journal: Analyst 2019-RSC
Authorship: Lead author
Content: In this paper, an optimized microfabricated micro-detector for MACS technique is reported. The NMR performance limits of the device are characterized by standard NMR methods. A significant highlight of this article is the NMR spectroscopy of single embryo Zebrafish samples.
Contributions: Conceptualization, Microfabrication, data collection, formal analysis, investigation, validation, writing.

1.3.2 Side projects

Within the course of this thesis, multiple collaborations were established. These collaborations led to two peer-reviewed publications.

A non-resonant kinetic energy harvester for bioimplantable applications[SA3]:
Journal: Micromachines 2018-MDPI

Authorship: Fourth author
Content: In this paper, design and verification of a linear non-resonant kinetic energy harvester for implantable devices are discussed. The energy harvester employs coils and permanent magnets to convert motion to the electrical signal.
Contributions: Microfabrication, formal analysis, investigation, validation.

A sub-cm^3 energy harvester for in-vivo biosensors [SA4]:
Journal: Microelectronic Engineering 2020-Elsevier
Authorship: Second author
Content: This article reports the characterisation of the kinetic energy harvester. The performance of the device installed on a linear shaker was studied in the first step. In the next step, the device was employed for an *in vivo* characterisation by embedding it on a wrist band and for different activities.
Contributions: Microfabrication, formal analysis, investigation, validation.

1.3.3 Conference contributions

Intermediate results of this research were presented in conferences.

On-chip capacitors for MACS NMR detectors
Conference: Euromar 2017
Authorship: First and presenting author
Content: This poster discusses preliminary results on the optimization of the on-chip capacitors for MACS micro-detectors. The poster presentation won the best poster award at the EUROMAR 2017 conference held in Warsaw.

1.3.4 Book Chapter

Within the course of this thesis, there was a contribution to a book chapter on coil fabrication techniques for miniaturized magnetic resonance with a focus on magic angle coil spinning.

Micro and Nano Scale NMR: Technologies and Systems: Innovative Coil Fabrication Techniques for Miniaturized Magnetic Resonance Detectors [SA5]
Book: Wiley-2018
Authorship: Contributing author
Content:The book chapter introduces the reader to miniaturization of NMR detectors and the application of different kinds miniaturized detectors into various NMR techniques.

2 Starting point

The current chapter provides an introduction to the fundamental concepts required for this thesis. Most of the information contained in this chapter were collected from four well known textbooks [12–15]. Additional theoretical concepts and deductions from this chapter have also been reported in a research article in Concepts in Magnetic Resonance, Part B (Wiley) journal [SA1].

Atoms in the matter are made up of proton, electron and the neutron. The proton and neutron together make up the nucleus of an atom. In addition to mass and electric charge, the nucleus has two other important properties namely, magnetism and spin. Although, the natural chemical and physical properties remain unaffected by nuclear magnetism and nuclear spin, they do serve as an excellent non-invasive means to identify the internal structure of a physical substance.

'Spin is an intrinsic property of the particle and is a form of angular momentum'[13]. Even at absolute zero temperature where all rotational angular momentum ceases to exist, an elementary particle always has spin. As a result the majority of nuclei (consists of proton and neutron) also possess spin and the nuclear spin quantum number is denoted by I. The overall spin of a nuclei is derived from spins of protons and neutrons. For e.g., the ^{1}H nucleus has a single proton, hence has spin, I = 1/2, whereas its isotope deuterium (^{2}H) nucleus, containing one unpaired proton and one unpaired neutron, has ground state nuclear spin, I = 1. Nuclei with a net nuclear spin, I = 1/2, are known as a spin-1/2 system whereas nuclei with net nuclear spin, I > 1/2, are called quadrupolar nuclei. There are a few other isotopes in nature such as ^{4}He, ^{12}C, ^{16}O etc. which have zero unpaired protons and neutrons. As a result they have a net nuclear spin, I = 0 and they are considered NMR inactive.

Therefore, an NMR active nuclei has atleast one unpaired proton or neutron and consequently different isotopes display unique behaviour from an NMR perspective. Similarly, the nuclear spin also possesses a 'magnetic moment'. The ratio of the magnetic moment of a nuclear spin to its angular momentum is called the *gyromagnetic ratio* and this ratio is unique for an isotope. Table A.1 in Section A2 lists a selection of nuclear isotopes and their properties such as spin quantum number, gyromagnetic ratio, and natural abundance. Equation 2.1[1] describes the relationship between the magnetic moment of a nuclear spin with its angular momentum.

$$\widehat{\mu} = \gamma \cdot \widehat{S} \tag{2.1}$$

[1]The wider hat symbol is a quantum mechanical operator

The atomic nucleus and in turn the nuclear spin can interact with its environment because it possesses an electric charge and might carry a magnetic moment, which interacts with electric and magnetic fields respectively. The interaction with its surrounding maybe external or may originate internally.

2.1 Nuclear spin interactions

One of the simplest, yet important internal interaction is the coupling between two neighbouring nuclear spins due to their respective magnetic fields, also known as dipolar coupling. The interaction can be either between two same isotopic spins (homonuclear) or two different isotopic spins (heteronuclear). In most cases, for nuclei lying a few bonds apart in a molecule, the coupling between the spins is also influenced by the bonding electrons. In such cases, the interaction is known as indirect dipolar coupling or *J-coupling*. The strength of nuclear spin coupling without the intervention of the electron clouds, also known as direct dipolar coupling, is proportional to their internuclear distance as a function, r^{-3}. Another mechanism of internal spin interaction is how a nuclear spin experiences a slightly different magnetic field due to the magnetic field generated by the induced currents in the electron clouds. This is known chemical shift interaction or electron shielding. For a spin system, I > 1/2, the electric quadrupole moment of the nucleus can couple strongly with the electric field gradients generated by the surrounding electron clouds. This is known as electric quadrupolar interaction.

External spin interaction arises in the presence of an applied magnetic field. This manipulation of the nuclear spin by the application of various kinds of magnetic fields forms the basis of NMR. The strong coupling of the nuclear spins to external magnetic fields is a remarkable feature of NMR and leads to extraordinary possibilities.

In the absence of an external stimulus, the ensemble of nuclear spins are randomly oriented with zero net magnetization and the energy levels are degenerate. The presence of a strong static magnetic field ($\vec{B_0}$) leads to splitting between the energy levels[2] resulting in a net magnetization along the direction of the applied magnetic field. Upon the application of a transverse magnetic field ($\vec{B_1}$), interaction of the nuclear spin with this radio-frequency (RF) field induces transitions between the split energy levels and consequently there is a net magnetization perpendicular to the static magnetic field. This transverse magnetization starts to rotate in a plane perpendicular to B_0 until it reaches equilibrium. The rotation of the transverse magnetization is called precession and the frequency of precession is equal to the precession frequency of the nuclear spin, also known as '*Larmor frequency*'.

The precession of transverse magnetization leads to an oscillating magnetic field which induces an electrical current in a nearby conductor. The oscillating induced current is known as Free induction decay (FID) or the NMR signal. A relationship between the Larmor frequency, gyromagnetic ratio of the nucleus and the static magnetic field is given in Equation 2.2.

[2] A nuclear spin with spin quantum number I has (2I+1) energy levels. Splitting occurs when the degeneracy of the energy levels is broken and this phenomenon is known as Zeeman splitting.

Another form of coupling in which the nuclear spin interacts with an external stimuli is through weak gradient fields which, as they are called, provide a magnetic field gradient along different coordinate positions.

$$\omega_L = -\gamma B_0 \tag{2.2}$$

The Zeeman splitting of the nuclear spin energy levels, say for a ^1H nucleus (I= 1/2), leads to two energy states with the lower energy state (α) is populated slightly higher than the higher energy state, β. The relative population difference between the two energy states can be written as shown in Equation 2.3.

$$\frac{\Delta N}{\Sigma N} = \frac{N_\alpha - N_\beta}{N_\alpha + N_\beta} = \frac{e^{-E_\alpha/k_BT} - e^{-E_\beta/k_BT}}{e^{-E_\alpha/k_BT} + e^{-E_\beta/k_BT}} \approx \frac{\gamma h B_0}{4\pi k_B T} \tag{2.3}$$

where,
E = hν = h$\omega/2\pi$ = h$\gamma B_0/2\pi$,
B_0 = static magnetic field (T),
h = Planck's constant (6.63× 10^{-34} Js),
γ = Gyromagnetic ratio (rad/sT),
T = Temperature (K),
k_B= Boltzmann's constant (1.38×10^{-23} J/K).

Expanding the exponential as a power series and approximating it to the first two terms (e^x ≈ 1 + x) yields a population difference of 40 ppm for a magnetic field strength, B_0, of 11.74 T at 298 K. Therefore, the inherent insensitivity of NMR experiment stems from the minute population difference between the states.

2.2 Solid state NMR

Although, the pioneering NMR experiments were carried out both on liquid as well as solid state samples, liquid state NMR had briskly evolved into a powerful spectroscopic technique as compared to NMR of solids. Historical progression in the field such as Fourier Transform (FT)-NMR spectroscopy, pulse sequence techniques, technical advancements in cryogenics and superconducting magnets, and NMR instrumentation had been hugely responsible for liquid state NMR to be widely adopted as a standard analytic tool.

The prime impediment to the development of NMR in the solid state was the natural linewidths of the resonance lines on offer. Spectral resolution in the case of NMR spectroscopy of solutions is typically in the range of 0.1 to 1 Hz whereas those in cases of solid state samples, can be as large as 180 kHz. A popular example that is often stated is the comparison of linewidths between ^1H NMR spectra of water and ice.

The difference in spectral linewidths arises from the rapid molecular tumbling (Brownian motion) or motional averaging, occurring in liquids but mostly being absent in the case of solids. The broadening of the resonance lines is due to fact that the various internal nuclear

spin interactions in solids are anisotropic. The magnetic dipolar interactions between nuclei is the primary source of line broadening. The other secondary sources include the rest of the internal nuclear spin interactions such as electron shielding (chemical shift), electron spin-nuclear spin interactions, indirect electron coupled nuclear spin-spin interactions, and quadrupolar interactions. In principle, information from solid state NMR spectra is far more richer than its liquid state counterpart since the latter is described by a motionally averaged isotropic Hamiltonian and the former by the full anisotropic Hamiltonian. In fact, a wealth of data can be obtained by suppressing one kind of interactions and 'liberating' the others. However, it is often the case that small interactions are overshadowed by the more prominent ones and the measurement is hampered by these large sources of broadening. Hence, significant efforts were undertaken to establish techniques to move towards 'high resolution' solid state NMR by manipulating these anisotropic effects.

The successful pioneering attempts towards obtaining 'liquid like' NMR spectra from solids were reported by Andrew and colleagues [16, 17] and then independently by Lowe [17] with their introduction of the technique called 'Magic Angle Spinning' (MAS). In their experiments, they introduced motional averaging into the sample by rotating it about an axis that is at an (magic) angle of 54.74° to the magnetic field. Rapid specimen rotation at the magic angle leads to an equivalent effect on the anisotropic interactions as the rapid molecular tumbling in liquids, resulting in narrow spectral linewidths.

A few years down the line Ostroff and Waugh [18] and Mansfield and Ware [19] developed an alternative approach to line narrowing in solids by imposing motional averaging in the spin space as opposed to in coordinate space. In their set of experiments, they applied a sequence of RF pulses which imposed time dependence (similar to molecular tumbling) on the spin terms and pulse sequences were devised to average the time-dependent interactions to zero. This method is now popular as multiple pulse NMR. Unlike MAS where almost all of the anisotropic interactions are averaged out, multiple pulse technique can be used to suppress one interaction while retaining the information from others. Although these two techniques were perceived to be competitive approaches in the beginning, at present they are considered complementary techniques [20] in solid state NMR.

After a while, Pines, Gibby and Waugh [21, 22] introduced a method to perform high-resolution NMR of low γ nuclei or 'chemically dilute spins' in solids by repeated transfer of polarization from high γ nuclei or abundant spins (typically protons). The irradiation of the protons by a high power resonant RF pulse during the observation of the rare spin (^{13}C, ^{15}N) eliminated the line broadening in the NMR spectrum of rare spins due to their dipolar coupling with the protons. Additionally, the proton polarization transfer by using Hartmann-Hahn condition [23] enhanced the weak NMR signals from the low γ nuclei. Cross-polarization magic angle spinning experiments (CP-MAS) by Schaefer and Stejskal [24], where ^{13}C NMR spectra was observed from solid state specimens by removing the J-couplings and heteronuclear dipolar interactions using CP along with anisotropic chemical shift and weak homonuclear interactions using MAS, truly opened the door for high-resolution solid state NMR. Additionally, isotopic dilution with deuterium [25] has been described as an another

approach where ^1H spectral resolution of the order of 100 Hz was reported for per-deuterated microcrystalline proteins.

In the following sections, the focus will be exclusively on MAS NMR and its development.

2.3 MAS NMR

MAS technique [16, 17], today is considered to be the most effective method to overcome the spectral broadening due to anisotropic interactions in solid state NMR spectroscopy. Spinning the sample at the magic angle, i.e. at 54.7° with respect to the static magnetic field axis, B_0, at speeds exceeding the magnitude of anisotropic interactions, averages them either to zero or non-zero isotropic values. Multiple pulse irradiation technique is limited by its inability to remove anisotropic chemical shift interactions and prevent line broadening due to residual heteronuclear dipolar interactions. Hence, a combination of multiple pulse NMR along with MAS, known as combined rotation and multiple pulse spectroscopy (CRAMPS) technique [20] was developed. Along with CRAMPS, CP-MAS method [24] for low abundant nuclei has made MAS an important tool to study polycrystalline, amorphous and biomolecular solids.

The Hamiltonian, $\mathscr{H}$, of a nuclear system described in Equation 2.4, includes all the interactions such as the Zeeman splitting, dipolar broadening, chemical shift anisotropy and quadrupolar interactions. This Hamiltonian can then be manipulated by the introduction of an external stimulus or perturbation such as RF fields, sample spinning etc., which render the system Hamiltonian time dependent.

$$\mathscr{H} = \mathscr{H}_z + \mathscr{H}_d + \mathscr{H}_{cs} + \mathscr{H}_Q + \mathscr{H}_o + \mathscr{H}_{RF}(t) \tag{2.4}$$

The Hamiltonian, $\mathscr{H}_d$ describing the magnetic dipolar interaction, i.e., the direct interaction between two magnetic dipoles, say $\vec{\mu}_1$ and $\vec{\mu}_2$ separated by a distance, $\vec{r}$, can be derived from the energy of their interactions as follows in Equation 2.5:

$$\vec{E}_d = -\vec{\mu}_1 \cdot \vec{B_{\mu 2}} \tag{2.5}$$

$$\vec{E}_d = -\vec{\mu}_1 \cdot \left(\frac{\mu_o}{4\pi|r|^3}(3(\vec{\mu}_2 \cdot \hat{r})\hat{r} - \vec{\mu}_2)\right) \tag{2.6}$$

$$\vec{E}_d = -\vec{\mu}_1 \cdot \left(\frac{\mu_o}{4\pi|r|^3}(3(\hat{r} \cdot \hat{r}^T)\vec{\mu}_2 - \vec{\mu}_2)\right) \tag{2.7}$$

$$\vec{E}_d = -\frac{\mu_o}{4\pi|r|^3}(3\vec{\mu}_1(\hat{r} \cdot \hat{r}^T)\vec{\mu}_2 - \vec{\mu}_1 \cdot \vec{\mu}_2) \tag{2.8}$$

where $\hat{r}$ is a unit vector in the direction of the line joining the two spins[3] and μ_o is the permeability constant.

Substituting the terms into quantum mechanical operators, i.e., E_d into $\mathscr{H}_d$, $\vec{\mu}_1$ into $\gamma_1\hbar\widehat{I_1}$ and $\vec{\mu}_2$ into $\gamma_2\hbar\widehat{I_2}$, where $\hbar$ is the reduced Planck's constant, we obtain:

[3]The hat symbol denotes a unit vector

$$\mathscr{H}_d = -\frac{\mu_o}{4\pi}\frac{\gamma_1\gamma_2\hbar}{|r|^3}(3\widehat{I_1}(\hat{r}\cdot\hat{r}^T)\widehat{I_2} - \widehat{I_1}\cdot\widehat{I_2}) \tag{2.9}$$

Converting the unit vector, $\hat{r}$, into spherical coordinates as shown in Equation 2.10 where, θ is angle between the magnetic field, B_0 and the vector connecting the two spins.

$$\hat{r} = \begin{pmatrix} \sin\theta\cos\phi \\ \sin\theta\sin\phi \\ \cos\theta \end{pmatrix} \tag{2.10}$$

In the presence of an external high magnetic field, the Hamiltonian described in Equation 2.9, truncates into Equation 2.11

$$\mathscr{H}_d = -\frac{\mu_o\gamma_1\gamma_2\hbar^2}{16\pi^3|r|^3}\frac{3\cos^2\theta - 1}{2}(3\widehat{I_{1z}I_{2z}} - \widehat{I_1}\cdot\widehat{I_2}) \tag{2.11}$$

$$F(\theta_\mathrm{m}) = \frac{1}{2}\cdot(3\cdot cos^2\theta_\mathrm{m} - 1) \tag{2.12}$$

The Hamiltonian, $\mathscr{H}_d$, contains the spatial factor, $F(\theta_\mathrm{m})$, shown in the Equation 2.12. When the sample is spun at the magic angle, the spatial factor goes to zero, hence the magnetic dipolar interaction is averaged to zero [17]. Optimum lineshape is observed when the spinning frequency (ω) is high enough to suppress the magnitude of all the anisotropic interactions. Spinning sidebands in MAS appear as an integer multiple of the rotation speed [26, 27]. The presence of additional spinning sidebands in the NMR spectrum may hinder the interpretation of the spectrum.

Average-Hamiltonian theory [29] makes it possible to write the time-dependent Hamiltonian as a series of time-independent Hamiltonians. This theory, although does not describe spinning sidebands, was used to characterize the Hamiltonians when the spinning frequency exceeds the anisotropy of the interactions, i.e. faster spinning [30]. For inhomogeneous interactions, such as from a two-spin system chemical shift anisotropy, the resonance linewidths are largely frequency independent. However, for homogeneous interactions, such as the multiple homonuclear dipolar couplings, up to a factor of 10 higher spinning frequency is necessary for narrow linewidths [30]. Sometimes, even a factor of 10 higher frequency is not enough to average all interactions by MAS. As a result MAS hardware technology has seen significant advances which has breached specimen rotation speeds beyond 100 kHz [31] and steadily increasing to 110 kHz [32], 126 kHz, [33], 140 kHz [34] and 170 kHz [35] in rotors of diameters down to 0.5 mm, which has enabled the study of samples containing spin populations with anisotropic interactions up to 50 kHz [36].

Therefore, recent advances in MAS NMR technology have resulted in improved structural investigation of ^1H and other spin-1/2 systems [37]. However, for NMR spectroscopy of solids with quadrupolar nuclei, MAS alone is not adequate to completely remove the anisotropic broadening due to the interaction of the nuclear electric quadrupole moment with the electric field gradient [38]. The inhomogeneous broadening on the order of MHz is much stronger

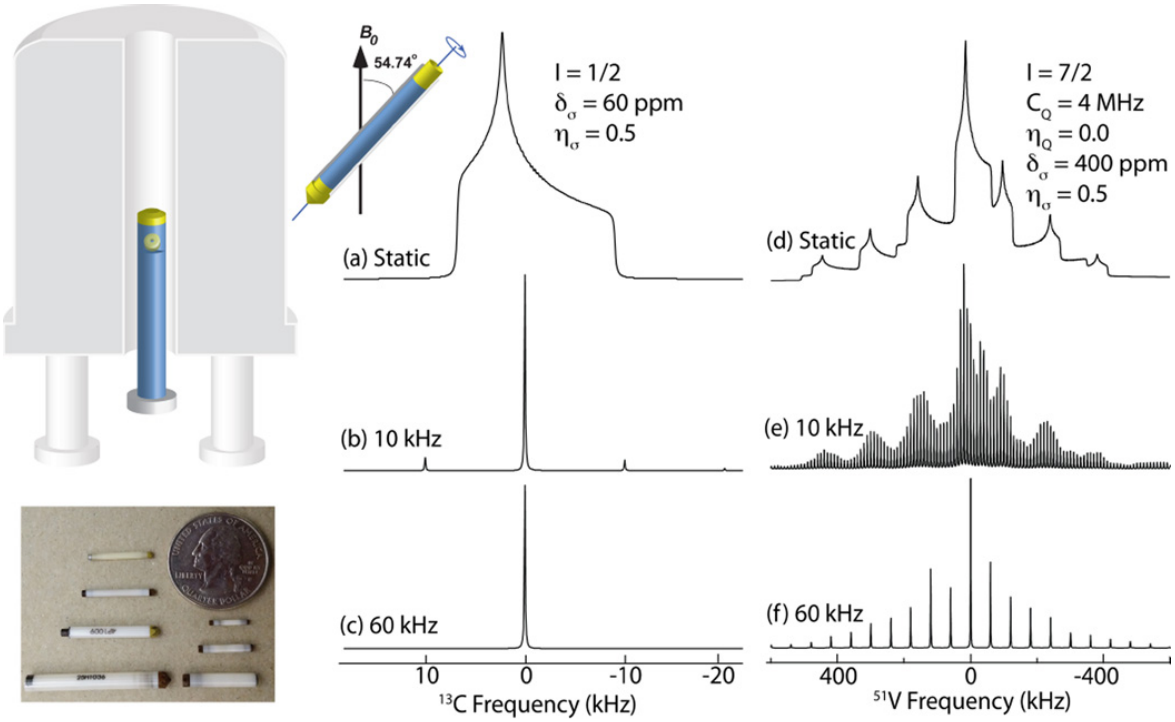


Figure 2.1: **Left**: Schematic representation of the MAS arrangement along with various rotors available at different diameters. Smaller the rotor faster the spinning speed. **Middle**: Illustration of the improved spectral resolution for a spin-1/2 nucleus system (^{13}C). From a static sample, the spectrum is quite broad due to chemical shift anisotropy (CSA) as shown in (a). Under the MAS condition of 10 kHz, the CSA get averaged out into an isotropic peak and spinning sidebands which represent the Fourier components of the MAS frequency as shown in (b). Under the MAS condition of 60 kHz, the MAS frequency exceeds the magnitude of the CSA as shown in (c). **Right**: Illustration of the effect of MAS on NMR lineshapes in a spin-7/2 nucleus (quadrupolar) system (^{51}V). From a static sample, the broadening of lineshapes is observed due to a combination of of quadrupolar and CSA as shown in (d). Under the MAS condition of 10 kHz, the CSA get averaged out into an isotropic peak and spinning sidebands as shown in (e). Under the MAS condition of 60 kHz, spinning sidebands are still observed as shown in (f). This shows that even 60 kHz rotation rates are not sufficient to completely average either the CSA or the quadrupolar interactions. Therefore, to get improved spectral information from quadrupolar nuclei higher rotation rates are necessary. Printed with permission from Polenova *et al.* [28]. Copyright (2015) ©ACS publications

than the broadening due to dipolar and chemical shift interactions. MAS NMR was used for the suppression of first-order quadrupolar interactions in ^{23}Na nucleus through extremely precise setting of the magic angle [39]. The initial approaches for the removal of the second-

order quadrupolar interaction involved sample spinning around two angles. Double rotation experiments (DOR) [40, 41] were conducted by spinning the sample around two angles simultaneously whereas dynamic angle spinning (DAS) approach was achieved by rotation around two angles sequentially [42]. However, these two techniques did not catch on because of the requirement of complex probeheads to achieve double rotation. However, an alternative approach of MAS based correlation experiments, multiple-quantum MAS (MQMAS) [43] and satellite-transition (STMAS) [44], achieved with conventional MAS probeheads using two dimensional experiments have made acquiring high-resolution spectra of quadrupolar nuclei more convenient.

Figure 2.1 [28] shows a typical MAS setup and describes the effect MAS spinning has on solid state samples. NMR spectrum was obtained from a spin-1/2 system (^{13}C) and spin-7/2, i.e., a quadrupolar (^{51}V) system at various spinning speeds. The line shape from the static sample is significantly broad due to anisotropic and quadrupolar interactions respectively. However, spinning the sample under low speed MAS conditions (10 kHz), leads to the averaging of the chemical shift interactions in the nuclei which results in narrow lineshapes and spinning sidebands. Under high speed MAS conditions (60 kHz), the sidebands disappear from the spin-1/2 spectrum indicating that MAS frequency exceeds the magnitude of anisotropic interactions. However, in the case of quadrupolar nuclei, MAS speeds of (60 kHz) are not sufficient for complete averaging. Therefore, higher rotation rates are required.

Higher sample rotation rates can be achieved by reducing the diameter of the rotors. Under reliable operation, specimen rotation of up to 170 kHz [35] using rotors of diameters down to 0.5 mm has been demonstrated [45]. The relationship between rotor diameter and maximum achievable rotation frequency can be expressed based on the material properties of the rotor as shown in Equation 2.13 [45]. The stability of the rotor is mainly governed by its tensile strength. Secondary factors to stable spinning include rotor alignment with respect to its bearing, quality of sample filling inside the rotor and quality of pneumatic (compressed N_2 or He gas) actuation of the rotor. As a rule of thumb for the current MAS technology, the product of maximum stable spinning frequency and rotor diameter can be expressed approx. as 90 kHz mm.

$$\nu = \frac{\sqrt{3}}{\pi} \cdot \sqrt{\frac{TS \cdot \delta_w}{D}} \cdot \frac{1}{\phi_r} \tag{2.13}$$

where,
ν = spinning frequency (rad/s),
TS = Tensile strength of the material,
D = density of the material,
δ_w = relative wall thickness of the material,
ϕ_r= rotor diameter.

2.3.1 Sensitivity issues with state of the art MAS technology

In addition to NMR being intrinsically a low sensitivity approach, the requirements of sample rotation in solid state NMR introduced additional bottlenecks with respect to sensitivity. The issues arise due to the drastic reduction in the filling factor of MAS experiments as the sample which was filled into a rotor was far away from the detector. This was more severe in the case of DOR. Filling factor is defined as fraction of volume occupied by the sample inside the detector or the coil. The aforementioned problem was aggravated when the amount of specimen available was limited. In Figure 2.2, the black dots represent the sample filling fractions of different MAS technologies available until now. The signal-to-noise ratio (SNR) of the experiment will be lower with the reduction in the filling factor because only noise is picked by the NMR detector in the region without sample.

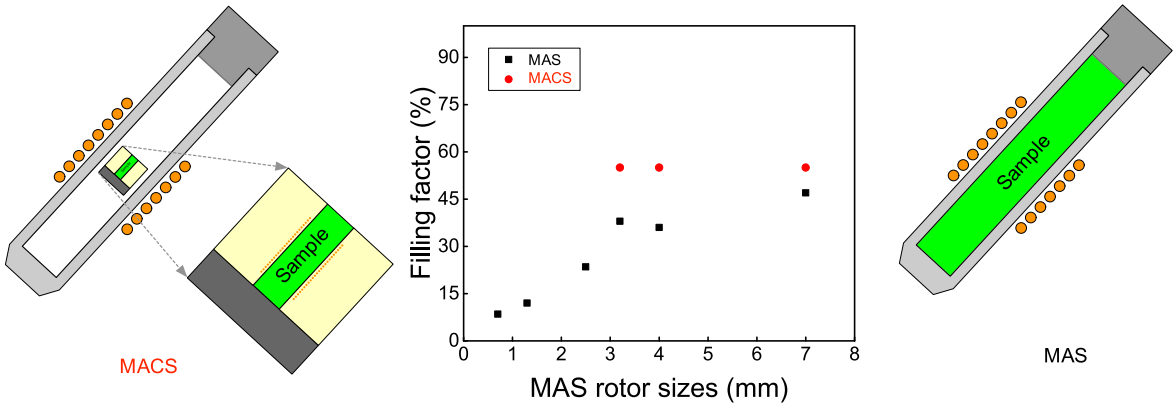


Figure 2.2: Filling factors associated with MAS rotors of different sizes. The air gap between the MAS rotor and the probe coil has been conservatively estimated to be around 0.5 mm by visual inspection. For the case of 3.2 mm and 2.5 mm MAS systems, thin walled rotors have been considered. The MACS detector sizes correspond to the inner diameter of the rotors they fit in. The MACS detector is consists of a 500 µm diameter coil connected to an on-chip capacitor. Adapted from Adhikari *et al.* [46] Copyright 2018 ©Wiley.

Therefore, MAS technique is in dire need of boosting its sensitivity. There have been multiple approaches to enhance the sensitivity of an NMR experiment. Some of these methods in combination with MAS provides the opportunity to alleviate the sensitivity issues associated with MAS and this thesis reports on the hardware strategies that have been developed and is in development over the years to overcome this problem.

2.3.2 Sensitivity enhancement techniques for solid state NMR

A self-evident approach to enhance the sensitivity of any NMR experiment is the brute force approach of increasing the strength of the magnetic field, B_0. It has been established that

the sensitivity scales to $7/4^{th}$ power of the static magnetic field strength [4]. However, this approach is incredibly expensive as well time consuming with the state-of-the-art 1.2 GHz (28.2 T) magnet costing over 12.5 million Euros [47] and taking over 5 years to go from 1 GHz to 1.2 GHz NMR.

Another strategy is to tweak the critical element behind the low intrinsic sensitivity in NMR, i.e. the Boltzmann distribution of the spins across energy levels. This has provoked the NMR community to come up with techniques to boost the population difference between energy levels and this method of achieving higher net magnetization by establishing non-Boltzmann populations is known as hyperpolarization. Hyperpolarized nuclei display spin polarization by a factor of 10^4-10^5 above Boltzmann distribution numbers under thermal equilibrium conditions.

One hyperpolarization approach to enhance the sensitivity of an NMR experiment is by transferring polarization from electron spins to nuclear spins through dynamic nuclear polarization (DNP) technique. The electron magnetic moment is approx. 660 times larger than the nuclear magnetic moment of proton. Albert Overhauser [48] proposed the idea of enhancing the signal intensities (ideally by 660) associated with NMR by transferring polarization of unpaired electrons to the nearby nuclei. This was done by saturating the electron spin resonance (ESR) of the conduction electrons using microwave irradiation which is popularly known as the Overhauser effect. The experimental verification by Carver and Slichter [49] further strengthened this idea of increasing the polarization of one species by saturating the transition in another. There have been other DNP polarization mechanism proposed based on microwave irradiation such as the solid-effect, the cross-effect, and thermal-mixing [50].

DNP in combination with MAS soon followed [51–53] with experiments done at 1.4 T on a sample of coal (contains many free electrons) and mixtures of polymers. However, extending the method to higher static magnetic fields (B_0) was restricted by lack of strong microwave sources needed to saturate the electron transition at higher frequencies. The breakthrough arrived in the form of a microwave source known as the gyrotron oscillator which could supply 100 W of 140 GHz irradiation for performing DNP experiments at 5 T [54]. Subsequent work has seen an improvement in these millimetre wave regime microwave sources with the development of a 250 GHz [55] gyrotron which in combination with a low temperature (100 K) MAS probe offered proton signal enhancements of around 170. This success has motivated the development of subsequent high-frequency gyrotrons at 330 GHz [56] and 460 GHz [57]. The high field DNP MAS [58–60] activity has been further stimulated by the introduction of chemically synthesized biradicals as a substitute for the monomeric polarizing agents yielding a factor of 4 larger signal intensities [61]. Further improvements in sensitivity, suitability and polarization transfer efficiency at high fields has been observed with biradicals such as TOTAPOL [62], PyPol, AMuPol [63] and TEMTriPols [64].

Another exciting hardware development has been in the field of MAS rotors. Recently, Chen *et al.* have demonstrated that moving from traditional cylindrical rotors into spherical rotor domain [65] would be beneficial to couple microwaves for DNP [66]. Moreover, the improved mechanical stability offered by the spherical geometry enables faster rotation speed

than achievable with cylindrical rotors. They have also been reported to facilitate easier sample exchange as well as optimizing real estate inside narrow bore of probeheads with improved stator design. Sample rotation speeds of 4.6 kHz and 28 kHz were observed with 9.5 mm and using 4 mm rotors respectively. Although the preliminary investigations showed sensitivity degradation due to poor filling factors [65], an updated stator design in combination with reduced rotor diameter (2 mm) [67] have demonstrated significant sensitivity enhancement along with faster spinning in the range 57 kHz to 68 kHz. Although the technology is at a development stage, the spherical rotor setup holds a promising future in the field of DNP MAS.

Another promising approach to produce highly spin-polarized samples is by using para-Hydrogen (p-H_2), a spin isomer of Hydrogen, in hydrogenation reactions to transfer polarization to an unsaturated molecule [68]. Two popular approaches, namely, PASADENA [69–71] and ALTADENA [72], where the hydrogenation takes place inside and outside the magnet respectively, have been developed and signal enhancements of around 10 000 [73] has been reported. These experiments with para-hydrogen are generally classified as para-hydrogen induced polarisation (PHIP). Another PHIP variant is the signal amplification by reversible exchange (SABRE) [74], a non-hydrogenative method, i.e. a technique to hyperpolarize sample without their chemical modification. Recently, PHIP technique has been demonstrated in a microscale [75, 76] and picomolar sensitivity has been demonstrated. PHIP techniques have been generally popular in the low field domain and as such have not made rapid inroads into solid state NMR [77, 78].

Nuclear spin polarization can also be enhanced by polarization transfer from an optically pumped nuclei [79, 80] such as ^{3}He or ^{129}Xe through spin polarization induced nuclear Overhauser enhancement (SPINOE) technique which has led to a 50 times increase in the proton NMR signal strength [81]. The optical pumping methods have been combined with MAS [82, 83] where laser-polarized ^{129}Xe was inserted into a spinning rotor and continuous flow was maintained using He as a carrier to hyperpolarize proton spins on the sample surface. However, the lack of generality is the limiting factor for these methods. Only certain metabolites can be hyperpolarized, meaning that the significant sensitivity boost is not realized for all analytes.

Optical pumping methods have also been utilized to hyperpolarize ^{13}C nuclei in diamond in a 9.4 T static magnetic field, through nitrogen-vacancy (NV) centers in diamond, a form of crystal defect [84]. More recently, the NV centers have been introduced as magnetic field sensor towards detecting single nuclear spin [85–88]. Small volumes of nuclear spins (10^4-10^6) from proton emanating from liquid and solid state samples placed on the surface of the diamond were detected using NVs created 2.5 to 20 nm below the diamond surface [85, 86]. The near surface NVs were able to sense protons from a detection volume less than 5 nm^3. There have been further attempts at single-proton spin detection by bringing the NVs as close as down to 2 nm from the diamond surface [88]. However, as promising as it seems, the technique is at a nascent stage and would take a few more years to mature.

Another classical approach to boosting sensitivity is to improve the conditions on the detection side of the NMR experiment. The weak NMR signal generated by the precessing

nuclei is acquired with the help of RF inductors. These inductors, also called coils, are tuned with the help of other passives to the Larmor frequency of interest and matched to 50 Ω for the efficient reproduction of the spectral information. As an alternative for the nuclear induction method, a few other detection schemes such as mechanical detection [89], SQUID (Super conducting quantum interference device) detection [90], and magnetometry [91] have been reported. However, these substitutes have not matured into widespread utilization in the NMR community.

Unfortunately, when it comes to RF coils, there is no one single design that is an universal fit for all NMR experiments. A homogeneous B_1 field along the direction that is transverse to the B_0 field is one of the foremost criteria for designing NMR receiver coils [92]. Other important characteristics include high SNR or sensitivity, sufficient bandwidth to observe the full range of spectral information and material compatibility (avoiding paramagnetic materials). As per convention, in order to have a high SNR, the magnetic coupling between the receiver and the sample has to be as high as possible. This can be achieved by matching the size of the coil physically to that of the sample. This led to the emergence of micro-coils or micro-detectors (diameter < 1 mm) to improve the mass sensitivity when the volume of the sample available was limited [3, 7, 93–95]. As an example, if we consider that around 10 nmol of material of interest, is dissolved into observation volume of 100 nl (typical volume of micro-coils) would result in a sample concentration of 100 mM. In contrast, mixing the same amount of material with 250 µl of solvent (typical observation volume in a 5 mm sample tube) yields a sample concentration of 40 µM. Therefore, using a micro-coil, the observed sample has concentration of 100 mM as opposed to 40 µM concentration in a commercial 5 mm saddle coil, which leads to the conclusion that significant enhancement in the mass sensitivity could be achieved with a micro-coil when the amount of sample available is limited.

However, the drawback of reducing the size of sample, as in the case of micro-coils, means that the thermal noise from the coil dominates the sample noise. Therefore, reducing it would be another way to increase the SNR as the reduction in noise brings about decrease in the coil resistance. This can be accomplished by using a coil wire which behaves like a superconductor at an elevated temperature [96] or by using cryogenically cooled coils [97]. However, there is a cost disadvantage to this thermal noise reduction approach as high temperature superconducting wires are much more expensive as compared to regular copper wires and there is always the handicap of maintaining a large temperature difference between the sample and the coil in miniaturized detectors [98].

Although initially limited to liquid-state, micro-coils have also become widely applicable in the field of solid-state NMR [10, 99] owing to significant sensitivity increase in addition to stronger RF irradiation that can be achieved with this approach. This has enabled the NMR spectroscopists to broaden the horizon of solid-state NMR.

2.4 Micro-coils in NMR

Micro-coils have been widely used in liquid state NMR spectroscopy to improve the sensitivity of the NMR experiment when the amount of sample available is limited [3]. A micro-coil handles sample volumes typically in the range of few microlitres down to volumes in the nanolitre regime and facilitates high RF excitation frequencies in the MHz range to be applied to the sample [100, 101]. They are especially useful when the amount of sample available is limited or in the case of expensive samples.

Hoult and Richards [4] have as a part of their experiments on SNR of NMR detectors reported that the B_1-field per unit current i generated from the coil was a measure of sensitivity of the detector coil. This was based on the argument that the signal detected from a sample by a coil is proportional to the induced magnetic field in the sample by an unit current passing through the coil. This is known as the 'principle of reciprocity'. They extended the formulation of the SNR of an NMR experiment proposed by [50] into an expression shown in the form of Equation 2.14.

$$SNR \propto \frac{{\omega^2}_{\mathrm{o}} \cdot (\frac{B_1}{i}) \cdot V_s}{\sqrt{4 \cdot k_{\mathrm{b}} \cdot T \cdot R_{\mathrm{coil}} \cdot \Delta f}} \tag{2.14}$$

where,
ω = nuclear precession frequency (rad/s),
V_s = Sample volume,
R_{coil} = Resistance of the coil,
T = Coil Temperature (K),
Δf= Spectral bandwidth (Hertz),
B_1/i = ratio of magnitude of transverse magnetic field induced in the RF coil by unit current, i.

The Equation 2.14 assumes an optimal filling factor, which is defined as the amount of field occupied by the sample. Peck *et al.* [102] simplified the Equation 2.14, for solenoids, to be expressed as SNR per unit sample volume formulated in Equation 2.15.

$$SNR_{\mathrm{puv}} \propto \frac{{\omega_{\mathrm{o}}}^2[n/d\sqrt{1+(\frac{h}{d})^2}]}{\sqrt{n^2 d {\omega_{\mathrm{o}}}^{1/2}/h}} \propto \frac{{\omega_{\mathrm{o}}}^{7/4}}{d} \tag{2.15}$$

where,
d is the diameter of the coil. Thus, the from Equation 2.15 it can be concluded that sensitivity drawback can be significantly overcome by reducing the size of the coil.

2.4.1 NMR Figures of merit

The improvement in sensitivity offered by micro-coils, however, comes at a cost. Since these coils have high filling factors, the sample is usually located in close proximity to the wires. This has a negative effect on the resolution of the spectral lines as a result of B_0 field distortions

caused due to the susceptibility variations at the coil/sample interface. There have multiple approaches to eliminate this issue such as immersing the coil susceptibility matched liquid and using thick-walled sample containers [8, 93], employing zero-susceptibility wires for coil construction [103] and using susceptibility-matched plugs at the ends of the sample container [104]. However, using thick-walled capillaries decreases filling factor of the coil, which leads to a reduction in the sensitivity.

Therefore, sensitivity and resolution can be described as mainstays for any NMR experiment and the basis on which an experiment can be qualified. *Sensitivity* is defined in terms of minimum amount of nuclear spins which is necessary to generate a signal that can be deciphered above the background noise. '*Resolution*, on the other hand, is defined as the capability to clearly distinguish between multiple features from the acquired signal.

There are different ways to calculate the sensitivity of an NMR experiment. One method is to calculate the time-normalized concentration sensitivity, S_c which is based on sample concentration. Additionally, the sensitivity of an NMR experiment is a function of its SNR and acquisition time, t_{acq}. The strength of the signal scales linearly with the t_{acq} and on the other hand the noise also increases with time and scales quadratically as $t_{acq}^{1/2}$ [3]. Therefore, the time-normalized concentration sensitivity, S_c, can be expressed as shown in Equation 2.16:

$$S_{\mathrm{c}} = \frac{SNR}{C_s \cdot {t_{\mathrm{acq}}}^{1/2}} \tag{2.16}$$

where
C_s is the sample concentration.

Lacey *et al.* introduced a more consistent approach for calculating sensitivity with micro-coils and mass- and volume-limited samples, termed as mass sensitivity and the normalized limit of detection [3] as shown in Equation 2.17 and Equation 2.18 respectively. The normalized limit of detection can be defined as the amount of sample that needs to be observed to yield an SNR value of 3.

$$S_{\mathrm{m}} = \frac{SNR}{mol \cdot {t_{\mathrm{acq}}}^{1/2}} \tag{2.17}$$

$$nLOD_{\mathrm{m}} = \frac{3 \cdot mol \cdot {t_{\mathrm{acq}}}^{1/2}}{SNR} \tag{2.18}$$

where *mol* is the mole amount of the sample that resides within the active volume concentration.

The spectral resolution of an NMR experiment can be characterized by measuring the spectral linewidth at 50 % of peak intensity, also known as full-width-at-half-maximum (FWHM) [3]. Another characterization method is to measure the baseline resolution of the spectra. This is done by determining the spectral line width at 0.55 % and 0.11 % of peak intensity.

Another important Figure of merit that can assess sensitivity is the probe efficiency [4, 11]. It is described in the Equation 2.19 and is a measure of the electrical power, P, required to generate a transverse field for 90° rotation of the magnetization vector.

$$\eta_P = \frac{B_1}{i \cdot \sqrt{r_c}} = \frac{B_1}{\sqrt{P}} = \frac{1}{4 \cdot \tau_{\pi/2} \cdot \sqrt{P}} \tag{2.19}$$

Clark *et al.* [105] have previously reported that for a solenoidal geometry, the probe efficiency can be expressed in terms of the coil Q factor, coil volume and its frequency, ν and scaling factor α based on the aspect ratio (l_{coil}/d_{coil}) of the coil as shown in Equation 2.20:

$$\eta_P = \frac{B_1}{\sqrt{P}} = \alpha\sqrt{\frac{Q_{coil}}{V_{coil} \cdot \nu}} \tag{2.20}$$

2.4.2 Micro-coil topologies

Reducing the size of detector has its own set of challenges, especially in terms of design and fabrication. Downsizing of coil geometries which have been successful at the macro scale is not always straightforward or feasible. Nonetheless, there have been plenty of creative solutions put forward to tackle this problem and miniaturization has been accomplished in a wide variety of approaches [6, 8, 106–108]. This has churned out multitude of micro-coils over the last few years employing variety of geometries and a slew of manufacturing techniques to materialize these micro-coils [108].

The most popular form of micro-coil geometry have been the μ-Solenoids [93, 102, 109, 110] which were produced by wrapping metal wires or tracks around support structures such as glass capillaries, cured epoxy or polymers. Moreover, a comprehensive guideline has been established on optimizing the μ-Solenoid geometry for RF homogeneity and SNR [111, 112]. The μ-Solenoid geometry is still popular since it offers highest sensitivity [4] and highly uniform magnetic field in the center of coil.

Another topology that has been extensively reported in the micro-NMR literature are the planar μ-coils [113–115] and the design rules and fabrication methods have been thoroughly investigated [116]. Their ease of fabrication as compared to the μ-Solenoids have made them highly popular for integration with microfluidics [114, 115]. However, their sensitivity is inferior compared to the μ-Solenoids. Another direction that the micro-coil development has advanced is in the evolution of linear geometries. In contrast to spiral and solenoidal micro-coils, linear geometries such as the striplines [117–119] and the μ-slot [120, 121] employ a single current path and the RF field is concentrated close to the sample by constriction of the cross-section of the current path. The conductor accommodates a standing wave with current anti-node at the sample region and nodes at the ends. These linear geometries demonstrate excellent sensitivity and spectral resolution and can be easily integrated with microfluidics [119].

Other micro-coil geometries such as the Helmholtz pair [122–124] and the Helmholtz μ-saddle geometry (modified Helmholtz pair) [125–127] have also been reported. These two

configurations offer excellent spectral resolution for NMR experiments. Since the direction of B_1 field is perpendicular to their axis, in contrast to solenoidal geometry, sample loading can be done along the axis of the static magnetic field, B_0. As a result, the B_0 field cuts across fewer material interfaces, thus leading to minimal distortion. Recent advancements in micro-manufacturing have made the classic Helmholtz pair [124, 128] and the saddle coil geometry [129] an attractive option to combine NMR with microfluidics. Additionally, the feasibility of producing two decoupled orthogonal saddle coils observing the same sample region [126, 127] opens up new avenues in multi-nuclei NMR spectroscopy.

2.4.3 Micro-coils in solid-state NMR

The MAS technique [16, 17], where the sample is spun at the magic angle, i.e. at 54.7° with respect to the static magnetic field axis, B_0, has been extensively adopted in solid-state NMR. Therefore, in order to maintain the highest possible filling factor, RF coils in the MAS probes are also oriented at the magic angle and thus generating an RF magnetic field, B_1 which is not perpendicular to B_0. Thus, only the horizontal component of this RF field, B_1, contributes to the transverse magnetic field capable of rotating the magnetization vector onto a plane perpendicular to B_0.

Hence, due to this constraint, solenoidal geometry is preferred to the saddle coils in MAS configurations as 82 % ($B_1 \sin(54.7\,^\circ)$) of B_1 field generated by the RF coil is at disposal for the former and only 58 % ($B_1 \sin(35.3\,^\circ)$) of B_1 field for the latter. Additionally, the advantage of minimum B_0 field distortion offered by saddle coils is also negated by their orientation along the magic angle.

The sensitivity issues associated with MAS technique has been well documented and micro-coils have been propped up as a solution to alleviate these concerns. The early approach involved the "piggyback" micro-MAS [9] technique, where a μ-Solenoid based resonator along with a sample holder was mounted onto an existing stator of a commercial MAS probe. The precision machined sample holder was then spun at the magic angle with the help of a standard MAS rotor. This was shortly followed by the MACS technique where again a μ-Solenoid based resonator along with a sample container was integrated into the standard MAS rotor and inductively coupled with the existing coil of a commercial MAS probe [10]. The MACS approach involved the co-rotation of the micro-coil ensemble and the sample and proved extremely versatile unlike the piggyback method where major modifications to the probehead along with precise alignment of the micro-coil circuit to the rotor axis were necessary. Planar transmission line resonators in Helmholtz arrangement were also discussed as an alternative to μ-Solenoids for MACS [130], however they offered lower sensitivity boost as compared to μ-Solenoids (3 in comparison to range of 6 to 14). Additionally, a Helmholtz arrangement has been reported with sample rotation capabilities [123], however, rotation at the magic angle has not been demonstrated. Rapid development in μ-Solenoid research has also resulted in smaller MAS probes with detector size going down to ≤ 1 mm [35, 131].

Therefore, solenoidal geometry has been considered the most suitable for solid-state NMR spectroscopy using MAS [132]. Moreover, due to its versatility, the MACS technique has emerged as a serious contender to boost sensitivity in MAS NMR spectroscopy.

2.5 MACS NMR

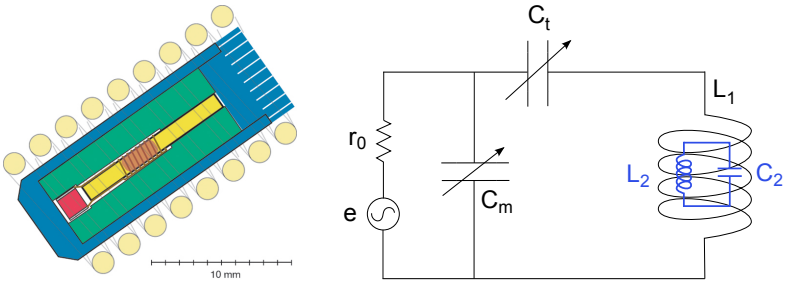


Figure 2.3: a) Schematic of magic-angle coil spinning insert. The micro-coil insert is fabricated by handwinding a copper wire around a capillary and the leads of the wire are soldered to a high Q capacitor. Reproduced with permission from Sakellariou *et al.* ([10]). Copyright (2007) ©Nature. All rights reserved. b) Basic circuit diagram for inductive coupling between the probe coil, L_1 and the micro-coil, L_2]. Reprinted (adapted) with permission from Sakellariou *et al.* ([10]). Copyright (2007) ©Nature.

Houlton [133], in 1997, presented that the SNR of an NMR experiment with small samples could be significantly improved by using a flux enhancer, i.e., a tuned circuit conforming to the size of the sample which was inductively coupled [134] to the larger coil. Sakellariou *et al.* [10] applied these findings to MAS and pioneered the MACS technology where an inductively coupled micro-coil resonator was spun along with the sample. This technique offered sensitivity enhancements of the order of 6 to 14 for a 4 mm MAS probe for nanolitre sample volumes [10, 135]. In addition the sensitivity boost, MACS technology has the added advantage that no additional modifications to MAS hardware is required. Moreover, the isotropic susceptibility effects from the constituents of the micro-coil are averaged to zero and thus eliminated because of rotation at the magic angle [16, 17].

The micro-coil resonator was produced by manual winding of copper wires around quartz capillaries and the ends of the wire soldered to a discrete capacitor. The micro-resonator along with capillary was then centred inside a MAS rotor using machined Shapal-M (AlN) cylinder as shown in Figure 2.3a. Therefore, the strenuous and labour intensive process of fabricating this micro-detector and sample filling can be considered a disadvantage in comparison to standard MAS experiments where only sample preparation is required. Additionally, MACS technique is also adversely effected by induced eddy currents in the spinning micro-coil ensemble which would lead to sample degradation and spectral line broadening.

The basic foundation that is indispensable to the functioning of the MACS technique is the wireless inductive coupling between the rotating micro-coil and the standard coil in the MAS probe as shown in Figure 2.3b. Since the micro-coil is not tethered to any terminals, its rotation at the magic angle is feasible.

In NMR aside from the MACS technique, inductive coupling has found application in integration of microfluidics with NMR [114, 136] to improve throughput and sensitivity, in flow-NMR [137], liquid-state NMR in general [138], MR microscopy of brain tissue with resonant coils [139] and broadband coil [140], and tracking of the MR-catheter during interventional MRI (iMRI) [126]. A micro-coil which is inductively coupled with an external larger coil has been also developed as a solution to get around the need for impedance matching [141] using bulky capacitors and inductors and lossy coaxial cables [142–145]. There is also a comprehensive review on the practice of inductive coupling methods in MR probe design [146].

The subsequent sections will focus on the fundamental concepts of inductive coupling. The signal acquisition using the wireless coupling approach will be compared to the tethered wire method. The theory and calculations for inductive coupling between two coils have been based from three well known sources in NMR literature [15, 146, 147].

2.5.1 Inductively coupled micro-coils

The concept of inductive coupling [134] in basic electronic theory has been well established for many years. The underlying principle of resonant inductive coupling is explained in the simplified circuit diagram as shown in the Figure 2.4. The micro-resonator is a combination of micro-coil L_c, with a resistance R_c and a capacitor, C. This ensemble is coupled to the larger primary coil with an inductance L_p and resistance R_p. The capacitors, C_t and C_m act as tuning and matching capacitors respectively for the coupled system. The two coils have a mutual inductance, M_{cp}, which means that magnetic flux from these respective coils cuts across the region enclosed by each other.

Using Kirchhoff's voltage and current law, following equations are derived from Figure 2.4.

$$V_x = I_c \cdot j\omega M_{\mathrm{cp}} - I_x \cdot (R_p + j\omega L_{\mathrm{p}}) \tag{2.21}$$

$$I_c \cdot (R_{\mathrm{c}} + j\omega L_{\mathrm{c}}) - I_x \cdot j\omega M_{\mathrm{cp}} + \frac{I_c}{j\omega C} = 0 \tag{2.22}$$

The coupling strength between them hinges on a number of factors such as proximity, alignment, their respective electrical characteristics and is defined by a constant denoted as coupling factor k. In the case of two solenoids, one of the criteria for maximum coupling is that their respective axis is concentric and they show zero coupling when they are perpendicular to each other The mutual inductance, M_{cp}, can be expressed in terms of the individual inductances, L_c and L_p, and coupling factor k, as shown in Equation 2.23:

$$M_{cp} = k\sqrt{L_c L_p} \tag{2.23}$$

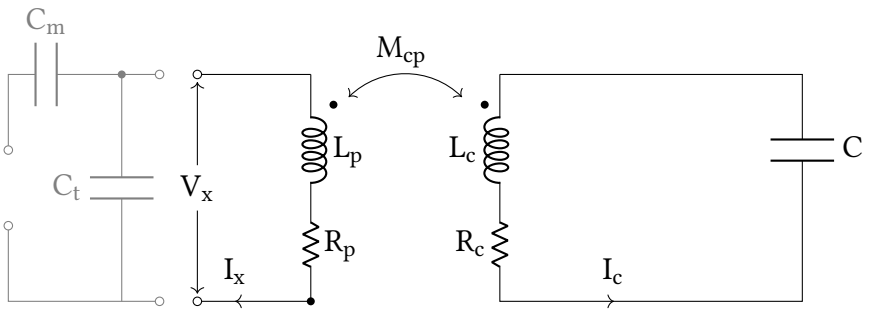


Figure 2.4: Topology of a LC resonator inductively coupled to a primary coil. A tuned micro-coil L_c with the capacitor C is coupled through mutual inductance M_{cp} to the primary coil L_p. The capacitors, C_t and C_m, perform the functions of tuning and matching respectively. A voltage, V_x is induced across coil, L_p.

The effective impedance, Z_x or Z_{eff} can be obtained by combining Equation 2.21, Equation 2.22 and Equation 2.23 as shown in Equation 2.24:

$$Z_{eff} = Z_p + Z_{ceff} = R_p + j\omega L_\mathrm{p} + \frac{\omega^2 k^2 L_\mathrm{c} L_\mathrm{p}}{R_\mathrm{c} + j\omega L_\mathrm{c} + \frac{1}{j\omega C}} \tag{2.24}$$

For concentric solenoids, the coupling constant, k can be defined approx. as a ratio of their respective volumes, V_C and V_p, by Equation 2.25:

$$k = \sqrt{\frac{V_c}{V_p}} \tag{2.25}$$

where V_c is the volume of the micro-coil and V_p is the volume of the primary coil.

Based on the strength of the coupling between the coils, systems can be classified as overcoupled, tightly coupled, critically coupled or loosely coupled [134]. The critical coupling coefficient, k_c can be expressed in terms of quality factors of the individual coil system as shown in Equation 2.26 [134]:

$$k_c = \frac{1}{\sqrt{Q_c Q_p}} \tag{2.26}$$

where $Q_c = Q_{\mu R} = \omega L_\mathrm{c}/R_\mathrm{c}$ is the quality factor of the micro-resonator (assuming the capacitor has infinite Q) and $Q_p = \omega L_\mathrm{p}/R_\mathrm{p}$ is the quality factor of the primary coil.

In the MACS technique, the sample excitation efficiency is at the highest when almost all of the applied power gets dissipated in the micro-coil and a very negligible fraction in the primary coil. Therefore, this efficiency, E, as shown in Equation 2.27 can be defined as fraction of the total applied power that gets dissipated in the micro-resonator.

$$E = \sqrt{\frac{P_c}{P_{total}}} = \sqrt{\frac{P_c}{P_c + P_p}} \tag{2.27}$$

Assuming the resonance condition, i.e., the micro-resonator is tuned to the Larmor frequency, the effective impedance, Z_{eff} in Equation 2.24 can be simplified to include only DC resistances. Additionally, since the same current, I_x, is flowing through both coils, Equation 2.27 can be expressed only in terms of coil resistances, R_c and R_p as shown in Equation 2.28:

$$E = \sqrt{\frac{{I_x}^2 R_{ceff}}{{I_x}^2 R_{ceff} + {I_x}^2 R_p}} = \sqrt{\frac{R_{ceff}}{R_{ceff} + R_p}} = \sqrt{\frac{1}{1 + \frac{R_p}{R_{ceff}}}} = \sqrt{\frac{1}{1 + \frac{R_p}{\frac{\omega^2 M_{cp}^2}{R_c}}}} \tag{2.28}$$

Substituting Equation 2.25 and Equation 2.26 into Equation 2.28, the inductive coupling efficiency in the MACS configuration can be obtained in terms of either coupling factor, k, and critical coupling factor, k_c or in terms of Q factors, Q_c and Q_p and coil volumes, V_c and V_p respectively.

$$E = \frac{1}{\sqrt{1 + (\frac{k_c}{k})^2}} = \frac{1}{\sqrt{1 + \frac{V_p}{V_c Q_c Q_p}}} \tag{2.29}$$

The coupling efficiency, E, can also be applied to predict the enhancement in the B_1 field obtained from the MACS resonator as compared to primary coil. Taking the ratio of their respective probe efficiencies and combining Equation 2.20 and Equation 2.27, the ratio of their respective B_1 field is obtained as shown in the Equation 2.30:

$$\frac{\frac{B_1^{coil}}{\sqrt{P_c}}}{\frac{B_1^{probe}}{\sqrt{P_p}}} = \sqrt{\frac{Q_c V_p}{Q_p V_c}} \tag{2.30}$$

$$\begin{aligned} \frac{B_1^{coil}}{B_1^{probe}} &= \sqrt{\frac{P_c}{P_p}} \sqrt{\frac{Q_c V_p}{Q_p V_c}} \\ &= E \sqrt{\frac{Q_c V_p}{Q_p V_c}} \end{aligned}$$

where B_1^{coil} is the B_1 field generated by the micro-coil in the MACS arrangement and B_1^{probe} is the B_1 field generated by the primary coil in the probe in standalone operation, i.e., in the standard MAS arrangement.

Combining Equation 2.20 and Equation 2.30, the relative enhancement in the B_1 field can be expressed in terms of the quality factor, Q_c, of the micro-resonator as shown in Equation 2.31:

$$\frac{B_1^{coil}}{B_1^{probe}} = Q_c\sqrt{\frac{1}{1+\frac{Q_pQ_cV_c}{V_p}}} = Q_c\sqrt{\frac{1}{1+(\frac{k}{k_c})^2}} \tag{2.31}$$

Therefore, by observing Equation 2.29, it can be inferred that when the coupling factor is much larger to the critical coupling, $k >> k_c$, the inductive coupling efficiency, E, is close to 100 %. Under this condition, the two coils are considered to be overcoupled and bulk of the applied power gets dissipated in the micro-coil resonator. Under the critical coupling condition, $k = k_c$, the applied power gets dissipated equally between the micro-coil and coil in the probe. Therefore, at first glance, overcoupled regime looks to be desired mode of wireless coupling. Additionally, according to Equation 2.31, the B_1 field enhancement in the MACS arrangement, when the coils are undercoupled, i.e., $k << k_c$ is directly a function of quality factor of the micro-resonator.

2.5.2 Effect of frequency offset of MACS inserts

For Equation 2.29, the inductive coupling efficiency, E, was derived for a micro-resonator tuned to the exact Larmor frequency. However, in reality, it is quite challenging to fabricate a micro-resonator tuned precisely to required frequency. Imperfections in micro-coil fabrication will lead to some degree of offset from the target frequency. So naturally, it is necessary understand the effects of imperfect tuning on the enhancement in sensitivity.

To understand the loss in sensitivity, necessary modifications have to be made to Equation 2.28. Since the micro-resonator is tuned away from the Larmor frequency, pure resistance terms in the equation have to be replaced by real part of the impedance Z_{ceff}.

$$Re(Z_{eff}) = Re(\frac{\omega_L^2k^2L_cL_p}{R_c + j\omega_LL_c + \frac{1}{j\omega_LC}}) = \frac{R_c(\omega_L^2M_{cp}^2)}{R_c^2 + (\omega_LL_c - \frac{1}{\omega_LC})^2} = \frac{(\omega_L^2M_{cp}^2)}{(1+4Q_c^2(R_c\frac{\Delta\omega}{\omega_L})^2)} \tag{2.32}$$

Using the non-ideal terms calculated in Equation 2.32 for R_{eff} in the efficiency Equation 2.28, the modified Equation 2.33 is obtained to describe the coupling efficiency, E, when the micro-resonator is not tuned to the Larmor frequency.

$$E \approx \frac{1}{\sqrt{1+(\frac{k_c}{k})^2(1+4Q_c^2(\frac{\Delta\omega}{\omega_L})^2)}} \tag{2.33}$$

The significance of Equation 2.33 is illustrated in Figure 2.5, where the loss in sensitivity gain is estimated for ± 50 MHz offset in the tuning frequency for the micro-resonator when its Q factor, Q_c is in the range from Q= 12 to 50 at 500 MHz. It can be clearly observed that the higher the Q factor of the micro-resonator the narrower the bandwidth for its tuning offset from the target frequency. Therefore, a high Q micro-detector in the MACS arrangement is

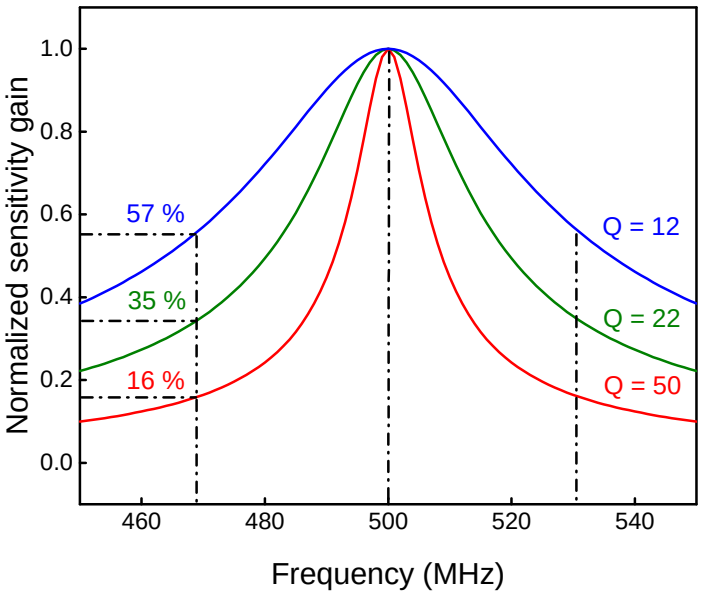


Figure 2.5: Relative sensitivity gain from MACS with respect to the deviation from the Larmor frequency at various Q factors. Adapted with permission from [148] Copyright 2019 ©Royal Society of Chemistry.

much more susceptible to higher SNR losses due to mis-tuning as compared to the one with relative low Q factor.

On the other hand, as observed from Equation 2.29 and Equation 2.31, high Q is also imperative for high coupling efficiency and sensitivity. Therefore, the ideal scenario would be a high Q micro-detector tuned exactly to the Larmor frequency of interest. However, limitations in fabrication techniques compels this proposition quite challenging.

Moreover, the coupling of a micro-detector tuned to the Larmor frequency with a tuned primary coil causes de-tuning of the coupled system. Higher the Q factor of the micro-resonator, further away is the tuning from the desired frequency. To re-tune to the desired frequency and match the impedance of the coupled system to 50 Ω, the capacitance range of the tuning and matching capacitors, C_t and C_m respectively, should be broad enough when the Q factor is high [147]. This also introduces a bottleneck for MACS technique in terms of SNR degradation. Nonetheless, the assertion that the micro-resonator Q is a vital cog in the MACS technique cannot be understated.

2.5.3 Effect of Q factor of the micro-resonator

Therefore, it is important to find out the close to ideal Q factor, if not the optimum value, of the micro-resonator for MACS technique. Additionally, it is imperative that wireless coupling technique is compared to the standard configuration of direct connection using wires for the same micro-coil. This can be investigated from the sensitivity offered by each method.

The sensitivity of any micro-coil is directly related to its probe efficiency as shown in Equation 2.19. Assuming the micro-resonators are tuned to the Larmor frequency, the impedance term transforms into pure resistance term.

$$SNR_{direct} \approx \frac{B_c}{I_c\sqrt{R_c}} \tag{2.34}$$

$$SNR_{wirless} \approx \frac{B_c}{I_x\sqrt{R_{eff}}} \approx \frac{B_c}{I_x\sqrt{R_p(1+k^2Q_cQ_p)}} \tag{2.35}$$

Under resonance condition, the ratio of the magnitude of the current flowing through micro-coil and the primary coil can be expressed as shown in Equation 2.36

$$\frac{I_c}{I_x} = \frac{\omega M_{cp}}{R_c} = \frac{\omega k\sqrt{L_cL_p}}{R_c} \tag{2.36}$$

Therefore combining Equation 2.34, Equation 2.35, and Equation 2.36 the SNR ratio of wireless coupling technique to direct connection method is expressed as shown in Equation 2.37:

$$\frac{SNR_{wirless}}{SNR_{direct}} = \frac{\frac{B_c}{I_x\sqrt{R_p(1+k^2Q_cQ_p)}}}{\frac{B_c}{I_c\sqrt{R_c}}} \frac{k\omega\sqrt{L_pL_c}}{\sqrt{R_pR_c}\sqrt{1+k^2Q_pQ_c}} = \frac{k\sqrt{Q_pQ_c}}{\sqrt{1+k^2Q_pQ_c}} \tag{2.37}$$

Considering a 4 mm MAS system with the primary coil having a Q factor of 200, the essence of Equation 2.37 is illustrated in Figure 2.6. For different realistic scenarios of volume ratios ((V_c or $V_{\mu R}$)/(V_p or V_{MAS}) = k^2) between the micro-resonator and the primary MAS coil, SNR penalty incurred for wireless mode of micro-coil operation is presented as a function of the Q factor of micro-resonator, $Q_{\mu R}$ or Q_c. At first glance, it can be inferred that a minimum micro-resonator Q of 20 is desired to have SNR loss in the wireless configuration at less than 15 %. This number also fits well into Equation 2.33, which describes the relationship of Q factor to mis-tuning.

For nominal values of $Q_p = 200$, $Q_{\mu R} = Q_c = 20$, and $k = 0.03$, $SNR_{wireless}/SNR_{direct} = 0.88$. That means a 12 % loss in SNR occurs due to the wireless approach. Improving the quality factor of the micro-detector as well increasing coupling k between the detector and primary coil will further reduce the SNR loss.

2.6 Microfabricated MACS detectors

The vast majority of reports on MACS NMR spectroscopy [10, 99, 149–153] has employed a MACS detector that was produced by winding a copper wire around a capillary manually and soldering the ends of the wire to a commercial capacitor. However, this approach of serial fabrication of MACS resonators is not reproducible and prone to imperfections. Additionally, the process itself is tedious and requires finely honed skills for coil winding and soldering. Further, the non-magnetic capacitors as well the soldering interface may lead to distortion in

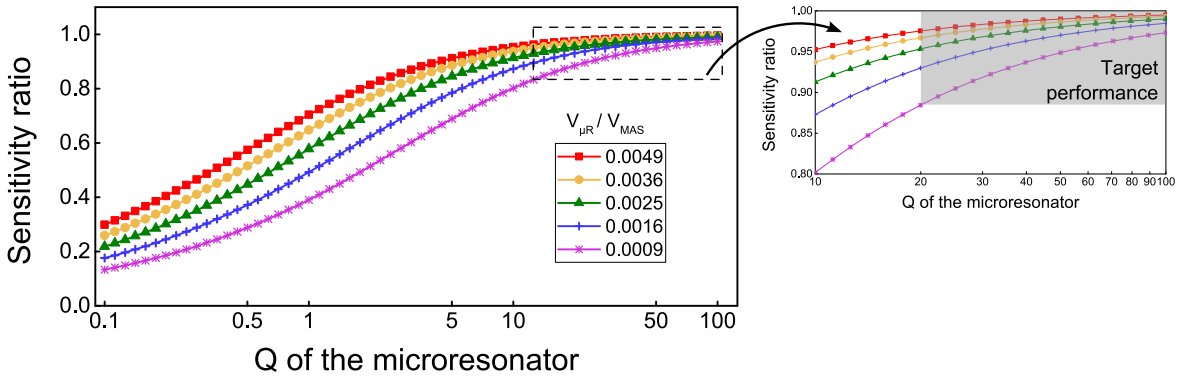


Figure 2.6: Ratio of the SNR in an inductively coupled configuration to the SNR in a tethered configuration, versus the quality factor of the micro-resonator $Q_{\mu R}$ (Equation 2.38). Each curve represents a different volume ratio between the micro-resonator and the outer MAS coil indicated as in the inserted table. Q of the primary coil, Q_P, is taken as 200. Adapted from [46] Copyright 2018 ©Wiley.

B_0 field if the susceptibility artifacts cannot be averaged out by rotation at the magic angle. They also contribute towards additional heating effects due to induced eddy currents [154, 155]. More often than not it might also be difficult to achieve stable MAS rotation, especially at high rotation speeds, if the capacitor and coil ensemble is not centered inside the rotor.

These grievances led to the development of first reported microfabricated MACS detector by Badilita *et al.* [11] based on the combination of automated wirebonding technology [156, 157] and wafer-scale microfabrication techniques [158] as shown in the Figure 2.7. This added a degree of sophistication to the fabrication of micro-resonators and introduced a new approach to produce these detectors in a parallel manner. However, combining the wirebonded micro-coil with an on-chip capacitor degraded the electrical performance of these devices. This was attributed to the poor Q factor of the interdigitated on-chip capacitors. The linewidth of the spectral lines in the NMR spectrum acquired using these detectors was also quite poor1 ppm. Further, the reported aspect ratio of the micro-coil was approx. 0.65 which lead to poor homogeneity of the B_1 field generated by the coil. To add to these issues, handling these detectors proved tricky as well because of the exposed coil as shown in the Figure 2.7a.

These microfabricated devices were improved by implementing some modifications such as improving the B_1 field homogeneity by increasing the aspect ratio of the coil, replacing the gold coil wire with copper, device packaging to enable easy handling, optimize the capacitance for a given footprint and so on [159, 160]. As a result, these modified detectors demonstrated improvements in line resolution going from 1 ppm to 0.03 ppm. However, sensitivity enhancement was still not optimal with the on-chip interdigitated capacitor exhibiting poor Q factor. Moreover, thermal characterization, to study the effect of induced eddy currents, of both these devices were not performed.

Another microfabricated MACS device that has been reported is the monolithic MACS insert [130]. The design for these devices was based on the transmission-line resonator (TLR),

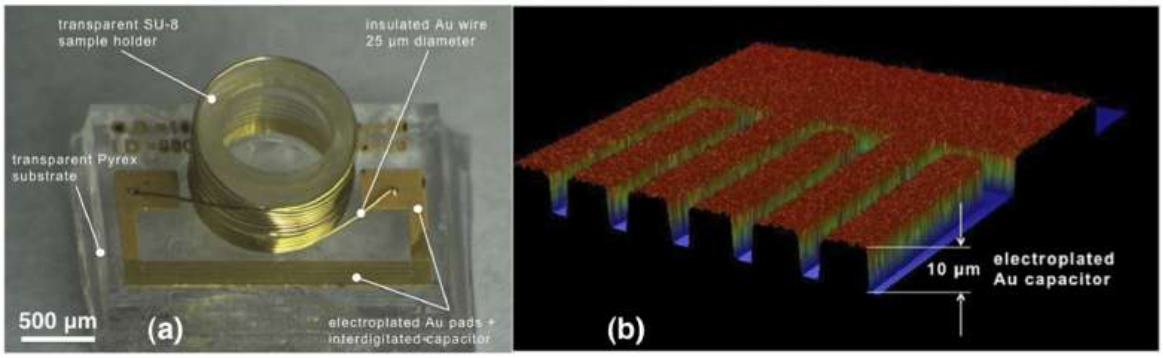


Figure 2.7: a) Microscope image of the microfabricated NMR insert; b) Profile of the electroplated on-chip capacitor. Printed with permission from Badilita *et al.* [11]. Copyright (2012) ©PLOS publications

with the sample sandwiched between two such planar devices to form a volume detector which is self-resonant. The Q factor for these devices were reported be around 50. Nonetheless, only a factor 3 times enhancement in sensitivity was demonstrated with these detectors as compared to around 6 to 14 for handwound detectors. Since the self-resonance in these devices was achieved using capacitance that is parasitic in between copper tracks, the Q factor of the capacitor is considered to be poor. The reported spectral resolution of 0.1 ppm was also quite average. Although, the fabrication process was much simpler as compared to the wirebonded MACS detectors, it was not as robust, because these TLR's had to be mounted manually on sample containers made of plastic cylinders. Therefore, the mass production potential of these monolithic MACS detectors is much less than the corresponding wirebonded MACS devices.

2.7 Discussion

The wirebonded resonant devices [11] have demonstrated immense potential towards mass-fabrication of MACS detectors. However, detector performance is currently the limiting their reach in the NMR community. Therefore, immediate goal is to improve the inductive coupling efficiency of these detectors which can be accomplished by increasing their Q factor. Additionally, a characterization on the effect of induced eddy currents on the spectral quality from these devices is also in need of the hour.

Equation 2.37 established the minimum required Q of the micro-resonator, $Q_{\mu R}$, to have considerable sensitivity enhancement from these devices. $Q_{\mu R}$ depends both on the Q factor of the micro-coil, Q_c, as well as the capacitor Q factor, Q_{cap}. This can be described in Equation 2.38.

$$Q_{\mu R} = \frac{Q_{cap} \cdot Q_c}{Q_{cap} + Q_c}. \tag{2.38}$$

Since the micro-coil Q factor, Q_c, is somewhat fixed [156], the on-chip capacitor has to be redesigned to improve its Q factor. The integration of a high Q on-chip capacitor, optimized for its thermal performance, with a wirebonded micro-coil would be the major challenge to overcome. From Equation 2.38, it can be observed that for an extremely high Q_{cap}, ($Q_{cap} >$ 2500), $Q_{\mu R} \approx Q_c$.

The growth of these microfabricated MACS devices is intertwined with their mass-production efficiency. Therefore, establishing a robust wafer-scale manufacturing process capable of producing 1000s of such devices on a substrate has the possibility to revolutionize MACS NMR spectroscopy.

Further, the application of the resonant MACS detectors is limited to the frequency to which they are tuned. This makes it necessary to have detectors at different frequencies to measure different nuclei or to conduct NMR experiments at different magnetic field strengths. A concept for non-resonant variety of MACS detector with broadband performance across the frequency spectrum is also envisaged.

3 MEMS capacitors for MACS

The inductively coupled micro-detectors employed for MACS NMR technology has resulted in enhanced sensitivity of the MAS NMR experiments [10]. The micro-detector, which is essentially a micro-coil, is tuned to the Larmor frequency of interest with the help of a tuning capacitor. The most common implementation of the MACS technique has seen the tuning capacitor as a discrete element soldered [10, 152] to the ends of a handwound micro-coil. Other variations of the MACS micro-detector has the capacitance originating from an on-chip capacitor [11, 160] or from the parasitic effects between the windings of the coil [130].

The limitations, described in Section 2.6, imposed by the use of soldered commercial capacitors on the MACS detector in MACS experiments have led to the development of the capacitor integrated with the micro-coil [11, 130, 160]. Therefore, the on-chip capacitor plays an important role in the MACS device. Along with their function to tune the device to Larmor frequency, they also contribute to minimizing the footprint of the detectors. Further, the on-chip capacitor avoids the accumulation of bulk metal on the soldered joints at the coil-capacitor interface.

In the beginning of this chapter, a brief overview on RF MEMS capacitors is provided. Different capacitor designs that could be implemented with the micro-coil is also outlined. Further, simulation of various characteristics of the selected capacitor designs along with their fabrication are also addressed in this chapter. Benchtop as well as NMR characterization followed by a discussion and analysis of the results completes the chapter.

The primary results of this chapter were presented as a poster at EUROMAR 2017. Further, a detailed review and analysis of the results along with fabrication and characterization have been reported as a research article in Concepts in Magnetic Resonance, Part B (Wiley) journal [SA1].

3.1 RF MEMS components in micro-NMR

Passive RF components such as inductors, capacitors, diodes, varactors, trimmers, transmission lines are indispensable in NMR. A typical micro-detector or a micro-coil used in NMR is essentially an inductor. Capacitors and varactors (variable capacitors) are typically used either for tuning and matching the impedance of the micro-coils or in trap/tank circuits. Transmission lines are useful in signal transmission and trap/tank circuits, whereas diodes are utilized in NMR for switching between transmit and receive modes [161].

With the evolution in the field of micro-NMR, the coils or detectors have been miniaturized in order to match the size of detector to that of the sample [8]. A multitude of microfabrication

(MEMS) techniques have enabled the construction of various types of micro-coils [108]. However, the presence of RF passive components such as capacitors as discrete elements hinder further miniaturization efforts. Hence, on-chip passives have been developed to overcome this drawback [162].

The primary concern with the on-chip passive components is that they do not offer the high quality factors as that achieved with the off-chip elements [163]. In the case of inductors, minimizing substrate losses and their series resistance, has yielded improved Q-factors with values in the range of 25 to 80 [113, 164].

In addition to the Q-factor, the self-resonant frequency (SRF), the inductance (L) and the capacitance (C) of an inductor and a capacitor respectively are the most important characteristics used to define the performance of these components. The wirebonded micro-coils have been reported to have a quality factor of around 50 with a self-resonant frequency around 2.6 GHz [156]. These micro-coils have been previously combined with off-chip discrete commercial capacitors for tuning and matching their impedance to the required values. Moreover, most NMR detectors involve the use of high-Q (>10000) off-chip capacitors as tuning and matching elements which are either soldered to a PCB [165] and connected to the coil via transmission lines, or connected directly to the leads of the coil wire [10]. The discrete capacitor, albeit offering very high Q-factors of around 10 000 [166], has other disadvantages such as being too bulky, susceptibility artefacts, eddy current heating, for MAS applications. Therefore, the benefits of having a capacitor on-chip are immense.

Kentgens *et al.* [9] were the pioneers in introducing a non-discrete capacitor in MAS experiments by mechanically integrating a micro-coil in a custom-made parallel plate capacitor. The LC resonator was then mounted on a MAS stator and featured micro-coils down to 200 µm diameter. Ryan *et al.* [114] managed to obtain capacitance on-chip by taking advantage of inter-winding capacitance from a micromachined spiral coil to tune it to the required Larmor frequency. These planar resonators, integrated with microfluidic lab-on-a-chip devices were then inductively coupled to the coil in the probehead. The first micromachined on-chip capacitors in NMR were reported by Badilita *et al.* [11], where an interdigitated capacitor was integrated with a wirebonded micro-coil to obtain micro-resonators and Koo *et al.* [98], where a parallel plate capacitor was integrated with a spiral coil to obtain a microfluidically cryocooled micro-resonator. Both approaches involved standard microfabrication techniques such as lithography, etching, and electroplating. In the former case, the micro-resonator was inductively coupled to a coil in the MAS probehead, whereas in the latter case it was inductively coupled to a secondary coil, which in turn was electrically connected to the MR system through a transmission line. Sakellariou *et al.* [130] introduced a coupled pair of self-resonant transmission line resonators (TLRs) into the MAS rotor as a solution to avoid lumped elements inside the rotor. The capacitance in this case was distributed in between the windings of the spiral coil.

However, all these innovative approaches had some drawbacks for application in MAS either relating to mechanical or electrical properties. In the case of piggyback MAS arrangement employed by Kentgens *et al.* [9], electrical contact was not secure during spinning because the micro-coil was soldered to the custom-made capacitor disk. Moreover, the approach

also necessitated hardware alterations to the commercial probe. The planar resonators from Ryan *et al.* [114] were exclusively designed for microfluidic lab-on-a-chip applications. Although Sakellariou *et al.* [130] modified the planar spiral coil into a coupled TLR setup, the capacitance in this case is parasitic within the coil and hence lossy. The interdigitated capacitor described by Badilita *et al.* [11] suffers from low quality factors and therefore leads to signal losses during acquisition as explained in Section 2.5.3. However, the compactness of the wirebonded micro-coil and absence of long leads renders it a suitable choice for MACS application. Although the cryocooled resonator from Koo *et al.* [98] is bulky for the MACS arrangement, the compactness and flexibility offered by the parallel plate capacitor represents a useful proposition to integrate with a wirebonded micro-coil.

3.2 On chip capacitors for MACS

For the integration of an on-chip capacitor with a wirebonded micro-coil, as shown in Figure 3.1a , the salient features of a capacitor have to be studied and then evaluated. The two most common designs reported in the literature, shown in Figure 3.1b and Figure 3.1c, are the interdigitated and parallel plate variants, respectively. Irrespective of the design, a capacitor can be represented by an equivalent circuit model as shown in Figure 3.1d, which describes a non-ideal capacitor having a capacitance, C, with resistances, R_{C_S} and R_{C_p}, in series and parallel, respectively. The former is known as the equivalent series resistance (ESR) of the capacitor, originating from the structure itself and the latter is the insulation resistance from the dielectric. Additionally, the capacitor leads have an inductance, L_C, which is parasitic in nature.

The non-idealities in the capacitor are grouped together and expressed in terms of power factor (PF). The power factor is expressed as a function of the phase angle, ϕ, which is the angle by which the alternating current leads the applied voltage in a capacitor. In an ideal capacitor, the phase angle is 90°. However, a realistic capacitor with its imperfections will have a phase angle less than 90°. Since the phase angle describes the losses in capacitor, the Q-factor of a capacitor is expressed in terms of this phase angle and the relationship between the phase angle, power factor and Q-factor is represented in Equation 3.1.

$$\mathrm{PF} = \cos(\phi) = \frac{1}{Q_{cap}} \tag{3.1}$$

Therefore, according to the Equation 3.1, the Q-factor of a capacitor tends to infinity when the phase angle is 90°. Hence, for the Q-factor to be maximum, the non-idealities surrounding the capacitor such as the ESR should be kept to a minimum. Further, the operating range of the capacitor is defined by its self-resonant frequency beyond which the inductive component will dominate the capacitive behaviour.

Additionally, in the case of MACS experiments, the capacitor structure will be undergoing rotation at very high magnetic fields, typically beyond 7 T. This results in eddy currents

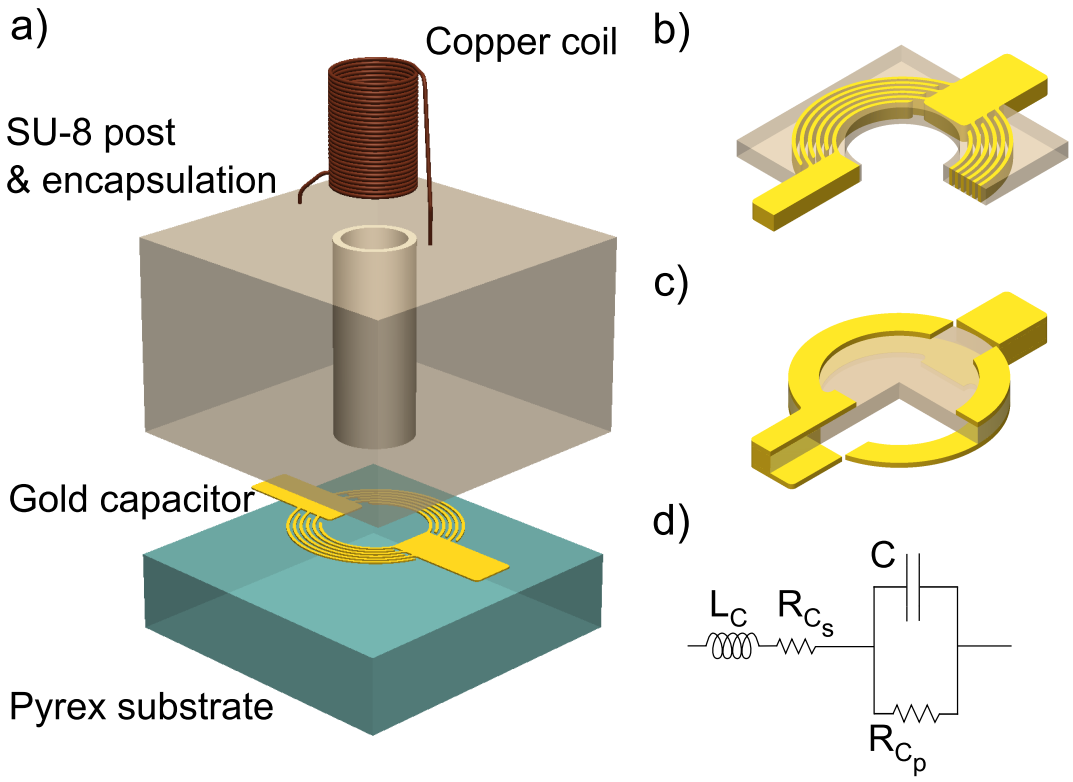


Figure 3.1: a) Exploded view of the MACS insert; b) Interdigitated capacitor design; c) Parallel plate capacitor design; d) Electric circuit model of a non-ideal capacitor. Note that the Figures are not to scale. Adapted from [46] Copyright 2018 ©Wiley.

being induced in moving conductive materials of the capacitor. Although induced eddy currents find applications in levitation [167], in electricity generation, or can be used in position sensors [168] and electromagnetic brakes [169], in the case MACS-NMR, induced eddy currents are entirely parasitic, causing heating and slowing down of the MAS rotor, and hence should be kept to an absolute minimum.

Examining these basic electrical and thermal characteristics of the capacitor using simulation models then verifying them using fabricated structures form the backbone of the current chapter.

3.3 Simulations

The simulation study was organized according to the two effects that were to be analyzed. The non-idealities in the electrical behaviour of the capacitor structure was one and thermal effects due to the induced eddy currents in the metallic parts of the capacitor was the other. The two capacitor structures mentioned in Figure 3.1 were evaluated for these effects.

3.3.1 Evaluation of the Q-factor

The on-chip capacitor structures were simulated for their electrical parameters in ANSYS® HFSS™ environment. The scattering-parameters of the respective structures were computed across a frequency range of 100 MHz to 2000 MHz.

The structure for interdigitated capacitor was defined by having nine finger electrodes, with its thickness as an adjustable parameter, and was built upon a pyrex substrate of thickness 500 µm, which resembles typical substrates in manufacturing. The electrodes, which are separated by a distance of 20 µm, have a width 20 µm. Further, a 1 mm SU-8 dielectric, an epoxy-based photopolymer with a relative dielectric constant ϵ_r of 3.24 and a loss tangent $\tan(\delta)$ of 0.015 at 1 GHz [170] was modeled on top of the electrodes, to resemble the actual conditions of an encapsulated MACS resonator. A lumped port was defined between two perfectly conducting contact pads. Likewise, the structure for the parallel plate capacitor was defined by having a capacitor plate on top of a pyrex substrate of thickness 500 µm which was meant to function as the bottom plate, followed by a 10 µm SU-8 dielectric on it. The second plate of the capacitor, which acts as the top plate, was defined on the dielectric layer. The plates have a width of 150 µm. Both capacitor structures were embedded in a SU-8 dielectric of thickness 1 mm and a lumped port was defined between the two perfectly conducting contact pads. The electrical losses were introduced into the capacitor structures via the impedance boundary condition.

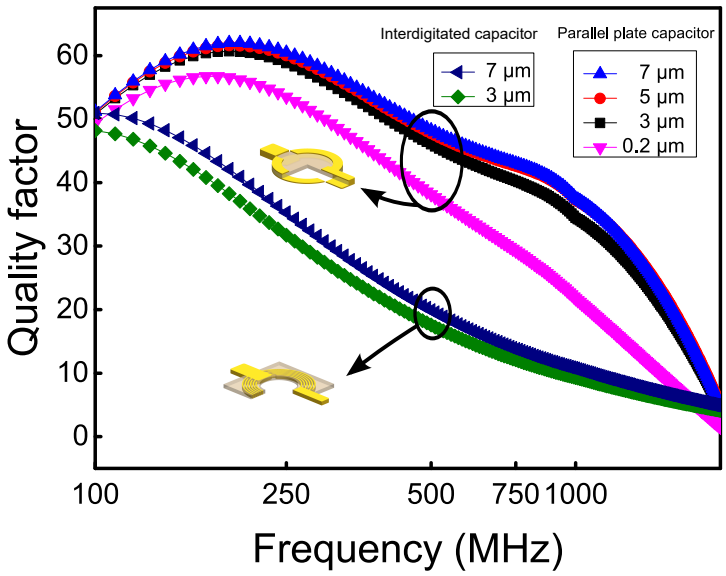


Figure 3.2: Comparison of the quality factor of the interdigitated and parallel plate capacitors of various electrode thicknesses. Adapted from [46] Copyright 2018 ©Wiley.

The extracted S-parameter values from the simulation were converted into impedance values. The Q-factor values for the respective structures shown in Figure 3.2 were then computed from the impedance plots.

The simulated values of the Q-factor for the interdigitated capacitor with electrode thicknesses of 3 µm and 7 µm at 500 MHz was found to be approximately 17.5 and 19.8, respectively. Similarly, the Q-factor numbers for the parallel plate variant of the capacitor for plate thicknesses of 3 µm, 5 µm and 7 µm at 500 MHz was evaluated to be 46, 47.7 and 48.3, respectively.

Hence, it was concluded from simulation experiments that parallel plate capacitor exhibited better electrical performance as compared to the interdigitated version. The observed simulation behaviour could be argued on the basis that the electrical field lines diverge into the lossy substrate in the case of the interdigitated capacitor, whereas the lines converge between the plates in the case of the former. Moreover, smaller cross-section of the interdigitated electrodes led to higher resistance. Additionally, it was observed that the self-resonant frequency of the capacitor structures was close to 2 GHz, well beyond the intended operating range of 100 MHz to 700 MHz for the capacitor.

3.3.2 Induced eddy currents in the capacitor

The rotation of the MACS detector inside a homogeneous magnetic field causes eddy currents to be induced in the cross section of all metal tracks, including the coil wire and capacitor structure due to flux variations. The current flow will be such that it generates a field opposing the rate of change of flux in the metal cross section. The generation of induced eddy currents in a micro-coil and in plain and hollow cylinders spinning in a static magnetic field, and the resulting consequences in magnetic resonance, has been evaluated before in [154, 171]. The reported methods have been applied to the capacitor structures and the resultant heating has been studied and explained in the following section with help of qualitative formulae as well as simulation models.

3.3.2.1 Analytical formulations

A similar approach to one reported by Aguiar *et al.* [154] for a micro-coil was adopted to obtain a qualitative formula for the power dissipation due to induced eddy currents in the capacitor structures. The capacitor structures were modeled in the form of a ring with a thickness h, width b, and radius r, which is a good approximation for both interdigitated and parallel plate capacitor geometries. Figure 3.3 illustrates the positioning of the rotating capacitor structures with respect to the static magnetic field, B_0. Observing the arrangement from a rotating frame of reference in which the conducting part is stationary and the field is rotating, the axial component of the static magnetic field, B_y, also appears stationary, therefore, plays no role in flux variations. On the other hand the perpendicular component, B_x (B $\sin(\alpha)$), rotating with angular frequency, ω, generates eddy currents in the capacitor because it experiences variations in magnetic flux, ϕ.

The magnetic flux associated with capacitor from the perpendicular component, B_x, and the emf generated due to the induced eddy currents from the flux variations is analytically approximated using Gauss' law of magnetism and Faraday's law of induction. Accordingly Equation 3.2 gives the numerical representation of the flux formation in the metal.

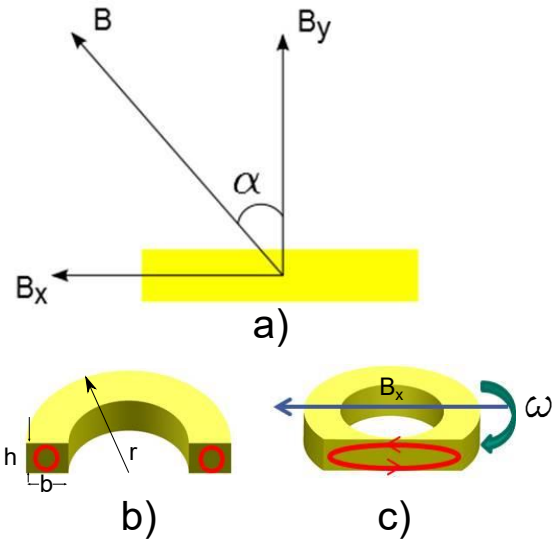


Figure 3.3: Eddy current formations in the capacitor as illustrated by the current loops due to rotating magnetic field component B_x. The behaviour of the induced eddy currents are such that the current flow is generating a field opposing the flux variations. Hence, this opposing field could be generated by current trajectories which are b) circular or c) elliptical in nature.

$$\phi = B \cdot A = B_{\mathrm{x}} \cdot A \cdot cos(\theta) \tag{3.2}$$

where,
ϕ = flux linkage
B_0 = static magnetic field (T),
A = area of the current loop (m^2) crossed by the flux
θ = angle between the area vector and magnetic field vector, in this case is zero.

The behaviour of the induced eddy currents is such that the current flow is generating a field opposing the flux variations. The current trajectories of the induced eddy currents generating this opposing field are elliptical and circular in nature depending on the conductor cross sections as shown in Figure 3.3. The area of the current loops at 4 sectors of the ring are estimated in terms of dimensions of the ring. The circular trajectory at two sectors shown in Figure 3.3b are taken as a rectangle with dimensions of h and b, whereas the elliptical ones in Figure 3.3c are considered as a rectangle with dimensions of h and r.

Differentiating Equation 3.2 with respect to time provides the emf generated in the ring due to the induced eddy currents. The resistance to the eddy current path is calculated using half the cross-sectional thickness, h, of the ring. From the induced emf, V, and the resistance,

R, the relationship between power dissipation due to the eddy currents, the ring/capacitor geometry and the spinning frequency ω can be evaluated.

The emf generated by the circular current trajectories shown in Figure 3.3b are described in Equation 3.3. Additionally, resistance to this current path, R, is also calculated.

$$\phi = B_x \cdot h \cdot b \cdot cos(\omega \cdot t) \tag{3.3}$$

$$V = -\frac{d\phi}{dt} = \omega \cdot B_x \cdot h \cdot b \cdot sin(\omega \cdot t)$$
$$R = \frac{\rho \cdot 2 \cdot (h+b)}{r \cdot \frac{h}{2}}$$

The power dissipation in the metal due to circular trajectories is estimated using the calculated emf and the resistance. This is described by Equation 3.4.

$$P = \frac{V^2}{R} \tag{3.4}$$

$$= 0.5 \cdot \omega^2 \cdot {B_x}^2 \cdot (r \cdot h^3 \cdot \frac{b^2}{\rho \cdot (h+b)}) \cdot sin^2(\omega \cdot t)$$

Similarly, for the elliptical current trajectories described in Figure 3.3c, the induced voltage as well as the resistance are described in Equation 3.5.

$$\phi = B_x \cdot h \cdot r \cdot cos(\omega \cdot t) \tag{3.5}$$

$$V = -\frac{d\phi}{dt} = \omega \cdot B_x \cdot h \cdot r \cdot sin(\omega \cdot t)$$
$$R = \frac{\rho \cdot 2 \cdot r}{b \cdot \frac{h}{2}}$$

Further, the dissipated power is calculated as a function of the emf and the resistance and is expressed in Equation 3.6.

$$P = \frac{V^2}{R} \tag{3.6}$$

$$= 0.5 \cdot \omega^2 \cdot {B_x}^2 \cdot (r \cdot h^3 \cdot \frac{b}{\rho}) \cdot sin^2(\omega \cdot t)$$

In both cases it could be concluded that the heat dissipation from the induced eddy currents in the capacitor has a substantial dependence on its geometry, especially its thickness which shows a cubic dependency. Additionally, the amount of dissipated power exhibits a quadratic relationship with the speed of rotation of the metal structure in the magnetic field.

3.3.2.2 Simulation of induced eddy currents

The eddy current behaviour in the capacitor due to its simultaneous spinning with the sample in a magnetic field is an underlying issue that was also studied with the help of finite element method (FEM) simulations in COMSOL Multiphysics®. The simulation was performed with the AC/DC module of the software employing magnetic and electric fields physics.

A cylindrical air domain having a diameter of 3 mm and a thickness of 400 µm was defined as the simulation domain and Ampere's law of current was assigned to this domain. A model of an interdigitated capacitor having two fingers and a parallel plate capacitor with a plate distance of 10 µm, each concentric to the rotation axis, were defined in the simulation domain. The perpendicular component of the static magnetic field 11.74 T, i.e, $11.74 \sin(54.7°) = 9.55$ T was defined perpendicular to the rotation axis using a magnetic potential boundary condition for the exterior boundaries. A velocity term was designated for the capacitor structures. The thickness of the structures and the spinning speed were assigned as parameters and were varied from 1 µm to 10 µm and from 1 kHz to 10 kHz, respectively. Both capacitor structures were designated gold as the material. The finite element mesh (triangular) was relatively coarse for the cylindrical air domain surrounding the metal structures and finer mesh (free tetrahedral) size of 0.5 µm was assigned to the conductors to resolve current distributions. The maximum thickness and the spinning speed were limited to 10 µm and 10 kHz respectively keeping in mind the skin depth for gold at around 300 MHz and the maximum rotation speed of a 4 mm MAS rotor.

The eddy current distribution in the capacitors rotating in an uniform field is shown in Figure 3.4. It can be observed that the induced eddy currents flow in an elliptical trajectory and these currents are situated in cut planes of the capacitor that lie parallel to the axis of rotation.

The results from the parametric studies are described in Figure 3.5. The magnitude of induced eddy currents varies linearly with the rotation speed and the thickness of the metal structure, as derived in Equation 3.3 and Equation 3.5. It can also be concluded that the heat

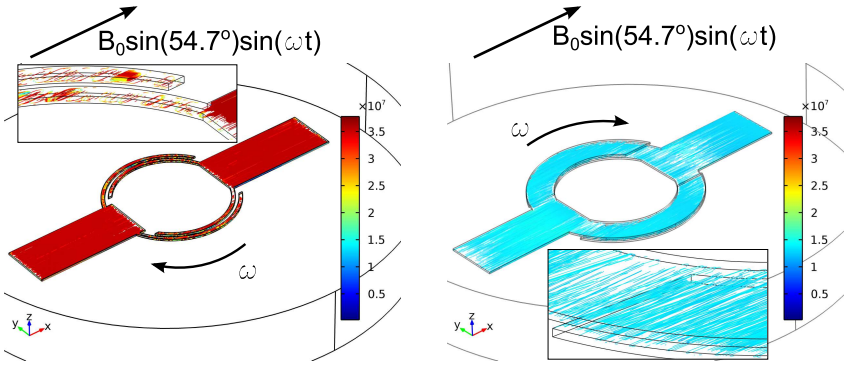


Figure 3.4: Induced eddy currents in a) an interdigitated capacitor of thickness 8 µm and b) parallel plate capacitor of plate thickness 3 µm. The insets show the trajectory of the induced eddy currents in the structures. Adapted from Adhikari *et al.* [46] Copyright 2018 ©Wiley.

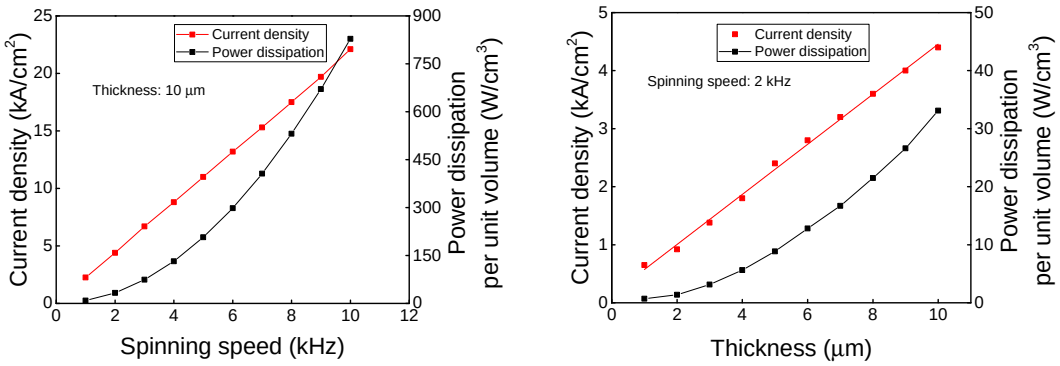


Figure 3.5: Simulated current densities and specific power dissipation in a parallel plate capacitor structure due to induced eddy currents as a function of a) spinning speed and b) thickness of the structure. The red and black lines show the best-fit curves. Adapted from Adhikari *et al.* [46] Copyright 2018 ©Wiley.

dissipation due to the induced eddy currents increases drastically at higher spinning speeds and higher metal thicknesses. Therefore, the desired thickness of the metal has to be kept to a certain minimum value taking into account skin depth considerations such that resistance of the capacitor structure is also at a minimum. It can also be observed that the heat dissipation also increases (quadratic behaviour) at higher speeds. Therefore, efficient cooling of outer surface of the rotor in addition to good thermal coupling is important.

Hence, the on-chip capacitor had to be a compromise with regards to various design requirements arising from electrical and thermal effects and fabrication constraints.

3.4 Fabrication

The outcome from the results of simulations of Q-factor and induced eddy currents was to find a middle ground for the electrode thickness of the fabricated capacitor structures. For the parallel plate capacitor structure, the thickness was limited to 3 µm, whereas the limit for the thickness of the interdigitated capacitor was set to 8 µm. This is because of the higher Q-factor values of the parallel plate capacitor. Therefore, the parallel plate capacitor is already at an advantage with respect to eddy currents because of thinner electrodes.

From Figure 2.6, a required minimum Q-factor is determined from the volume ratios of the MACS detector and outer MAS coil. Applying the requirement of a minimum signal transfer efficiency of 90 %, the required Q-factor of the MACS resonator is calculated to be 20. The microfabricated capacitors are required to have a footprint of less than 2 mm × 2 mm to be compatible with the inner diameter of MAS rotors below 4 mm. The on-chip capacitors should provide capacitance in the range between 0.6 pF to 10 pF, to tune the micro-resonator from 50 MHz to 1 GHz for inductances of micro-coils which are typically in the range of 100 nH to 600 nH. This frequency range covers the Larmor frequencies of most nuclei for magnetic field strengths up to 23.5 T. The requirements are summarized in Table 3.1. The capacitors should be designed such that heat dissipated due to induced eddy currents in the metal is as low as possible without compromising the Q-factor. The net temperature rise due to induced eddy currents in the structure must remain lower than 20 °C at 10 kHz.

Table 3.1: Desired parameters for MACS detectors with footprint less than 2 mm × 2 mm. Adapted from Adhikari *et al.* [46] Copyright 2018 ©Wiley.

Parameter	Value	Details
L	max: 600 nH min: 90 nH	$10 \leq$ no. of turns ≤ 25 500 μm $\leq$ diameter $\leq$ 1000 μm
C	max: 10 pF min: 0.3 pF	1 μm $\leq$ plate distance $\leq$ 10 μm 150 μm $\leq$ plate width $\leq$ 450 μm
$Q_{\mu R}$	max: No upper limit min: 20	$Q_c \geq 65$ $Q_{cap} \geq 30$
f_o	max: 1 GHz min: 70 MHz	f_o - 0.03 · $f_o \leq f_o \leq f_o$ + 0.03 · f_o

3.4.1 Interdigitated capacitors

The on-chip capacitors were produced by a combination of MEMS fabrication techniques such as lithography, electroplating, etching, and dicing.

For interdigitated capacitors, a straightforward process flow was designed starting with the evaporation of a seed layer of Cr/Au of thickness 10 nm and 50 nm, respectively on a 500 µm

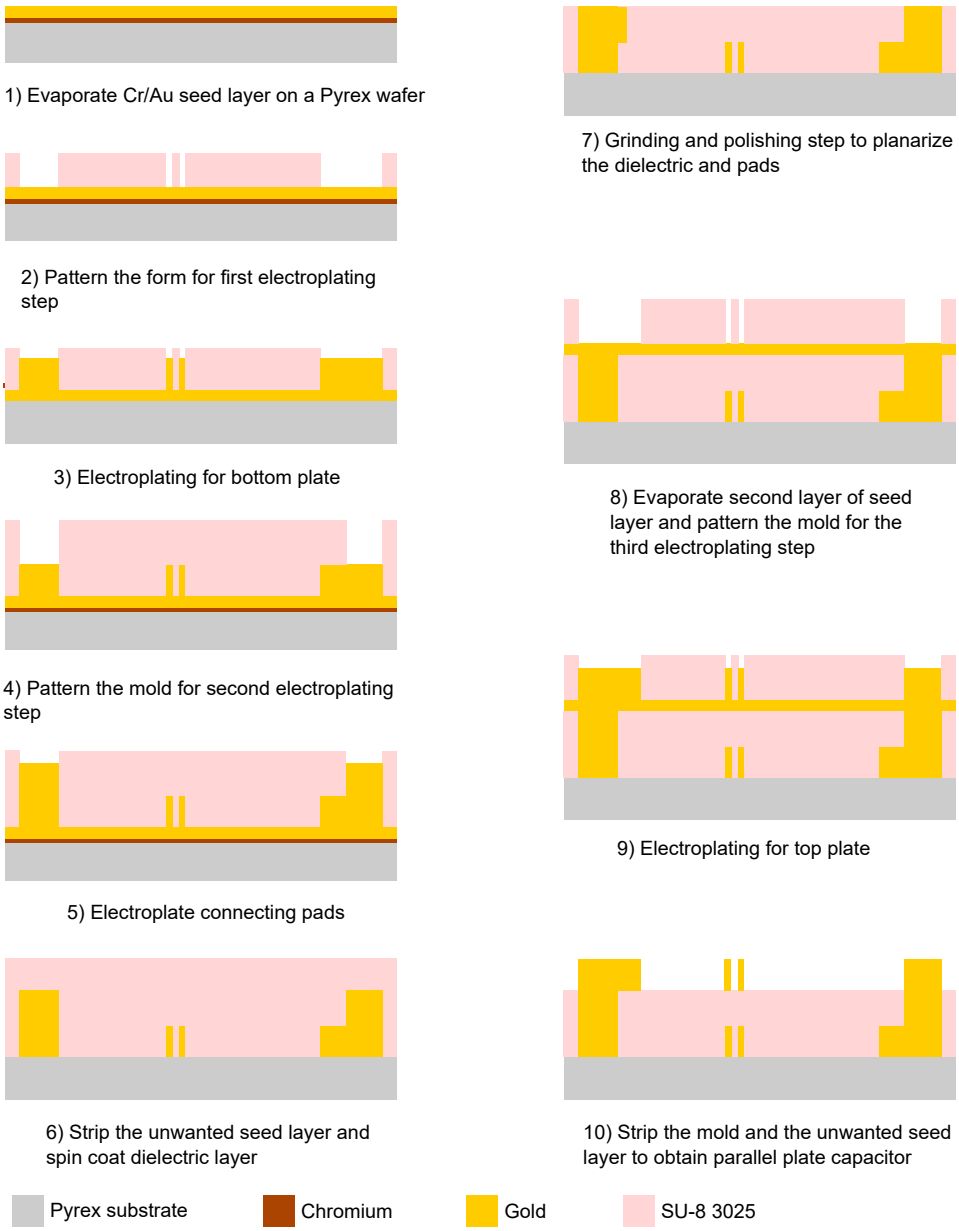


Figure 3.6: Description of the process flow to fabricate the parallel plate capacitor.

thick pyrex wafer (BF33® from SCHOTT glass Malaysia). Subsequently, an electroplating resist mold[A7] (SU-8 3025 from micro resist technology GmbH, Berlin) was spin coated (PRIMUS STT 15, ATMvision AG) and patterned using a mask aligner (EVG®620, EV Group) with an exposure dose of 400 mJ/cm^2, followed by gold electroplating[A7] of the interdigitated electrodes and contact pads up to the required thickness of 8 µm. The electroplating mold was stripped in O_2-plasma environment[A7] and the seed layer was etched away to obtain the required capacitors on the substrate.

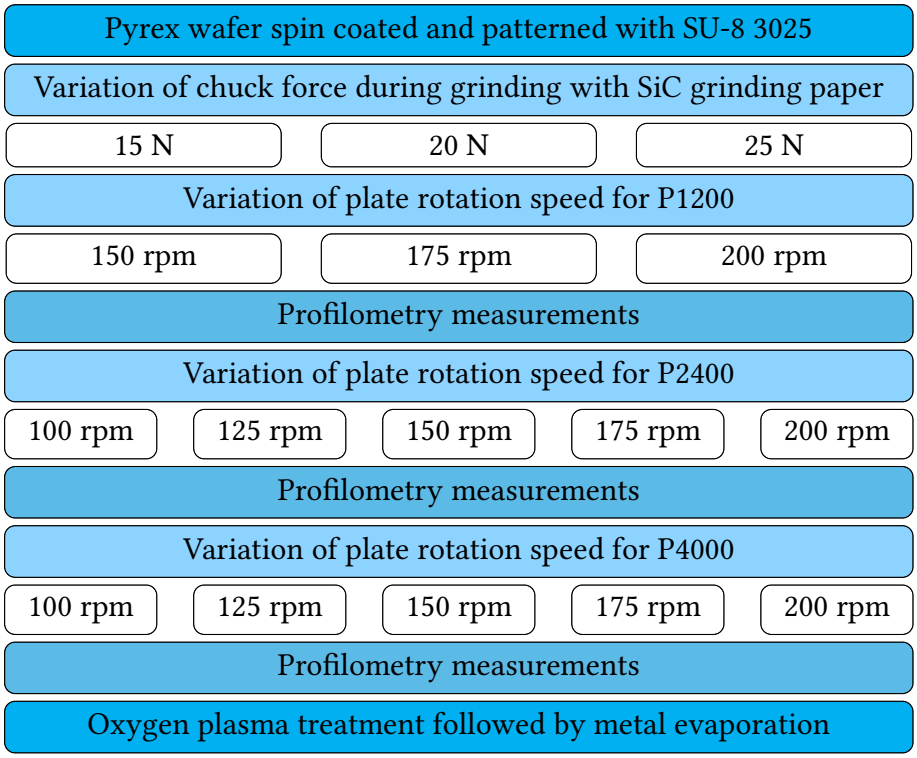


Figure 3.7: Experimental plan for grinding the SU-8 dielectric layer using various grades of grinding paper at different rotation speeds

3.4.2 Parallel plate capacitors

The fabrication process flow for a parallel plate capacitor was more complex as compared to the interdigitated capacitor. It followed a three-step electroplating process as described in Figure 3.6, one for the bottom plate, another step to raise the contact pads, and a final electroplating step for the top plate.

Similar to fabrication of interdigitated capacitors, a seed layer of Cr/Au of thickness 10 nm and 50 nm was evaporated on a dehydrated 500 µm thick pyrex substrate. The bottom plate of the capacitor having a thickness of 3 µm was fabricated by combination of spin coating, patterning a 20 µm electroplating mold from SU-8 3025[A7] as shown in Figure 3.8a and subsequent gold electroplating[A7] as shown in Figure 3.8b. The electroplating mold was then stripped[A7] in O_2-plasma environment using an RF power of 1200 W and a chamber pressure of 450 mTorr (R^3T STP from Muegge GmbH) as shown in Figure 3.8c. The substrate was then rinsed in standard Acetone, Isopropanol and DI water in that order for 10 min each[A7].

Following dehydration baking at 150 °C on a hot plate for 5 min and a 10 W O_2-plasma activation (Etchlab 200 from Sentech instruments GmbH), a 20 µm second electroplating mold[A7] for the pads from SU-8 3025 was patterned as shown in Figure 3.8d. Subsequently, the thickness of the contact pads was raised by 3 µm to 10 µm as shown in Figure 3.8e by a

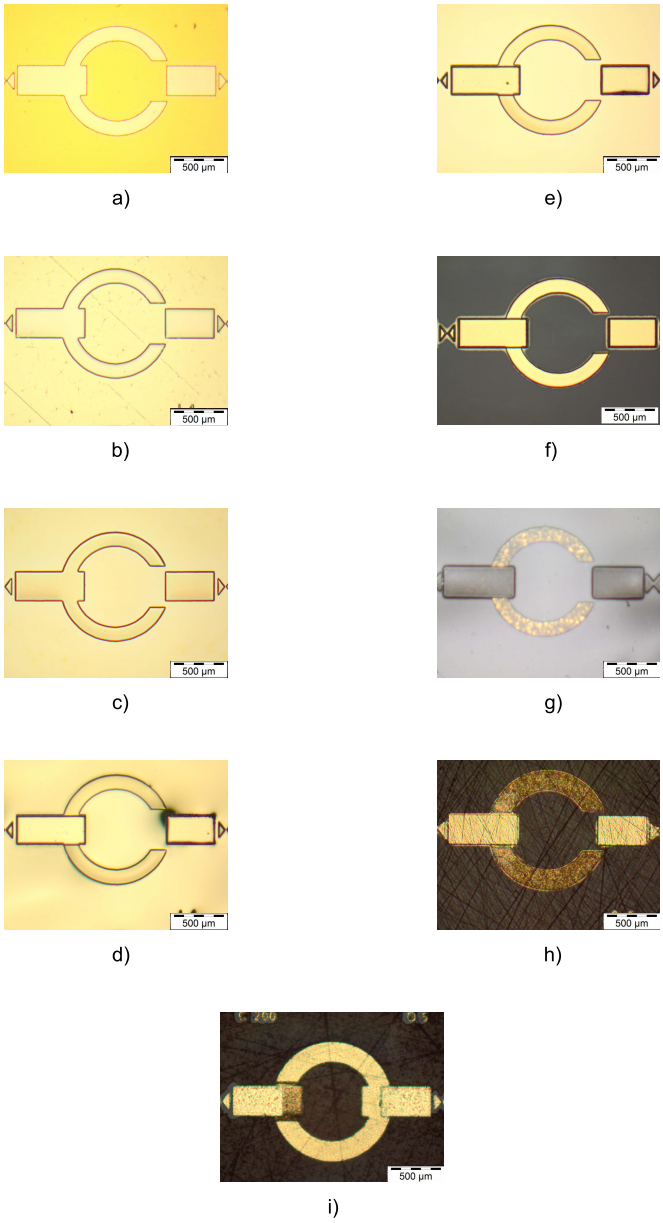


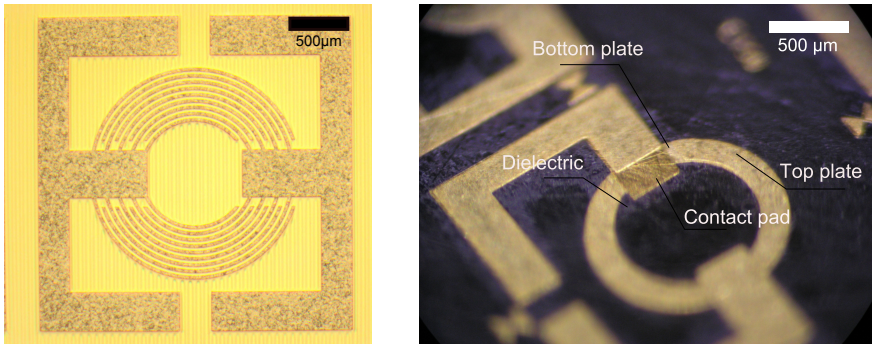
Figure 3.8: Images showing the substrate under various stages during the fabrication of parallel plate capacitor. a) SU-8 electroplating mold; b) Bottom plate electroplated; c) Electroplating mold stripped; d) SU-8 electroplating mold for contact pads; e) Contact pads electroplated; f) Unwanted seed layer etched; g) SU-8 dielectric dispensed; h) Grinding and polishing step; i) Top plate electroplating and second seed layer stripped.

second electroplating step. This also defines the distance between the plates. Following the electroplating step, electroplating mold was then stripped[A7] in 1200 W O_2-plasma environment

as done earlier and the unwanted seed layer was stripped away by wet etching using metal etchants (Au 200 gold etchant and Cr-200 chromium etchant from Microchemicals GmbH) as shown in Figure 3.8f. The substrate was rinsed afterwards in standard Acetone, Isopropanol (IPA) and DI water in the order for 10 min[A7] each and dehydration baked at 150 °C on a hot plate for 2 min.

Then, the substrate was treated with 10 W O_2-plasma and a 20 µm thick SU-8 3025 resist[A7] was patterned as shown in Figure 3.8g. This SU-8 layer serves as dielectric for the capacitor. The dielectric layer was subsequently ground to level of the contact pads with the help of a grinding process as shown in the Figure 3.8h. Grinding process is used in the semiconductor industry for planarizing the substrate after the deposition of multiple layers. The grinding step was accomplished with the help of silicon carbide grinding papers (Struers GmbH) with different grades such as P1200, P2400 and P4000 corresponding to grit sizes of 15 µm, 7 µm and 2.5 µm respectively. A design of experiment (DOE) study was conducted to optimize the grinding process and the experimental plan is described in Figure 3.7.

Following the planarization step, the surface of the dielectric is on the same level as that of the contact pads. The substrate is then treated with 10 W O_2-plasma for a period of 15 min. Subsequently, a gold seed layer of thickness 200 nm was evaporated on the substrate and after the dehydration baking step, a 20 µm thick third electroplating mold[A7] from SU-8 3025 was spin coated and patterned on the seed layer following which the top plate of the capacitor was defined by electroplating[A7] upto a thickness of 3 µm. The electroplating mold was subsequently stripped[A7] in 1200 W O_2-plasma and the seed layer etched by wet etching to obtain parallel plate capacitors as shown in Figure 3.8i.



(a) (b)

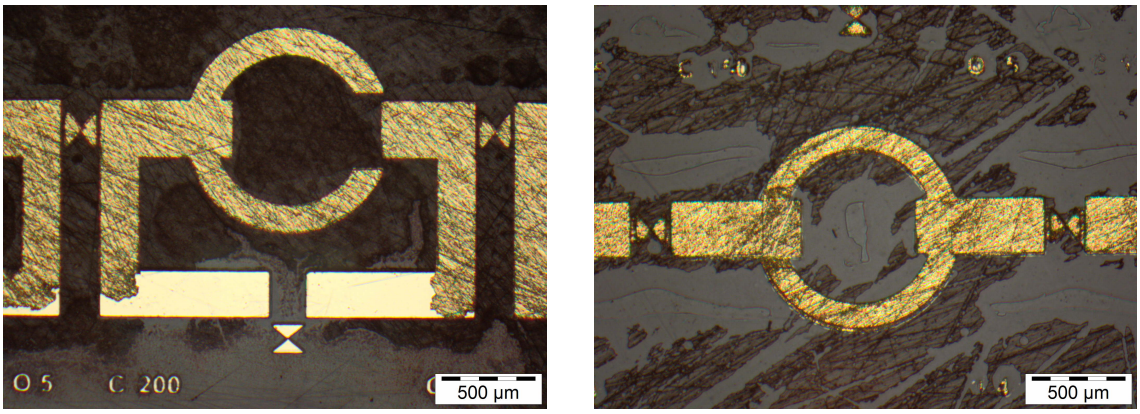
Figure 3.9: a) Fabricated interdigitated capacitor with nine fingers; b) Fabricated parallel plate capacitor with a dielectric thickness of 10 µm. The extended pads in the fabricated capacitors were used for electrical characterization using an RF probe having a 500 µm pitch. Adapted from Adhikari *et al.* [46] Copyright 2018 ©Wiley.

The fabricated devices are shown in Figure 3.9 with an interdigitated capacitor having nine electrodes shown in Figure 3.9a and a parallel plate capacitor shown in Figure 3.9b respectively.

3.4.3 Failure mode effects and Analysis

An FMEA (Failure mode effects and Analysis) study is a rigorous process of estimating process complications and focused on improving the performance and reliability of devices.

To this end, a FMEA study was performed to understand the complications during fabrication steps and improve the reliability of fabricated on-chip capacitors. At the outset, the surface analysis of the substrate after stripping the electroplating mold using a microscope revealed the presence of SU-8 residues on the seed layer (evaporated gold). This hindered the wet etching of the unwanted seed layer on the substrate after electroplating. Therefore, a 1 µm layer of anti-reflection coating layer (BarLi)[A7] was spin coated on top of the seed layer and treated before the application of SU-8 electroplating mold. This alleviated the issues of short contact between the electroplated pads due to the presence of stray seed layer on the substrate.

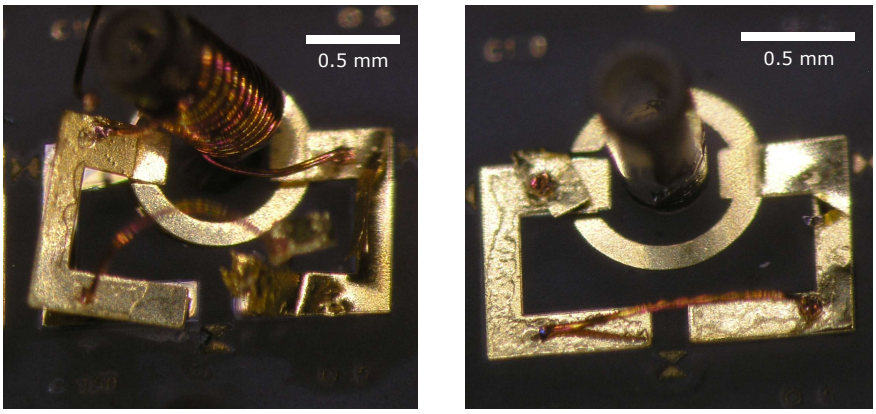


(a) (b)

Figure 3.10: Removal of a) the contact pads; and b) dielectric (SU-8) layer during grinding and polishing process.

A design of experiments (DOE) study described in Figure 3.7 was vital in finding the optimum parameters along with the SiC grinding papers for planarizing the dielectric. A combination of excessive force, lower plate rotation speed and/or prolonged grinding times resulted in removal of the electroplated pads and the dielectric layer as shown in the Figure 3.10. This would result in the final surface being uneven and making it unsuitable for the fabrication of parallel plate capacitor, thus rendering the processed substrate unusable for further processing.

Another issue that occurred during the fabrication process was that the top plate of the capacitor along with the contact pads started to peel off during the wirebonding process as shown in the Figure 3.11. The delamination of the electroplated pads suggested poor adhesion of the seed layer for the third electroplating step which was due to impurities on the polished substrate. To overcome this issue, prolonged treatment of the polished substrate in O_2-plasma



(a) (b)

Figure 3.11: Delamination of contact pads during wirebonding.

at 10 W of power (Etchlab 200 from Sentech instruments GmbH) was undertaken. The time duration of the O_2-plasma treatment was increased from 5 min to 20 min following which the seed layer was evaporated followed by the electroplating process. Under the condition of increased O_2-plasma treatment, contact pads were not affected by the forces during the wirebonding and successful wirebonds were formed.

3.5 Characterization

The fabricated on-chip capacitors were evaluated for their electrical characteristics as well as for their behaviour under fast spinning conditions in a static magnetic field. The performance characterization was done to verify the observations from simulation studies and to select a suitable capacitor for the MACS detectors.

3.5.1 Electrical characterization

The micro-resonator reported for MACS experiments in this work has an on-chip capacitor as compared to commercial discrete elements used in early approaches [10, 149, 150]. The former, however, has a lower quality factor (5 to 40) compared to the latter (10 000) [166] due to the intrinsic losses associated with non-ideal dielectric materials.

The electrical characterization of the microfabricated capacitors was performed on an impedance analyzer (Agilent E4991A) connected to a probe station (Cascade Microtech MPS150) set up with a Z-probe (Z0-20-K3N-GS-500, Cascade Microtech GmbH). Open circuit, closed circuit, and 50 Ω calibration of the Z-probe was carried out prior to measurements using an impedance standard substrate.

Following the calibration of the probe to 50 Ω, the frequency dependent capacitance and phase angle of the interdigitated and the parallel plate capacitors on the wafer were measured.

From Figure 3.12a, it was observed that the 8 µm thick electroplated interdigitated capacitor with nine electrodes yielded a measured capacitance of 1.25 pF with the self-resonant frequency of the device at around 1.3 GHz. On the other hand, a capacitance of around 3.8 pF was obtained from the parallel plate capacitor with plate thickness of 3 µm, plate width of 150 µm and plate distance of 3.5 µm with the self-resonant frequency measured at 1.9 GHz as shown in Figure 3.12b.

The capacitance provided by the parallel plate capacitor was verified analytically with Equation 3.7.

$$C = \frac{\epsilon \cdot A}{d_c} \tag{3.7}$$

where $\epsilon = \epsilon_0 \epsilon_r$ is the dielectric permittivity, A is the area of a capacitor plate, and d_c is the distance between the plates.

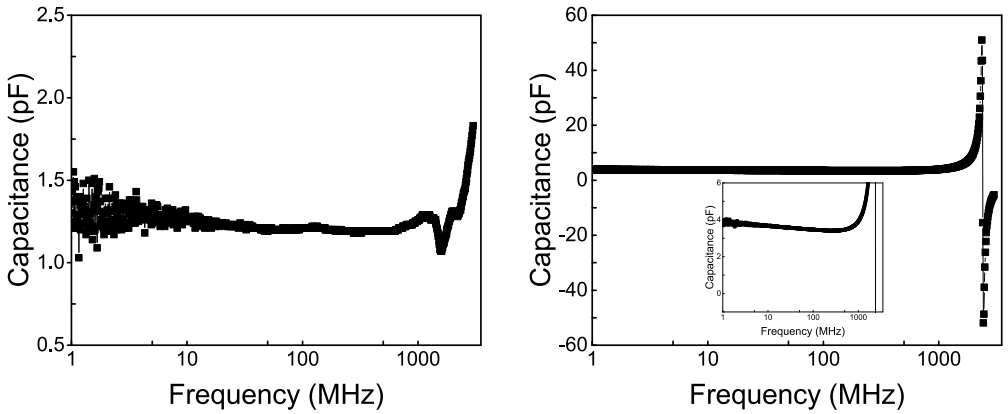


Figure 3.12: Frequency dependent measured capacitances of the a) nine finger interdigitated capacitor and the b) parallel plate capacitor with a dielectric thickness of 3.5 µm. Adapted from Adhikari *et al.* [46] Copyright 2018 ©Wiley.

The reported dielectric constant value for SU-8 at 1 GHz of 3.24 [170], was used to calculate the analytical value of capacitance offered by the parallel plate capacitor which came to 3.71 pF from Equation 3.7. This value agrees closely with the measured capacitance of 3.8 pF. The capacitance offered by the plate capacitor can be further increased to a maximum of 13 pF by decreasing the distance between the plates down to 1 µm and the other way around, increasing the plate distance to 10 µm results in the capacitance to be around 1.2 pF. An alternative method to increase or decrease the capacitance would be to have a dielectric material with a higher or lower dielectric constant than SU-8 respectively.

Another important characteristic of the capacitors is their quality factor. The quality factor of the capacitors was assessed from the measured phase angle values shown in Figure 3.13 and were obtained from the respective phase angle values using Equation 3.1. At 500 MHz, from Figure 3.13a and Figure 3.13b, it was evaluated that the measured phase angle of the

interdigitated capacitor and the parallel plate capacitor was 86.5° and 87.9°, respectively. The corresponding Q-factor of the capacitors were computed to be 16.3 and 27.5, respectively, as shown in Figure 3.14. These Q-factor values are in accordance with RF simulation studies shown in Figure 3.2 on the respective capacitors. The juxtaposition of the Q-factor and the self resonant frequency values of the two respective capacitor shows that the parallel plate capacitor has a superior electrical performance as compared to interdigitated one. This behaviour can be explained due to the reason that in the case of parallel plate capacitor, most of its electric field is confined inside the interplate dielectric, whereas the field of the interdigitated capacitor diverges out and penetrates the bulk of the encapsulation material which is lossy.

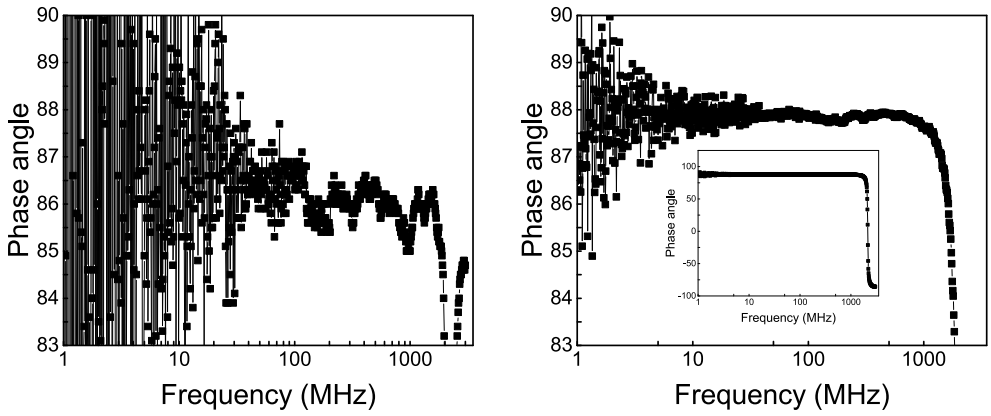


Figure 3.13: Frequency dependent measured phase angle of the a) interdigitated capacitor and b) parallel plate capacitor. A phase angle of 86.5° and 87.9° was recorded for the interdigitated and the parallel plate capacitor, respectively. Adapted from Adhikari *et al.* [46] Copyright 2018 ©Wiley.

3.5.2 Thermal characterization

Sample heating is valid problem during MACS experiments because it results in the deterioration of spectral resolution and the degradation of certain biological samples. In the case of MACS experiments, the dissipated heat from induced eddy currents in capacitor electrodes causes a rise in the temperature of the sample contained in the MACS insert. Hence, it is necessary to perform in-situ characterization of the sample temperature inside the insert under conditions of spinning at the magic angle in a magnetic field.

The sample temperature inside the MACS insert can be measured at various spinning speeds using the principle of chemical shift thermometry. One of the methods in chemical shift thermometry employs ethylene glycol as a reference sample [172]. The frequency difference between the $-OH$ and $-CH_2$ peaks in ethylene glycol is a linear function of temperature.

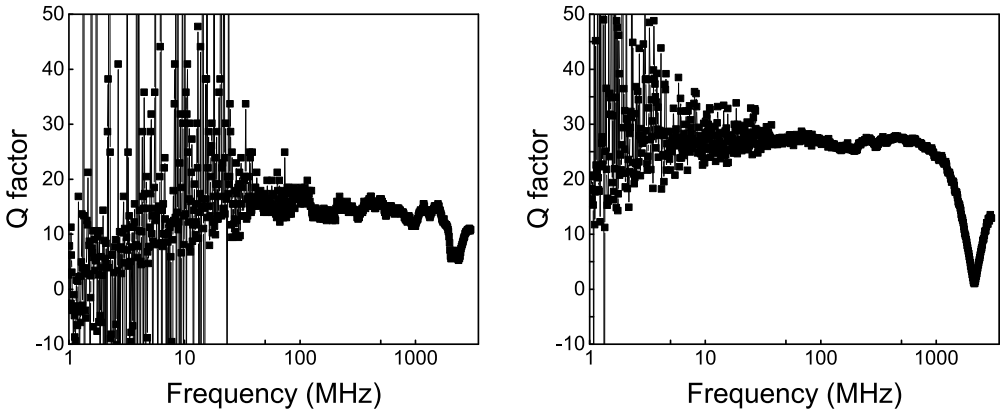


Figure 3.14: The quality factor of the a) interdigitated capacitor and b) parallel plate capacitor computed from phase angle values using Equation 3.1. Q-factor values of 16.3 and 27.5 were observed for the interdigitated and the parallel plate capacitor, respectively. Adapted from Adhikari *et al.* [46] Copyright 2018 ©Wiley.

The increase in sample temperature during the MACS experiments can be correlated with spinning speeds by obtaining the NMR spectrum of ethylene glycol at the respective spinning speeds. One of the important features of chemical shift thermometry using ethylene glycol is that the difference between the chemical shifts of $-OH$ and $-CH_2$ groups is not affected by small amounts of drift in the magnetic field strength.

Initially, the chemical shift difference ($\Delta\delta_c$) between $-OH$ and $-CH_2$ was calibrated to assigned temperatures as shown in Figure 3.16. The $\Delta\delta_c$ at 17 °C is about 1.73 ppm. To perform the calibration, 99 % ethylene glycol was dispensed into a 5 mm tube and the condition inside the tube was set using a temperature control unit. The chemical shift difference between the $-OH$ and $-CH_2$ peaks was subsequently noted down at stipulated temperatures. It was confirmed that the temperature and chemical shift are in close correlation with the calibration Equation 3.8 reported in [172]

$$T[K] = 466.5 - 102 \cdot \Delta\delta_c \tag{3.8}$$

With this method, the thermal reading inside a region of interest can be established with an accuracy of ±1 °C [172]. Upon the conclusion of the calibration experiments, the temperature inside the active volume of a MACS detector was determined. This was carried out by dispensing 150 nl of 99 % ethylene glycol inside the MACS detector following which the detector was fit snugly inside the MAS rotor. Thermally conductive Shapal-M ceramic spacers [10, 130, 152] were used for effective dissipation of heat away from the sample region. Additionally, the spacers aided in centering the MACS insert inside the rotor. Subsequently, the rotor was placed inside the MAS probe and the spinning speed was varied from 2.5 kHz to 9.5 kHz during which the ^1H chemical shift was recorded. The NMR signal was acquired

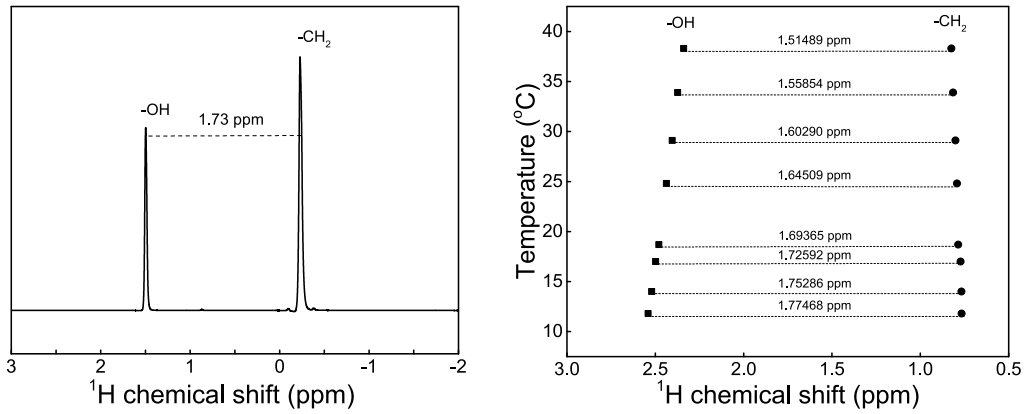


Figure 3.15: a) The chemical shift difference between the -OH and $-CH_2$ peaks in ethylene glycol at 290 K or 17 °C; b) The chemical shift difference between the -OH and $-CH_2$ peaks measured for various temperatures. Adapted from Adhikari *et al.* [46] Copyright 2018 ©Wiley.

using the MAS probe coil, since the dummy MACS chip comprised of only the on-chip capacitor sans the micro-coil. The BCU (Bruker cooling unit) temperature unit of the spectrometer was set to 288 K for all experiments. It could be observed from Figure 3.16 that thicker electrodes lead to more heat dissipation. Hence, using the parallel plate capacitors, there was less dissipation leading to lower sample temperatures. The observed temperature increase in Figure 3.16 also captures the heating due to the friction between the rotor and air while spinning. However, in the MACS arrangement this contribution to the overall heating is negligible because the sample is far away from the sidewalls of the rotor where the heat due to drag is being generated.

3.6 Discussion

As a result of the limitations imposed by the use of soldered discrete capacitors in MACS experiments, on-chip microstructured capacitors were proposed. The solution of on-chip capacitors offers the benefit of customization whereby the required geometry and the capacitance values can be achieved. Moreover, the capacitors can be structured in symmetrical fashion which leads to an exact and mechanically balanced MACS device. However, the low quality factor of these on-chip passives were a significant disadvantage when using them as a part of MACS resonator because of detrimental effects towards signal transfer. Therefore, the goal of this chapter was to develop designs for capacitors on-chip that would possess minimum required quality factors as well as satisfy other requirements to function under the constraints of MAS.

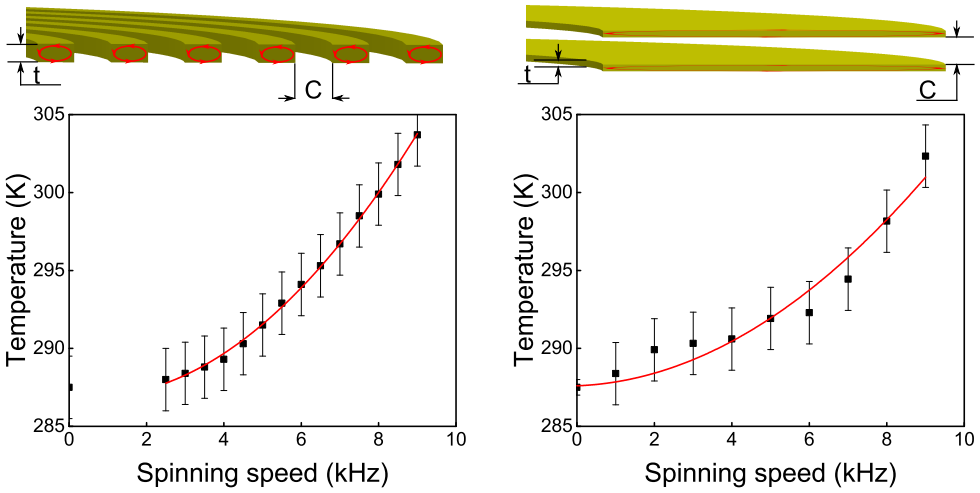


Figure 3.16: Measurements with ethylene glycol for analyzing the temperature increase due to the induced eddy currents in a) an interdigitated capacitor with a metal thickness of 8 µm and b) parallel plate capacitor of plate thickness 3 µm. Each graph is shown with best-fit curves (solid red lines) to a square dependence of the temperature with spinning speed. Adapted from Adhikari *et al.* [46] Copyright 2018 ©Wiley.

Two variants of microstructured on-chip capacitors were considered, namely the interdigitated and parallel plate capacitors. Although the fabrication process for the former variant is straightforward, the obtained quality factor values were quite poor(< 20). On the other hand, the complexity in fabrication steps for the latter was a good trade-off for higher quality factors, with a Q-factor enhancement of ≈1.5 as compared to the former variant. Furthermore, wafer level distribution of capacitor characteristics of the parallel plate variant showed better consistency as compared to the interdigitated design. This was attributed to the process variations in electroplating, where the interdigitated structures were affected by fluctuations in electroplating thickness as compared to the parallel plate counterparts. This is because the capacitance of the plate capacitors are affected by the thickness of the dielectric rather than the thickness of the plates. The capacitor characteristics are summarized in Table 3.2 and are also compared with discrete commercial capacitors (Temex ceramics and Knowles). It can be observed from Table 3.2 that commercial capacitors have quite large footprints, thereby constraining their compatibility with MAS systems smaller than 3.2 mm. Although, no data was available on the heating due to induced eddy currents from these discrete elements, the connection to the ends of a micro-coil is done using solder joints with thicknesses of hundreds of µm which leads to increased heating effects due to induced eddy currents. Although, the amount of solder can be minimized by spot welding technique [99, 152], this is still responsible for significant sample heating. Therefore, in spite of the very high Q-factors offered by commercial capacitors, all these drawbacks does not make them viable for MACS resonators.

It has been observed that in the case of on-chip capacitors, the extent of induced eddy currents can be greatly restricted by limiting the thickness of the metal electrodes. However, reducing the thickness of the metal structures would lead to a decrease in the Q factor. Nonetheless, it was illustrated in Figure 3.14b that in the case of parallel plate capacitor, the proportion of decrease in the Q factor due to reduced plate thickness was not critical to drastically affect the overall electrical performance of the MACS system. On the contrary, for the interdigitated capacitor, the depreciation in Q factor with reduction in thickness is significant to deteriorate the NMR signal transfer. Moreover, from the Table 3.2, it can be observed that the parallel plate capacitor offers higher capacitance density for a specified footprint as compared to the interdigitated capacitor. The interdigitated capacitor is also limited by the capacitance density offered within a specified footprint due to limitations imposed on thickness of electrodes by induced eddy currents. Alternatively, capacitance density could be increased by replacing SU-8 with high-k dielectrics such as Al_2O_3, AlN, Ta_2O_5 and HfO_2 [173] as the dielectric layer. Thin films (100s of nm) of these dielectrics can be grown on top of metal electrodes using techniques such as atomic layer deposition (ALD) or chemical vapour deposition (CVD) [173–175]. However, these dielectrics exhibit lower breakdown voltages as compared to the SU-8 dielectric which would affect the reliability of the MACS devices. Therefore, these high-k dielectrics were not considered as an option to be used as a dielectric for the fabrication of on-chip capacitors.

Consequently, it can be summarized that parallel plate design compared favourably as compared to the interdigitated one to be integrated in a MACS device. The metrics of Q factor and induced eddy currents showed that former offers adequate performance characteristics needed for MACS application. Additionally, this design also provides flexibility with respect to capacitance values by means of modifying the interplate distance to correspond to different footprints, thus allowing for scaling down MACS devices that could be spun at higher speeds.

Table 3.2: Table of capacitor characteristics. Adapted from Adhikari *et al.* [46] Copyright 2018 ©Wiley.

Capacitor type	Capacitance range (pF)	Q-factor	Eddy current heating (°C)	Footprint (mm^3)
Discrete [166, 176]	0.1-6.8×10^6	10000	No Data	1.8×1.0×0.8
Interdigitated	0.4-3.8	16	5	1.8×1.8×0.008
Parallel plate	1-13	27.5	5	1.1×1.1×0.016

4 Microfabricated MACS inserts

The micro-detector utilized to enhance sensitivity of MAS experiments has two main components, viz., the on-chip capacitor and the inductor. The various attributes of the former were comprehensively discussed and evaluated in the previous chapter. The integration of the inductive component with the on-chip capacitor and the consolidation of various aspects of this micro-resonator as an insert which can be seamlessly incorporated in the MAS rotor is the focus of this chapter.

The rotating micro-coil experiments were carried out using 50 µm to 80 µm thick copper wires [10] which were manually wound around a quartz capillaries which acted as sample holders. The piggy-back MAS experiments were also conducted with 50 µm copper wires manually wound around a vespel holder. The handwound micro-coils were typically 1 mm long solenoids having diameters from 400 µm to 750 µm. However, as we have discussed in the previous chapter, the adoption of 50 µm to 80 µm thick copper wires will lead to higher heat generation due to induced eddy currents in the rotating micro-coil. While numerous MACS papers further down the line report on micro-coils built with 30 µm diameter wire [150, 151], hand-winding such delicate structures, and soldering or spot welding [99, 152] their fine wire ends to a discrete capacitor is a labouring and cumbersome process. This represents a major bottleneck towards obtaining a large number of such detectors in a robust manner and with reproducible performance. Additionally, aluminum nitride (Shapal-M) inserts were used to aid in heat dissipation away from the sample region due to eddy currents generated as a result of coil spinning.

Another issue in the design of MACS inserts is related to the mechanical balancing of the devices, a crucial aspect needed for fast spinning. Manual fabrication of the coil, and subsequent manual integration of a discrete capacitor, represents a built-in limitation due to lack of achievable precision.

Wirebonding [157] is an innovative technique for micro-coil fabrication and Badilita *et al.* [11] reported this method for MACS coils. The use of an automatic coil winder has facilitated a robust integration of thin, 25 µm diameter wires. Additionally, microfabrication of the devices is advantageous to other methods by ensuring a mechanically balanced device due to precise alignment offered by accuracies associated with photolithography technique employed for fabrication of the on-chip capacitor and sample holder. However the length of the micro-coil was only around 300 µm to 500 µm. Moreover, the fabricated detectors were quite delicate and required scrupulous handling during sample filling and NMR measurements.

Therefore, the goal is to fabricate micro-coils with coil lengths in the range of 1 mm to 1.5 mm, to push the envelope with respect to the coil lengths achieved with microfabrication

in combination with wirebonding. Additionally, the objective was also to obtain detectors that are reproducible, robust and easy to handle so as to seamlessly facilitate NMR measurements.

In this chapter, the simulation of various characteristics of the MACS inserts along with their fabrication are described comprehensively. Electrical as well as NMR characterization followed by a discussion and analysis of the results completes the chapter.

The analysis of the results along with fabrication and characterization of the inserts described in this chapter have been reported as a research article in Analyst (Royal Society of Chemistry) journal [SA2].

4.1 Simulations

The simulation studies were performed to evaluate the maximum sensitivity enhancement that could be achieved with the help of MACS inserts and also to compare the enhancement from the two capacitor variants. The distortion in the B_0 field arising from various material susceptibilities in the MACS chip was also evaluated.

4.1.1 B_1 field simulation

.

Simulation of expected B_1 field enhancement from the MACS resonator for a 4 mm MAS system was executed in COMSOL Multiphysics®. The simulation was performed with the RF module of the software employing the physics of electromagnetic waves in the frequency domain.

A spherical air domain having a diameter of 10 mm was defined as the simulation domain which was sufficiently large so that the solution is not affected by the exterior boundaries. The two variants of the micro-resonator were defined in the CAD environment of the software. The modeled micro-coil has 24.5 turns with a length of 1 mm. The interdigitated capacitor (10 fingers) variant was modeled with a thickness of 10 µm and the parallel plate capacitor was modeled with a plate distance of 10 µm and plate thickness of 3 µm. Copper was the defined material for the micro-coil whereas gold was assigned to the capacitors. Both micro-resonators were inductively coupled to a 8 turn coil made of copper with a diameter of 4.5 mm and a length of 4 mm, which represents the commercial coil in the MAS probe. The ends of the probe coil were connected to two perfectly conducting leads and a lumped port was defined between them. A driving voltage of 1 V was applied at the port through a 50 Ω characteristic impedance. The conductive surface losses in the coils and capacitors were accounted for with the help of an impedance boundary condition.

The finite element mesh was relatively coarse for the spherical air domain and the outer probe coil. A finer mesh (free tetrahedral) size of 4 µm was assigned to the micro-coil and the capacitors.

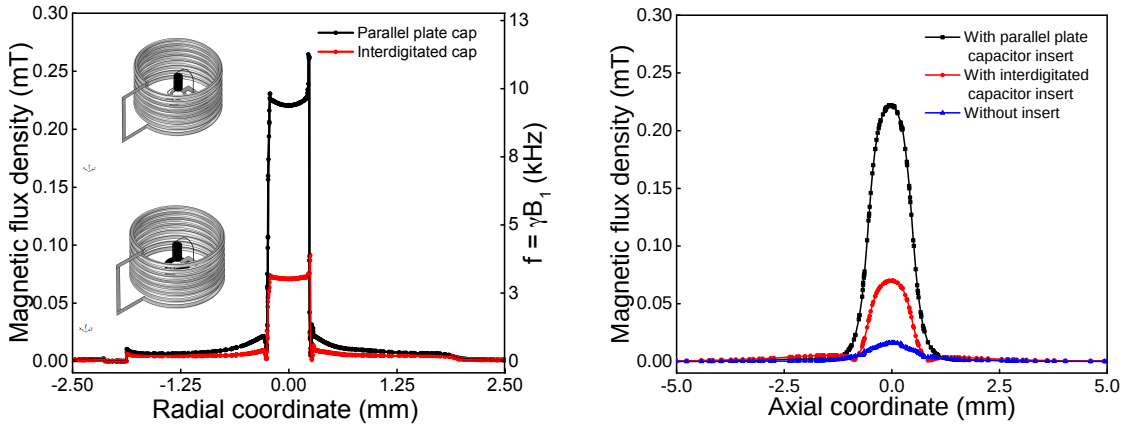


Figure 4.1: Comparison of simulated B_1 field enhancement obtained from MACS resonators with two capacitor types. a) B_1 field values are taken from cut line through center of coil perpendicular to the coil axis; b) B_1 field values are taken along coil axis.

4.1.2 B_0 field simulation

The variation in material susceptibilities [103, 177] is an important factor determining the spectral lineshapes. B_0 field distortions in the sample region caused by the proximity of the coil material and the sample was a major hindrance to high-resolution NMR using micro-coils. The use of susceptibility matching fluids and zero-susceptibility wires have been reported as a means [8] to achieve high-resolution micro-coil NMR. In the case of rotating micro-coils, the anisotropic material susceptibility effects can be averaged to zero and thus eliminated by spinning the micro-coil ensemble at the magic angle [178]. Although, the anisotropic susceptibility effects get averaged out in the case of MACS technique, B_0 field simulation was done to study the effects of SU-8 and copper wire used in the construction of the micro-detector.

The volume magnetic susceptibility values described in Table 4.1 implemented in the simulation model shown in Figure 4.2a were reported by Wapler *et al.* [179]. The coil is essentially modeled as a sheet of copper which is equivalent to tightly wound copper coil.

Table 4.1: Relative permeability of various materials in the MACS device [179]

Material	Relative permeability
Air	1
Copper	0.999994
Water	0.999992
SU-8	0.999985

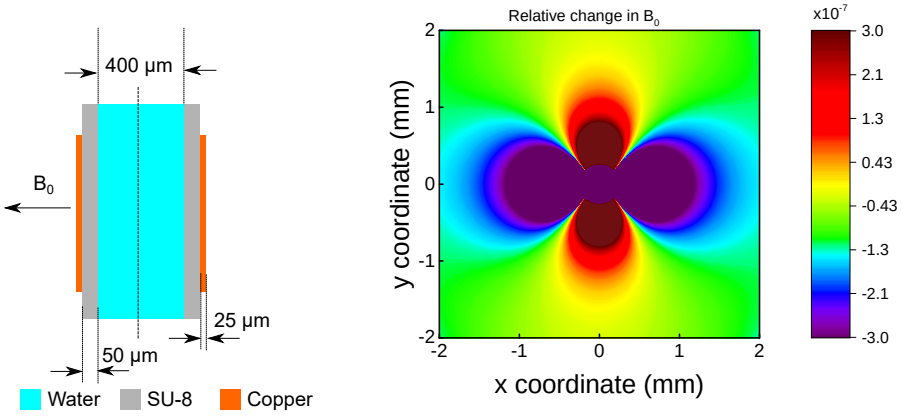


Figure 4.2: a) 2D illustration of the simulation model which describes the various material interfaces in the MACS detector; b) 2D graph depicting the contours of the local magnetic field variations arising from various magnetic susceptibilities. The static magnetic field is defined perpendicular to the axis of the cylinders (z-direction).

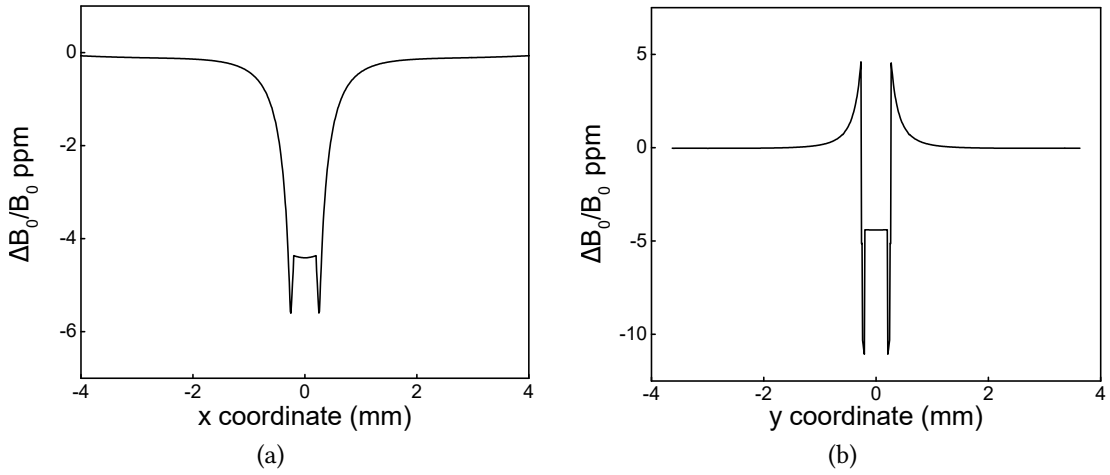
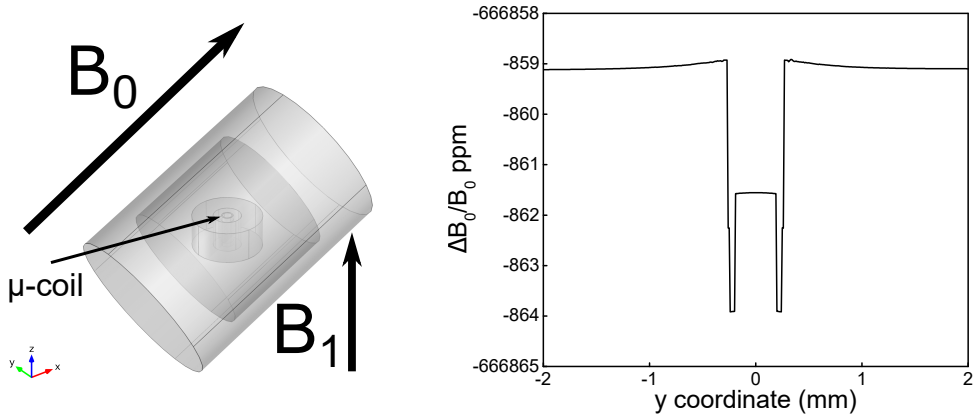


Figure 4.3: 1D graph depicting the perturbation in local magnetic field arising from various magnetic susceptibilities along the two directions perpendicular to applied magnetic field (x-direction and y-direction). The static magnetic field is defined perpendicular to the axis of the cylinders (z-direction).

The distortion in the B_0 field due to various material susceptibilities was simulated using COMSOL Multiphysics®. The simulation was performed with the AC/DC module of the software and magnetic fields, no currents physics being chosen as the preferred physics to simulate the susceptibility effects.



(a) (b)

Figure 4.4: a) Simulation model illustrating the static magnetic field at an angle 54.7° to the rotation axis (z-direction) of the micro-coil (innermost cylinder); b) 1D graph depicting the perturbation of the local magnetic field arising from various magnetic susceptibilities along a direction transverse to the applied magnetic field (y-direction).

A cylindrical air domain having a diameter of 7 mm and a length of 10 mm was generated and defined as the simulation domain. The micro-detector model shown in Figure 4.2a was defined in the CAD environment of the software inside the domain. The whole simulation domain was assigned the magnetic flux conservation boundary condition. The exterior boundaries were defined with magnetic flux density value of 11.7 T whereas the curved exterior surface of the cylinder had zero magnetic flux density. Thus, a homogeneous magnetic field was established inside the simulation domain. As described in Figure 4.2a, the innermost region is the sample region which was assigned with water (blue). The other constituent materials defined were SU-8 (grey) and copper (brown).

The entire micro-detector was treated as cylinder with a circular cross-section. Initially, the static magnetic field, B_0, was defined perpendicular to the cylindrical axis. The goal was to observe contours of the perturbation field as shown in Figure 4.2b which is similar to the dipole pattern of the magnetic field perturbation described by Schenck [177] for a circular cylinder placed transverse to the static magnetic field, B_0.

Subsequently, the magic angle case was simulated by positioning the micro-detector at an angle of 54.7° to the static magnetic field, B_0, as shown in the Figure 4.4a. However, the coil in this case is not rotating. The results from the simulation show that there are no adverse susceptibility jumps or distortion in the sample region and performance is better than the case where the sample is perpendicular to the B_0 field. This was the main goal of the simulation study to check for any extreme cases of distortions which would destroy the spectral quality of the NMR measurements. Since the detector is rotating at the magic angle under experimental conditions, majority of the line broadening due to isotropic susceptibility gets averaged out.

Moreover, Olson *et al.* [94, 95] have demonstrated experimentally that even in the static case, placing the sample at the magic angle with respect to the B_0 field leads to improved spectral resolution.

4.2 Fabrication

Following the fabrication of on-chip capacitors using process steps described in the previous chapter, fabrication procedure of inductive part of the MACS devices is described in this section. The main aspect of micromanufactured micro-coils is the automatic wirebonding technique. The wirebonding method of obtaining micro-coils necessitated yoke or support structures as described in [11, 110, 156, 157] on top of the capacitors. Kratt *et al.* [157] employed poly-methyl methacrylate (PMMA) support structures for wirebonding manufactured using x-ray lithography. Hollow SU-8 [11, 110, 156] cylinders fabricated using regular lithography techniques have been popular as wirebonding support structures. High aspect ratio Polydimethyldisiloxane (PDMS) [180] pillar structures realized by UV imprinting could be an alternative for the SU-8 based yokes. Kamberger *et al.* [181] developed high filling factor coils using a water soluble poly-vinyl alcohol (PVA) support structures and PMMA encapsulation.

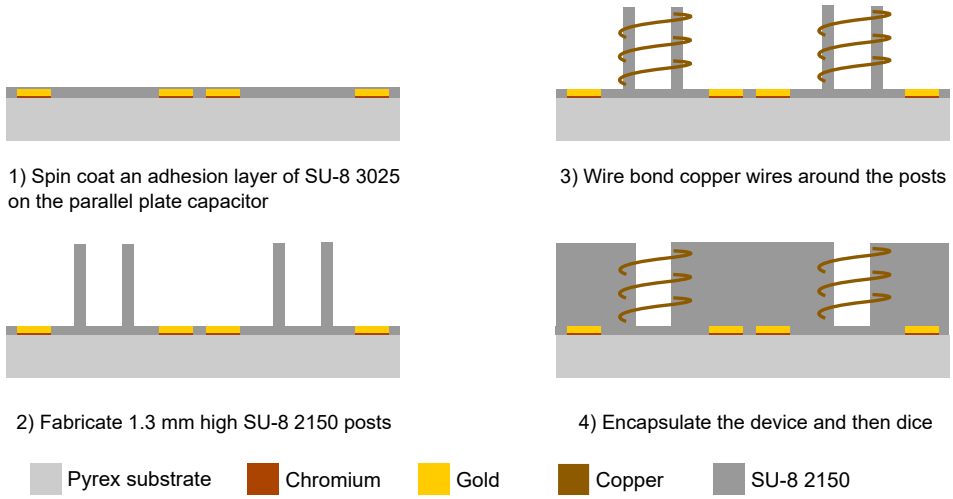


Figure 4.5: Description of the process flow to fabricate the micro-coil and to obtain individual MACS detectors.

Although PMMA posts display good strength and stability, X-ray fabrication is an expensive and tedious process. Strong ^1H NMR background signal from PDMS makes it a no-go in NMR applications. The high filling factor coil fabrication technique, although quite promising, has a lot of issues associated with PVA and PMMA casting. PVA had significant volume shrinkage which necessitated multiple casting steps and subsequent PMMA encapsulation resulted in PVA getting absorbed into PMMA or vice versa. Additionally, the glass transition temperature of PVA (85 °C), hinders the use of copper wires during wirebonding(150 °C). Moreover, the

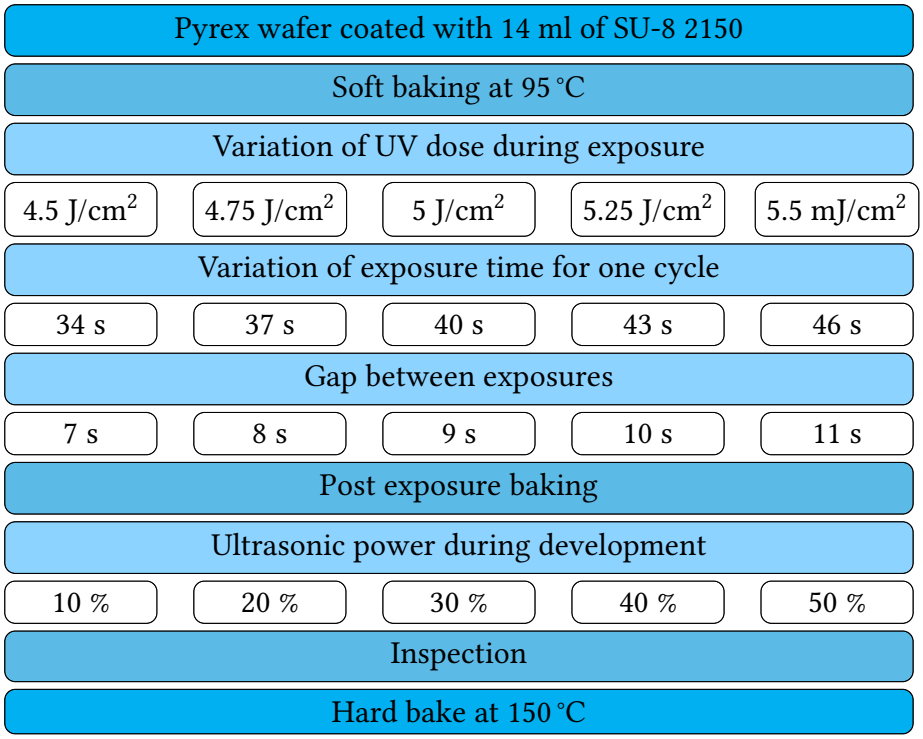


Figure 4.6: Experimental plan for fabrication of SU-8 pillars

entire process involved utilizing precision pins for alignment which means that it does not provide the lithographic accuracy needed for the detectors rotating at the magic angle. On the other hand, SU-8 based support structures employed lithographic techniques for fabrication. However, these SU-8 cylinders had a maximum thickness/height of around 800 µm, with coil length being less than 500 µm.

There have been multiple reports on high aspect ratio (HAR) SU-8 fabrication [182, 183] with heights of around 1 mm to 1.5 mm [184, 185] achieved with multiple coating/casting techniques. However, the aim of this work is to achieve heights in the range of 1.25 mm to 2 mm in combination with wall thickness of 50 µm to 100 µm to obtain higher filling factors. This amounts to an aspect ratio in the range of 12.5 to 40.

4.2.1 HAR SU-8 lithography

Figure 4.5 describes the process flow to obtain the final MACS detectors through the fabrication of high aspect ratio SU-8 yokes/sample holders required for the wirebonded micro-coils followed by packaging of the detectors in SU-8. Following the fabrication of on-chip capacitors, the substrate is then treated with 10 W O_2-plasma for a period of 5 min. Then, a 5 µm thick layer of SU-8 3005 is spin coated onto the substrate to improve the wetting behaviour of SU-8 2150 resist. Subsequently, around 14 ml SU-8 2150 resist is deposited onto the substrate in two coating steps.

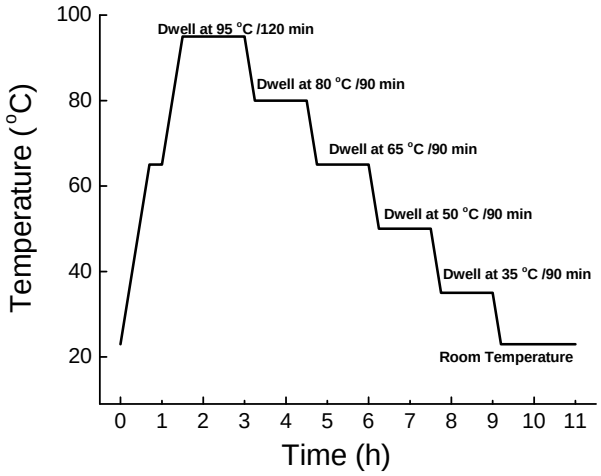


Figure 4.7: Optimized post exposure bake cycle for HAR SU-8 structures [159].

In the first coating step, the substrate was heated to 80 °C on a programmable hotplate (PR 5 SR from Detlef Gestigkeit-Elektrotechnik, Duesseldorf) whose surface is leveled. A flat-leveled surface is critical in maintaining uniform resist thickness. Also, the adhesion layer of SU-8 3025 resist aids in the efficient planarization of SU-8 2150 on the substrate. With the substrate at 80 °C, 8 ml of SU-8 2150 is statically deposited with the help of a pipette. Then, the hotplate was ramped up from 80 °C to 95 °C over an interval of 15 min. The substrate was held at 95 °C for time interval of 9 h. This soft baking step is important to remove the solvent because a high solvent content will lead to the generation of high film stress during post-exposure baking. Moreover, it also improves resist-substrate adhesion. At the end of the baking step, the hotplate temperature was brought down to 80 °C at the rate of 1 °C/min. Subsequently, 6 ml of another layer of SU-8 2150 resist was cast on the prebaked resist film. Then, similar to the previous soft bake process, the hotplate was ramped up from 80 °C to 95 °C over an interval of 15 min and the substrate was held at 95 °C for time interval of 10 h. After the soft bake process, the substrate temperature was brought down to room temperature at the rate of 1 °C/min. Since minimum diffusion of solvent takes place from the new layer into the prebaked layer [183], the net solvent content is reduced after 14 h of softbaking time and hence the softbaked film is less susceptible to internal stress during further processing.

Next step was the pattern transfer onto the resist film by masked irradiation using a UV lamp at a wavelength of 365 nm with the help of an i-line filter. A soft contact was established between the mask and the resist during exposure to avoid air gaps which results in T-shaped SU-8 pillars with negatively sloped sidewall angles instead of vertical walls [186]. An estimated UV exposure dose was obtained from literature [184, 185] and subsequently a detailed design of experiment (DOE) study was conducted as shown in Figure 4.6 to obtain the exact exposure dose of about 5.2 J/cm^2. The 5.2 J/cm^2 exposure dose was achieved through multiple exposure steps which was necessitated due to long exposure time needed for the dose. The multiple

exposure technique also helps to prevent overheating the surface of the film from continuous exposure as well as improved absorption rate of the UV light. Therefore, the overall exposure dose was divided into small exposure times of 37 s each with an exposure gap of 10 s.

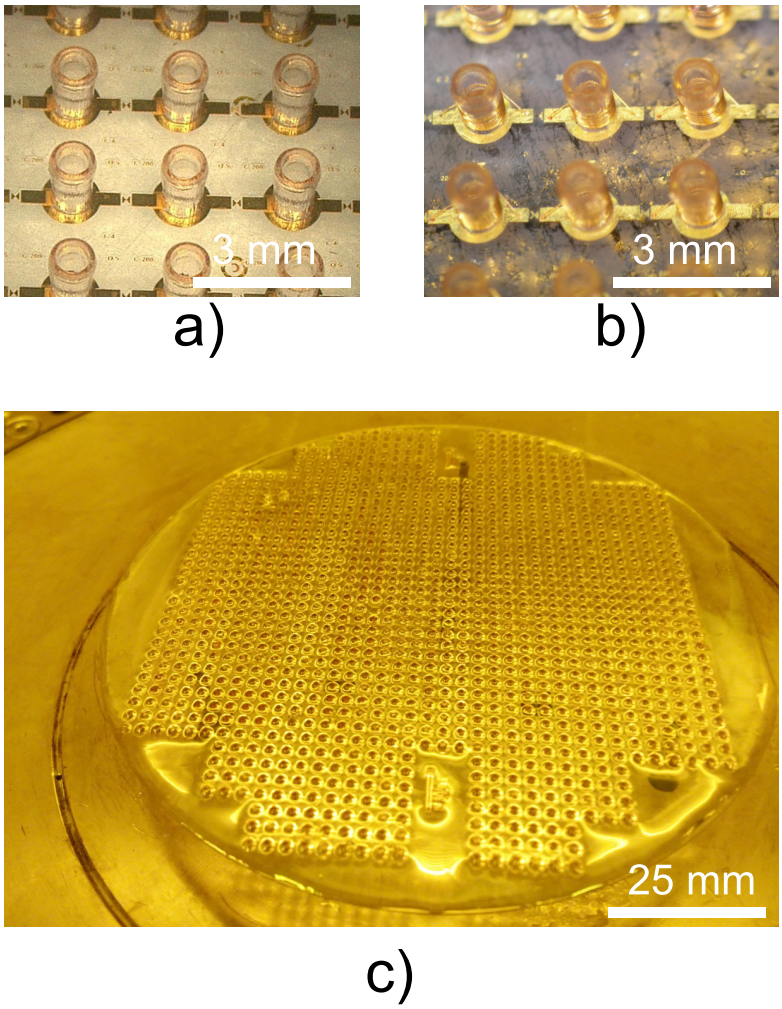


Figure 4.8: Images showing the substrate under various stages during the fabrication of micro-detector. a) SU-8 support structures fabricated using HAR SU-8 lithography; b) Wirebonded micro-coils which form an LC resonator with the on-chip capacitor; c) Substrate encapsulated to improve the physical handling of the detectors.

Following the exposure step, the substrate was placed on the flat-levelled hotplate for the post exposure baking step (PEB). The PEB process for 1.3 mm thick SU-8 structures was optimized in this work [159] and similar heating and cooling cycles shown in Figure 4.7 were programmed on the hotplate. The optimized post-exposure baking conditions were critical [185] in reduction of residual stress in the 1.3 mm thick film which would otherwise result in debonding of the SU-8 structures from the substrate. Hence the substrate cooling after the PEB was over 10 h.

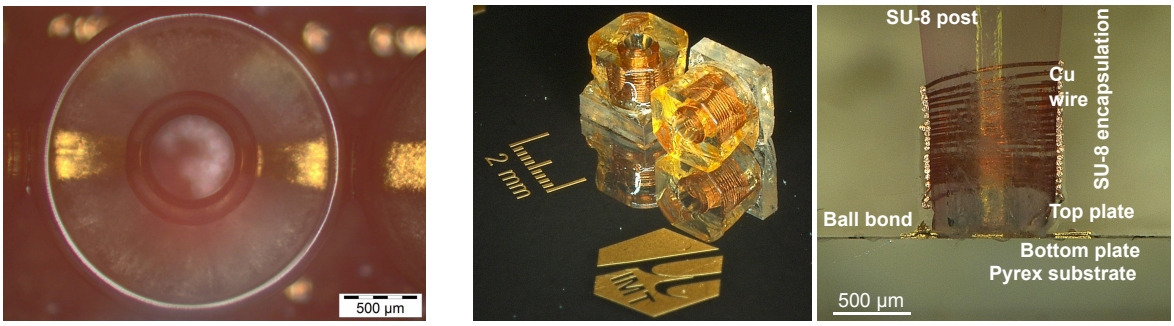
The SU-8 structures after the post exposure bake was subjected to development using PGMEA (Propylene glycol methyl ether acetate) solution (Microchemicals GmbH, Ulm) for a period of 2 h. Ultrasonic agitation (SONOREX SUPER 10P, BANDELIN electronic GmbH & Co. KG) was additionally used to effectively develop the non-crosslinked regions inside the pillars until the substrate. The ultrasonic waves in the kilohertz frequency range causes additional pressure at the surface of the resist and speeds up diffusion of developer molecules into the resist. A 30% power was found to be optimal for the development of HAR SU-8 structures. The substrate was subsequently rinsed in isopropanol (IPA) for 1 h. An additional hard bake step at 150 °C after rinsing was observed to be beneficial in improving the adhesion of the SU-8 pillars on the substrate. The fabricated SU-8 pillars with an O.D/I.D of 850 µm/700 µm are shown in Figure 4.8a.

4.2.2 Wirebonded micro-coils

As already mentioned in the previous sections, the inductive part of the MACS detector, i.e. the μ-Solenoids were manufactured through the wirebonder-assisted coil fabrication technique [11, 110, 156]. The bondhead from the automatic ball-wedge wirebonder (ESEC WB 3100®, Oerlikon AG Switzerland) equipped with a ceramic bottleneck capillary (SU-35100-5100F, SPT) and an insulated copper wire of diameter (thickness) 25 µm and 50 µm (X-wire^{TM} Microbonds Inc.) is programmed to follow a trajectory according to an in-house developed MATLAB®code A13. The wirebonding process starts with free air ball (FAB) generation set by the electrical flame-off (EFO) parameters. Since the copper wire after the ball formation is susceptible to oxidation, it is protected by a constant stream of pure nitrogen gas at a rate of 25 l/min. After the FAB generation a ball bond is formed on the contact pads by optimizing ultrasonic power (US) power, impact force (IF) and temperature. Meanwhile after the formation of the ball bond, the MATLAB®code becomes active until the formation of the wedge-bond. The wedge-bond is formed also by optimizing ultrasonic power (US) power, bond force (BF) and temperature. The initial and final coordinates of the coil trajectory have to coincide with the coordinates at the end of the ball-bond and at the beginning of the wedge-bond respectively. The optimized bond parameters used for the micro-coil fabrication for a 25 µm thick copper wire is described in A15. One batch of fabricated wirebonded micro-coils is shown in Figure 4.8b.

4.2.3 Back end processing

Following the fabrication of micro-coil on top of the on-chip capacitor, the substrate containing the detectors is encapsulated in SU-8 2150. The encapsulation is important to provide protection to fragile bond connections of the micro-coil and also to enable easy handling of the MACS detectors during NMR spectroscopy. Another important role of the encapsulation is to push the air interface far away from the sample. Therefore, SU-8 2150 was itself chosen to provide continuous material susceptibility.



(a) (b)

Figure 4.9: a) Perfectly encapsulated MACS detector on a substrate; b) **Left**: MACS detector separated from the substrate with the help of a semi-automatic dicing saw. **Right** Cut section of the MACS device showing the various components of the MACS detector. Adapted with permission from [148] Copyright 2019 ©Royal Society of Chemistry.

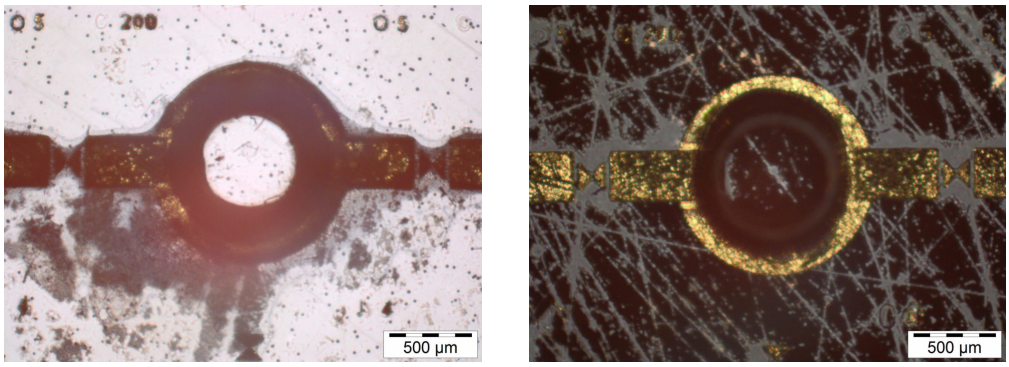
The encapsulation process was similar to HAR SU-8 fabrication done in Section 4.2.1. However, in this case the dispensing of SU-8 was accomplished in a single step. The dispensing of SU-8 was done carefully so as not to destroy the coils as well as to avoid SU-8 inside the pillars. A typical substrate after the PEB step is shown in Figure 4.8c. An individual detector after the resist development is shown in Figure 4.9a. The vital things to take care was to avoid air bubbles inside the encapsulated detector and to ensure the absence of SU-8 inside the sample region.

Following the encapsulation step, the detectors were separated with the help of a semi-automatic dicing saw (Disco DAD 320) with equipped with a diamond coated dicing blade of thickness 200 µm. The dicing process was accomplished in multiple steps of 500 µm each to obtain detectors shown in Figure 4.9b. The final footprint of each detector was 2 mm × 2 mm.

4.2.4 FMEA

An FMEA study was done to recognize the obstacles during the fabrication of SU-8 pillars and wirebonding process as well as to improve the reproducibility of the process steps, thus enhancing the yield of the MACS detectors.

One of the critical aspects during the fabrication of the MACS detectors was the reliability of the wirebonding process. Ball and wedge bond formation was greatly affected by the cleanliness of the pads. The presence of SU-8 residues on the contact pads as shown in the Figure 4.10 hindered fabrication of coils on the on-chip capacitors. Additionally, if ball bond and wedge bond formation were even remotely possible on these contact pads, the imperfect bonds would lead to an increased resistance of the entire device which would then result in decreased Q factors. Moreover, the presence of SU-8 residues is also detrimental to the bondhead capillaries reducing their operational life.



(a) (b)

Figure 4.10: SU-8 residues on contact pads left over after the HAR SU-8 lithography process hinders the fabrication of micro-coil using wirebonding. The cleanliness of the contact pads is critical to the formation of stable ball and wedge bonds during the wirebonding process.

The proposed solution to the issue of SU-8 residues on the contact pads as shown in Figure 4.11 was to introduce a sacrificial layer between the contact pads and SU-8. Experiments were then conducted to determine the minimum required thickness of the proposed sacrificial layer. AZ positive tone resists were chosen as the prospective sacrificial layer because they were easy to process and straightforward to strip either using acetone or a concentrated developer solution. Different series of AZ resists are also available which offer resist thickness in the order of 0.5 µm to 3 µm (AZ® 1500 series) [187], 3 µm to 30 µm [188] (AZ®4500 series) and up to 15 µm to 100 µm [189] (AZ®40XT).

The tests were initially carried out with AZ® 1505 resist which was spin coated at 3000 rpm and resultant thickness of the sacrificial layer after further patterning and processing the resist was around 0.7 µm. SU-8 pillars were then fabricated on the substrate with the AZ® 1505 layer on top of the contact pads. However, after development of bulk SU-8, residues were still observed on the contact pads.

Since the SU-8 residues persisted with a sacrificial AZ® 1505 resist, tests were then continued with the aim of coating a thicker sacrificial layer. The experiments were carried out using AZ® 4533 positive tone resists. The experimental plan for these tests with AZ® 4533 is described in Figure 4.12. By varying the rotation speed of the chuck, the coated resist thickness of the AZ® 4533 resist was controlled. The cleanliness of the contact pads started to improve as the sacrificial coating got thicker and at a thickness of 5 µm, the contact pads were consistently observed to be free from residues after stripping the sacrificial coating followed by O_2 plasma treatment for 5 min. Thus, employing a 5 µm thick sacrificial layer between the SU-8 and the pads resulted in improved yield in the wirebonding process. Figure 4.13a shows the residue free contact pads after the HAR SU-8 process and Figure 4.13b shows the successful coils fabricated on the top of these 'clean' pads.

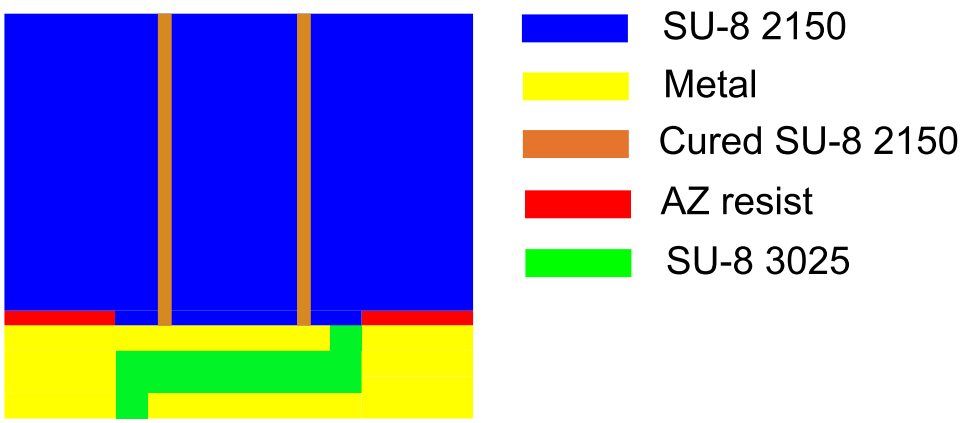


Figure 4.11: Proposal to iron out the obstacle of SU-8 residues on the contact pads. The solution was to avoid the SU-8 coming in direct contact with the contact pads. This was achieved with the help of an AZ sacrificial layer between the contact pads and SU-8 resist.

Another issue that arose during the fabrication process was the hydrophobicity of the SU-8 2150 resist on the surface of the pyrex substrate. This hindered the uniform coating of the thick resist throughout the surface of the resist, especially along the borders. Therefore, to circumvent this adversity, a thin layer (5 µm) of SU-8 3005 resist was spin coated on the substrate to improve the wetting behaviour of the SU-8 2150 resist. As a result, with static dispensing of SU-8 2150, it was straightforward to uniformly coat and planarize the resist on the wafer.

The DOE process described in Figure 4.6 was essential to optimize the UV exposure parameters for the thick resist because a lower exposure dose resulted in weak adhesion of the SU-8 pillars on the substrate. On the contrary, a higher exposure dose lead to the partial cross-linking of resist in the sample region (inside the cylinder), thereby causing the developer solution ineffective. Ultrasonic agitation during development was also crucial in avoiding partially closed SU-8 cylinders.

Numerous pitfalls were also experienced during the encapsulation process of the devices. Again, the hydrophobic behaviour of SU-8 2150 was a cause of major hindrance. However, instead of spin coating, which would damage the wirebonds, a thin layer of SU-8 3005 was statically dispensed throughout the substrate. The substrate was then baked for 2 h at 80 °C to reduce the solvent content and then was followed by static dispensing of SU-8 2150 to fully encapsulate the devices. One common issue that was observed and then subsequently avoided was thick SU-8 getting unintentionally dispensed inside the sample region as shown in the Figure 4.14a. The issue was also solved by minor modification to the photo-mask. The second issue faced during dispensing was the trapped bubbles inside the encapsulated devices as shown in the Figure 4.14b. This is detrimental to the spectral resolution during NMR experiments.

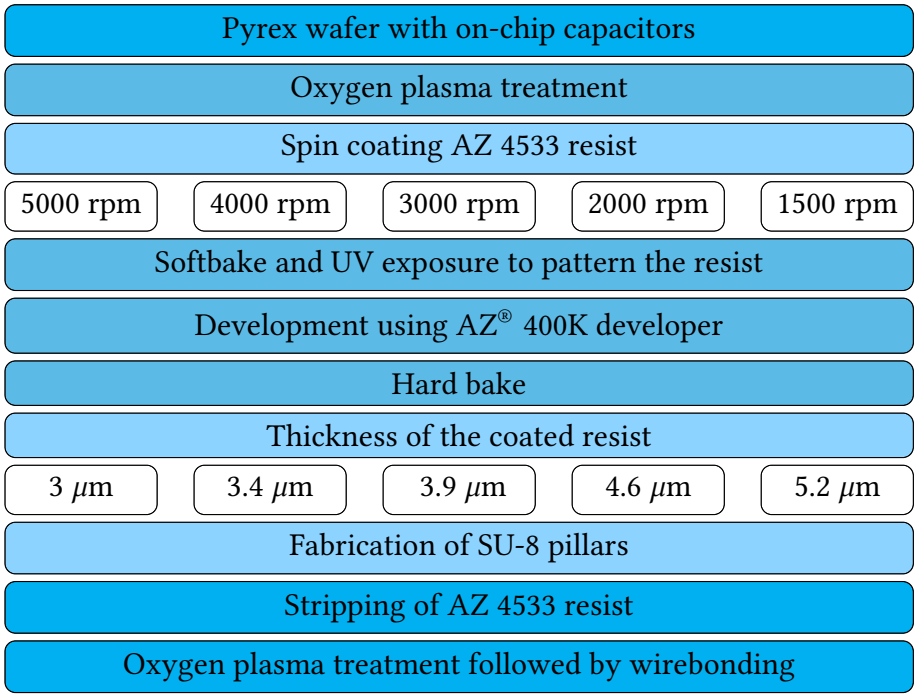
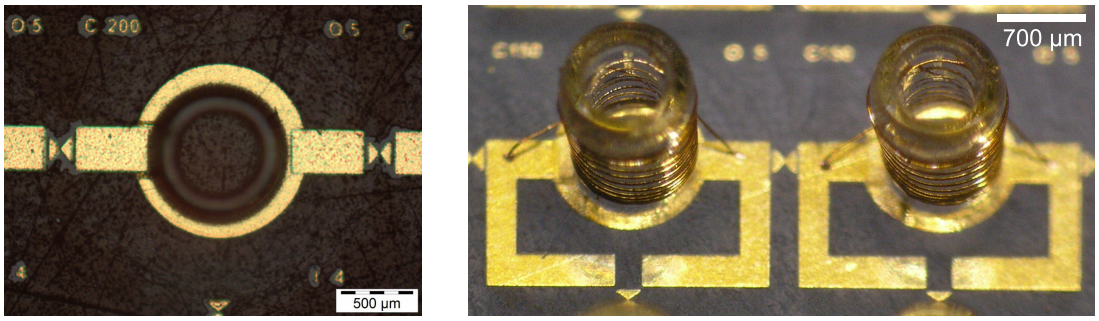


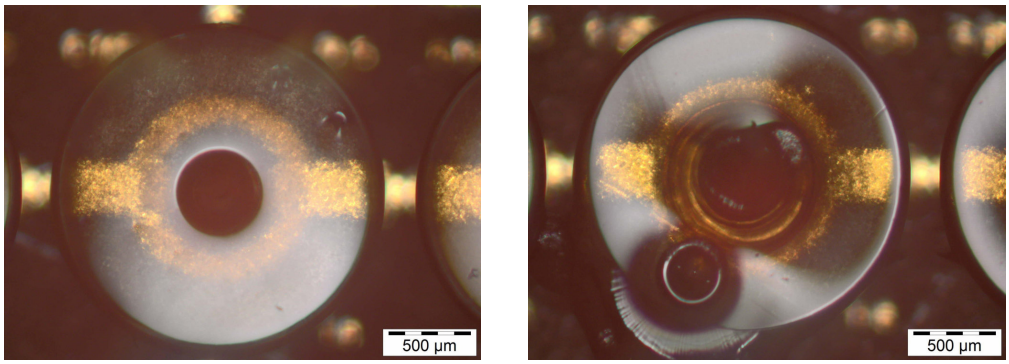
Figure 4.12: Experimental plan to optimize the thickness of the sacrificial layer



(a) (b)

Figure 4.13: a) Contact pad devoid of SU-8 residues after the HAR SU-8 lithography process due to the application of AZ 4533 resist layer on the contact pads; b) Successful and efficient wirebonding process on contact pads without residues.

Figure 4.15 shows an additional complication that arose after the encapsulation process. The warping of substrate shown in Figure 4.15 was due to internal stress from dispensed resist during encapsulation process. This was a critical hurdle for the subsequent substrate dicing process. The substrate warping was subsequently fixed by ensuring complete coverage of SU-8 2150 on the substrate and performing the post exposure bake of the encapsulated resist at 80 °C and the subsequent substrate cooling over a prolonged period of 8 h.



(a) (b)

Figure 4.14: a) Sample region blocked by SU-8; b) Trapped air bubbles inside the encapsulated detector.

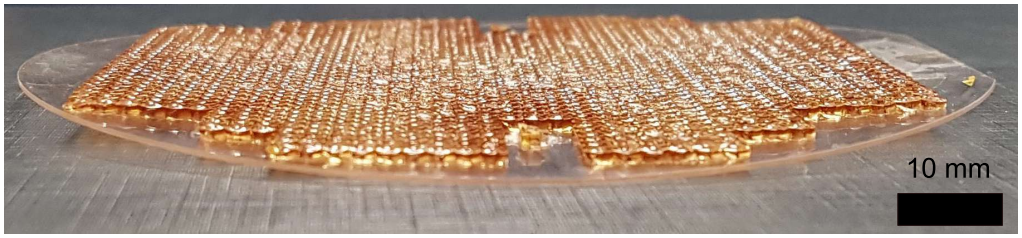


Figure 4.15: Warping of substrates due to internal stress during encapsulation process. This hinders the substrate dicing process.

4.3 Characterization

A combination of on-chip capacitor and wirebonded micro-coil form the MACS detector. The characterization of individual on-chip capacitors was described in the previous chapter. In this chapter, the characterization of individual micro-coil as well the complete characterization of the MACS detectors is explained in detail.

To characterize the operational capability of a MACS sensor, performance indices were established. The performance index of the MACS detector can be associated with its quality factor, resonant frequency and the NMR spectral linewidth obtained using it. The behaviour of the detector was assessed from the measured value of these indices. The scheme of implementation to determine the sensor performance has been described in this section.

4.3.1 Electrical and thermal characterization

Initially, the micro-coils were characterized separately like the on-chip capacitors. The performance of the micro-coil (inductor) was defined by its quality factor, self-resonant frequency and eddy current heating, analogous to the on-chip capacitors. The micro-coils

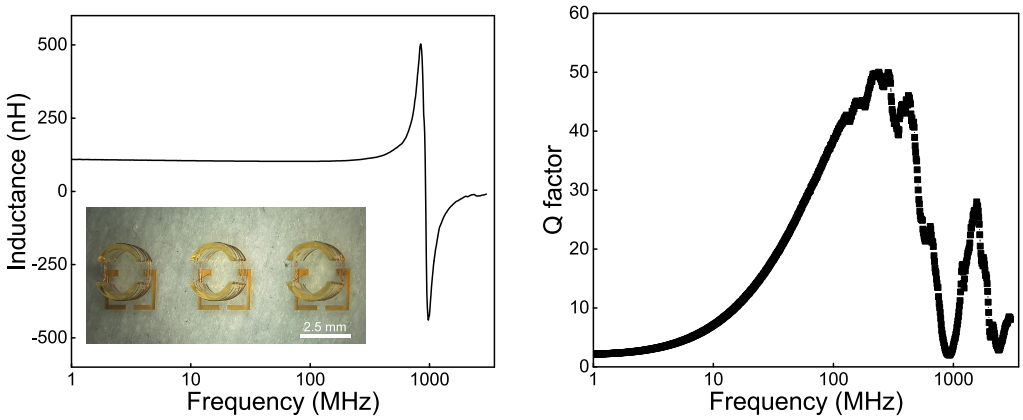


Figure 4.16: a) Frequency response of a micro-coil fabricated from a 25 µm thick copper wire having a diameter of 2.55 mm, 5.5 number of turns and a length of 0.8 mm. The inductance and the self-resonant frequency (SRF) were measured to be about 120 nH and 921 MHz respectively; b) Measured Q factor of the micro-coil. The maximum Q is around 50.

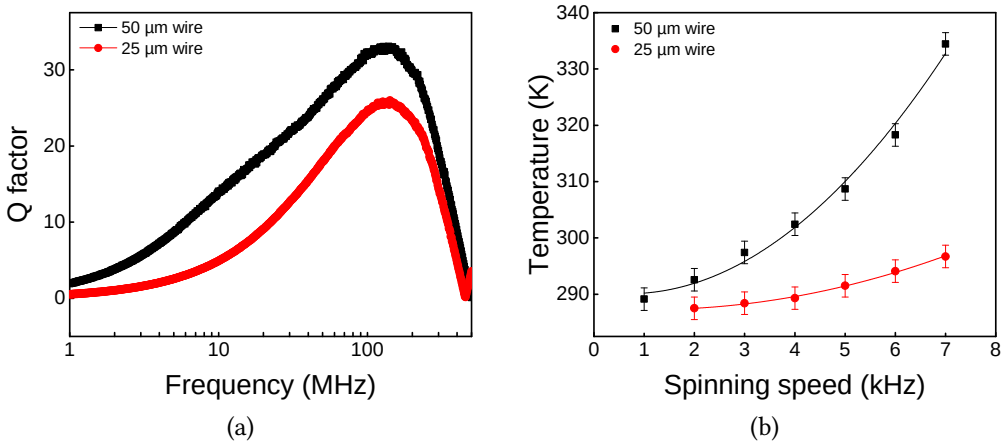


Figure 4.17: a) Q factor of the MACS devices fabricated with 50 µm and 25 µm insulated copper wire; b) Temperature rise in the sample region of the MACS detectors with 50 µm and 25 µm insulated copper wire. The maximum value of the resonator Q factor moderately increases (from 22 to 32), however the temperature rise is significant when using thicker wire (50 µm) compared to thinner wire (25 µm). The coil diameter was 850 µm with 13.5 number of turns. Adapted with permission from [148] Copyright 2019 ©Royal Society of Chemistry.

reported by Kratt *et al.* [156] had an average quality factor of around 50 with their self-

resonant frequency around 2.6 GHz and were fabricated from 25 µm thick insulated gold wire. The micro-coil part of the micro-resonator fabricated in this work were made from 25 µm and 50 µm thick insulated copper wire (X-wire^{TM} Microbonds Inc.). The thickness of the insulation is ≈ 75 nm.

Similar to the characterization of the capacitors, the wirebonded micro-coils were characterized using an impedance analyzer (Agilent E4991A) connected to a probe station (Cascade Microtech MPS150) set up with a Z-probe (Z0-20-K3N-GS-500 from Cascade Microtech GmbH). Open circuit, closed circuit, and 50 Ω calibration of the Z-probe was carried out prior to measurements using an impedance standard substrate.

Following the calibration of the probe to 50 Ω, the frequency dependent inductance and Q factor of the micro-coils on the wafer were measured using an impedance analyzer. The inductance and self-resonant frequencies (SRF) of various micro-coils fabricated from 25 µm thick copper wire having three different diameters of 550 µm, 850 µm, and 2.55 mm respectively with different number of turns were measured. The results from the calibration are described in detail in Section A8. Five coils of each type (specific diameter and number of turns) were fabricated using the wirebonding technique and subsequently their electrical properties were measured. The length of micro-coils was fixed at 800 µm, with an exception for coils with number of turns in the range from 3 to 5. As an example, the inductance and Q-factor of a 2.55 mm coil, with 5.5 number of turns as a function of frequency are represented in Figure 4.16a and Figure 4.16b respectively. The inductance and the self-resonant frequency (SRF) were measured to be about 120 nH and 921 MHz respectively whereas the maximum Q factor was evaluated to be around 50 which is similar to the value reported by Kratt *et al.* [156]. While choosing a micro-coil, care must be taken that the SRF is much higher, atleast 500 MHz, than the Larmor frequency of interest.

After the micro-coils were evaluated individually, the characterization of the micro-coil and capacitor combination, i.e., the micro-resonator, was undertaken. The electrical and thermal behaviour of the detectors, i.e., the Q factor and temperature rise due to eddy currents respectively, of a micro-coil with a diameter of 850 µm with 13.5 number of turns were evaluated. A comparison was made for micro-resonators made up of micro-coils fabricated with 50 µm and 25 µm thick insulated copper wire. There was negligible background signal from the wire insulation. The inductance and SRF of this micro-coil was measured to be 100 nH and 1.75 GHz respectively (Section A8).

The maximum value of the resonator Q factor moderately increases (from 22 to 32) for the thicker wire (50 µm) as shown in the Figure 4.17a. However, the temperature rise is significantly higher (approx 40 °C at 7 kHz) when using thicker wire compared to thinner wire (25 µm) as shown in the Figure 4.17b. Therefore, the Q factor improvement obtained using the 50 µm wire is considerably negated by the temperature rise due to induced eddy currents. This temperature rise in the sample region would lead to a drastic reduction in the spectral quality. Hence, the 25 µm thick insulated copper wire was chosen for the micro-detector.

4.3.2 Resonance splitting due to inductive coupling

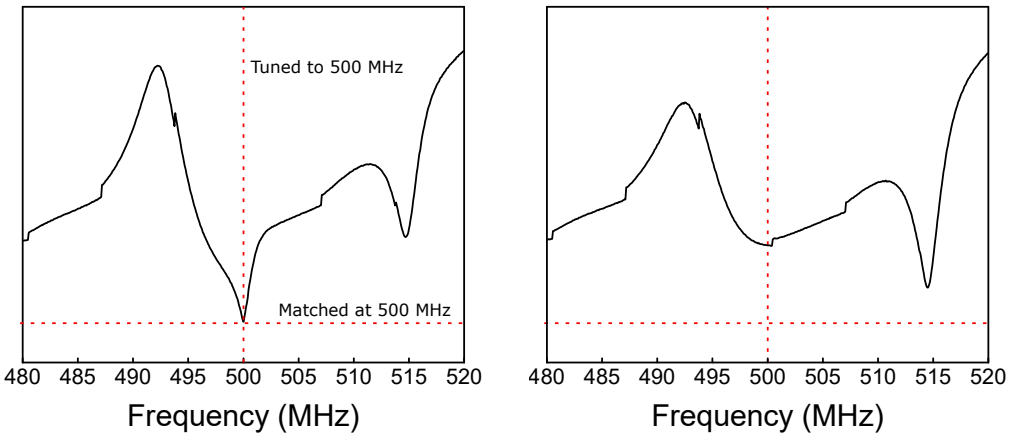


Figure 4.18: a) The coil in the MAS probe tuned and matched to 50 Ω at 500 MHz; b) Changes to the reflection curve upon the introduction of a MACS resonator having a resonant frequency 500 MHz into the MAS probe. The coil in MAS probe is now loaded with the tuned MACS resonator and as a result the coupled system is de-tuned and de-matched. The S_{11} reflection curves were acquired by directly connecting the output port from ^1H channel in the MAS probe to a vector network analyser.

In the MACS resonant inductive coupling mode, the introduction of the MACS detector into the tuned and matched MAS probe results in de-matching of the coupled system due to resonance splitting. With the help of the matching capacitor in the probe and to a smaller extent the tuning capacitor, the tuning and matching of the coupled system to Larmor frequency of interest and to 50 Ω can be achieved. Depending on conditions such as the coupling co-efficient, k, between the two coils and their respective resonant frequencies, the magnitude resonance splitting can be beyond the tuning and matching range of the capacitors in the probe. Therefore, this splitting behaviour was evaluated with microfabricated NMR detectors in the vicinity of 500 MHz.

The assessment of resonant splitting was done with the help of S_{11} reflection curves. These curves were acquired by directly connecting the output port from ^1H channel in the MAS probe to a vector network analyser (E5071C, Keysight® Stuttgart, Germany). Upon the introduction of the MACS resonator (Resonant frequency = 501 MHz) into the MAS probe, the reflection (S_{11}) curve changed as shown in the Figure 4.18, indicating the inductive coupling between the MACS chip and MAS probe coil. However, the range of the tuning and matching capacitors was not large enough in the MAS probe to tune and match the reflection curve at 500 MHz.

Similarly, the change in reflection curves was also observed upon introduction of the MACS inserts at various frequencies between 460 MHz and 540 MHz as shown in the Figure 4.19. For

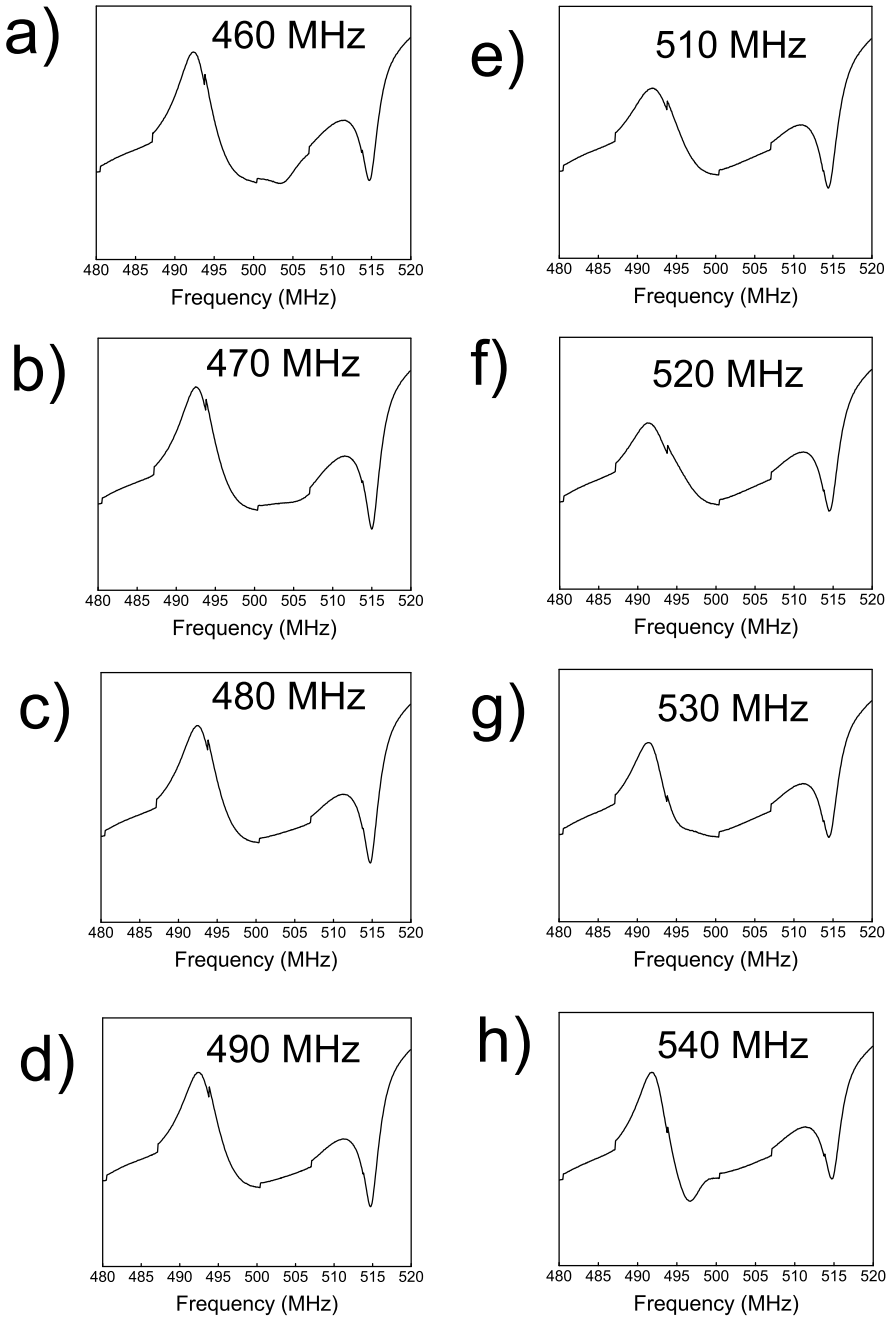


Figure 4.19: Changes to the reflection curve upon the introduction of a MACS resonator having a resonant frequency of a) 460 MHz; b) 470 MHz; c) 480 MHz; d) 490 MHz; e) 510 MHz; f) 520 MHz; g) 530 MHz; h) 540 MHz into the MAS probe.

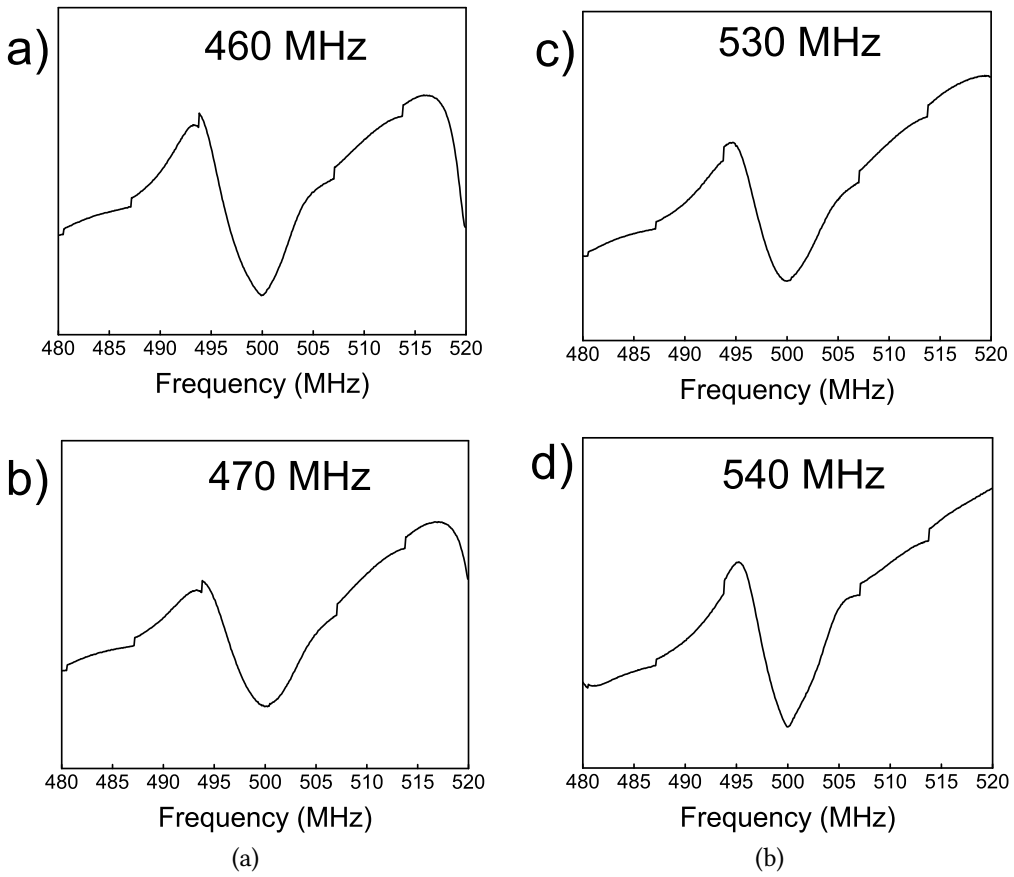


Figure 4.20: Tuning and matching the reflection curve of the inductively coupled system back to 500 MHz. This was achieved only with MACS detectors having a resonant frequency of a) 460 MHz; b) 470 MHz; c) 530 MHz; d) 540 MHz. With MACS detectors from 480 MHz to 520 MHz, the inductively coupled system could not be tuned back to 500 MHz using the available range of the tuning and matching capacitors in the MAS probe.

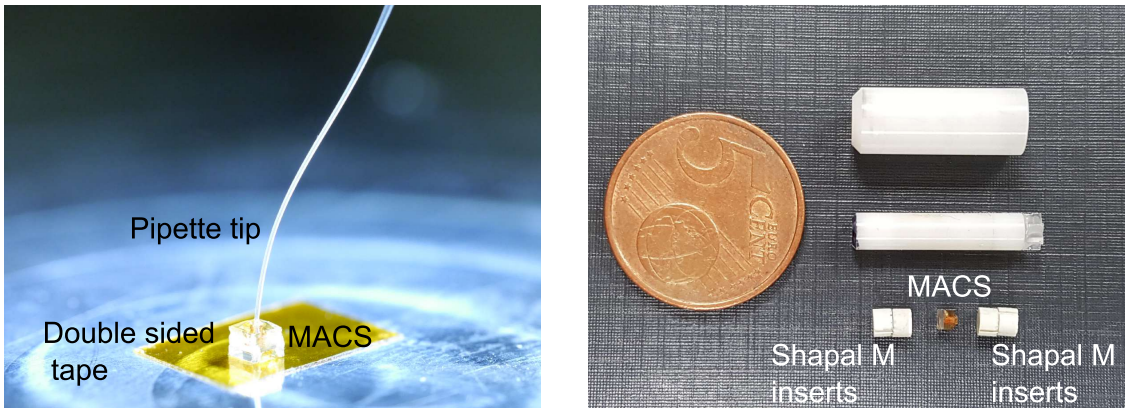
the MACS inserts with frequencies between 480 MHz to 520 MHz, the inductively coupled system could not be tuned back to 500 MHz using the available range of the tuning and matching capacitors in the MAS probe. However, a visible dip in the reflection curve close to 500 MHz was observed with MACS inserts resonating at 460, 470, 530 and 540 MHz. Subsequently, the modified reflection curves from these four instances were tuned and matched at 500 MHz as shown in Figure 4.20.

This splitting behaviour can be explained from the coupling behaviour between the two coils. The splitting of the resonance, $\delta\omega$, is equal to $k\omega_L$. Therefore, closer the resonant frequency of the MACS insert to 500 MHz, stronger is the coupling between the coils and larger the splitting. However, the frequency offset of the MACS inserts from the Larmor

frequency results in reduction in the sensitivity enhancement which has been discussed in Section 2.5.2. Another way to reduce the splitting is to reduce the coupling between the MACS coil and MAS probe coil either by reducing the size or decreasing the Q-factor of the former. However, the adverse effects of low quality factor MACS detectors have been described in Section 2.5.3. Therefore, the NMR performance evaluation of the microfabricated MACS inserts was accomplished with inserts having resonant frequencies in the range from 460 MHz to 470 MHz and 530 MHz to 540 MHz.

4.3.3 NMR characterization

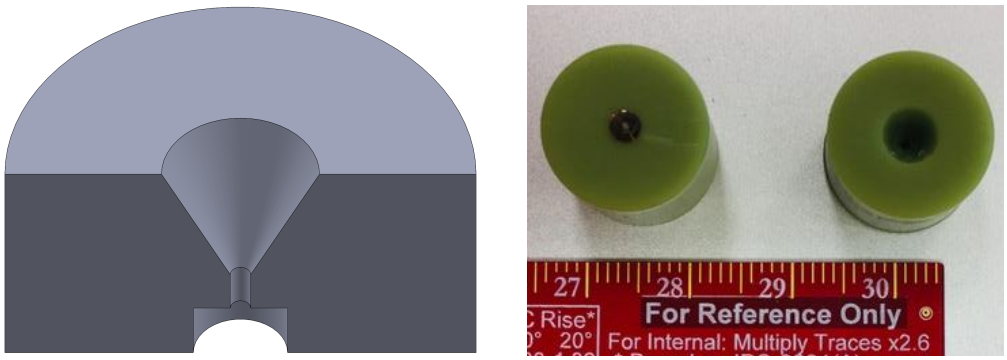
Following the analysis of the electrical efficiency of the microfabricated MACS detectors, NMR performance evaluation was undertaken. For this task, liquid as well as solid state samples were used. Although, MAS technique is predominantly used in solid-state NMR, experiments with liquid state samples were conducted to achieve optimum shimming conditions as well as to thoroughly evaluate the effects of material susceptibilities on the spectral lineshape.



(a) (b)

Figure 4.21: a) Filling liquid samples inside the MACS insert using an Eppendorf pipette tip; b) MACS inserts are centered with the help of Shapal-M inserts inside the MAS rotor. The Shapal-M inserts also aid in thermal management during NMR experiments. Adapted with permission from [148] Copyright 2019 ©Royal Society of Chemistry.

Liquid state samples were dispensed into the MACS inserts with the help of a 20 µl Eppendorf pipette and tips (GELoader) under a microscope as shown in Figure 4.21a. The sample region was sealed at the top using a Biofilm (Applied Biosystems) tape, following which the MACS device is plugged into the MAS rotor with the help of tweezers and centered using Shapal-M inserts (Goodfellow GmbH) as shown in Figure 4.21b. A step-by-step guide is provided in Section A6.



(a) (b)

Figure 4.22: a) CAD section drawing of a funnel for filling MACS (solids, powders). b) 3D printed funnels.

A sample filling tool was designed and fabricated using a 3D printer (MiiCraft) as shown in the Figure 4.22 to facilitate the packing of powders (solid state sample) inside MACS inserts. The bottom part of the tool houses the insert and small channel helps to directly funnel the sample inside the MACS insert. The powder was packed tightly into the MACS device with the help of 400 µm diameter drill bit.

The amount of sample inside the coil is associated with the wall thickness of the sample container/coil support. The wall thickness was established such that the micro-coil can offer the highest possible filling factor and at the same time offer reliable support for coil winding (wirebonding) process. The sample volume for a container with an outer diameter of 850 µm and a wall thickness of 75 µm with a length of 1 mm is ≈ 380 nl.

4.3.3.1 RF amplification

For the NMR performance evaluation of the MACS device, the NMR spectrum from a MACS device was directly compared to the NMR spectrum obtained with a dummy MACS insert, i.e., without MACS signal enhancement. A dummy MACS insert is an otherwise identical MACS device which does not contain a resonator coil. Therefore, the sample volume which is, 380 nl, is identical to the actual MACS device, but the RF excitation and signal reception are performed directly by the static MAS coil. All the NMR experiments were performed on a wide bore 11.7 T Bruker AVANCE III NMR spectrometer equipped with a 4 mm HRMAS probe.

The RF amplification that can be obtained with the MACS insert have been determined with the help of ^1H nutation experiments using a sample of adamantane (Sigma Aldrich). A nutation experiment, which is an array of NMR spectra at increasing pulse widths at a specified power level, helps in identifying the $\pi/2$-pulse, RF field homogeneity, off-resonance effects and nonlinear pulse behaviour in a device. The results from the ^1H nutation spectrum for the MACS device as well as the dummy insert is shown in Figure 4.23. A $\pi/2$-pulse

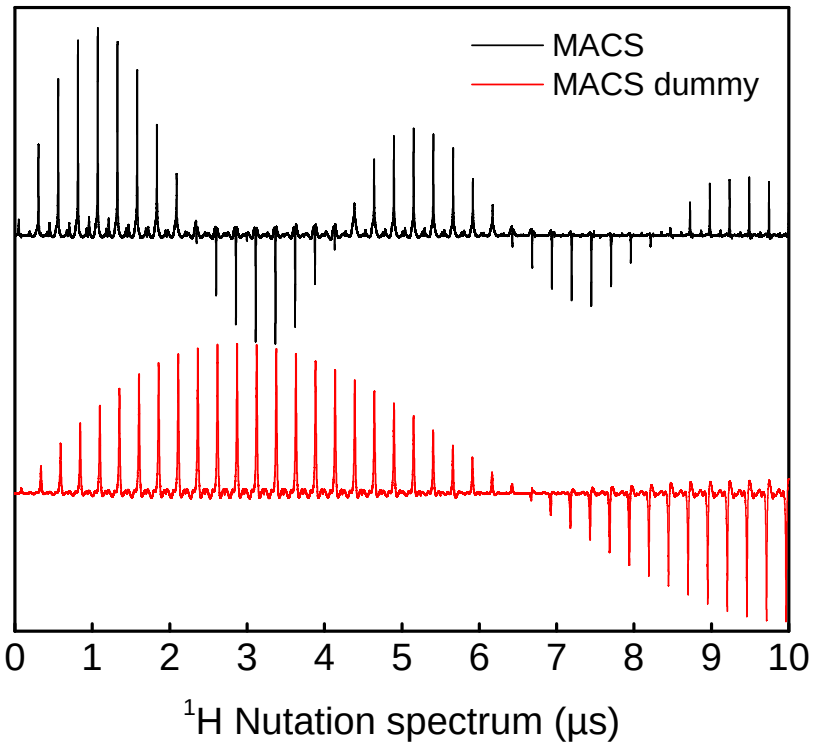


Figure 4.23: Comparison of the nutation spectrum for MAS and MACS coils using a sample of adamantane at an excitation power of 24 W. The reduction in the $\pi/2$-pulse in the case of MACS gives an indication of the B_1 field enhancement inside the sample region. The ratio of amplitudes at 450°/90° from the nutation spectrum suggests an RF field homogeneity of 60% for the MACS inserts. Adapted with permission from [148] Copyright 2019 ©Royal Society of Chemistry.

at 24 W was achieved in 1.1 µs using the MACS insert (resonant at 463 MHz), versus 3.3 µs obtained for experiment with the dummy MACS device. The probe efficiency as described in Equation 2.19 of these arrangements calculated from the measured nutation spectrum was around 1089 µT/$\sqrt{\text{W}}$ and 363 µT/$\sqrt{\text{W}}$, respectively. The RF enhancement of approx. 3 was obtained from the MACS device by calculating the ratio of the respective probe efficiencies. An RF field homogeneity value of 60% was observed by computing the ratio of amplitudes at 450°/90° from the nutation spectrum. The low B_1 field homogeneity of the insert suggest that the sample at the center of the container experiences a much stronger RF field than at the edges of the container. Additionally, this also means that a simpler pulse sequence (e.g. HMQC) would lead to better sensitivity than a complex sequence having multiple number of RF pulses (e.g. HSQC). The RF field homogeneity could be improved by increasing the sidewall thickness of the sample containers, as well as limiting the sample region to the active region of the coil. However, this in turn would lead to the reduction in the filling factor of

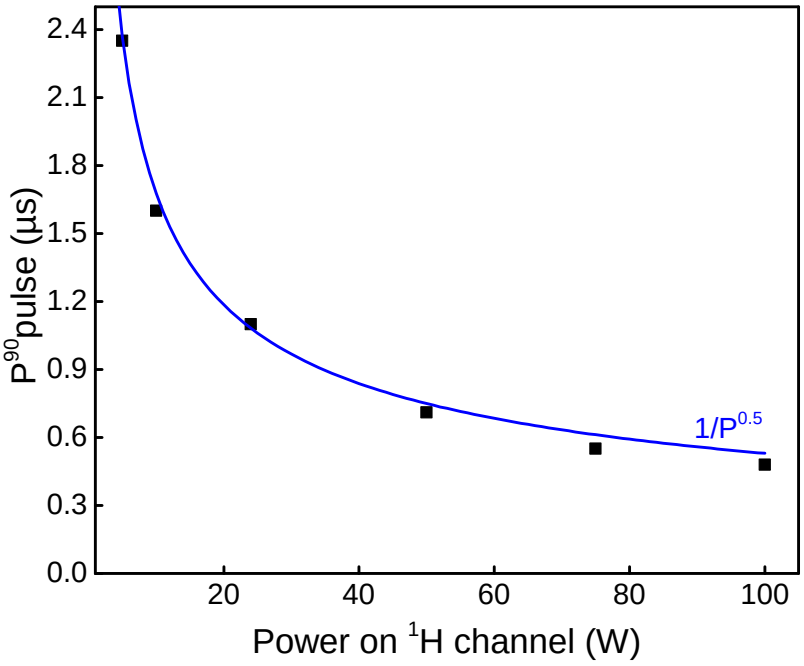


Figure 4.24: The $\pi/2$-pulse length at different excitation power levels on the ^1H channel for the MACS device. Adapted with permission from [148] Copyright 2019 ©Royal Society of Chemistry.

MACS inserts which is detrimental to the sensitivity enhancement. The B_1 field homogeneity from the commercial coil in the 4 mm MAS probehead was around 75%.

In addition, the nutation experiments were also performed using a sample of adamantane at various power levels from 5 W to 100 W on the ^1H channel. This was done to examine breakdown behaviour of MACS detectors and to evaluate the operational range these inserts. The $\pi/2$-pulse length at each power level was noted down and the values are presented with respect to the power level as shown in the Figure 4.24. The observed deviation at shorter $\pi/2$ pulse lengths was due to the shape of the excitation pulse. As the pulse lengths gets shorter, the rise time and fall time (approx. 75 µs each) are in the same order of magnitude as the pulse length itself. The pulse lengths were measured with the help of an oscilloscope. RF nutation frequency upto 500 kHz was achieved at a power level of 100 W on the ^1H channel of the amplifier.

4.3.3.2 Sensitivity enhancement and linewidth evaluation

For concrete evaluation of the sensitivity enhancement offered by the MACS devices, experiments were conducted with a MACS insert (resonant at 466 MHz) and a dummy insert at various spinning speeds. Since both inserts have identical sample volume, i.e., 380 nl, comparison of the signal obtained from those two inserts provides a accurate picture of the

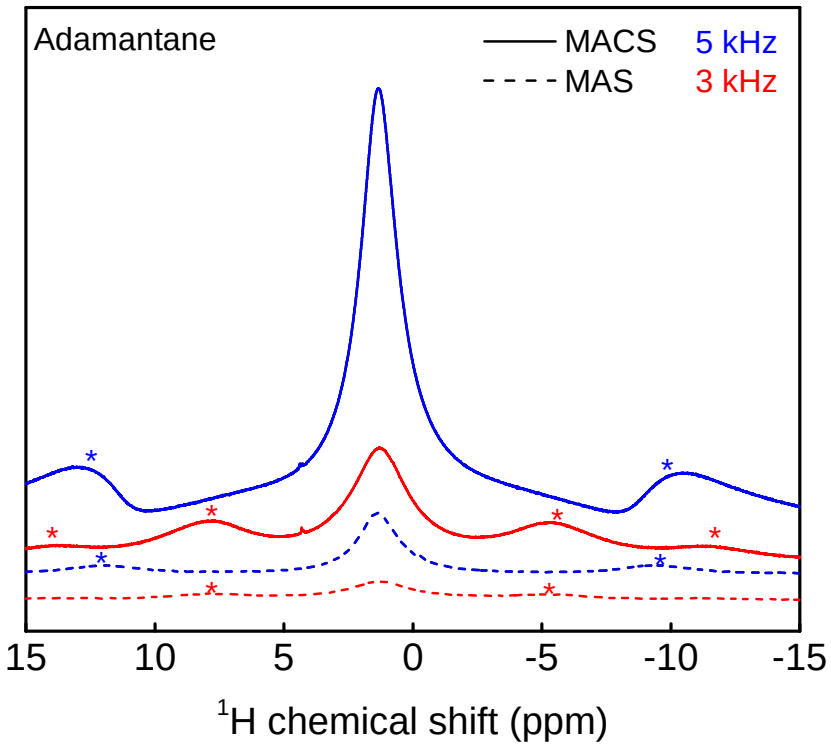


Figure 4.25: Evaluation of the sensitivity enhancement achieved with a MACS insert using an adamantane sample at two spinning speeds (3 kHz and 5 kHz). The SNR improvement with the insert is estimated to be around 6. A $\pi/2$-pulse of 1.1 µs and 3.3 µs was used for the MACS and MAS experiments respectively at an excitation power was 24 W and 16 averages were taken. Adapted with permission from [148] Copyright 2019 ©Royal Society of Chemistry.

improvement in NMR sensitivity. The MACS and MAS NMR spectra of adamantane at 3 kHz and 5 kHz is shown in Figure 4.25. A factor of 6 increase in sensitivity from these resonant inserts can be observed from the measurements. The signal-to-noise (SNR) ratio of an NMR experiment [4] for microscopic samples significantly depends on the geometry of the receiver coil (filling factor), as well on the excitation efficiency (B_1/i). Hence, due to the improved filling factor provided by the MACS inserts, a further improvement in the SNR is observed, in addition to the RF field gain.

Additionally, it is noted that the sensitivity enhancement reported in the Figure 4.25 is not a limitation of the MACS insert [147], but rather related to the limited range of the tuning and matching capacitors of the vendor-supplied MAS probe. As explained in Section 4.3.2, MACS resonators in the range of 471 to 529 MHz could not be used for measurements due to the large magnitude splitting in the reflection curve induced by the coupling of MACS detectors with the coil in the MAS probe. Because of the limited capacitance range, the reflection curve

could not be tuned and matched at 500 MHz. The limitation in the sensitivity enhancement to a factor of 6 in the present experimental setup has been explained with the help of analytical equations in Section 2.5.2.

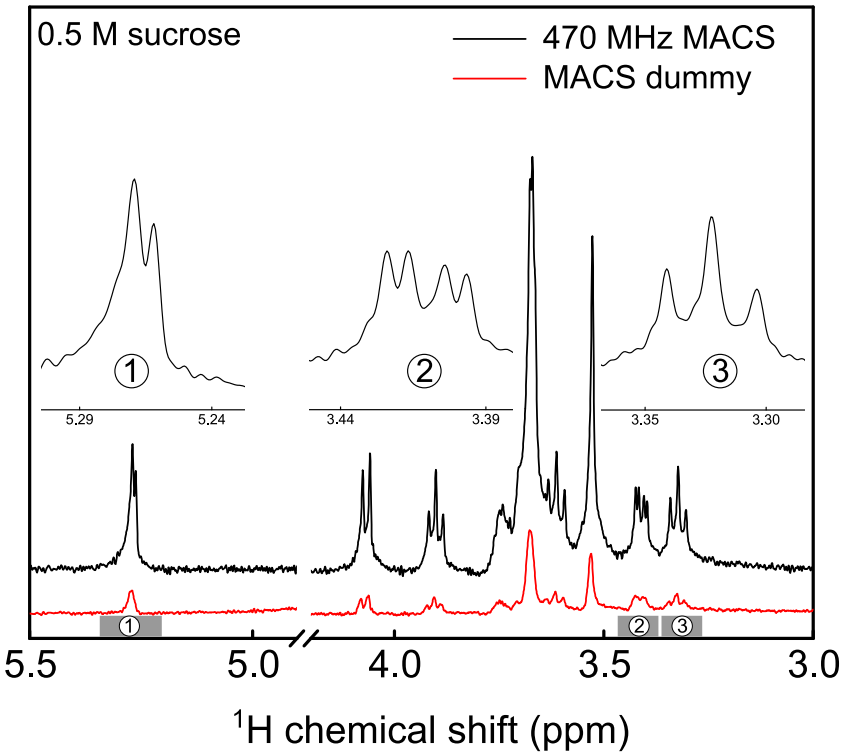


Figure 4.26: Comparison of NMR spectrum of 500 mM sucrose obtained from a MACS and a dummy MACS insert acquired from a volume of 380 nl. The NMR acquisition using a dummy MACS insert is essentially a MAS experiment with equal amount of sample volume as the MACS experiment. A 30 % splitting in the anomeric proton doublet peak was observed using a MACS insert and the singlet proton peak linewidth was around 4 Hz. A $\pi/2$-pulse of 1.1 µs and 3.3 µs was used for the MACS and MAS experiments respectively at an excitation power was 24 W and spinning speed of 3 kHz. Adapted with permission from [148] Copyright 2019 ©Royal Society of Chemistry.

Apart from sensitivity enhancement offered by the MACS inserts, spectral resolution of the NMR spectrum is also an important Figure-of-merit to gauge the quality of the MACS device. The spectral resolution offered by the MACS detectors is influenced by its material susceptibilities as well as the thickness of the conductive parts of the detector (induced eddy currents). The spectral linewidth was assessed using a 500 mM sucrose sample in D_2O. The NMR experiment was performed with a 470 MHz MACS detector as shown in the Figure 4.26. The spectral quality and the limit of detection of the NMR experiment was evaluated from the doublet of the anomeric proton in sucrose. A 30 % splitting in the anomeric proton doublet

peak was observed and the linewidth of the singlet proton peak was around 4 Hz. The SNR of the anomeric proton peak was calculated to be approx. 40 under an acquisition time of 1 s for the single scan experiment. From these values, the normalized limit of detection [190] ($nLOD_\omega$) was evaluated to be approx. 13 nmol$\sqrt{s}$ at 500 MHz. The concentration limit of detection ($cLOD_\omega$) as introduced by Finch *et al.* [119] in the framework of metabolite profiling is approx. 320 mM$\sqrt{s}$. Although the $cLOD_\omega$ value is quite high as compared to the one reported for stripline resonator [119], this was attributed to the small sample volume of the MACS device. Moreover, comparing the SNR obtained from a similar volume of sucrose solution in a dummy MACS insert confirmed the factor of 6 sensitivity improvement. The NMR acquisition using a dummy MACS insert is essentially a MAS experiment with equal amount of sample volume as the MACS experiment. Therefore, this approach facilitates a direct comparison in sensitivity between MACS and MAS technique.

4.3.3.3 Homonuclear 2D NMR experiments

As the structure of molecules become more complex, one-dimensional (1D) NMR spectroscopy becomes inadequate to interpret the signals arising from various scalar or second order coupled couplings. The resonance multiplets arising from these couplings may overlap and therefore is very tedious to distinctly identify them from a 1D NMR spectrum. Hence, two-dimensional NMR spectroscopic methods were invented, starting with the correlation spectroscopy (COSY) sequence [191], to circumvent this issue of overlapping resonances by the addition of a second dimension to the NMR spectrum.

The basic approach to conducting 2D NMR experiments consists of sample excitation followed by evolution of magnetization for a period of time after which a second set of RF pulses are applied followed by acquisition for another period of time. Thus in a 2D NMR pulse sequence, the spectrum after Fourier transformation of the NMR signal is a function of two frequency components. A 2D COSY experiment follows this scheme of sample excitation, signal evolution, sample mixing and signal acquisition. The simplicity and utility of the COSY sequence in decluttering the spectrum and in determining the internuclear coupling upto three bond lengths has rendered it quite popular and widely used among NMR spectroscopists.

Inorder to evaluate the effectiveness of the MACS insert for 2D NMR spectroscopy, a COSY (cosyqf90) experiment was performed on uniformly ^{13}C-labeled glucose under MAS conditions of 6 kHz. A 340 mM glucose solution in D_2O was prepared and dispensed into a resonant MACS detector at 468 MHz. The solution was prepared by dissolving 67.3 mg of uniformly ^{13}C-labeled glucose (Deutero GmbH) in 1 ml of the D_2O solution. A $\pi/2$-pulse of 1.1 µs at a power of 24 W was used for sample excitation and 480 t1 increments were collected with 4 averages and a relaxation delay of 1 s and 2048 data points were collected in the t2 domain over a spectral width of 4.5 kHz as shown in the Figure 4.27. The acquisition time was 46 min. The chemical shifts were reported relative to Trimethylsilyl propionate (TSP) solution and solvent suppression was undertaken using a 20 µW pulse. The observation of cross peaks in the 2D NMR spectrum, which illustrates the nuclear coupling in the glucose solution,

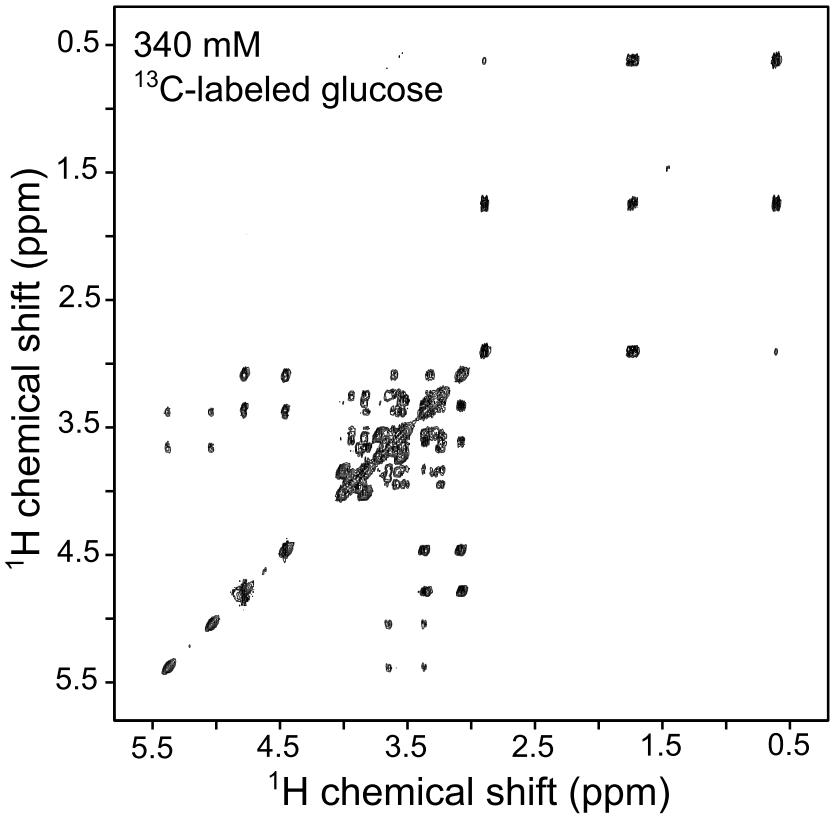


Figure 4.27: ^{1}H-^{1}H COSY spectrum of 340 mM uniformly $^{13}C_6$-labeled glucose in D_2O obtained using the MACS detector. A $\pi/2$-pulse of 1.1 µs at a power of 24 W was used for sample excitation and 480 t1 increments were collected with 4 averages and a relaxation delay of 1 s and 2048 data points were collected in the t2 domain over a spectral width of 4.5 kHz as shown in the Figure 4.27. The chemical shifts were reported relative to Trimethylsilyl propionate (TSP) solution and solvent suppression was undertaken using a 20 µW pulse. The total measurement time was 46 min. Adapted with permission from [148] Copyright 2019 ©Royal Society of Chemistry.

with adequate resolution within a short experiment time proves the excellent sensitivity enhancement as well as the spectral resolution offered by the MACS inserts.

The COSY experiment was also repeated with a solid-state sample to calibrate the insert for a solid-state experiment and to observe for any deviations. Experiments were performed with L-Alanine powder samples under MAS conditions of 6 kHz and a resonant MACS insert at 466 MHz as shown in the Figure 4.28. L-alanine, the left handed form of alanine, has one of the simplest structures among amino acids. A $\pi/2$-pulse of 1.1 µs at a power of 24 W was used for sample excitation and 256 t1 increments were collected with 4 averages and a relaxation delay of 1.5 s and 8192 data points were collected in the t2 domain over a spectral width

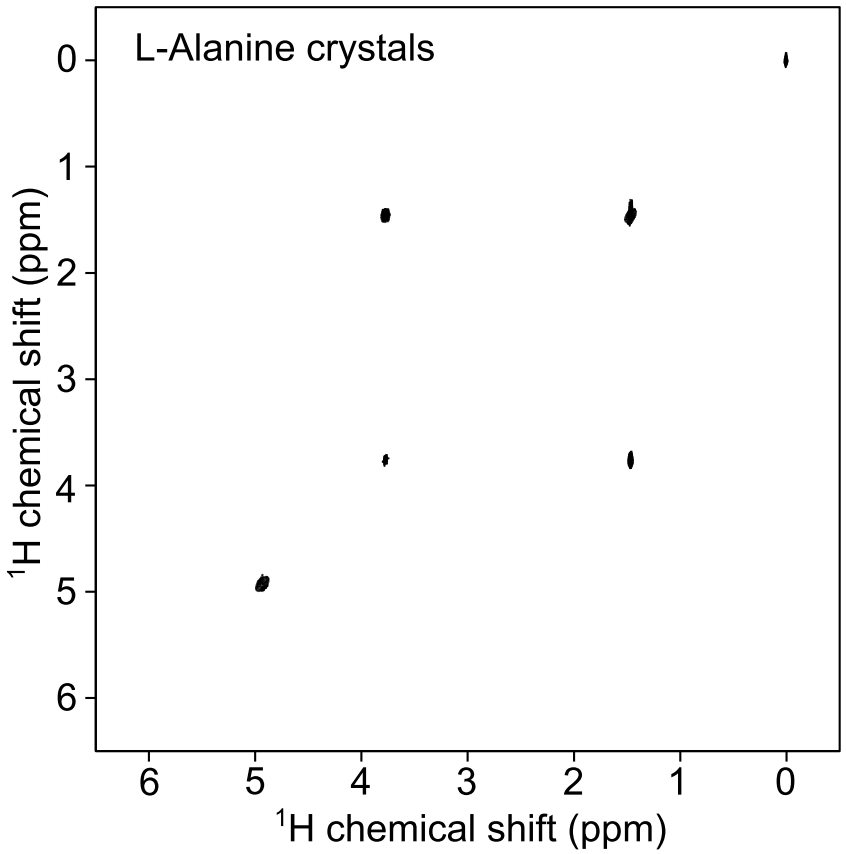


Figure 4.28: ^1H-^1H COSY spectrum of L-Alanine obtained using the MACS detector under MAS conditions of 6 kHz. A $\pi/2$-pulse of 1.1 µs at a power of 24 W was used for sample excitation and 256 t1 increments were collected with 4 averages and a relaxation delay of 1.5 s and 8192 data points were collected in the t2 domain over a spectral width of 5 kHz. The total measurement time was 40 min.

of 5 kHz. The acquisition time was 40 min. Once again the off-diagonal elements illustrate the ^1H-^1H coupling in L-alanine.

4.3.3.4 Heteronuclear NMR with MACS

In contrast to homonuclear experiments, heteronuclear 2D NMR provides information based on the coupling between two different. types of nuclei. Therefore, the chemical shift of one observed nucleus occupies one dimension and chemical shift of the other nucleus occupies the second dimension.

For situations when one of the observed nuclear spins is abundant and the other one is dilute, e.g. ^1H and ^{13}C respectively, the SNR is enhanced by transferring the polarization from the former to the latter. The experiments using this technique in heteronuclear experiments are called "inverse" correlation experiments. Heteronuclear single-quantum correlation spec-

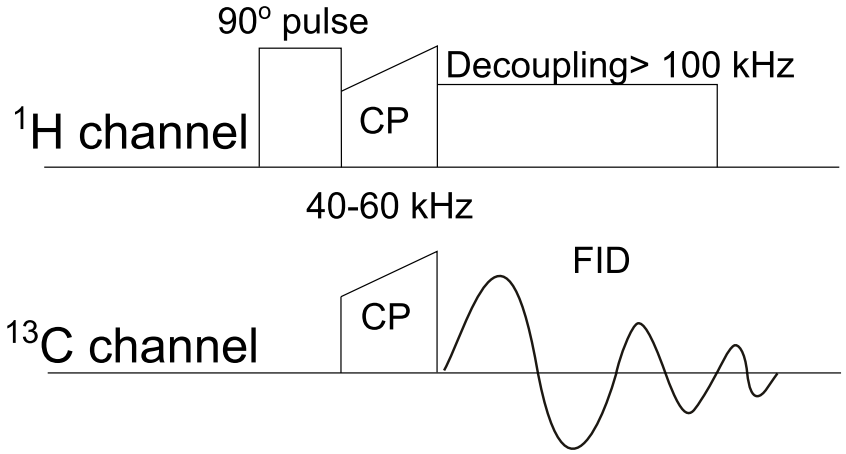
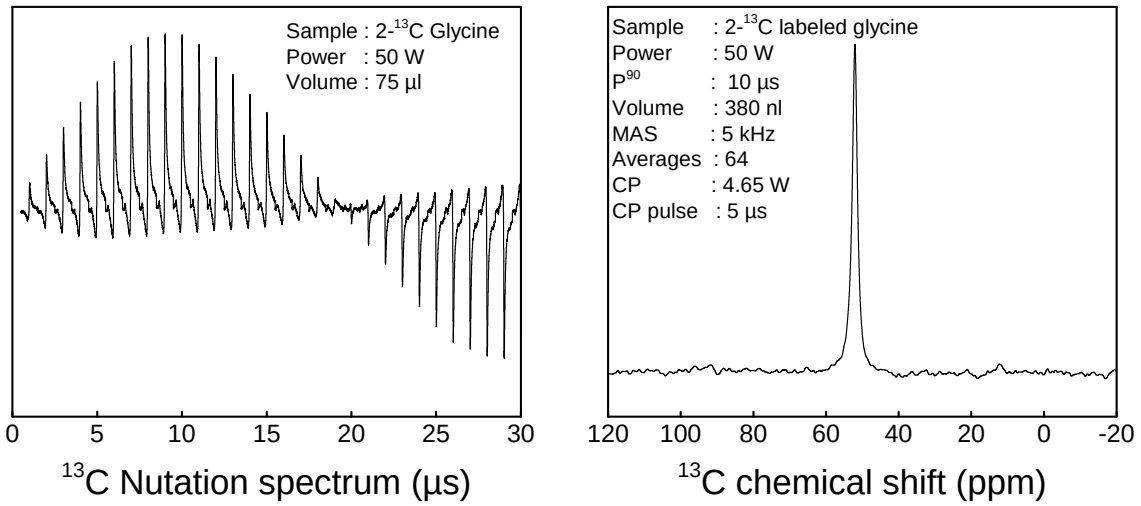


Figure 4.29: Anatomy of a cross-polarization (CP) experiment in NMR



(a) (b)

Figure 4.30: a) Nutation spectrum for the ^{13}C MAS coil at 50 W; b) CP experiment on 2-$^{13}C_6$-labeled glycine. Adapted with permission from [148] Copyright 2019 ©Royal Society of Chemistry.

troscopy (HSQC), heteronuclear multiple-quantum correlation spectroscopy (HMQC) and heteronuclear multiple-bond correlation spectroscopy (HMBC) are some of the most common "inverse" experiments in use today. The direct measurement technique, heteronuclear correlation spectroscopy (HETCOR), where the "heteronucleus" is measured in the direct dimension has been used occasionally since the advent of HSQC.

In the inverse experiments, polarization transfer from abundant spin to the dilute spin is an important step. This transfer of polarization, also known as cross-polarization (CP), is used

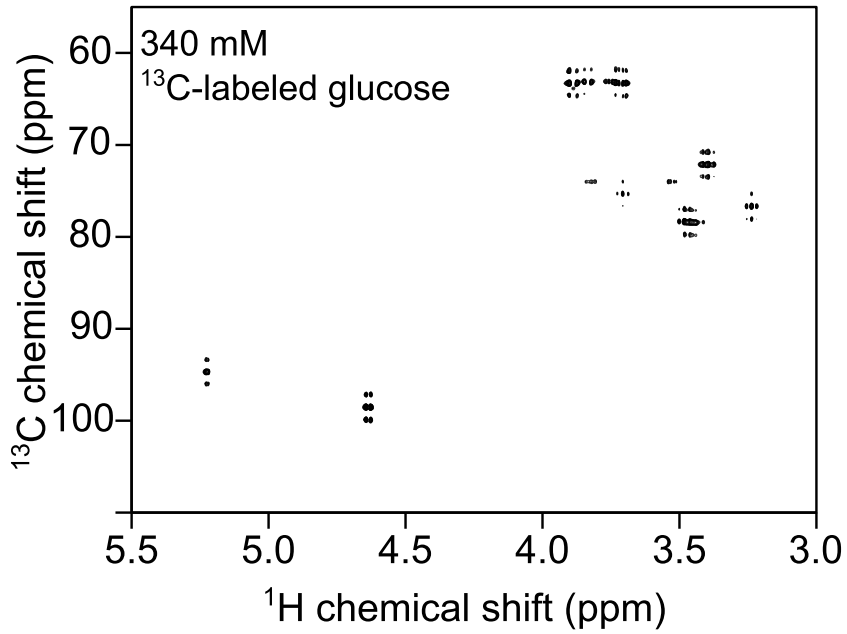


Figure 4.31: 2D HMQC NMR spectrum of 340 mM $^{13}C_6$ labeled glucose solution in D_2O showing ^1H -^{13}C correlations using a 380 nl ^1H MACS insert. The ^1H nucleus is excited by the MACS coil at 24 W using a $\pi/2$-pulse length of 1.1 µs and the excitation of ^{13}C nuclei is done using the HRMAS probe coil at 50 W and ^{13}C $\pi/2$-pulse of 10 µs. A ^1H decoupling power of 10 W is used to decouple the ^1H spins from the ^{13}C spins. The spectrum was acquired in 8 min 47 s. Adapted with permission from [148] Copyright 2019 ©Royal Society of Chemistry.

to enhance sensitivity of low-γ solid-state NMR experiments by a factor on the order of the ratio of their respective gyromagnetic ratios. The general scheme of the cross-polarization technique is shown in Figure 4.29. A $\pi/2$-pulse is used to excite the high-γ nucleus and the spin coherence is transfered to the observed low-γ nucleus through a double irradiation period. High decoupling power is applied to the high-γ nucleus during the acquisition of low-γ nucleus FID to improve the linewidth. The important criteria for efficient transfer of polarization is the Hartmann-Hahn match where the RF field from the former spin should be equal to the latter spin.

CP-MAS experiments using the MACS insert were conducted on a sample of 2-^{13}C-labeled glycine sample (Sigma Aldrich). Similar to alanine, glycine also has a very basic structure in the amino acid family. Hence, it has been used for either benchmarking or calibration experiments. For the purpose of cross-polarization, nutation experiments for the ^{13}C MAS coil were performed at 50 W and ^{13}C $\pi/2$-pulse of 10 µs was recorded as shown in the Figure 4.30a. Subsequently, CPMAS experiments were conducted at 5 kHz spinning speed with a $\pi/2$-pulse of 1.1 µs at 24 W on the ^1H channel as shown in Figure 4.30b. The polarization transfer was achieved under Hartmann-Hahn match conditions at 4.65 W and a pulse duration of 5 µs. The

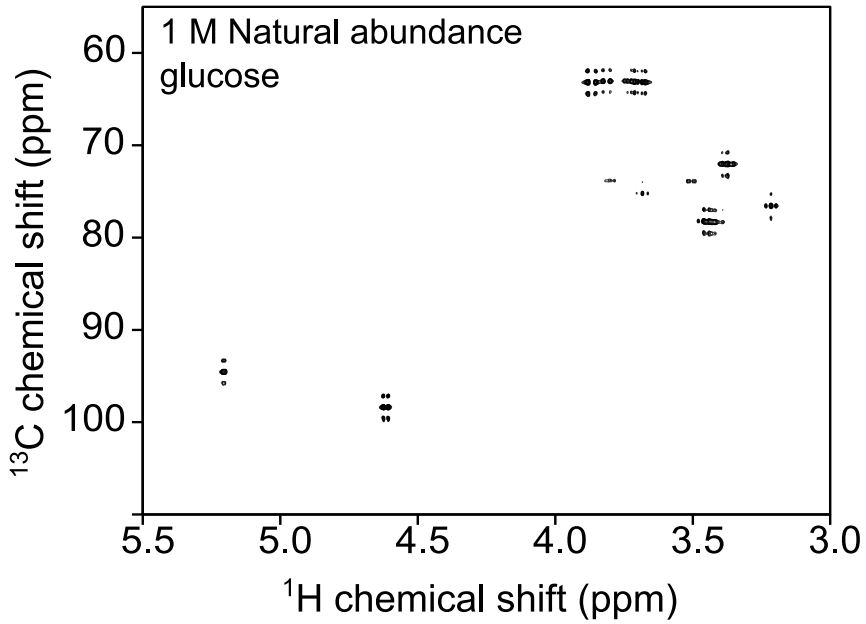


Figure 4.32: 2D HMQC NMR spectrum of 1 mM natural abundance glucose solution in D_2O showing ^{1}H -^{13}C correlations using a 380 nl ^{1}H MACS insert. The ^{1}H nucleus is excited by the MACS coil at 24 W using a $\pi/2$-pulse length of 1.1 µs and the excitation of ^{13}C nuclei is done using the HRMAS probe coil at 50 W and ^{13}C $\pi/2$-pulse of 10 µs. A ^{1}H decoupling power of 10 W is used to decouple the ^{1}H spins from the ^{13}C spins. The spectrum was acquired in 28 min 18 s.

^{1}H-^{13}C decoupling during acquisition was achieved using the WALTZ decoupling scheme with an RF pulse of 100 kHz. The advantage of using MACS inserts for CP-MAS experiments is that high decoupling as well as cross-polarization frequencies can be achieved at relatively low powers, thus avoiding sample deterioration or probe damage due to high power irradiation. Additionally, for low-γ nucleus, higher excitation bandwidths can be achieved with MACS inserts at relatively low powers.

The use of a ^{1}H tuned MACS detector for heteronuclear experiments (^{1}H-^{13}C HMQC) was first proposed by Aguiar *et al.* [155] to implement the approach of "inverse" detection to study low-γnuclei using the MACS technique. The advantage of using ^{1}H tuned MACS inserts is that higher decoupling field strengths (250 kHz) can be applied at relatively lower power (25 W). Therefore, the microfabricated MACS insert was also benchmarked for performance with respect to heteronuclear experiments.

A tuned MACS insert at 465 MHz was used for the 2D HMQC experiments. The ^{1}H nucleus was excited by the MACS coil at 24 W using a $\pi/2$-pulse length of 1.1 µs and the excitation of ^{13}C nuclei was done using the HRMAS probe coil at 50 W and ^{13}C $\pi/2$-pulse of 10 µs. A cross polarization power of 24 W facilitates the polarization transfer from ^{1}H to ^{13}C spins in the sample. A ^{1}H decoupling power of 10 W was used to decouple the ^{1}H spins from the ^{13}C

spins, thereby allowing the removal of line broadening induced by heteronuclear dipolar and J-coupling.

Experiments were initially performed on enriched samples and then repeated for natural abundance samples. To this end, a 340 mM (0.13 µmoles) uniformly ^{13}C-labeled glucose (Deutero GmbH) sample and 1 mM natural abundance glucose (Sigma Aldrich) solution in D_2O were used. The HMQC spectrum, of the enriched sample shown in Figure 4.31 was acquired in 8 min 47 s and the natural abundance sample shown in Figure 4.32 was acquired in 28 min 18 s. In both cases, a fine J-splitting both in direct and indirect dimension is observed. The spectral resolution of the ^{1}H NMR measurements in both cases was around 7 Hz. The excellent spectral resolution in a short measurement time allows extraction of more coupling information rather than peak assignments. The "inverse" experiments were performed with micro-resonator tuned to ^{1}H Larmor frequency rather than ^{13}C, because of low efficiency on the high frequency channel. The introduction of a ^{13}C micro-resonator inside a ^{1}H MAS probe coil will result in high frequency current flowing through the on-chip capacitor rather than the micro-coil because the capacitor acts as a short at the high frequency.

4.3.3.5 Metabolomic studies

The pioneering attempts to perform metabolomic studies using MACS inserts was reported by Wong *et al.* [149]. The authors evaluated the possibility of using handwound MACS detectors as a metabolomic tool by identifying metabolites from 500 µg of bovine muscle and human tissues, with a reported linewidth of 0.1 ppm. This was followed by another generation of handwound inserts [150] which improved the spectral resolution down to 0.02 ppm for a 250 µg rabbit kidney tissue. The steady progress in the spectral quality was accomplished by minimizing susceptibility and eddy current effects from the rotor insert and micro-coil, respectively. Subsequently, the application of these high resolution MACS (HR-MACS) inserts was expanded to perform metabolic profiling on intact organisms like yeast cells [153] and *Caenorhabditis elegans* worms [151]. The suitability of MACS inserts for metabolomic applications have been comprehensively reviewed by Torres and Wong [135].

Microfabricated MACS inserts have emerged as a metabolic profiling tool, addressing the disadvantages of handwound MACS inserts related to their fabrication and operation and reporting linewidths of 1 ppm [11] and 0.1 ppm [130], respectively. Although metabolomic studies have been performed on tissue samples, yeast cells and *C. elegans* worms, the potential of MACS inserts on embryos which have a size similar to the detector geometry has not been explored. Embryonic stages of the zebrafish (*Danio rerio*) have become an increasingly used animal model [192] not only in developmental biology [193, 194] and genetics [195], but also for neuroscience [196], human disease modeling [197, 198], drug development [199, 200] and toxicology [201]. Several reporter tools have been explored [202] and among them HR-MAS experiments have been utilized for metabolic profiling, previously using 100 intact embryos inside the MAS rotor [203, 204]. They were aged between 27 hpf (hours post fertilization) to 96 hpf and were spun at 5 kHz. The treatments were started at 3 hpf, but the measurements were done 24 hours later, hence at 27 hpf.

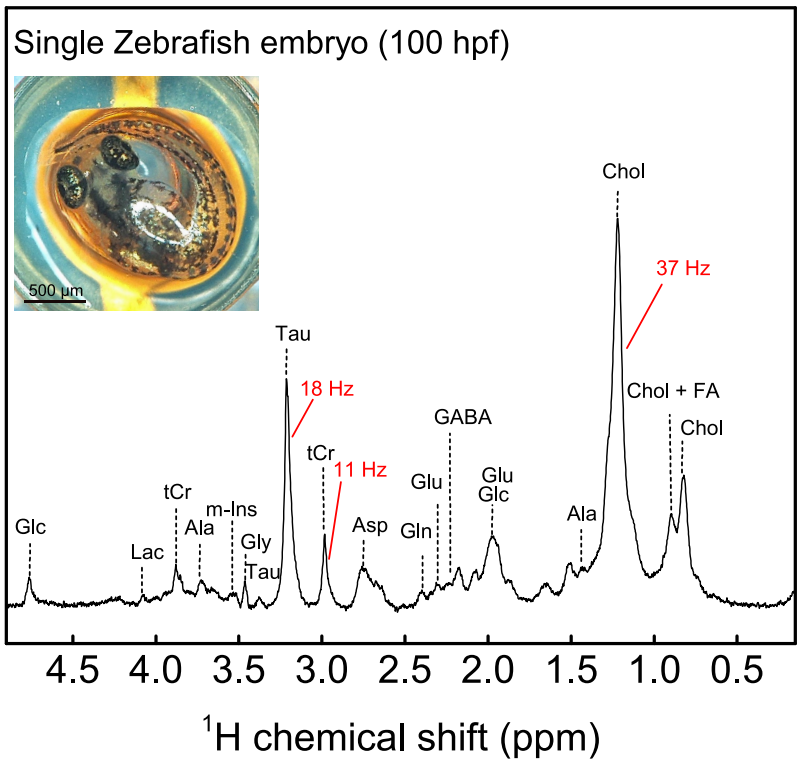


Figure 4.33: ^1H MAS NMR spectrum of a single Zebrafish embryo spun at 5 kHz after solvent suppression using a 20 µW pulse. The metabolic profile of the embryo shows a number of fatty acids, sugars etc. among other metabolites. The inset shows the photograph of an intact zebrafish embryo on top of the MACS orifice before loading. Ala, alanine; Asp, aspartate; Glc, glucose; Gln, glutamine; Glu, glutamate; Gly, glycine; Lac, lactate; Tau, taurine; m-Ins, (myo)-inositol; tCr, total creatine; GABA, gamma-aminobutyric acid; Chol, cholesterol; FA, fatty acid. A $\pi/2$-pulse of 1.1 µs at an excitation power of 24 W was used and 256 averages were taken with a repetition time of 1 s. Adapted with permission from [148] Copyright 2019 ©Royal Society of Chemistry.

MACS inserts would bring significant enhancement in the detection of metabolites in these embryos. The access provided by the MACS inserts to assess inter-individual metabolite differences and thus enabling MAS-NMR spectra of single zebrafish embryos would represent a significant advancement for metabolism studies in this model organism. Moreover, these miniaturized detectors would lead to a considerable decrease in the centrifugal forces experienced by the biological specimen during spinning. Hence, these inserts would constitute a powerful new tool for metabolic profiling of biological systems.

100 hpf stage zebrafish embryos (For ethics statement, refer Section A1), as shown in Figure 4.33, are freely swimming in a 10 cm petri dish (633180, Greiner Bio-One) containing E3 medium, but do not yet require feeding, as they are relying on their yolk for nutrition.

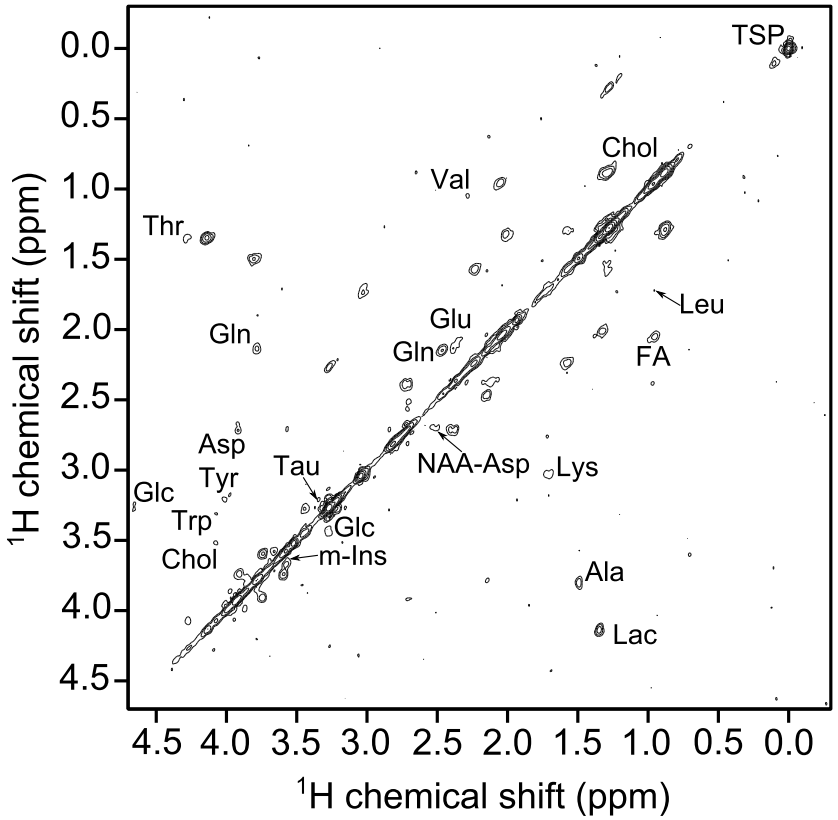


Figure 4.34: ^1H-^1H COSY NMR spectrum of a single Zebrafish embryo under MAS condition of 5 kHz after solvent suppression using a 20 µW pulse. Additional metabolites like Tyrosine, Leusine, L-Tryptophan (Trp) etc. were detected. A $\pi/2$-pulse of 1.1 µs at an excitation power of 24 W was used. 512 t1 increments were collected with 32 averages and a relaxation delay of 1 s and 2048 data points were collected in the t2 domain over a spectral width of 5.5 kHz. Adapted with permission from [148] Copyright 2019 ©Royal Society of Chemistry.

One of the embryos was first placed on top of a MACS device resonant at 467 MHz next to the orifice using a 20 µl Eppendorf pipette and tips (GELoader) as shown in Figure 4.33. Subsequently, the embryo is successfully inserted into the sample volume of the 700 µm orifice MACS detector with the help of capillary force by absorbing the liquid inside. The rest of the sample volume is filled up with the E3 medium. This is followed by sealing of the sample region at the top using a Biofilm tape (Applied Biosystems).

^1H NMR spectrum was initially obtained as shown in Figure 4.33 under MAS conditions of 5 kHz. The solvent signal was suppressed using a pre-saturation pulse of 20 µW. The total experiment time was 6 min 30 s. Almost all the metabolites that have been reported from 100 embryos [203, 204] have been identified in the ^1H NMR spectrum shown in Figure 4.33. The assignment of metabolites was done by referencing the ^1H spectra of the compounds to

previously reported data [205, 206]. The metabolite peaks in the NMR spectrum have been referenced to Trimethylsilyl propionate (TSP) solution.

A two dimensional (2D) homonuclear correlation spectroscopy (COSY) experiment has been performed for improved clarity in the metabolite resonances in zebrafish embryos by helping to distinguish overlapping peaks. The COSY experiment was performed on an intact 105 hpf embryo.

The 2D NMR spectrum as shown in Figure 4.34 was acquired over a time period of 5 h 27 min by collecting 2048 data points in the t2 domain over the spectral width of 5.5 kHz. 512 t1 increments were collected with 32 averages and a relaxation delay of 1 s. The acquisition time was 115 ms and suppression of the water resonance was done using a power of 20 µW. The COSY spectrum further reveals additional metabolites in the specimen compared to the 1D spectrum, and also the correlation between the metabolite peaks. All metabolite resonances are referenced with respect to the trimethylsilyl propionate (TSP) solution. The MACS signal enhancement revealed 80 % of the metabolites as compared to previously published results, despite the acquisition of NMR signal from a single zebrafish embryo, in contrast to stronger metabolite signals from 100 embryos [203, 204].

A wide array of benchmarking and performance analysis of the microfabricated MACS inserts has been achieved. Through these experiments, a clear picture of performance indices of the MACS insert has been obtained. Though there were some limitations that were observed during the experiments, it can be concluded that significant enhancement in NMR sensitivity has been achieved and at the same time maintaining excellent spectral resolution.

4.4 Yield, risk, failure and reliability analysis

The analysis of yield, risk and reliability is an important part of the MEMS fabrication process. Although, the desired target in the MEMS fabrication process is to bring out only functional chips or devices, in practice there will always be process variations which would lead to defects in devices. The process of identifying the deviation in the process as well as the deviation in operation performance forms a part of risk, failure and reliability analysis. Therefore, the process of improving fabrication yield is interconnected with them.

4.4.1 Yield

Fabrication yield is a measure used to quantify the efficiency of the production process. The higher the yield, the better is the quality of the microfabrication process [207]. Substrate yield (SY) can be quantitatively defined as given by Equation 4.1:

$$SY = \frac{N_{working}}{N_{total}} \tag{4.1}$$

where $N_{working}$ and N_{total} are the number of working devices and total number of devices on a substrate.

Substrate yield was calculated for a one of the wafer at the end of microfabrication process. The yield has been computed based on wafer mapping process which has been described in Section A9 and shown in Figure A.7. Taking the total number of expected devices on the wafer to be 1154 and based on the number of working devices to be 210, the total yield at the end of the fabrication run stood at 18%. It was noted that number of functional capacitors at the end of fabrication steps for on-chip capacitors was 852. Therefore, the on-chip capacitor yield was calculated to 74%.

It is important to recognize that during the bring up of new process steps for device fabrication the total yield is typically < 40% [207]. Additionally, under the circumstances of operating under university environment further yield losses are expected.

There are two types of yield losses that were observed during the fabrication of devices. The contribution of the devices that were scrapped due to process deficiencies (850 for this case) to the yield can be categorized under catastrophic yield loss [207] and the category of devices that do not function within the desired specification (94 for this case) fall under parametric yield loss [207].

4.4.2 Risk analysis

The investigation and quantification of yield losses along with the identification of source of these loss during the fabrication process forms a major function of the risk analysis [207].

From the analysis of yield loss based on wafer mapping shown in Figure A.7, it was observed that catastrophic yield loss were quite high. These catastrophic yield losses were attributed to various defects during the fabrication process. Another important observation that was taken into account was the drastic increase in yield loss after the conclusion of the fabrication of capacitors. An analysis of risk for various process steps was performed and a summary of preventive action taken has been provided in Table 4.2.

Therefore, it can be noted from Table 4.2, that the substrate yield can be drastically improved by the addition of a sacrificial layer during the SU-8 process which has been described in Section 4.2.4.

4.4.3 Reliability and failure analysis

"Reliability is defined as the probability of operating a device for certain period of time under certain conditions without failure [207]".

Failure analysis provided concrete information on failure of devices during operation, the so called "field losses". There can be multitude of reasons for failure of devices starting from defects during fabrication up to failure due to extreme operating conditions.

For the microfabricated MACS inserts, around 5 MACS devices experienced failure during operation under MAS operating conditions at relatively low power levels of (10 W to 24 W).

Table 4.2: Risk analysis of the critical process steps during fabrication

Process element	Effect of failure	Detection	Preventive action	Action taken
Seed layer stripping	Short circuit between capacitor plates	Microscope and electrical and electrical	Avoid direct contact between SU-8 & seed layer	Spin coat Barli on top of seed layer
Grinding	Non-uniform dielectric layer	Profilometer	Control force and paper grit	DOE process for polishing
Delamination of top capacitor plate	No wirebonding possible	Visual	Improve adhesion of top capacitor plate	Additional plasma process before seed layer deposition
Unclean pads	No wirebonding possible	Visual	Avoid direct contact between SU-8 & contact pads	Sacrificial AZ 4533 layer patterned
Holes in SU-8 containers blocked by SU-8	No sample filling possible for NMR experiments	Visual	Improve wetting behaviour during encapsulation	Mask redesign and two step encapsulation process

The failure is attributed to the breakdown of the SU-8 dielectric between the capacitor plates as result of defects during the fabrication process. Some additional devices (10) experienced failure at higher power levels (≥50 W). Once again the expected reason for failure arises from the capacitor dielectric because the wirebonds and wirebonded coils were noticed to be intact under microscopic inspection.

4.4.4 Process capability index (Cpk)

The process capability index (Cpk) is a performance evaluation tool for manufacturing processes. It comes under the umbrella of statistical quality control measures in production [208]. This index is useful to evaluate the proximity of process performance to its specification limits taking into account natural variations of the process. It is a measure of accuracy and consistency of the process to adhere to its specifications. The rule of thumb is that larger the index, lower the likelihood of the device breaching the specification limits. The Cpk value for process can be determined by the mean value of the measurements in addition their distribution (standard deviation). Equation 4.2 gives the formula for numerical computation of the process capability index.

$$Cpk = min(\frac{Upp - Mean}{3\sigma}, \frac{Mean - Low}{3\sigma}) \tag{4.2}$$

where Upp and Low are the upper and lower limits of the desired specification of the process, mean is the average value of all the measured values, σ is standard deviation of the measurements taken after the process.

Table 4.3: Cpk values for gold electroplating thickness

Substrate	Upper limit (μm)	Lower limit (μm)	Mean (μm)	Std. deviation, σ (μm)	Cpk
1	10.5	9.5	9.91	0.142	0.95
2	10.5	9.5	9.95	0.153	0.99
3	10.5	9.5	9.95	0.135	1.11
4	3.5	2.5	2.98	0.125	1.30
5	3.5	2.5	2.98	0.123	1.31

Table 4.4: Cpk values for dielectric thickness after the grinding process

Substrate	Upper limit (μm)	Lower limit (μm)	Mean (μm)	Std. deviation, σ (μm)	Cpk
1	-	12	12.62	0.168	1.22
2	-	12	12.56	0.206	0.90
3	-	12	12.52	0.193	0.89
4	-	12	12.48	0.161	0.98
5	-	12	12.12	0.253	0.15

Table 4.5: Cpk values for SU-8 pillar height after HAR SU-8 fabrication

Substrate	Upper limit (μm)	Lower limit (μm)	Mean (μm)	Std. deviation, σ (μm)	Cpk
1	1400	1200	1303	23.01	1.41
2	1400	1200	1306	23.11	1.35
3	1400	1200	1306	22.37	1.39
4	1400	1200	1318	25.02	1.08
5	1400	1200	1316	25.57	1.10

In order to determine the capability of the processes employed for the fabrication of the MACS devices, the Cpk values are calculated. However, not all the processes could be effectively controlled with measurements. The gold electroplating process and the grinding process could be controlled by measuring the thickness using a profilometer (KLA-Tencor P1). Similarly, after the HAR SU-8 lithography process, the height of the SU-8 cylinders were measured under a stereomicroscope. Other processes such as wirebonding (ball size, ball shear test, wire pull test), wafer dicing (kerf width, chip size) could not be effectively controlled due to the lack of appropriate measurement tools.

Table 4.3 shows the Cpk values for the 3 µm and 10 µm electroplating process. 5 substrates were measured and 25 data points were taken from each substrate and tabulated. The indices suggest that process capability is in the 3σ range with one substrate showing a value close to 1.33 (4σ range). Therefore, it is expected that process will generate mid-level variations in the devices. Similarly, for wafer grinding process where thickness of the dielectric is reduced, the Table 4.4 suggests high degree of variations due to Cpk values< 1.

On the other hand, Table 4.5, the HAR SU-8 lithography process shows good consistency and stability with Cpk values close to 1.33. In the industry which follow six sigma quality control standards [208], Cpk index of $\geq$ 1.67 is required. However, introduction of new processes usually result in lower values and generally Cpk value of 1.33 is acceptable.

The measurement distribution as well as the Cpk trend for the process is illustrated and elaborated in Section A12. Therefore, it would be beneficial to use these tools to determine the reproducibility of the MACS detectors by assessing the consistency of the processes employed to fabricate these detectors.

4.5 Discussion

Table 4.6: Comparison of various MACS detectors for a 4 mm MAS system

	Capacitor	Coil	Wire thickness (μm)	δT at 5 kHz (°C)	Q_{MACS}	Resolution (ppm)	Sensitivity gain
MACS1 ([10])	Discrete	Handwound	30	7	70	0.02	6.7-14
MACS2 ([11])	Interdigitated	Wirebonded	25	-	-	1	-
MACS3 ([130])	Parasitic	Printed	17	2.5	50	0.1	3.4
MACS4 (this work)	Parallel plate	Wirebonded	25	5	22	0.03	6

A microfabricated MACS device that has been fully characterized with respect to its electrical properties as well as its thermal behaviour has been described in this chapter. The outlined detector is currently compatible with MAS systems $\geq$ 4 mm. The thermal characterization was done by measuring the temperature gradient/difference ($\nabla T/\delta T$) between the sample region and the periphery of the insert.

A historical overview of the various kinds of the single resonant MACS devices that have been reported has been provided in Table 4.6 and are compared with the device that has been presented here. The manually fabricated MACS inserts from [10] report the best Q factor values. However, they also have the highest sample heating due to induced eddy currents. Efforts to improve the thermal performance by using Shapal-M [150] housing to balance them have caused issues with susceptibility that cannot be averaged out. The microfabricated micro-resonators integrated with an interdigitated capacitor [11] offers the most unfavourable

electrical performance. The spectral resolution from these inserts were also quite poor. On the other hand, the monolithic MACS devices [130] offer the best thermal performance due to the elimination of μ-Solenoids in the final device. Nonetheless, the sensitivity enhancement achieved using these inserts was inadequate. As compared to all these devices, the performance of the MACS micro-detector reported in this work is somewhere in the middle. There is scope for improvement when it comes to sensitivity enhancement by using devices with resonant frequency close to the Larmor frequency (Section 4.3.2). The reported spectral resolution with the current microfabricated MACS device is similar to values reported by hand fabricated MACS inserts.

The rapid advances in HR-MAS technology, with size of the MAS detector reducing to ≤ 1 mm [131, 135, 209], has enabled NMR spectroscopists for sensitivity improvements as well as faster sample spinning. Therefore, MAS system has also moved towards the micro domain with reduction in detector sizes. The major contribution of the HR-μMAS probeheads is towards faster sample spinning, with spinning speeds ≥ 100 kHz achieved [33]. However, downsizing the detector in the MAS probehead leads to reduction in the sample filling factor (figure 2.2). Comparing the 0.7 mm MAS system with MACS device reported in this thesis, the latter offers higher filling factors (about 65%) as compared to the former (about 20%). Therefore, taking into account all the signal losses associated with the MACS technique, it can be conservatively estimated that current MACS inserts would offer a sensitivity improvement by a factor of 2 as compared to the 0.7 mm MAS system. It is also worth noting that 0.7 mm MAS probeheads are extremely expensive and require necessary modifications to the shim systems to improve the spectral resolution [210]. However, sample heating in HR-μMAS probeheads is caused only due to frictional heating rather than induced eddy currents.

The major development in this work has been to demonstrate a MACS insert which was manufactured in a robust and reproducible manner by means of microfabrication, with adequate electrical and thermal performance of both the passives integrated in the device. Microfabrication also offers the advantage that it eliminates any imprecision due to manual assembly, and ensures mechanically balanced devices, which is an important characteristic necessary for fast spinning speeds.

This thesis marks the coming-of-age of MACS devices, as their maturity opens doors for a wide range of NMR applications involving fast sample spinning at high SNR, crucial to obtaining finely resolved spectra, thereby addressing multiple categories of practitioners. As an application example, this work has demonstrated, for the first time, ^1H NMR metabolic profiling of an intact single zebrafish embryo. The results acquired with these micro-detectors are in good agreement with previous reports [135], proving the possibility of HR-MACS applications for low cell-count studies, as needed for example for human disease monitoring, drug development, or toxicity assessment. Further, improvement to metabolomic experiments can be foreseen by using a combination of slow spinning, MACS and the CMP (comprehensive multi-phase)-NMR [211] technique. This combination would be a promising concept to observe the metabolic activity of an intact single zebrafish embryo over a longer period of time through its multiple embryonic stages (e.g. from 10 hpf-100hpf).

5 Broadband MACS inserts

Thus far, only tuned detectors have been reported for application in MACS configuration, i.e., a micro-coil and a capacitor forming a micro-resonator tuned to the Larmor frequency of interest. For solenoid micro-coil geometries, either manual winding of a wire around a capillary [10, 152], or a modified wirebonder [11, 148] have been used. For a 2D MACS resonator approach, the planar coil has been defined by lithography and etching [130]. The capacitors required to tune the micro-resonator have been integrated with the manually wound coils by soldering a discrete element [10, 152] to the ends of the micro-coil. On-chip capacitors have been designed for integration with wirebonded micro-coils, this approach offering the flexibility to employ either interdigitated [11] or parallel plate capacitor structures [46]. The 2D MACS resonator features a capacitance that is distributed along the entire length of the micro-coil, between its tracks [130].

However, these resonant inserts have limitations which originate from the requirement to tune them to the target Larmor frequency. Fabrication imperfections such as winding pitch, coil height etc. might lead to deviation in the tuning frequency of the inserts. Additionally, the micro-resonators introduce resonance splitting, which may also lead to serious reduction in efficiency if the tuning and matching conditions of the coupled system are not met at the target frequency. The splitting in the reflection curve occurs due to the fact that the resonance of a coupled system is split when the coupling is larger than a critical value, i.e., critical coupling [147]. When this happens, it is vital that the capacitance range of tuning and matching capacitor is sufficient to recover tuning and matching of the probe coil loaded by the micro-resonator. Additionally, the tuned MACS micro-resonators cannot be operated in different magnetic field strengths or for different nuclei. Hence, there have been efforts to develop multi-resonant detectors for MAS [152, 212].

Takeda *et al.* [152] evaluated the feasibility of integrating a doubly-tuned MACS resonator in a doubly-tuned MAS probe and demonstrated enhancement factors of 5.4 and 7 for ^{1}H and ^{13}C channels respectively as compared to without the doubly-tuned insert. Further, a solution to extend a doubly-tuned insert to a triply-tuned MACS was also described. However, these double and triple resonant MACS inserts are designed such that each coil observes separate sample regions. The triple resonance micro-magic angle spinning (μMAS) probehead [212] reported by Brauckmann *et al.* provides high RF fields necessary for the heteronuclear and homonuclear decoupling in multi-nuclear NMR experiments as well as higher excitation efficiencies for quadrupolar nuclei. Hence, the probe offers improvements in resolution and sensitivity as compared to a regular MAS probe. Nonetheless, necessary modifications to the commercial probehead [9] does not make this a straightforward proposition for the NMR community.

Multi-resonant detectors have been successfully employed for wide range of applications such as metabolomics studies based on ^{23}Na, ^{31}P, ^{39}K, and ^{13}C nuclei, while ^{1}H is usually used for shimming [213, 214]. Cross polarization techniques rely on transferring the polarization from a high-gyromagnetic-ratio nucleus to another nucleus with a relatively low value [215–217] and so require different resonant frequencies for excitation and detection. In MR spectroscopy, ^{1}H MRI is applied to localize the phantom and then the X-channel is used for the spectroscopy [218, 219]. ^{19}F-^{1}H MRI has proven to be a useful technique to study the distribution of fluorine-containing drugs inside tissues, exploiting the fact that both proton and fluorine have high gyromagnetic-ratios [220]. Decoupling experiments [221, 222] also require detection in one channel, simultaneous to the excitation in the other channel. Therefore, the overlap of the field-of-views in different frequencies is an essential parameter which determines the decoupling efficiency. While these circuits benefit from passive amplification of the signal at the resonant frequencies, thus having the best performance at those specific frequencies, a second category of detectors have been developed, targeting operation in a broad range of frequencies, albeit with compromise on the sensitivity of the coils [223–228]. Wideband performance is a competitive advantage because the coil, being independent of the static magnetic field, can be adapted to different magnetic field strengths or to different nuclei without further tuning and matching. Davoodi *et al.* [161] have reported a comprehensive overview on various aspects of both multi-nuclear and broadband NMR detectors which addresses their performance issues and provides a solution for optimization based on application.

5.1 Lenz lens inserts in NMR

Spengler *et al.* [128] have introduced a novel wideband insert that operates as a "magnetic Lenz lens", tailoring the magnetic flux inside a tuned Helmholtz coil detector. The approach reported in this chapter is to exploit the intrinsically non-tuned nature of such a Lenz lens (LL) structure in order to achieve broadband operation for MACS inserts. In this section, a brief history of Lenz lens structures for NMR applications will be presented, including several preliminary considerations regarding the operating principles, relevant for the content of the this work.

The Lenz lenses, are governed by Lenz's law and provide local amplification in the magnetic field by focusing the magnetic flux from a primary coil into a spatial region of interest. The lenses are essentially made up of two conducting loops, an outer and inner, either in the form of wires or sheets. The outer loop (flux collector) collects the flux from the surrounding area and the inner loop (anti-coil) focuses this flux inside its borders. The loops are coupled to the primary coil through their respective mutual inductances. These findings were summarized by Schoenmaker *et al.* in this article [229].

Further, Jouda *et al.* [230] have comprehensively evaluated the SNR enhancement obtained for a microscopic sample placed inside a coil with a diameter much larger than the sample itself. The signal is then acquired using either an LC resonator or an LL insert, inductively

coupled with the larger coil. The SNR enhancement provided by the inductively coupled LC resonator was 10, while for the inductively coupled Lenz lens was 3.5, compared to the case when the signal was collected only using the large coil. Nevertheless, it is important to note that the SNR boost provided by the LL inserts is not specific to a certain frequency, but it is rather broadband.

The Lenz lens concept has already started to penetrate the NMR applications field, being recently exploited by Meier *et al.* [231] in diamond anvil cells (DACs) in order to shape the magnetic flux towards the sample in high pressure NMR experiments. This resulted in significant sensitivity (LOD_t=10^{-12} spins/$\sqrt{Hz}$) and pressure gains (up to 70 GPa) as compared to a micro-coil setup. Subsequently, significant advances were made to this setup using a double-stage Lenz lens arrangement [232, 233], which enabled high pressure NMR experiments up to 90 GPa with double the amplification of the B_1 field in the sample region as compared to the previous version.

As stated above, the Lenz lens structures, made up of two connected conducting loops, are intrinsically broadband structures. For an LC resonator, the coil can be modeled as an emf source in series with an inductor and a resistor. At the resonant frequency, the tuning capacitor cancels out the impedance of the inductor, therefore the current flowing in the circuit is maximized. This current flows inside the coil creating a magnetic field. The magnetic field produced by a micro-resonator MACS insert is maximum in its resonance mode. In a Lenz lens structure, the magnetic field from a macroscopic coil induces two emfs in the respective loops (coils), therefore, the current flowing in the coils is proportional to the difference of their emfs divided by the sum of their impedances. The emf is proportional to the reactance itself and hence the current in high Q structures is frequency-independent. The field at each point is the sum of the fields produced by each coil. Therefore, the field amplification at the sample volume is frequency-independent. In terms of the noise performance, extra noise introduced in a resonant MACS insert is amplified with the same factor as the signal at the resonant frequency, but for a LL MACS, the noise is the root of the sum squares of the noise produced by each coil, while the signal is proportional to the differential signal produced by each coil.

The main focus of this chapter is to investigate the possibility to implement the Lenz lens concept into MACS inserts in order to perform experiments in a broader frequency range. A theoretical rundown, both analytical as well as based on simulation, is provided to analyse the integration of Lenz lens configuration with the MAS probe coil. Various possible broadband MACS designs are explored and fabricated. Finally, NMR performance evaluation has been conducted on these fabricated designs.

5.2 Theoretical formulations

In a Lenz lens configuration, the coil pair is coupled to the primary coil through their respective mutual inductances [230]. Therefore, regardless of the geometry, each coil which has the dominant mutual inductance, acts as the flux collector and the other one acts as the anti-coil.

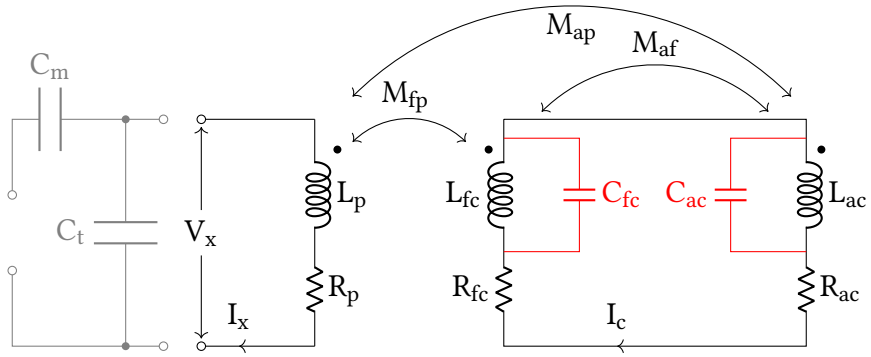


Figure 5.1: Topology of the broadband MACS insert inductively coupled to a MAS probe coil. L_p, L_{fc} and L_{ac} are the inductances of the primary coil, flux collector and anti-coil, respectively. These coils are also represented by their resistances, R_p, R_{fc} and R_{ac}, respectively. The flux collector and anti-coil have parasitic capacitance, C_{fc} and C_{ac}, respectively. The mutual inductance between each of the coils, i.e, M_{fp}, between flux collector and primary coil, M_{ap}, between anti-coil and primary coil and M_{af}, between anti-coil and focusing coil play a major role in the predicted sensitivity enhancement in the sample region. The capacitors, C_t and C_m, perform the functions of tuning and matching respectively.

A suitable design can ensure that flux is focused in the desired region of the insert while diminishing the flux in another region, e.g. an LL consisting of two loops, focuses the flux inside the inner loop and nullifies the flux in between loops. The design rules with the respective mutual inductance calculations will be addressed in this section in combination with FEM simulations of the geometries.

The electrical circuit diagram of a broadband MACS insert coupled to a MAS probe coil is shown in Figure 5.1. The insert consists of two electrically connected inductive loops, L_{fc} and L_{ac}, respectively. Both inductive loops are coupled to the primary coil, L_p, through mutual inductances, M_{fp} and M_{ap}, respectively. The stray interwinding capacitance, C_{fc} and C_{ac}, of the solenoid coils in the insert are also integrated in the circuit. They play a part in the self resonance of the individual coils. If the self-resonant frequency of any of the coils is less than the Larmor frequency, then it will lead to inefficiencies since the stray capacitance will act as a short leading to all the induced currents getting dissipated in the capacitor.

One of the major deviation to the circuit analysis reported by Jouda *et al.* [230], is the consideration of mutual inductance, M_{ap}, between the anti-coil and the primary coil. Since the detector design is based on solenoidal geometry, the mutual inductance between the two coils is a significant factor as opposed to being negligible in the case of planar design.

Based on Kirchhoff's voltage and current law, the following equations are derived from Figure 5.1.

$$V_x = -I_c \cdot j\omega M_{\mathrm{fp}} + I_x \cdot (R_p + j\omega L_{\mathrm{p}}) + I_c \cdot j\omega M_{\mathrm{ap}} \tag{5.1}$$

$$I_x \cdot j\omega M_{\mathrm{ap}} + I_c \cdot (R_{\mathrm{ac}} + j\omega L_{\mathrm{ac}}) + I_c \cdot (R_{\mathrm{fc}} + j\omega L_{\mathrm{fc}}) - I_x \cdot j\omega M_{\mathrm{fp}} + 2 \cdot I_c \cdot j\omega M_{\mathrm{af}} = 0 \tag{5.2}$$

From Equation 5.2, a relationship between the two currents, I_c and I_x is established.

$$I_c = I_x \cdot \frac{j\omega M_{\mathrm{fp}} - j\omega M_{\mathrm{ap}}}{R_{\mathrm{fc}} + R_{\mathrm{ac}} + j\omega L_{\mathrm{fc}} + j\omega L_{\mathrm{ac}} + 2 \cdot j\omega M_{\mathrm{af}}} \tag{5.3}$$

Substituting Equation 5.3 in Equation 5.1, the impedance, Z_x at the terminals is derived.

$$V_x = I_x \cdot (R_{\mathrm{p}} + j\omega L_{\mathrm{p}} + \frac{(j\omega M_{\mathrm{fp}} - j\omega M_{\mathrm{ap}}) \cdot (j\omega M_{\mathrm{ap}} - j\omega M_{\mathrm{fp}})}{R_{\mathrm{fc}} + R_{\mathrm{ac}} + j\omega L_{\mathrm{fc}} + j\omega L_{\mathrm{ac}} + 2 \cdot j\omega M_{\mathrm{af}}}) \tag{5.4}$$

$$Z_x = R_p + j\omega L_{\mathrm{p}} - \frac{(j\omega M_{\mathrm{fp}} - j\omega M_{\mathrm{ap}})^2}{R_{\mathrm{fc}} + R_{\mathrm{ac}} + j\omega L_{\mathrm{fc}} + j\omega L_{\mathrm{ac}} + 2j\omega M_{\mathrm{af}}} \tag{5.5}$$

Therefore, from Equation 5.5, it can be observed that independent of which mutual inductance, either M_{fp} or M_{ap} is higher, the impedance remains the same. Since the SNR is calculated directly based on the real part of the impedance (resistance), this holds true for the SNR as well. However, the important detail that needs to be recognized is the region where the SNR enhancement occurs based on the dominating mutual inductance among the two. This can be further visualized from simulations.

5.3 Design and simulation of broadband MACS inserts

The simulation studies were conducted to evaluate the maximum sensitivity enhancement that could be achieved using Lenz lens MACS (LLMACS) inserts. Three different designs of inserts compatible with the MAS arrangement are analyzed using FEM simulations.

Simulation of the theoretical B_1 field enhancement that could be obtained from various designs of the Lenz lens inserts that are compatible with the 4 mm MAS system was done in COMSOL Multiphysics®. The simulation was performed with the RF module of the software employing the physics of electromagnetic waves in the frequency domain.

A spherical air domain having a diameter of 10 mm was defined as the simulation domain which was sufficiently large so that the solution is not affected by the exterior boundaries. An 8 turns coil of diameter 4.5 mm wound from copper wire of thickness 250 µm was defined as the MAS probe coil in all the cases. The ends of the probe coil were connected to two perfectly conducting leads and a lumped port was defined between them. A driving voltage of 1 V was applied at the port through a 50 Ω characteristic impedance. The conductive surface losses in the structures were accounted for with the help of an impedance boundary condition. The finite element mesh was relatively coarse for the spherical air domain and the outer probe coil.

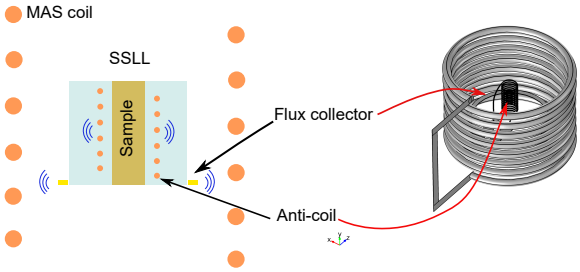
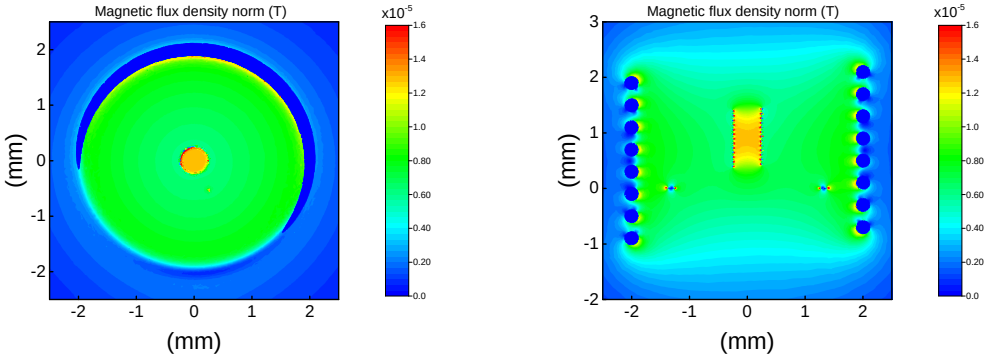


Figure 5.2: FEM simulation model of an SSLL insert inductively coupled to a primary coil which represents the coil in the probe. The SSLL device consists of a solenoid, defined as the focusing coil (anti-coil), which is connected to a thin metal strip on the substrate which acts as a flux collector to complete the LL geometry.



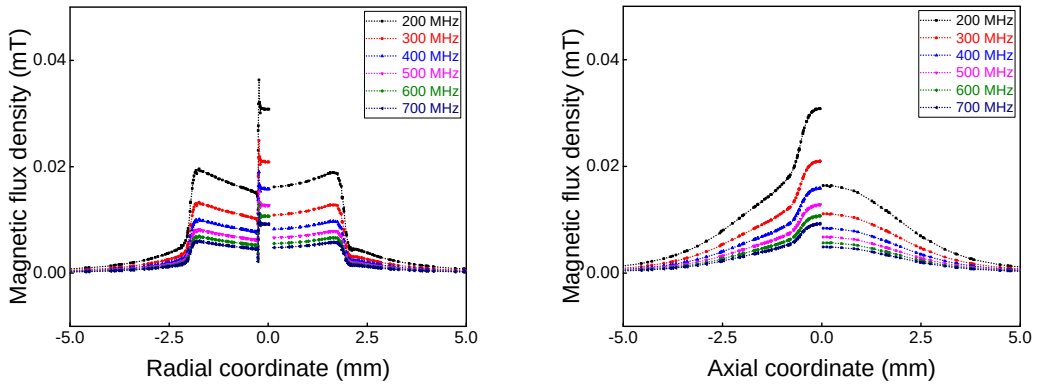
(a) (b)

Figure 5.3: Simulated B_1 field enhancement observed in the sample region with an SSLL insert in a) Cross section perpendicular to the coil axis; b) Cross section parallel to the coil axis with the help of 2D B_1 field maps. The higher B_1 field in the small region inside the anti-coil can be clearly observed.

5.3.1 Single solenoid Lenz lens inserts (SSLL)

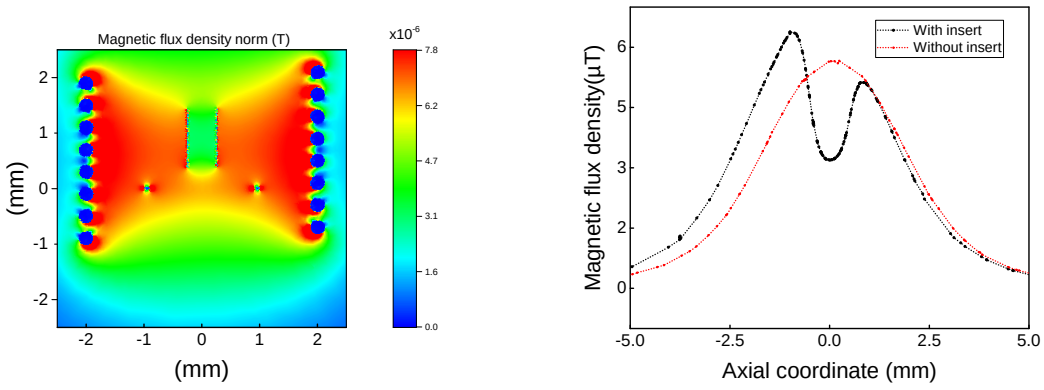
A 24.5 turn 550 µm diameter solenoid of height 1 mm having a wire diameter of 25 µm, defined as the focusing coil, is connected to a metal strip of width 100 µm and thickness 8 µm which acts as the flux collector as shown in Figure 5.2a. The outer diameter of the flux collector was 3 mm. The focusing coil (solenoid) was assigned copper from the material inventory and gold was assigned to the flux collector. A mesh (free tetrahedral) size of 4 µm was assigned to the micro-coil and the flux collector.

The detectors are inductively coupled to the probe coil. The entire model geometry with the MAS probe coil is shown in Figure 5.2. From Figure 5.3 and Figure 5.4, it was observed that the B_1 field is amplified by around a factor of 1.5 in the sample region. This amplification



(a) (b)

Figure 5.4: Simulated B_1 field enhancement observed in the sample region with (right-half of each image) and without (left-half of each image) an SSLL insert in a frequency range between 200 MHz to 700 MHz along a cut line a) through center of coil perpendicular to the coil axis; b) along the coil axis.



(a) (b)

Figure 5.5: Simulated B_1 field plot obtained in the sample region with an SSLL insert when the diameter of the flux collector is less than 2.5 mm. a) 2D B_1 field map showing lower magnetic flux inside the anti-coil compared to the surroundings; b) B_1 field in the sample region along the coil axis with and without the aforementioned SSLL insert. The dip in the curve shows the reduction in the magnetic field in the sample region for the SSLL insert with smaller flux collector.

is for the case where the mutual inductance between the outer loop and the primary coil is higher than the mutual inductance between the μ-Solenoid and the primary.

The case, where the latter mutual inductance is higher than the former has also been simulated as shown in Figure 5.5. It was observed that under this condition, the flux amplifi-

cation happens outside the sample region and in the sample region there is a reduction in the magnetic flux. Therefore, the diameter of the outer planar flux collector should be as close to the primary coil as possible to increase the mutual inductance between them.

An additional conclusion that was drawn from the simulations was that not all of the flux accumulated by the flux collector was focused into the sample region by the anti-coil. This is because the flux collector has a planar geometry and the anti-coil has solenoidal geometry. Therefore, there is a presence of stray B_1 field in between the Lenz lens loops. Hence, this single solenoid Lenz lens design is not optimal for a broadband MACS detector.

5.3.2 Double solenoid Lenz lens inserts (DSLL)

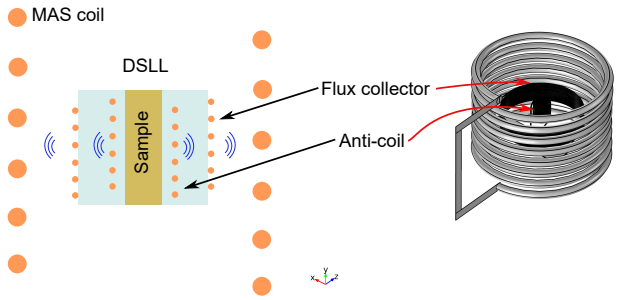
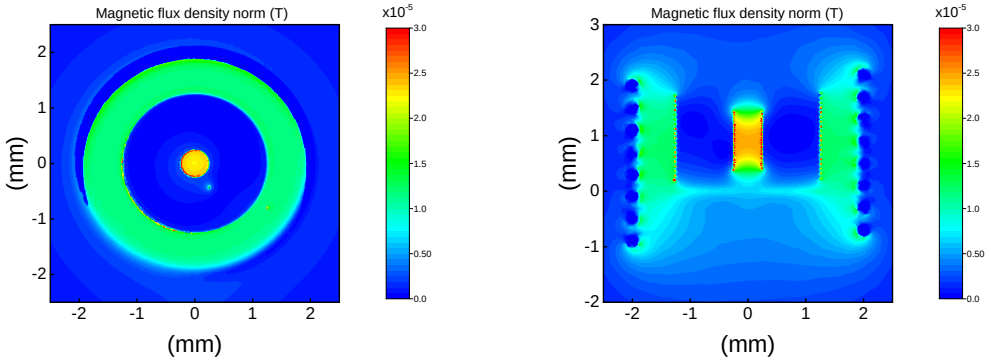


Figure 5.6: FEM simulation model of DSLL insert inductively coupled to a primary coil (largest coil) which represents the coil in the probe. The DSLL device consists of two concentric solenoids connected to each other, one of which (smallest coil) is defined as the focusing coil (anti-coil), and the other coil which acts as a flux collector to complete the LL geometry.

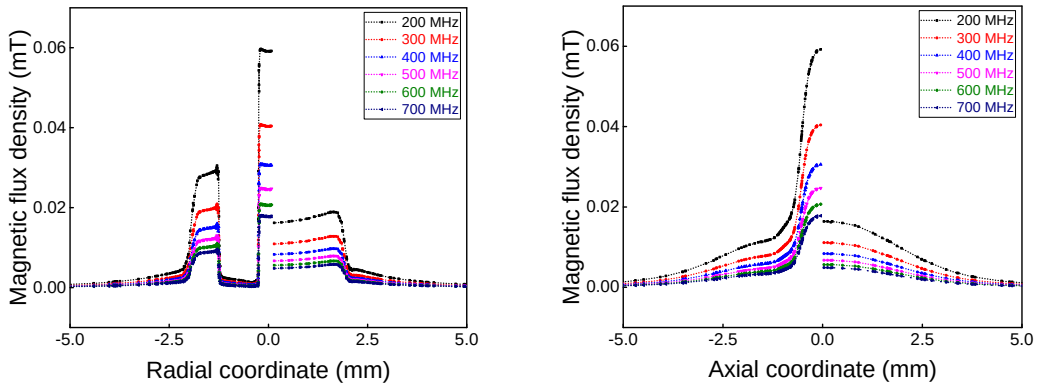
A 7.5 turn 550 µm diameter solenoid of height 0.6 mm made from 25 µm thick copper wire, defined as the focusing coil, is connected to a 24.5 turn 2550 µm diameter solenoid of height 0.8 mm made from 25 µm thick copper wire, which acts as the flux collector. The direction of windings is such that current flows in opposite direction in the coil pair. The contact pads with a thickness of 10 µm were assigned gold as the operating material. The finite element mesh size was 8 µm for the contact pads. A finer mesh (free tetrahedral) size of 4 µm was assigned to the two micro-coils.

The detectors are inductively coupled to the probe coil. The entire model geometry with the MAS probe coil is shown in Figure 5.6. From Figure 5.7 and Figure 5.8, it was observed that the B_1 field is amplified by around a factor of 3 in the sample region. The theoretical SNR enhancement was calculated to be approx. 2.5 considering the simulated net resistance for the DSLL arrangement increased by a factor of 1.4. For this double solenoid configuration complete cancellation of magnetic flux in between the two Lenz lens loops occurs and thus a higher amplification in the sample region was observed.



(a) (b)

Figure 5.7: Simulated B_1 field enhancement observed in the sample region with a DSLL insert in a) Cross section perpendicular to the coil axis; b) Cross section parallel to the coil axis. The B_1 field increase in the small region inside the anti-coil along with nullification of field between anti-coil and flux collector can be clearly observed.

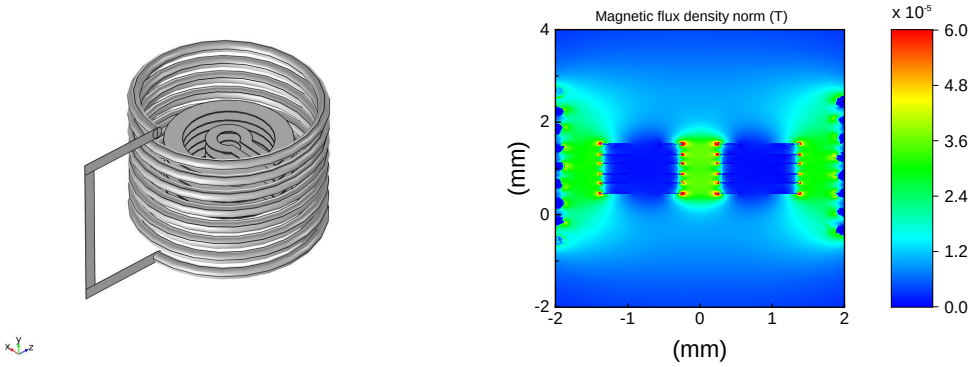


(a) (b)

Figure 5.8: Simulated B_1 field enhancement observed in the sample region with (left-half of each image) and without (right-half of each image) a DSLL insert in a frequency range between 200 MHz to 700 MHz along a) a cut line through center of coil perpendicular to the coil axis; b) along the coil axis.

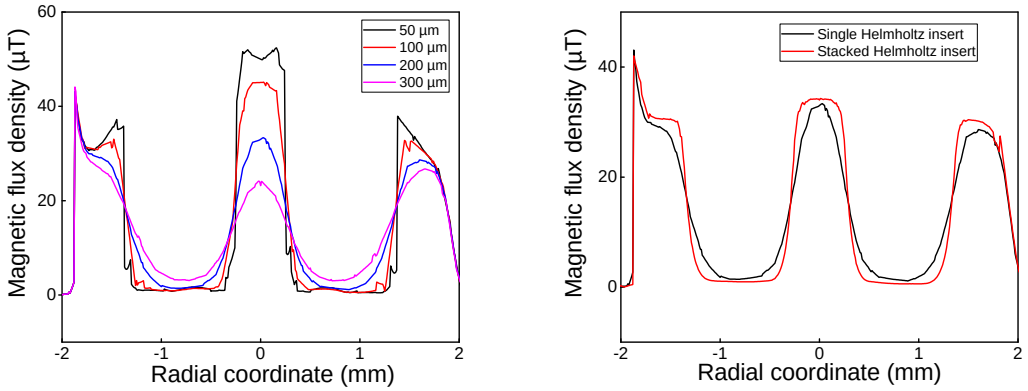
5.3.3 Helmholtz Lenz lens inserts (HHLL)

Two 8 µm thick Lenz lens shaped strips are defined separated by a distance of 200 µm to form a Helmholtz pair. Three such Helmholtz pairs separated by a distance of 200 µm are modeled inside a 8 turn primary coil of diameter 4.5 mm wound from copper wire of thickness 250 µm which acts as the MAS probe coil. The combination of three Helmholtz pairs are inductively



(a) (b)

Figure 5.9: a) FEM simulation model of stacked HHLL inserts inductively coupled to a primary coil which represents the coil in the probe at 200 MHz. The stacked HHLL device consists of three HHLL devices stacked on top of each other separated by a distance of 200 µm; b) Simulated B_1 field enhancement obtained in the sample region with stacked HHLL insert.



(a) (b)

Figure 5.10: a) Comparison of simulated B_1 field at 200 MHz from a) a standalone HHLL insert as a function of distance between them; b) a standalone and a stacked HHLL insert separated by a distance of 200 µm. A standalone insert has only one Helmholtz coil pair whereas the stacked insert has a stack of three Helmholtz coil pairs separated by a distance.

coupled to the probe coil. The entire model geometry is shown in Figure 5.9a. A mesh (free tetrahedral) size of 4 µm was assigned to the Lenz lens strips.

From Figure 5.9b and Figure 5.10a, it was observed that the B_1 field is amplified by around a factor of 2 in the sample region when the HHLL inserts were stacked with a gap of 200 µm

between them. For the Helmholtz configuration, complete cancellation of magnetic flux in between the two Lenz lens loops was observed.

The flux amplification was also evaluated for various separation distances between the HHLL inserts as shown in the Figure 5.10a. As separation distances between the inserts are increased, the flux amplification gets reduced because of the reduced coupling between the two neighbouring devices. Further, compared to a standalone Helmholtz insert, the stacked insert has a more homogeneous B_1 field distribution in sample region as observed from Figure 5.10b.

When it comes to thermal performance, stacked HHLL configuration was considered to offer better performance as compared to the SSLL and DSLL. This was due to the reason that the thickness of metallic strip of these HHLL inserts was limited to 8 µm whereas the copper wires of micro-coils in SSLL and DSLL have a thickness of 25 µm. Therefore, the thermal simulations conducted in Section 3.3.2.2 were taken as a reference and the results were extrapolated to LLMACS insert designs.

5.3.4 Conclusion

From the simulations, it was concluded that the DSLL insert offers the best B_1 field amplification among all the LLMACS designs. The double solenoid configuration was able to collect as well focus more flux from the primary coil into sample region as well as the nullification of flux in the region between the two connecting loops. The SSLL variant was not the most efficient due to the planar design of the flux collector, as only part of the flux collected by it was focused into the sample region and rest of it was distributed in between the collector and anti-coil. The B_1 field amplification from the HHLL configuration was marginally lower compared to the DSLL when the separation between the Helmholtz pair was 50 µm and decreased with increasing separation distance due to decreasing coupling between the coils. However, as described before, the HHLL would offer improved thermal performance, i.e., around nine times less heat dissipation, as compared to the DSLL.

5.4 Fabrication of broadband MACS inserts

The MACS detectors that were fabricated had a square shaped footprint. However, in the case of MALL detectors, a circular footprint would permit the fabrication of an anti-coil (flux collector) with a larger diameter (up to 2.5 mm) as compared to the diameter (up to 1.8 mm) for a detector with a square shaped footprint. A larger anti-coil results in the collection of increased magnetic flux from the primary coil which gets concentrated inside the focusing coil (inner coil). Additionally, in the case of SSLL detectors, it was observed from simulations in Figure 5.5 that the anti-coil diameter for a 4 mm MAS system has to be more than 2.2 mm which could be achieved only with detectors having a circular footprint. The dicing of the MALL detectors plays a major role in their resulting footprint. It was technically not feasible to achieve a circular footprint with typical dicing machines equipped with diamond coated

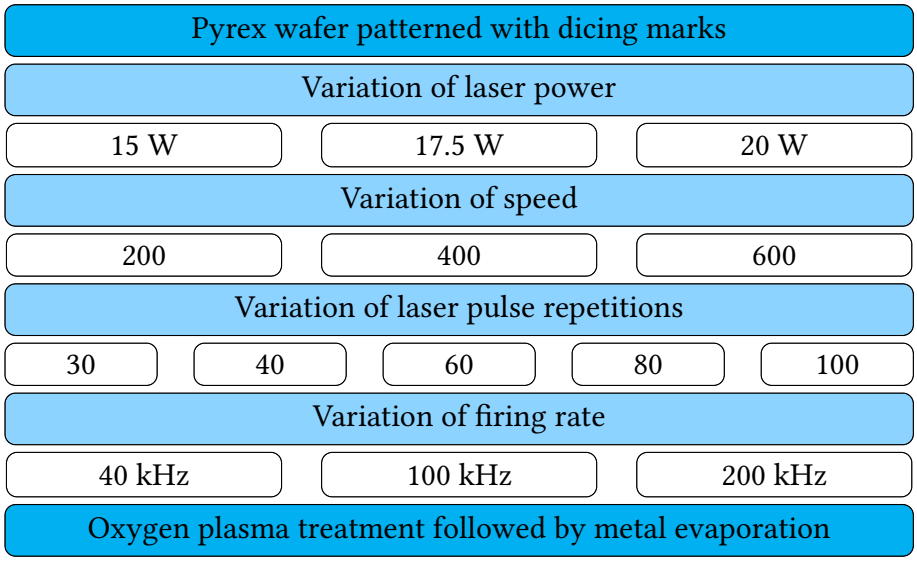


Figure 5.11: Experimental plan for dicing using a tunable ultrafast laser

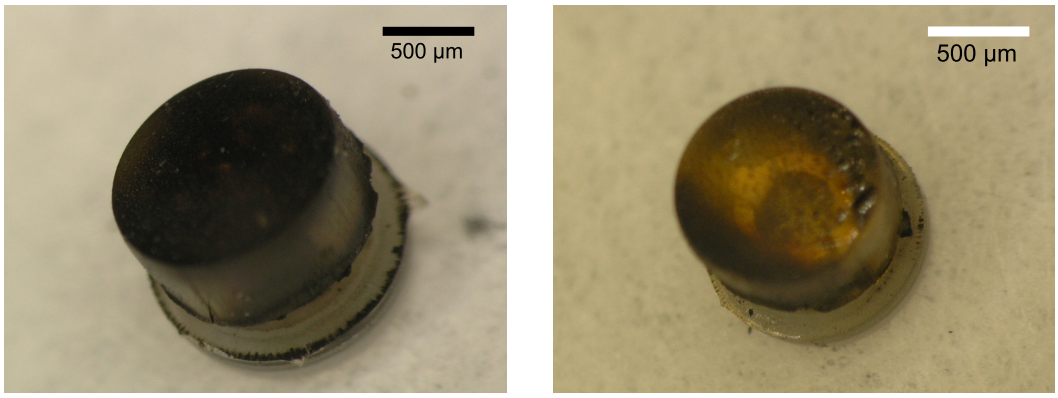
dicing blades. Hence, it was proposed to employ a laser based ablation process [234, 235], which offers flexibility with respect to footprint shapes, to cut the pyrex substrate instead of a standard dicing machines.

Experiments to cut the pyrex substrate were conducted using a femtosecond laser micromachining workstation (PS450-TO, Optec) equipped with a tunable ultrafast laser (Tangerine, Amplitude SYSTEMES) in infrared region with a wavelength of 1030 nm and a pulse length of 250 fs. Laser parameters such as laser power, speed, pulse repetitions and firing rate were optimized to cause least possible damage to the detectors. The optimization routine was conducted on a substrate containing only SU-8 cylinder blocks of diameter 2 mm and electroplated gold pads. The experimental plan for the optimization of laser parameters is shown in Figure 5.11.

At 60 % laser power (15 W), due to the relatively high firing rate of 100 kHz required to cut through glass, there was extreme local heating near the region of the laser beam as shown in the Figure 5.12a. As a result, the cured SU-8 encapsulation got charred. Additionally, there was some condensation observed on the SU-8 blocks. This is detrimental not only to wirebonds present inside the encapsulation, but also to the capacitor plates.

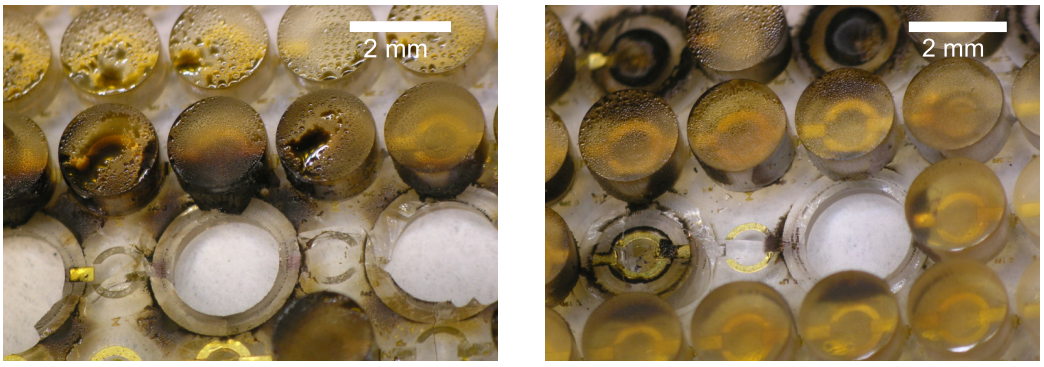
To reduce the heating, a lower firing rate of 40 kHz was tried out and power was increased to 80 % of the maximum laser power, i.e. 20 W. Using these parameters, charring of the cured SU-8 decreased as shown in the Figure 5.12b. Nonetheless, there was some blackening of the SU-8 pillars near the surface. Therefore, one could not completely avoid the charring of the SU-8 encapsulation.

With a higher firing rate, the surface of the surroundings of the diced blocks also got charred as shown in the Figure 5.13a. With lower firing rate parameters, the surface was much more clearer as shown in the Figure 5.13b. As a solution to the issues concerning the charring



(a) (b)

Figure 5.12: SU-8 blocks separated from the substrate using laser ablation with a power and firing rate of: a) 15 W and 100 kHz; b) 20 W and 60 kHz respectively. Due to extreme local heating near the region of the laser beam, the cured SU-8 encapsulation gets charred because of its organic content.



(a) (b)

Figure 5.13: Surroundings of the substrate where a SU-8 block was separated by laser applied with power and firing rate of: a) 15 W and 100 kHz; b) 20 W and 60 kHz respectively.

of encapsulated SU-8, a modified process flow was proposed as shown in the Figure 5.14 where about 90 % of material was removed from the 500 µm thick substrate by the laser beam on one side and further processing of metal, SU-8 structures and micro-coil manufacturing was conducted on the other side. Thereafter, with completion of wirebonding and the subsequent encapsulation step, individual detectors were separated with a small vertical force applied on them.

On a 500 µm surface (top side) thick pyrex substrate electroplated metal structures were fabricated similar to process steps illustrated in Section 3.4.1. Subsequently, the opposite

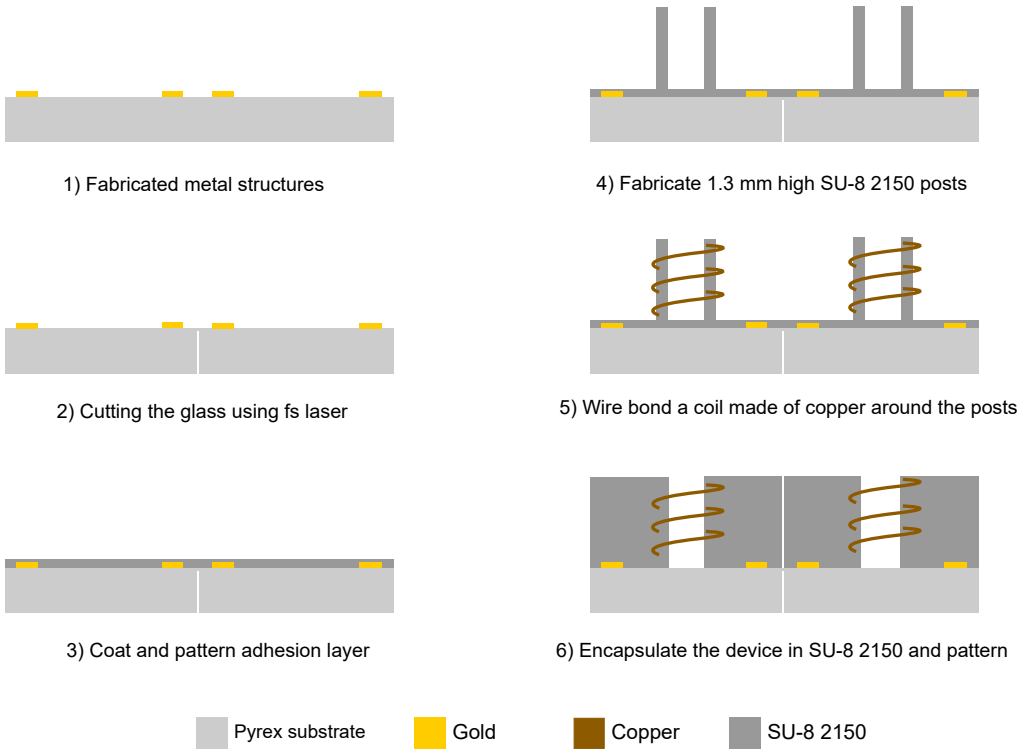
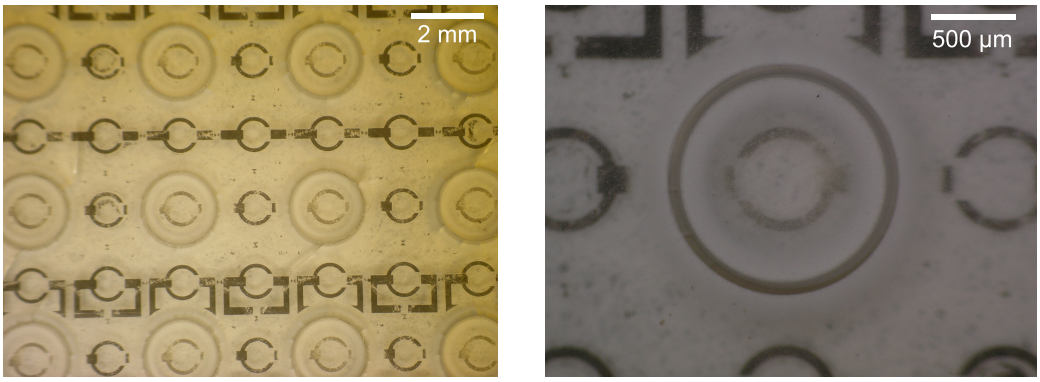


Figure 5.14: Description of process flow for the fabrication of single solenoid Lenz lens inserts.

surface (back side) of the substrate was subjected to laser parameter optimization following the experimental plan shown in Figure 5.11. The laser parameters were optimized such that the diced part was still attached to the substrate loosely and got separated only when a small vertical force was applied on it. In order to further reduce heating of the substrate due to laser beam, the overlap between two consecutive laser pulses was reduced by increasing the speed from 200 to 600. The laser power was set to 70 % of the laser power and the number of repetitions was increased to 100 to cut through 95 % of the glass as shown in Figure 5.15. Following the dicing process, HAR SU-8 processing was carried out on the top side of the substrate as described in Section 4.2.1. Following the SU-8 encapsulation process, the the cylindrical pieces were separated as shown in the Figure 5.16a with the application of a small force from the substrate shown in Figure 5.16b. A clean separation and the absence of dangling pieces left on the substrate suggested that laser dicing process was optimized.

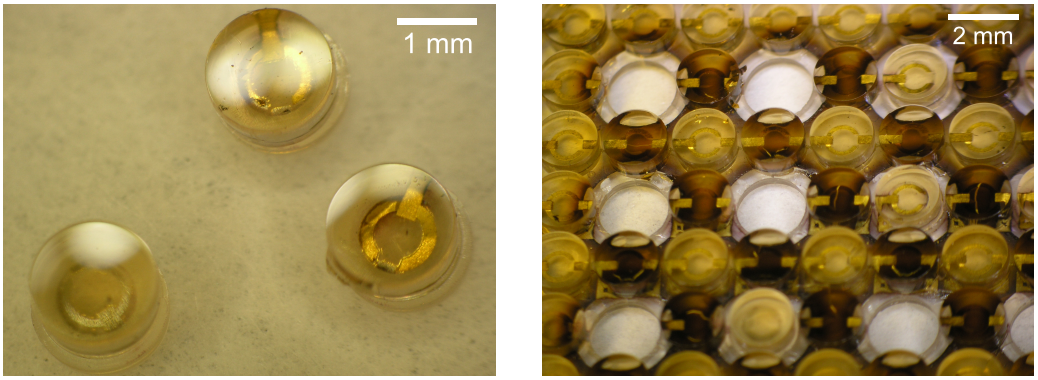
5.4.1 Fabrication of SSLL and DSLL inserts

Based on the simulation model shown in Section 5.3.1, for a SSLL insert, the outer flux collector is fabricated as a planar 2D structure and the anti-coil is realized as a solenoid whereas for a DSLL detector both loops are solenoid coils as simulated in Section 5.3.2.



(a) (b)

Figure 5.15: Substrate partially diced using a femtosecond laser. a) Top side view; b) Bottom side view. The dicing was done through the bottom side.



(a) (b)

Figure 5.16: a) Separated SU-8 blocks from the substrate; b) Surroundings of the substrate where a SU-8 block was separated by laser.

A 500 µm thick pyrex wafer was evaporated with 20 nm/60 nm chromium and gold and patterned to define alignment marks on the substrate. These marks function to align the diced pattern with further processing steps. Then, backside of the glass substrate was structured with the help of a femtosecond laser as shown in Figure 5.17a to facilitate separation of individual inserts from the substrate. A 20 µm SU-8 3025 mold[A7] was then spin coated and patterned for electroplating the flux collector and contact pads. Following the electrodeposition of 8 µm gold[A7], the SU-8 mold was stripped[A7] and the unwanted seed layer etched as shown in Figure 5.17b. Next, fabrication of HAR SU-8 pillars was carried out with the help of SU-8 2150 resist as detailed in Section 4.2.1. The hollow SU-8 pillars which act as sample holders and coil support structures were designed to have a height of 1300 µm and outer and inner diameter of 550 µm and 400 µm, respectively. The μ-Solenoids were then fabricated as shown

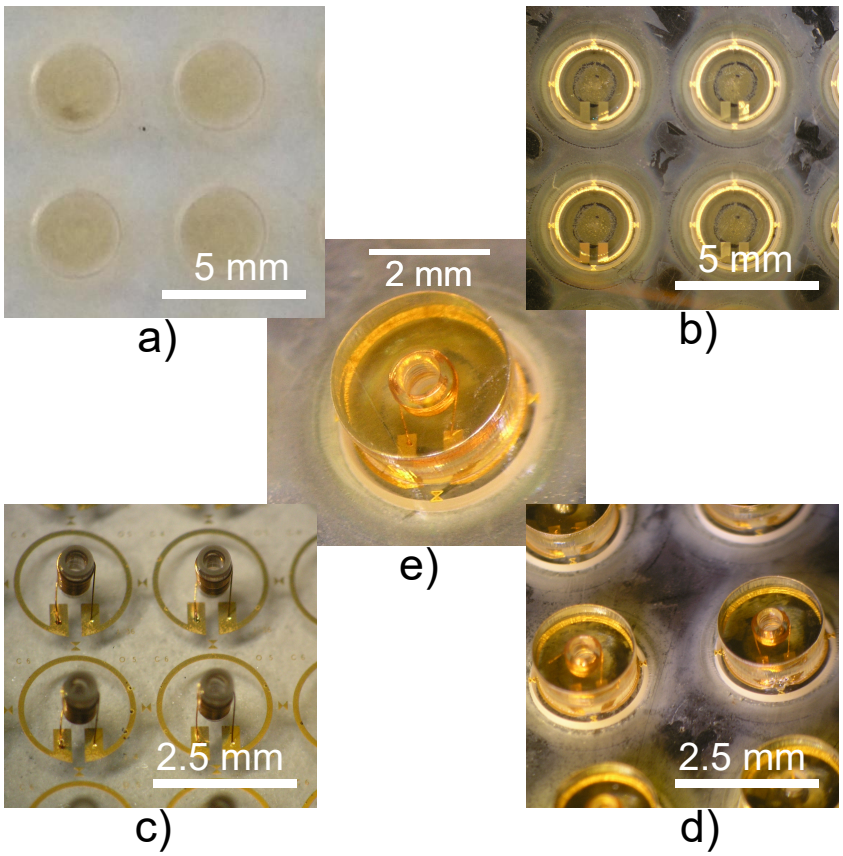


Figure 5.17: Images showing the substrate under various stages during the fabrication of SSLL inserts. a) Pre-diced (backside) substrate; b) Electroplated collector coil and contact pads on top side of the substrate; c) HAR SU-8 pillars and wirebonded micro-coil (anti-coil); d) Encapsulated SSLL detector; e) Individual SSLL detector.

in Figure 5.17c using automated wirebonding process elucidated in Section 4.2.2 using an in-house developed MATLAB®code (Section A13) and optimized wirebonding parameters for a 25 µm copper wire described in Section A15. This was followed by encapsulating the SSLL detector in SU-8 2150 following the process steps outlined in Section 4.2.3 as shown in Figure 5.17d. Thereafter, the individual detectors were separated from pyrex substrate by light application of force. The final footprint of detectors had a diameter of 2.9 mm whereas the inner diameter of the 4 mm MAS rotor is 2.96 mm.

For the double solenoid Lenz lens inserts, alignment marks on the substrate were initially defined by patterning 20 nm/60 nm chromium and gold evaporated layer. Following the laser structuring of the backside of the substrate as shown in Figure 5.18a, contact pads for wirebonding were defined by electroplating as shown in Figure 5.18a. Subsequently, two concentric hollow SU-8 pillars were fabricated as shown in Figure 5.18b with a height of 1300 µm as per the process steps illustrated in Section 4.2.1. The outer and inner diameter of the two

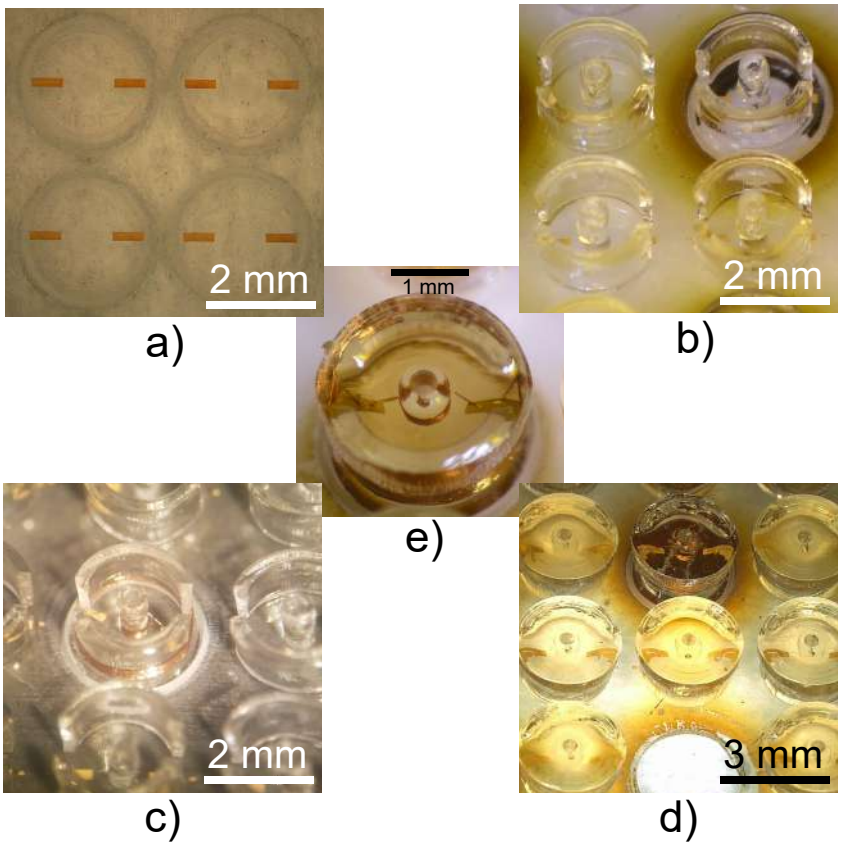
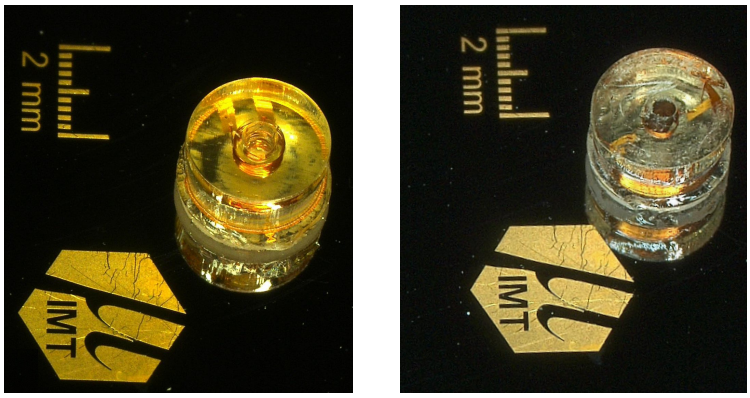


Figure 5.18: Images showing the substrate under various stages during the fabrication of SSLL inserts. a) Pre-diced (backside) substrate and electroplated contact pads on top side of the substrate; b) HAR SU-8 pillars concentric to each other; c) Wirebonded double solenoid micro-coils; d) Encapsulated DSLL detector and then separated from the substrate; e) Individual DSLL detector.

pillars were 2500 µm and 2300 µm and 550 µm and 400 µm, respectively. Two concentric coils were then wound on these pillars as shown in Figure 5.18c with a wirebonder as described in Section 4.2.2 using an in-house developed MATLAB®code described in Section A14 and optimized wirebonding parameters for a 25 µm copper wire described in Section A15. The wirebonding step was followed by the encapsulation process as chronicled in Section 4.2.3 and shown in Figure 5.18d. This was followed by separation of the DSLL inserts from the substrate by light application of force. The final detector footprint diameter of 2.9 mm was similar to the SSLL inserts, thus compatible with the 4 mm MAS rotor.

The separated SSLL and DSLL inserts are shown in Figure 5.19a and Figure 5.19b respectively.



(a) (b)

Figure 5.19: a) Separated SSLL insert; b) DSLL insert with a footprint diameter of 2.9 mm.

5.4.2 Fabrication of HHLL inserts

As proposed by Spengler *et al.* [128], four different designs were fabricated. The net sample volume of 180 nl was achieved by stacking the planar Lenz lenses on the substrate.

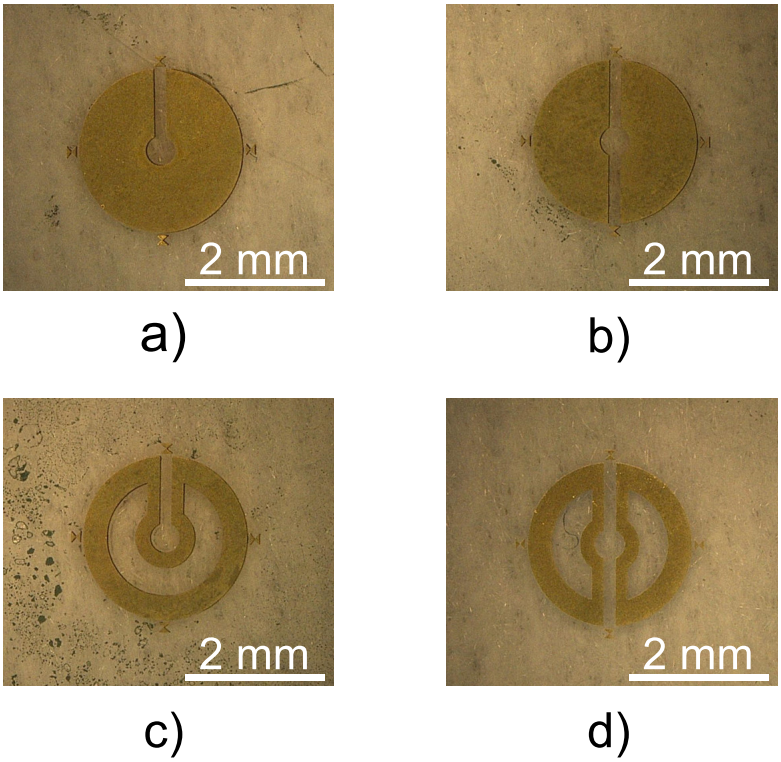


Figure 5.20: Electroplated electrodes of various designs of HHLL inserts. a) Single slit based disk; b) Double slit based disk; c) Single slit based ring; d) Double slit based ring.

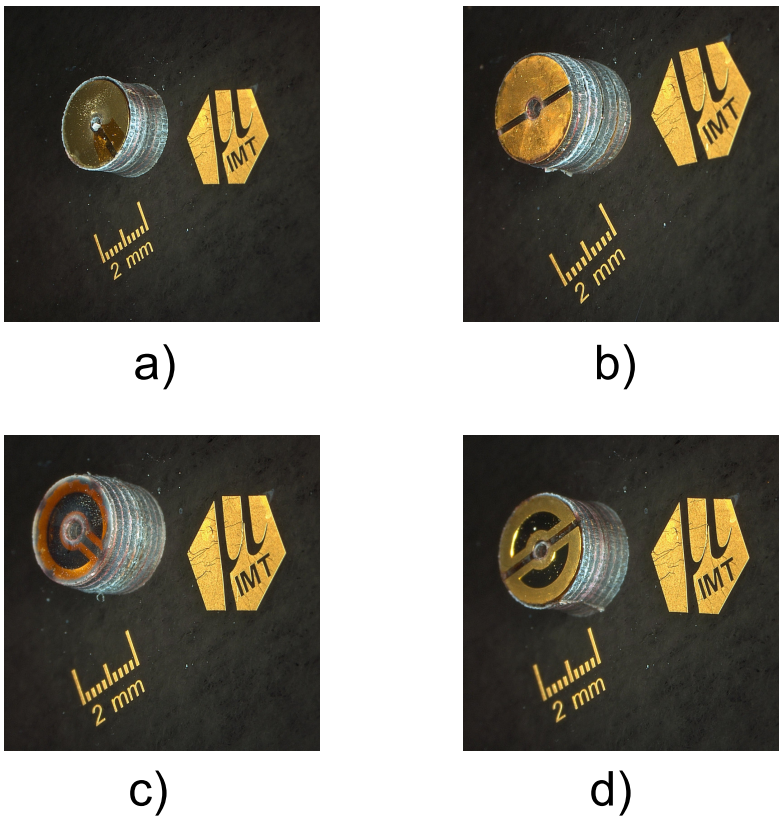


Figure 5.21: Fabricated stacked HHLL inserts. a) Single slit based disk; b) Double slit based disk; c) Single slit based ring; d) Double slit based ring. The footprint of the detector had a diameter of 2.9 mm.

For the Helmholtz lens inserts, following the laser dicing step, 20 nm/60 nm chromium and gold layer was evaporated on both sides of a 210 µm thick pyrex substrate followed by electroplating the Lenz lens structures on each side. This meant the separation distance between the Helmholtz coil pair was also 210 µm. The outer diameter of the flux collector (outer loop) was 2900 µm and inner diameter of the focusing loop was 500 µm. The cylindrical geometry of the microfabricated inserts enable reduced footprint, thereby facilitating faster rotation. Additionally, the reduced footprint of the detectors due to the cylindrical geometry permits the fabrication of a larger flux collector (outer). A larger flux collector results in the collection of more magnetic flux from the primary coil which gets concentrated inside the focusing coil (inner coil). Stacking of the Helmholtz coil pairs was achieved by compression bonding[A7]. A 5 µm thick layer of SU-8 3005[A7] was used as the adhesive medium for the bonding process. The critical step in this process was the partial baking of the spin-coated photoresist. This was done to ensure that the resist maintained its adhesive nature as well as that surface of the resist was uniform to facilitate optimum bonding process under high pressure (5 kN) and temperature (55 °C). After the two bonding surfaces of the substrates were brought into contact, compression bonding process was performed (EVG 510®EV Group).

Following the bonding process, the photoresist was cross-linked with an UV exposure dose of 300 mJ/cm^2 and thereafter baked at 65 °C for 2 h. Subsequently, laser ablation process was done to separate the HHLL detectors from the substrate.

The four different designs of Helmholtz inserts achieved by stacking on top of each other are shown in Figure 5.21.

5.4.3 Conclusion

The fabrication process for the SSLL insert was fairly straightforward, with electroplating of the pads followed by wirebonding the coils, once the laser ablation process was optimized. However, fabricating the double solenoids for the DSLL inserts was to some extent much more intricate. After the completion of the wirebonding process for the inner coil, the bondhead trajectory (Section A14) for the outer coil involved the position of the ball and wedge bonds inside the coil boundaries while at the same time maneuvering narrow space between the two coils without destroying the the inner coil. For the HHLL inserts, due to difficulties associated with handling substrates of thickness 50 µm and 100 µm, a 210 µm thick substrate chosen which meant reduced B_1 field amplification. Moreover, stacking of multiple substrates and followed by the laser ablation process to separate the stacked HHLL inserts was cumbersome. In spite of these issues, the major advantage offered by the HHLL inserts is their scalability. Unlike the wirebonded detectors where further downsizing the detectors to fit into smaller rotors was hindered by the wirebonding process, the size of the HHLL inserts can easily be reduced down to 1 mm with only design modifications on the lithography mask.

5.5 Characterization

The fabricated Lenz lens structures are characterized for their performance. The benchtop measurements for assessing the electrical properties of individual μ-Solenoids were initially conducted. This was followed by NMR characterization using various samples.

5.5.1 Electrical characterization

A detailed characterisation of micro-coils of diameters 0.55 mm, 0.85 mm and 3 mm with number of turns ranging from 3 to 28 was undertaken and described in Section A8. One important consideration was that the self-resonant frequency of the individual micro-coils that were to be used in LLMACS detectors was well above the Larmor frequency of interest (in this case 500 MHz). This was undertaken to reduce the influence of parasitic capacitance and thus ensure that the micro-coils operate as inductors. It was observed that in the case of coil with diameter of 0.55 mm, the self-resonant frequency of a 25 turns coil was around 1.5 GHz. However, as the diameter of the coil increases, the self-resonant frequency decreases. For e.g., the self-resonant frequency of a 3 mm coil with 15 turns and 7 turns was around 350 MHz and 1 GHz respectively. Therefore, the number of turns for a 3 mm outer coil was kept below 7

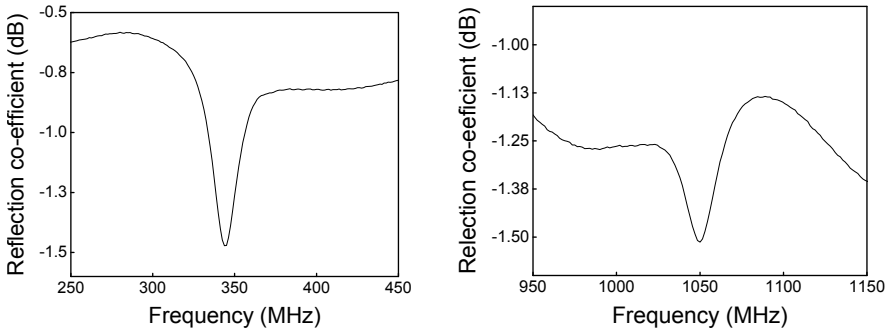


Figure 5.22: S_{11} measurements of the DSLL outer coil to evaluate the self-resonant frequency of the coil.

to minimize parasitic losses. This frequency behaviour was further verified by measuring the self-resonant frequency using a sniffer coil (Section A9) as shown in the Figure 5.22 which shows similar values to ones measured using impedance probes.

5.5.2 NMR characterization

NMR characterization of the various Lenz lens structures was done with liquid as well as solid-state samples. The NMR experiments were essentially undertaken to evaluate the sensitivity enhancement as well as the spectral quality offered by these broadband inserts.

5.5.2.1 SSLL

Nutation experiments were performed using a sample of 0.5 M sucrose at an excitation power of 24 W on the ^1H channel under MAS conditions of 5 kHz. The NMR signal was the highest at pulse length of 4 µs as shown in Figure 5.23.

The observed $\pi/2$-pulse of 4 µs was longer than the $\pi/2$-pulse of 3.3 µs observed with only the primary coil in the probe. This suggests that there is reduction in the B_1 field in the sample region.

Experiments were conducted with a SSLL insert at a $\pi/2$-pulse of 4 µs using a sample of 500 mM sucrose at an excitation power of 24 W under MAS conditions of 5 kHz to evaluate the sensitivity from the doublet of the anomeric proton in sucrose. However, the spectral quality was poor as shown in Figure 5.24 and did not improve after adjusting the shim coils in the MAS probe.

The simulation studies described in Section 5.3.2 suggested a B_1 field enhancement of only around 1.5 and the presence of significant B_1 fields outside the sample region. The poor spectral quality and lack of SNR boost in the sample region can be attributed to these causes.

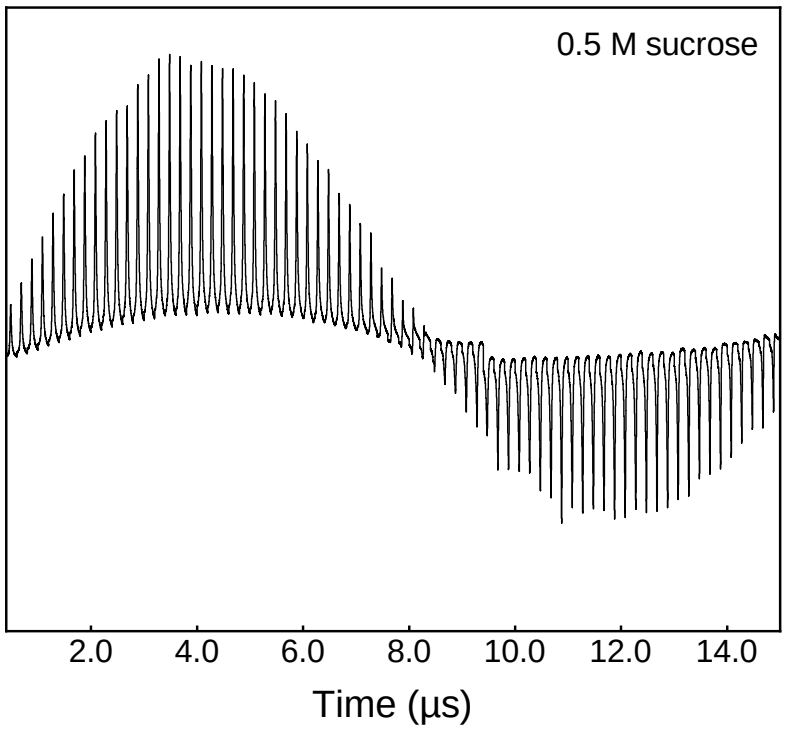


Figure 5.23: Nutation spectrum for SSLL insert. The nutation experiment for the SSLL insert was performed using a sample of 0.5 M sucrose at an excitation power of 24 W under MAS conditions of 5 kHz. The sample volume was 180 nl. A $\pi/2$-pulse of 4 µs was observed.

5.5.2.2 DSLL

Nutation experiments were performed using 0.1 M deionised water in D_2O at an excitation power of 24 W under MAS conditions of 5 kHz. The NMR signal was the highest at pulse length of 5 µs as shown in Figure 5.25.

The observed $\pi/2$-pulse of 4 µs was longer than the $\pi/2$-pulse of 3.3 µs observed with only the primary coil in the probe. This suggests that there is reduction in the B_1 field and conditions in the sample region are not optimal.

Experiments were conducted with a DSLL insert at a $\pi/2$-pulse of 5 µs using a sample of 500 mM sucrose at an excitation power of 24 W under MAS conditions of 5 kHz to evaluate the sensitivity from the doublet of the anomeric proton in sucrose. Although, the spectral quality was better than the one acquired from SSLL as shown in Figure 5.26, the reduction in sensitivity is significant when compared with the spectrum from a dummy insert.

The simulation studies described in Section 5.3.2 suggested a B_1 field enhancement of around 3, with a SNR boost of 2.2 in the sample region and close to zero B_1 field between the sample region and outer coil. However, a significant B_1 field was observed between the

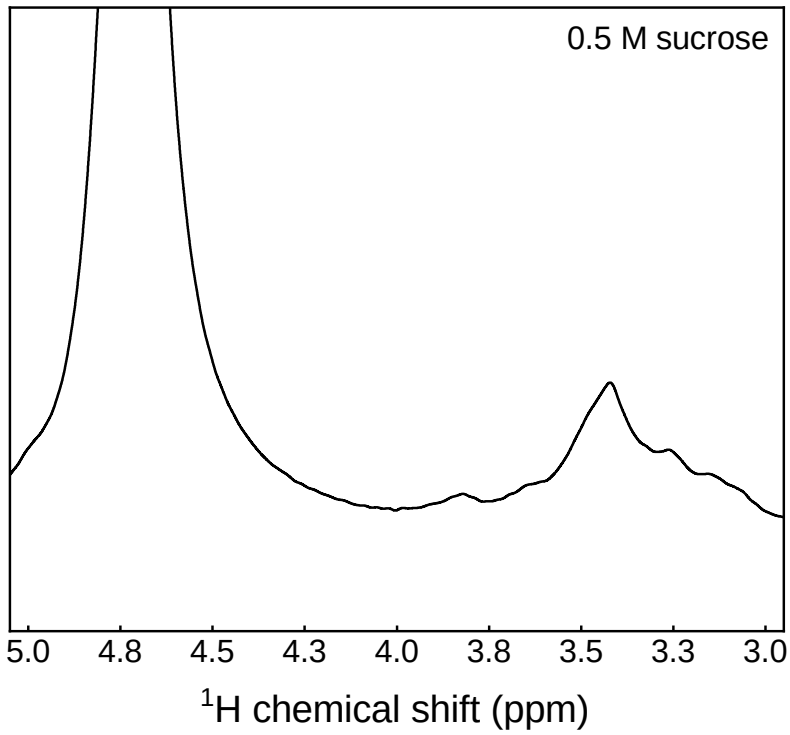


Figure 5.24: Evaluation of the sensitivity enhancement achieved with a SSLL insert. This was done by acquiring an NMR spectrum of 500 mM sucrose at an excitation power of 24 W under MAS conditions of 5 kHz. The sample volume was 180 nl.

primary coil and the outer coil (flux collector) of the Lenz lens structure. Therefore, it can be argued that the low sensitivity of the NMR experiment in this configuration is due to the presence of this B_1 field. Since the volume occupied by the B_1 field in this region is higher than the corresponding volume in the sample region, high amount of noise is picked up from this region.

5.5.2.3 HHLL

Nutation experiments were performed using a sample of adamantane at power levels from 1 W to 100 W on the ^1H channel.

Experiments were conducted with all four variants of the stacked HHLL inserts. However, NMR measurements did not lead to any significant signals that were observed.

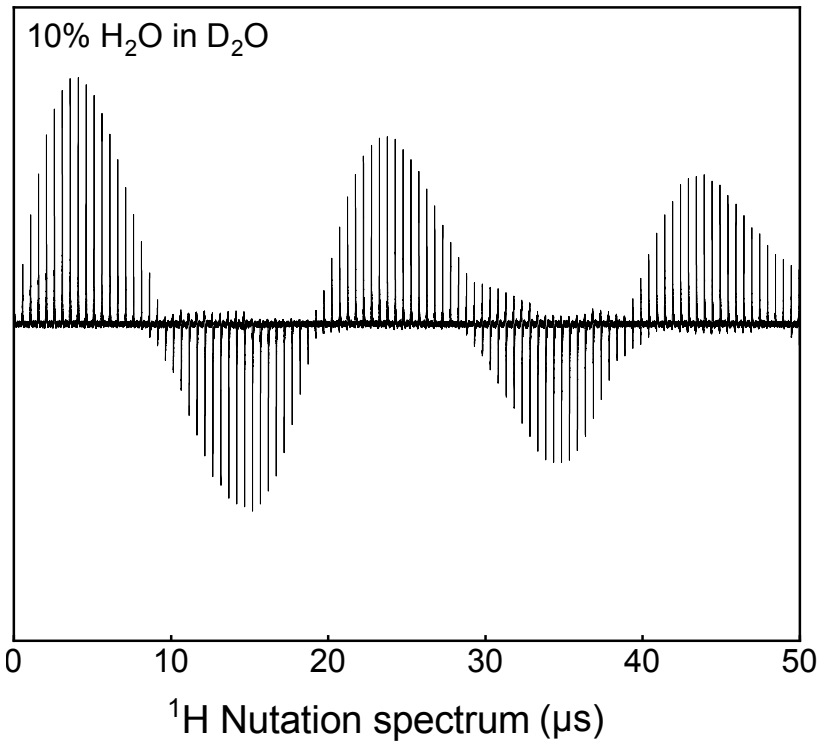


Figure 5.25: Nutation spectrum for DSLL insert. The nutation experiment for the DSLL insert was conducted using a sample of 0.1 M water in D_2O at an excitation power of 24 W under MAS conditions of 5 kHz. The sample volume was 180 nl. A $\pi/2$-pulse of 5 µs was observed.

5.6 Discussion

A novel concept for the development of broadband MACS detectors has been introduced. The integration of Lenz lens structures with the primary coil of the MAS probe was verified using analytical equations as well from FEM simulations. It was observed from simulations that the DSLL inserts offer the highest SNR boost whereas the HHLL inserts offer a good compromise between sensitivity boost and sample heating due to induced currents.

The major highlight from the development of broadband detectors has been their cylindrical geometry. This geometry of the microfabricated inserts enable reduced footprint, thereby facilitating faster rotation. Additionally, the reduced footprint of the detectors permits the fabrication of a larger flux collector (outer). A larger flux collector results in the collection of more magnetic flux from the primary coil which gets concentrated inside the focusing coil or the anti-coil (inner coil).

The concept of integrating laser dicing in the process flow to fabricate detectors can be extended for the fabrication of resonant MACS inserts. This would lead to an optimized geometry which would result in these inserts to be able to fit inside 1.7 mm rotors as opposed

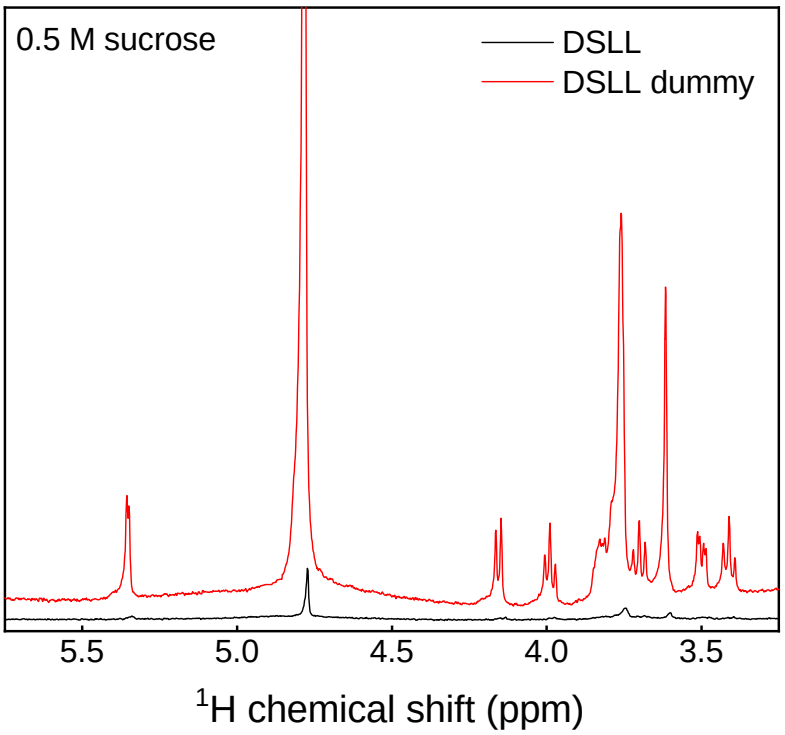


Figure 5.26: Evaluation of the sensitivity enhancement achieved with a DSLL insert. This was done by acquiring an NMR spectrum of 500 mM sucrose at an excitation power of 24 W under MAS conditions of 5 kHz and comparing it with the NMR spectrum from a dummy insert under similar excitation conditions. The sample volume was 180 nl.

to the inserts with square footprints which would not fit inside rotors with diameter less than 3.2 mm.

However, the NMR experiments with broadband MACS inserts did not run according to expectations. Using SSLL and DSLL inserts, a reduction in the B_1 field in the sample region was observed. There was no recorded NMR spectrum using HHLL inserts. These experiments suggest that the broadband inserts were not functioning according to their expected performance as noted from FEM simulations.

The ineffectiveness of these broadband inserts originates from the size of the outer coil (flux collector) of the Lenz lens structures. Ideally, the size of the flux collector should be as close to the primary static coil as possible, such that maximum magnetic flux from the primary coil is focused into sample region. In MAS configuration, the limitation arises from wall thickness of the MAS rotors and air gap between the spinning rotor and the coil in the probe. From Figure 5.7 and Figure 5.9b, it was observed that B_1 field in the region between the Lenz lens structures and the primary coil also gets amplified. Since the volume from this

region, approx. 10 ml, dominates the sample volume (180 nl), the coil in the probe picks up majority of the signal from this empty region rather than that from the region where sample is located. This was most meaningful explanation that could be provided for the non-functional nature of these inserts experimentally.

Additionally, experiments were also conducted at various power levels and varying pulse lengths to verify if at all it was possible to acquire signals only from the 'sample region'. However, the attempts were not successful. As a future work, MRI experiments could be performed using these inserts to obtain B_1 field maps to cross-verify these conclusions.

6 Conclusion and outlook

In spite of numerous endeavors towards miniaturization of NMR detectors [108], there is a compelling argument that the end users have not substantially reaped the benefits of the advancements in miniaturization in NMR [236]. To this end, this thesis reports on the development and scaling up of the fabrication of NMR micro-detectors as a part of the effort to address the gap in accessibility to miniaturized detectors for the NMR community.

6.1 Conclusion

The major contribution from this work is a microfabricated NMR micro-detector for MAS application that has been fully characterized with respect to its electrical, thermal and NMR performance. Additionally, a robust wafer scale fabrication process for these detectors has been demonstrated.

The microfabricated NMR micro-detector acts as a micro-resonator tuned to the Larmor frequency of interest using a combination of a micro-coil and an on-chip capacitor. The on-chip capacitor for the MACS sensor, which was introduced by Badilita *et al.* [11], has facilitated the move away from employing a soldered discrete component as a tuning capacitor. However, this change to have the capacitor on-chip significantly reduced the NMR performance of the sensor. Therefore, a comprehensive study was undertaken as a part of this work to evaluate the functioning of these on-chip passive components from the perspective of electrical as well as thermal characteristics. Among the two variants considered, the parallel plate capacitor was deemed to be the most suitable to be integrated in a MACS detector because it satisfied the criteria of minimum required Q factor as well as the intensity of eddy currents induced in the electrodes being lower. Additionally, this design also offered the flexibility to reduce the footprint of the detectors, if required, to combine with smaller diameter MAS rotors.

The on-chip capacitors were then combined with the inductive component of the micro-resonator, i.e., a micro-coil. A combination of SU-8 lithography and automated wirebonding aided in establishing a robust process flow to obtain the micro-resonator. Significant progress was made to SU-8 lithography step as compared to the existing process [11] and as a result the length of the micro-coil doubled and the diameter of the coils reduced by a factor of 1.3 to 1.8, thus improving the B_1 field homogeneity. A special emphasis was placed on establishing a reproducible process for these detectors. The wafer scale fabrication process flow established during this thesis allows to circumvent the serial manufacturing process of handwinding copper wires around capillaries and soldering/spot welding the ends of the wire to a discrete capacitor.

The batch fabricated MACS micro-resonators have been benchmarked with respect to their electrical, thermal and NMR behaviour. A factor of 6 sensitivity gain has been observed with these detectors. The normalized limit of detection ($nLOD_\omega$) [190], which is a measure of sensitivity, was evaluated to be approx. 13 nmol$\sqrt{s}$ at 500 MHz. This value is marginally better compared to the previous version [11]. Additionally, this value also compares favorably to other microfabricated solenoidal micro-coils that have been reported [109, 110, 165]. However, there has been a significant improvement in the linewidths offered by current device (0.01 ppm), as compared to the older variant (1 ppm) of the microfabricated MACS detector. This is attributed to all the modifications that have been implemented in the current device such as the coil wire, SU-8 packaging, higher aspect ratio of the micro-coil and so on.

The strong RF excitation power provided by MACS micro-coils has been demonstrated by conducting a heteronuclear 2D NMR experiment where this feature is harnessed during the ^1H decoupling step. Additionally, this thesis has demonstrated, for the first time, ^1H NMR metabolic profiling of an intact single zebrafish embryo, thus affirming the suitability of these detectors for metabolomic studies. The concentration limit of detection ($cLOD_\omega$) as introduced by Finch *et al.* [119] in the framework of metabolite profiling is approx. 320 mM$\sqrt{s}$. Although the reported value for the current device is higher as compared to the value for a stripline resonator [119], this is attributed to the very small amount of sample that the MACS detector can accommodate. There have been a few other efforts on metabolite profiling using the MACS technique [237] and the best reported ^1H resolution was 0.004 ppm [150]. The reported sensitivity enhancement was in the range of 3 to 14. Therefore, the current microfabricated MACS detector has still some room for improvements.

Further, a novel concept for a MACS micro-detector with operational capabilities across a wide frequency range has been introduced. The design of these broadband detectors were based on Lenz lens structures [128, 229], that are essentially two connected conducting loops sans tuning elements. Three different designs were conceptualized and FEM simulations displayed promising results with SNR improvements of >2 for the DSLL and HHLL designs. Innovative techniques were employed to materialize these designs including the novel double winding approach for the DSLL detectors and multiple substrate bonding method for the HHLL inserts. However, the experimental investigation of these detectors were not successful in replicating the simulation results. After conducting multiple investigations, a plausible argument to explain stark deviation in the NMR performance of these detectors was that bulk of the NMR signal was picked up from the empty region between the Lenz lens structures and the primary coil rather than that from the region where sample is located.

Finally, a new technology and a process flow has been demonstrated to singulate the MACS detectors by means of laser. This process will facilitate MACS inserts with cylindrical geometry, thus reducing their footprint and make them compatible with smaller diameter MAS rotors.

6.2 Outlook

Considering the advancements that have been reported in this thesis on the efforts to parallelize the production of MACS detectors, there is still some scope for improvements. The ease of deployment of these MACS detectors for NMR measurements along with their operational performance would define their acceptance in the NMR community.

A factor of 6 sensitivity enhancement using the current MACS micro-resonators was obtained. However, due to issues relating to the limited range of the tuning and matching capacitors of the MAS probe used in the project, the full scope of sensitivity gain offered by these detectors could not be realized (Section 2.5.2). Therefore, an HRMAS probe with a broader range of tuning and matching capacitors could be engaged to recover the additional 45 to 55 % loss in sensitivity due to 30 MHz mis-tuned detectors used in this thesis. Further reduction in footprint of these detectors would lead to their integration in MAS rotor sizes down to 2.5 mm. This would mean access to faster rotation speeds. Another route to achieving faster spinning speeds would be to combine these MACS inserts with spherical rotors [65, 67]. Moreover, by combining with spherical rotors, there is an opportunity for additional improvement in sensitivity enhancement by means of DNP [66].

There has been a steady growth in NMR-based metabolomic studies over the past two decades [238, 239]. This has extended into HRMAS studies [240, 241] due to the advantage that it enabled analysis with intact tissue samples as opposed to working with tissue extracts. This advantage was showcased in this thesis by acquiring metabolite information from a single intact zebrafish specimen. However, the best spectral resolution of 0.01 ppm offered by these detectors was inferior to accepted linewidth of 0.005 ppm [241] for HRMAS studies. One way to reach this target would be to integrate μ-gradient structures [242] or by the addition of passive shims [210] in the MAS stator or shim-on-chip designs [243] to achieve a more localized shimming of the field across the sample.

High-sensitivity, spectral resolution, spectral repeatability and sample preparation are seen as the four cornerstones for metabolic investigations. Due to the nl and μg sample amounts associated with the MACS experiments, sample preparation strategy is quite challenging and demands specialized skills and distinct set of tools [135, 244]. Different sample morphologies further compounds the issue. In this work, μ-pipettes and μ-funnels along with set of standard HRMAS sample preparation tools [238] were utilized for sample loading and have been explained in the Section 4.3.3. However, the strategies described here still involves plenty of manual operations and thus tied to the patience and skills of the operator. An automated sample loading and sealing strategy could go a long way towards ensuring sample integrity and data reproducibility, thus simplifying the task for the NMR spectroscopist.

Another useful tool designed for improving the micro-coil MAS NMR field was the broadband detectors introduced in this work. However, due to poor experimental performance of these detectors, they are yet to show their intended usefulness and further investigations are necessary. A rational approach would be to test their performance in MAS systems smaller than 4 mm as the air gap between the static coil and the rotor would be reduced. This would result in larger magnetic flux collection and thus increase in B_1 field amplification in the

sample region. A working broadband detector would bring about a large scale improvement in sensitivity of heteronuclear MAS NMR experiments.

Further, establishing a wafer scale manufacturing process for these MACS detectors will drastically reduce their manufacturing cost and this cost reduction will lead the way towards disposable-NMR procedures, thereby completely eliminating cleaning routines. This will greatly enhance throughput and reduce sample cross contamination.

Appendix

A1 Zebrafish husbandry and embryo culture

Ethics statement: All zebrafish husbandry was performed in accordance with the German animal protection standards and approved by the Government of Baden-Württemberg, Regierungspräsidium Karlsruhe, Germany (Aktenzeichen 35-9185.64/BH KIT).

Adult zebrafish (AB strain) were bred and raised following standard protocols [245]. Briefly, breeding couples were placed into mating tanks in the evening, and eggs were collected from natural spawnings in the morning. Unfertilized eggs were removed, and developing embryos were kept in 10 cm petri dishes (633180, Greiner Bio-One) containing E3 medium [246] without methylene blue at 28 °C. Hatching from the chorions (eggshells) occurred spontaneously 48 hours post fertilization (hpf).

A2 Larmor frequency of some common isotopes at 11.74 T

Table A.1: Larmor frequency of some common isotopes at 11.74 T

Isotope	Natural Abundance %	Gyromagnetic ratio ($\gamma/2 \cdot \pi$) (MHz/T)	Larmor frequency at 11.74 T (MHz)
^{1}H	99.984	42.576	499.842
^{2}H	0.0156	6.541	76.791
^{7}Li	92.41	16.546	194.250
^{13}C	1.108	10.705	125.676
^{15}N	0.366	-4.317	50.684
^{17}O	0.038	-5.771	67.758
^{19}F	100	40.053	470.222
^{23}Na	100	11.262	132.215
^{27}Al	100	11.103	130.349
^{31}P	100	17.235	202.339
^{51}V	99.75	11.177	131.217

A3 Magic angle spinning probe calibration

Meanwhile, calibration of the MAS probe to the magic angle has been undertaken. The precise setting of the magic angle is mandatory to obtain the maximum spectral resolution obtained by MAS. In order to adjust the magic angle, a sample is needed with an NMR line that is very sensitive to angle misalignment. Potassium bromide (KBr) is common sample used for the magic angle calibration with ^{79}Br being the nucleus observed. The Larmor frequency is 125 MHz at 11.7 T. The rotor is completely filled with sample of KBr and the sample is spun at 5 kHz.

^{79}Br spectrum of KBr is obtained at the initial set-up as shown in the Figure A.1a. The lack of significant number of sidebands suggest that the probe is off-magic angle. The magic angle setting is then slightly changed by turning the micrometer screw at the bottom of the probe. Another spectrum is obtained and the procedure is repeated until the magic angle setting is optimal. The spectrum at the best setting is shown in the Figure A.1b with significant number of sidebands which have higher intensity as well as narrower as compared to original spectrum.

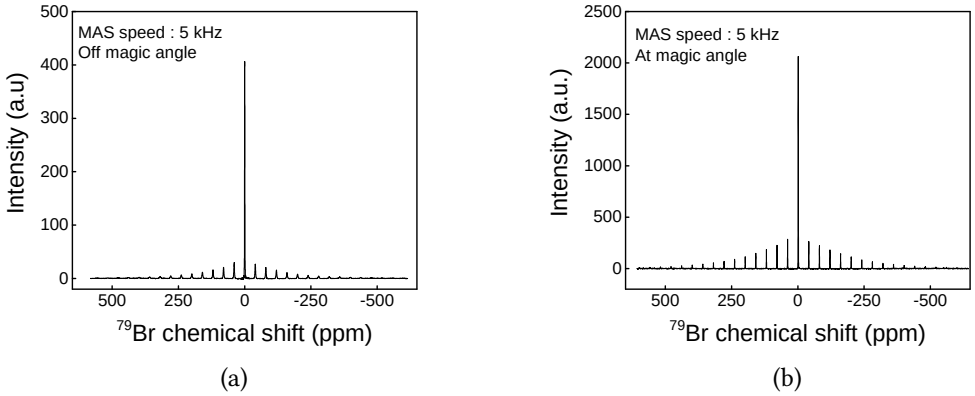


Figure A.1: a) ^{79}Br spectrum of KBr off magic angle. b) ^{79}Br spectrum of KBr at magic angle.

A4 Sample preparation for NMR experiments

During the course of this work, a number of samples of standard solutions of glucose, sucrose and ethanol with differing concentrations have been prepared. Deuterium oxide(D_2O) has been used as the solvent for all solutions.

For e.g. to prepare a 500 mM sample of sucrose in 10 ml of D_2O, it is important to calculate the amount by weight of sucrose that has to be dissolved in D_2O. This can be done by knowing the molar value and molecular weight of sucrose which is 342.3 g/mol. A concentration of 500 mM sucrose multiplied by the molecular weight of sucrose gives the amount of sucrose

in a litre of solution, i.e., 171.15 g. For a 500 mM concentration in 10 ml, amount of sucrose to be dissolved is 1.7115 g.

Similarly, molecular weight of other solutes such as glucose, TSP and ehtanol are 180.156 g/mol, 146.26 g/mol and 46.07 g/mol respectively.

A5 Calculation of proton concentration in a solution

The ^1H NMR spectrum of sucrose contains various signatures from the 22 proton nuclei in it. Therefore, to ascertain the sensitivity of the NMR experiment, the first step is to calculate amount of proton nuclei in the sample inside the detector. The density of sucrose and D_2O is 1.59 g/ml and 1.107 g/ml respectively. Considering that the sample volume in a MACS detector is 380 nl and 1.7115 g of sucrose was dissolved in 10 ml of D_2O, the amount of sucrose inside the MACS detector was calculated.

$$(380nl) \cdot \left(\frac{1.7115g}{1.7115g\left(\frac{1ml}{1.59g}\right) + 10ml}\right) = 0.0000587g \tag{A.1}$$

From the amount of sucrose, the amount of protons contained in that amount calculated.

$$(0.0000587g) \cdot \left(\frac{1mole}{342.3g}\right) \cdot \left(\frac{22moleH}{1mole}\right) = 3.77\mu mole \tag{A.2}$$

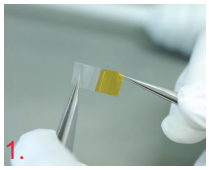
Therefore, 3.77 µmole of H was present in 380 nl of 500 mM sucrose.

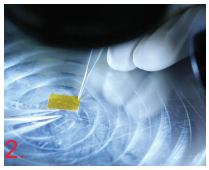
A6 Instructions for liquid sample filling

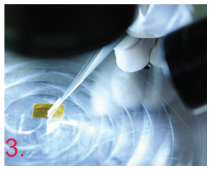
Cut a piece of Applied Biosystems® tape according to the upper area of the MACS chip. Remove the protective foil and keep it ready for the final step, i.e., sealing the sample inside the coil.

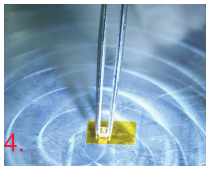
1) Take off one side of the double sided tape using the tweezers.
2) Stick the tape onto the sturdy metal base and bring it under the microscope.
3) Remove the upper cover of the tape.
4) Stick the MACS chip onto the tape with the help of tweezers. Try to ensure that the entire bottom surface of the MACS chip has stuck to the tape
5) Focus the lens on the sample holder (hole) of the MACS chip.
6) Charge the pipette with the sample. Ensure there are no bubbles along the long flexible tip. Fully insert the tip down to the bottom of the sample holder of the MACS chip and smoothly start to dispense the sample.
7) Focusing the microscope onto the bottom of the sample holder, make sure the liquid sample is nicely wetting the bottom of the sample holder. Continue filling the sample holder with the

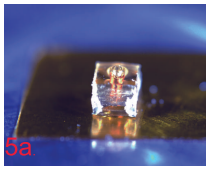
sample trying to remove the pipette tip as the sample holder gets filled up.
8) Upon complete removal of the pipette tip, a small amount of sample overflows onto the surface of the MACS chip.
9) Again make sure there are no bubbles inside.
10) With the help of the very sharp tweezers place the optical adhesive tape from Applied Biosystems® prepared in step 0) onto the top of the MACS chip, and using the flat tip tweezers press against the tape trying to eliminate any air bubble which may tend to get trapped in the sample holder. Seal the sample holder as fast as possible. This step may be very time critical for highly volatile sample (e.g. ethanol, ethanol mixture).
11) Remove the MACS coil from the double sided tape and insert it into a MACS rotor.

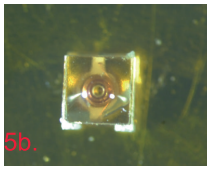


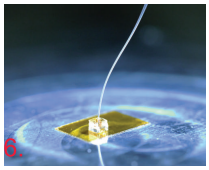


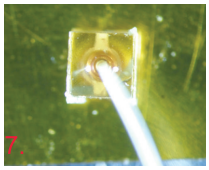


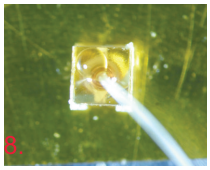


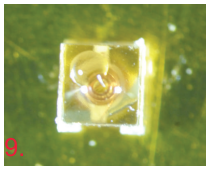


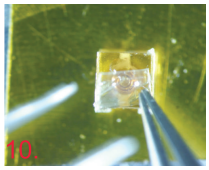


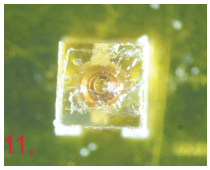












A7 Fabrication process parameters

Plasma cleaning

Pressure: 10 mTorr, O_2 flow rate: 50 sccm, Power: 120 W.

Plasma activation

Pressure: 10 mTorr, O_2 flow rate: 50 sccm, Power: 10 W.

Resist stripping using O_2 Plasma

Pressure: 450 mTorr, O_2 flow rate: 50 sccm, N_2 flow rate: 50 sccm, CF_4 flow rate: 70 sccm, Power: 1200 W, Temperature: 22 °C, Frequency: 2.45 GHz.

Electrodeposition of Gold

Duty cycle: 33%, Current density: 3 mA/mm^2, Deposition rate: 52.1 nm/min, Frequency: 0.67 Hz.

SU-8 3005 processing for 5 µm thick adhesion layer

Spin coating 4 ml of resist

Duration (s)	Acceleration (rpm/s)	Speed (rpm)
10	100	500
60	300	3000
10	500	0

Soft baking

Ramp up or down time (min)	Temperature (°C)	Dwell time (min)
1	95	5
5	22	-

Exposure: 150 mJ/cm^2

Post exposure bake

Ramp up or down time (min)	Temperature (°C)	Dwell time (min)
1	95	2
5	22	-

SU-8 3025 processing for 20 µm **thickness**

Spin coating 4 ml **of resist**

Duration (s)	Acceleration (rpm/s)	Speed (rpm)
10	100	500
60	300	4000
10	500	0

Ramp up or down time (min)	Temperature (°C)	Dwell time (min)
1	95	13
5	22	-

Exposure: 400 mJ/cm^2

Post exposure bake

Ramp up or down time (min)	Temperature (°C)	Dwell time (min)
1	95	5
5	22	-

Standard SU-8 development

Used PGMEA solution: 10 min, Fresh PGMEA solution: 20 min, Isopropanol: 20 min, Dehydration bake on a hotplate at 150 °C: 5 min.

AZ4533 processing for 4 µm **thickness**

Spin coating 4 ml **of resist**

Duration (s)	Acceleration (rpm/s)	Speed (rpm)
10	100	500
30	300	2500
10	500	0

Softbaking: 100 °C for 50 s on a hotplate.

Exposure: 150 mJ/cm^2

Development:AZ 726 MIF (metal ion free) developer for 2 min.

AZ BarLi anti-reflection coating

Spin coating 4 ml **of BarLi**

Duration (s)	Acceleration (rpm/s)	Speed (rpm)
10	100	500
30	300	3000
10	500	0

Baking: 200 °C for 1 min.

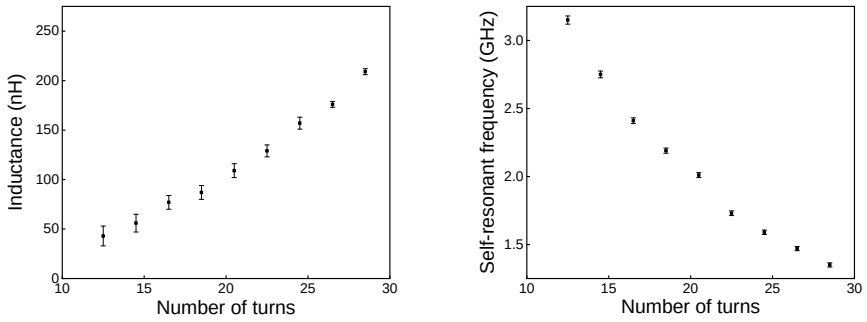
Wafer bonding

Temperature: 55 °C, Duration: 300 min, Force: 5 kN, Cool down duration: 300 min.

Standard cleaning

Acetone: 10 min, Isopropanol: 10 min, Rinse in DI water: 10 min, Dehydration bake on a hotplate at 200 °C: 5 min.

A8 Electrical characterisation of micro-coils

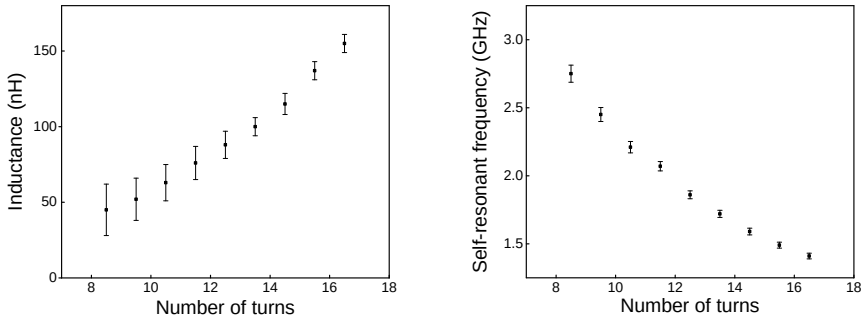


(a) (b)

Figure A.2: The inductance and self-resonant frequencies of various micro-coils fabricated from a 25 µm thick copper wire having a diameter of 550 µm with different number of turns.

The electrical characterization of the micro-coils was performed on an impedance analyzer (Agilent E4991A) connected to a probe station (Cascade Microtech MPS150) set up

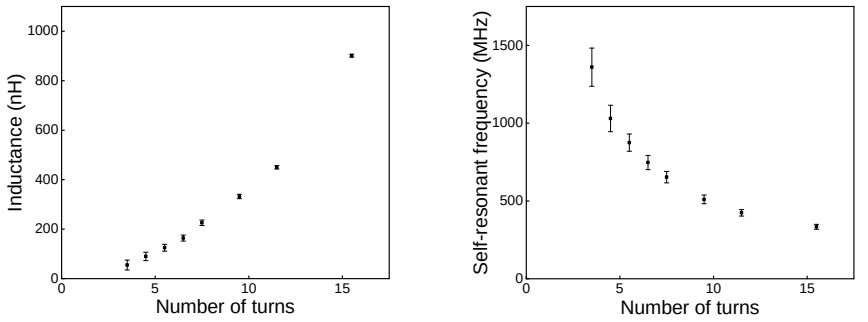
with a Z-probe (Z0-20-K3N-GS-500,Cascade Microtech GmbH). The inductance and self-resonant frequencies of various micro-coils having three different diameters of 550 µm, 850 µm, and 2550 µm respectively fabricated from 25 µm thick copper wire with different number of turns were noted down.



(a) (b)

Figure A.3: The inductance and self-resonant frequencies of various micro-coils fabricated from a 25 µm thick copper wire having a diameter of 850 µm with different number of turns.

Five coils of each type (specific diameter and number of turns) were measured and plotted as shown in the Figure A.2, Figure A.3 and Figure A.4 respectively. The length of micro-coils was fixed at 800 µm, except for coils with number of turns in the range from 3 to 5.



(a) (b)

Figure A.4: The inductance and self-resonant frequencies of various micro-coils fabricated from a 25 µm thick copper wire having a diameter of 2550 µm with different number of turns.

A9 Automated stage

After the SU-8 support structures on the wafer are wirebonded, the NMR sensors are characterized for their self-resonant frequency. To this end, an automated stage system is developed to characterize individual detectors on the wafer as shown in the Figure A.5. [1]

The mechanical assembly consists of an integrated xy-stage on which the wafer chuck is mounted. The wafer is held in place on the chuck using vacuum. The xy-stage facilitates motion of the wafer in a plane. The integrated xy-stage has a travel range 154 mm x 154 mm with a resolution of 1 µm. The diameter of the wafer is 100 mm. Therefore, the travel range is suitable for wafer scale measurements. The integrated XY stage is mounted on the top of a motorized focus block which provides movement in the vertical direction (Z). The focus block allows a travel range of 38 mm with a resolution of 20 nm . The entire setup is connected to the computer through a controller using RS 232 interface. The automated stage has been procured from PRIOR Scientific®. Using MATLAB® as the software interface, the stage movement is controlled and supervised from the control station (computer).

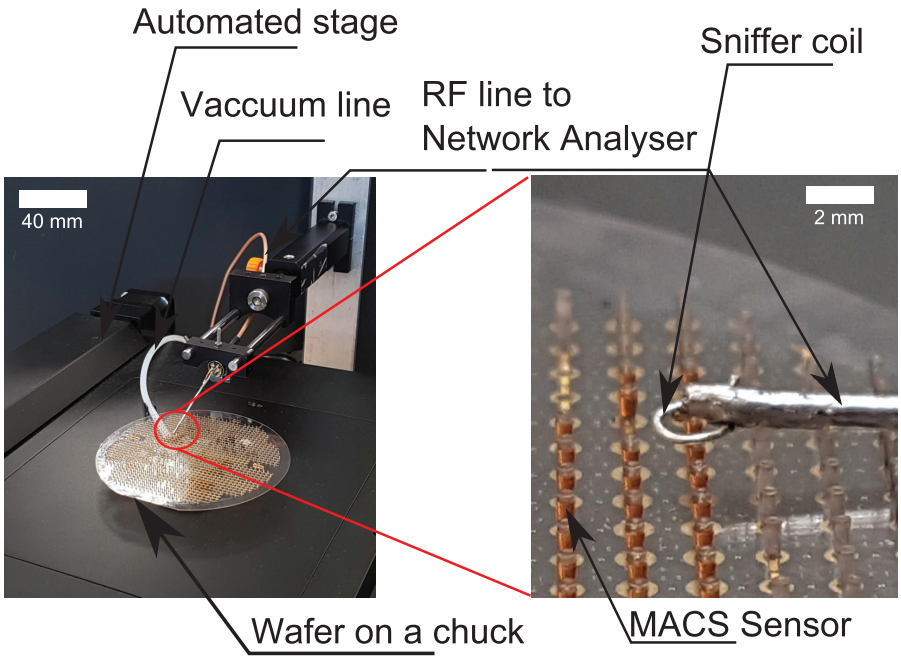


Figure A.5: Automated stage for RF characterization of the NMR sensors at the wafer scale.

The MACS sensors are characterized with the help of a undercoupled sniffer coil using a vector network analyser (E5071C, Keysight® Stuttgart, Germany). The network analyser is connected to the computer with help of USB/GPIB interface and MATLAB®. The sniffer coil which is inductively coupled to the MACS sensor is used to measure the S-parameter

[1] This work was done under the framework of a Master thesis by Pratik Choudhary [247]

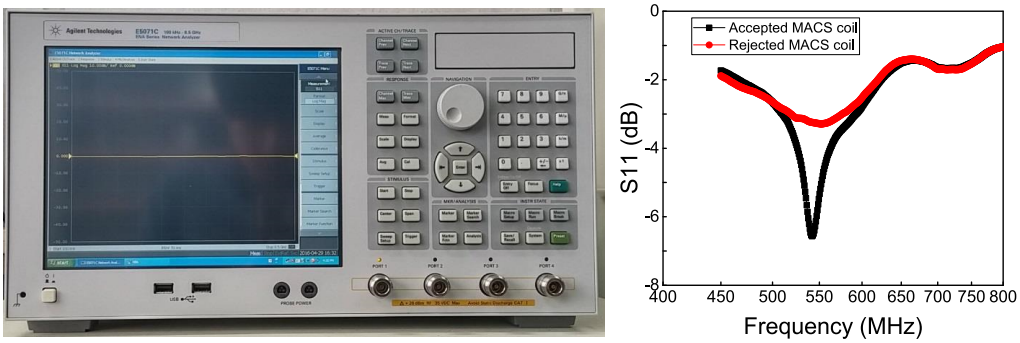


Figure A.6: S-parameter characterization of the NMR sensor using the vector network analyser. The S_{11} measurement differentiates between a working and non-working prototype.

(S_{11}) characteristics of the sensor using the network analyser as shown in the Figure A.6. The acquired data is plotted simultaneously in MATLAB® environment and stored in the computer. From the Figure A.6, it is inferred that a functional NMR sensor is characterized by a dip in S_{11} graph at the resonant frequency whereas the non-functional sensor does not show a significant dip. Moreover, from the S_{11} characterization, the other performance parameters of the NMR sensor, namely, the quality factor, inductance etc. can be derived.

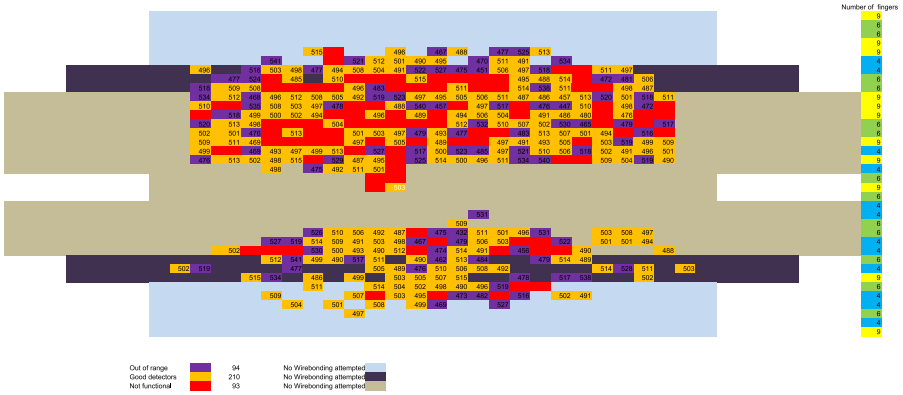
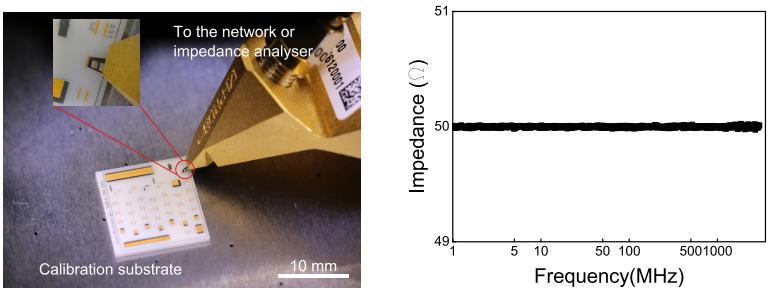


Figure A.7: Mapping of the characterized MACS coils on the wafer. Resonant frequency is in MHz.

The measured NMR sensors are then mapped onto the wafer as shown in the Figure A.7 at their respective positions and the resonant frequency tabulated. After the completion of data acquisition, the NMR sensors are separated into three categories as shown in the Figure A.7. For the test wafer, approx. 300 NMR sensors are fabricated on it. The detectors which satisfy the quality factor criteria (>25) and are close to the target resonance frequency (say, 500 MHz with a tolerance range of ± 3 %) are noted. The map shows that 210 sensors are within the tolerance range between 485 MHz to 515 MHz. These sensors are then followed up with the packaging and NMR characterization. From the collection, NMR sensors which are away

from the tolerance range and the sensors with resonant frequency close to 465 MHz (Larmor frequency of ^{19}F nuclei) are separated. Therefore, the number of sensors that can be recovered is also estimated.

A10 Calibration of Z probes



(a) (b)

Figure A.8: a) Calibration of the Z-probe with an impedance substrate; b) 50 Ω calibration of the Z-probe.

An impedance analyzer (Agilent E4991A) connected to a probe station (Cascade Microtech MPS150) set up with a Z-probe (Z0-20-K3N-GS-500) from Cascade microtech GmbH is used for electrical characterization of the capacitor and micro-coils. Open circuit, closed circuit, and 50 Ω calibration of the Z-probe was carried out prior to measurements using an impedance standard substrate. Figure A.8a shows the Z-probe in contact with the calibration substrate. The calibration substrate contains metal structures in different configurations in open, short and 50 Ω lines. The inductance, capacitance and resistance of each structure are input into the impedance analyser before the calibration process. Following the calibration process, verification is done on the 50 Ω line as shown in the FigureA.8b.

A11 Background signal from SU-8

The background signal that was observed from a blank rotor and SU-8 epoxy which is a constituent part of the MACS device is determined.

A broad peak was observed from SU-8 epoxy between 7-10 ppm as shown in the Figure A.9. The 4 mm zirconia rotor was filled with around five cylindrical blocks of SU-8 which are 1.5 mm thick and 2.85 mm in diameter and the MAS coil was used for excitation and acquisition. For the control experiment, clean empty zirconia rotors were employed.

An additional peak was observed in NMR spectrum of the blank rotor which was not present in the spectrum of the rotor with SU-8. This peak is attributed as a ringing artifact from the high Q MAS probe coil which has been isolated as shown in the Figure A.9b.

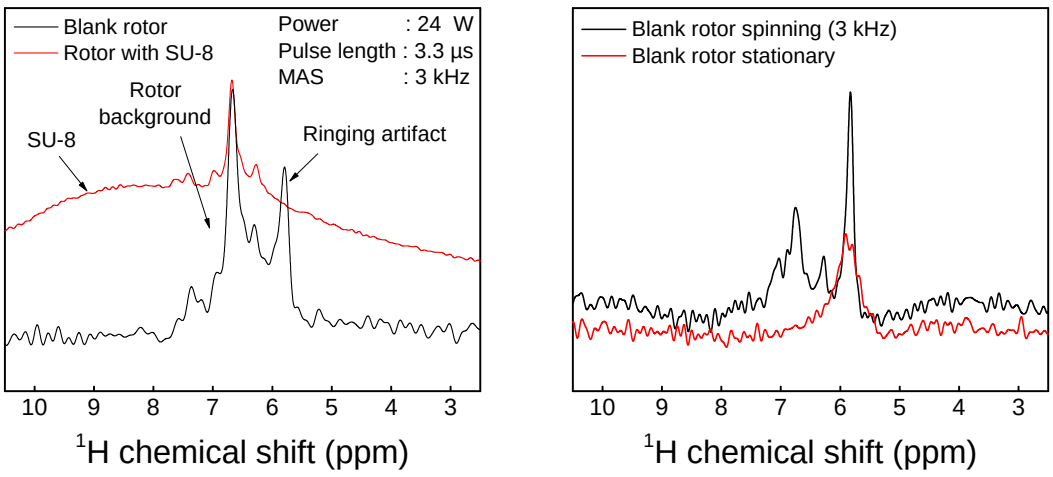


Figure A.9: a) SU-8 background spectrum acquired from five cylindrical blocks of SU-8 using the MAS coil for excitation and acquisition; b) Isolating the ringing artifact from the rotor background. Adapted with permission from [148] Copyright 2019 ©Royal Society of Chemistry.

A12 Process capability index

The process capability index is useful to evaluate the proximity of process performance to its specification limits taking into account natural variations of the process. It is a measure of accuracy and consistency of the process to adhere to its specifications. In the industry which follow six sigma quality control standards [208], Cpk index of ≥ 1.67 is required. However, introduction of new processes usually result in lower values and generally Cpk value of 1.33 is acceptable.

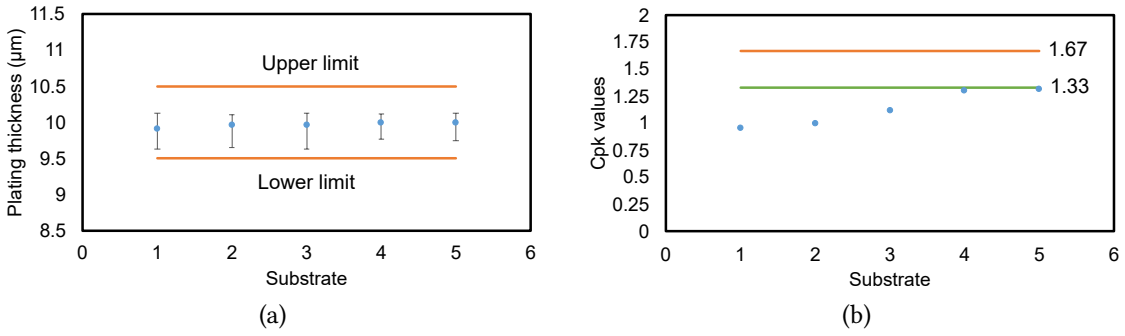
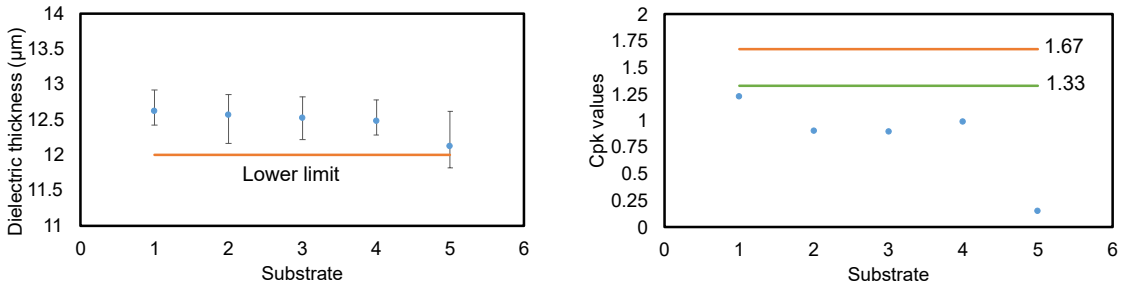
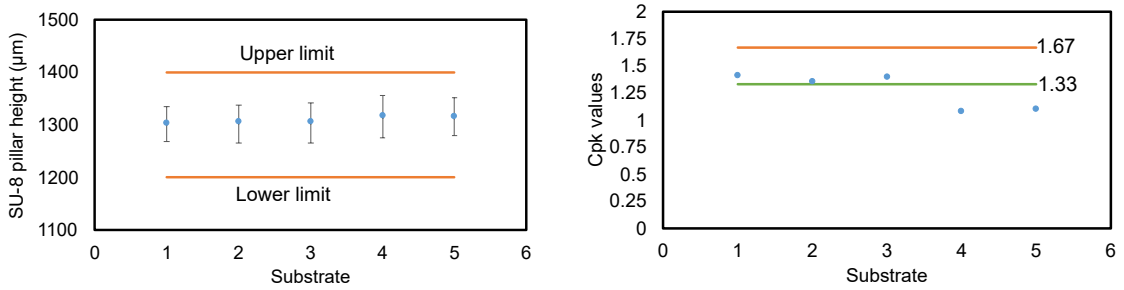


Figure A.10: a) Distribution of gold electroplating thickness for 5 substrates; b) Cpk values for gold electroplating thickness.



(a) (b)

Figure A.11: a) Distribution of dielectric thickness for 5 substrates; b) Cpk values for dielectric thickness.



(a) (b)

Figure A.12: a) Distribution of SU-8 pillar heights in 5 substrates; b) Cpk values for SU-8 pillar height.

The measurement distribution as well as the Cpk trend for the electroplating, dielectric grinding and HAR SU-8 lithography process is illustrated in Figure A.10, Figure A.11 and Figure A.12 respectively. The measurement values show that although the values are within the specification limits, there is significant variation in the process.

A13 Matlab code to generate the bondhead trajectory for a 850 µm coil

```
function coilsPad500

    Diameter = 1650e-6;
Windings = 0.5 + 11;
vTime = 10.2;
DistPerWinding = 85e-6;
```

```
Rotationangle = pi/2;

   vXEndPos = 0e-6;
vYEndPos = 1550e-6;
vZStartPos = 200e-6;
vZSearchPos = 80e-6;

   padSizeX = 400e-6;
padSizeY = 300e-6;
padPostDistanceBlankY = 200E-6;
   corrFactorZup = 0.99;
   corrFactorEnd = 200;
   postDiameter = 500e-6;
postHeight = 1400e-6;
   [postX,postY,postZ] = cylinder;
postX = postX * postDiameter/2;
postX = postX + vXEndPos/2; postY = postY * postDiameter/2;
postY = postY + padSizeY/2 + padPostDistanceBlankY + postDiameter/2; postZ = postZ *
postHeight;
   x.Vmax = 0.95;
x.Amax = 71.1;
x.Rmax = 67028;
y.Vmax = 0.95;
y.Amax = 71.1;
y.Rmax = 67028;
z.Vmax = 1880;
z.Amax = 533.0;
z.Rmax = 502714;
   Ts = 164.5e-6;
f = Windings/vTime;
vRampTime = 0.04;
vRampTicks = round(vRampTime/Ts);
vRampUp = -(1/(vRampTicks^2))*([0:vRampTicks-1] - (vRampTicks)).^2 + 1;
vRampDown = fliplr(vRampUp);
vRampCurve = cumsum(vRampUp);
vDiff = round(vRampCurve(end));
   t = [vRampUp, ones(1,round(vTime/Ts-2*vDiff-corrFactorEnd*vTime/Windings)), vRamp-
Down]; t = cumsum(t*Ts); time = 0:Ts:(length(t)-1)*Ts;
   circleOffset = pi/8;
   x.pos = Diameter/2 * (-1)*sin(2*pi*f*t+circleOffset);
x.pos = x.pos - x.pos(1);
x.pos = [x.pos(1) x.pos];
```

```
x.pos = x.pos + vXEndPos/2 - sin(circleOffset)*Diameter/2;

   y.pos = Diameter/2 * (-1)*cos(2*pi*f*t+circleOffset);
y.pos = y.pos - y.pos(1);
y.pos = [y.pos(1) y.pos];
y.pos = y.pos + padSizeY/2 + padPostDistanceBlankY + postDiameter/2 - (cos(circleOffset)*Diameter/2);

   DistanceZ = Windings*DistPerWinding;
zUpVmax = DistanceZ/vTime(end)*corrFactorZup;

   para.xstart = 0.0;
para.xend = DistanceZ;
para.vmax = zUpVmax;
para.amax = z.Amax;
para.rmax = z.Rmax;
para.drf = 1.0;

   seg = StandardMotionAlgo(para); [tZ, z.jerk, z.acc, z.vel, z.pos] = Movement(seg);

   if length(z.pos) < min(length(x.pos), length(y.pos))
error('z-axis: move too short')
end;
   z.pos = z.pos(1:end-5);

   zonly = length(z.pos) - length(x.pos);
x.pos = [x.pos, ones(1, zonly)*x.pos(end)];
y.pos = [y.pos, ones(1, zonly)*y.pos(end)];

   vPos(1) = 0;
vPos(2) = x.pos(1);
vPara(1) = x.Rmax/3000;
vPara(2) = x.Amax/300;
vPara(3) = x.Vmax;
vPara(4) = Ts; [acc, vel, pos] = int_rtab(GetRedRuckTable(vPos, vPara), Ts); xstart.acc = acc';
xstart.vel = vel'; xstart.pos = pos';
   vPos(1) = x.pos(end);
vPos(2) = vXEndPos;
vPara(1) = x.Rmax/1000;
vPara(2) = x.Amax/10;
vPara(3) = x.Vmax;
vPara(4) = Ts; [acc, vel, pos] = int_rtab(GetRedRuckTable(vPos, vPara), Ts); xend.acc = acc';
xend.vel = vel'; xend.pos = pos' + x.pos(end);
```

```
   vPos(1) = 0;
vPos(2) = y.pos(1);
vPara(1) = y.Rmax/3000;
vPara(2) = y.Amax/300;
vPara(3) = y.Vmax;
vPara(4) = Ts; [acc, vel, pos] = int_rtab(GetRedRuckTable(vPos, vPara), Ts); ystart.acc = acc';
ystart.vel = vel'; ystart.pos = pos';
   vPos(1) = y.pos(end);
vPos(2) = vYEndPos;
vPara(1) = y.Rmax/1000;
vPara(2) = y.Amax/10;
vPara(3) = y.Vmax;
vPara(4) = Ts; [acc, vel, pos] = int_rtab(GetRedRuckTable(vPos, vPara), Ts); yend.acc = acc';
yend.vel = vel'; yend.pos = pos' + y.pos(end);
   vPos(1) = 0;
vPos(2) = vZStartPos;
vPara(1) = z.Rmax/1000;
vPara(2) = z.Amax/10;
vPara(3) = z.Vmax;
vPara(4) = Ts; [acc, vel, pos] = int_rtab(GetRedRuckTable(vPos, vPara), Ts); zstart.acc = acc';
zstart.vel = vel'; zstart.pos = pos'; z.pos = z.pos + zstart.pos(end);
   vPos(1) = z.pos(end);
vPos(2) = vZSearchPos;
vPara(1) = z.Rmax/1000;
vPara(2) = z.Amax/10;
vPara(3) = z.Vmax;
vPara(4) = Ts; [acc, vel, pos] = int_rtab(GetRedRuckTable(vPos, vPara), Ts); zsearch.acc = acc';
zsearch.vel = vel'; zsearch.pos = pos' + z.pos(end);
   xyWait = length(xstart.pos) - length(ystart.pos);
if xyWait < 0
x.begin = [zeros(1,length(zstart.pos)), xstart.pos, ones(1,abs(xyWait)) * xstart.pos(end)];
y.begin = [zeros(1,length(zstart.pos)), ystart.pos];
else
x.begin = [zeros(1,length(zstart.pos)), xstart.pos];
y.begin = [zeros(1,length(zstart.pos)), ystart.pos, ones(1,abs(xyWait)) * ystart.pos(end)];
end

   x.posSize = length(x.begin);
z.posSize = length(zstart.pos);
zWait = x.posSize - z.posSize;
if zWait > 0
z.begin = [zstart.pos, ones(1,zWait) * zstart.pos(end)];
```

```
else
z.begin = zstart.pos;
end

   x.pos = [x.begin x.pos xend.pos];
y.pos = [y.begin y.pos yend.pos];
   z.pos = [z.begin z.pos];
endHeight = z.pos(end)
x.posSize = length(x.pos);
y.posSize = length(y.pos);
z.posSize = length(z.pos);
z.pos = [z.pos, ones(1,max(x.posSize-z.posSize,y.posSize-z.posSize)) * z.pos(end), zsearch.pos];

   x.pos = [x.pos, ones(1, length(z.pos)-length(x.pos))*x.pos(end)];
y.pos = [y.pos, ones(1, length(z.pos)-length(y.pos))*y.pos(end)];

   if Rotationangle > 0
for i=1:length(z.pos)
x.pos1(1,i)=(x.pos(1,i)*cos(Rotationangle)+sin(Rotationangle)*y.pos(1,i));
y.pos1(1,i)=(-1)*x.pos(1,i)*sin(Rotationangle)+cos(Rotationangle)*y.pos(1,i);
end
x.pos=x.pos1;
y.pos=y.pos1;
end;

   x.vel = [diff(x.pos), 0]/Ts;
x.acc = [diff(x.vel), 0]/Ts;
y.vel = [diff(y.pos), 0]/Ts;
y.acc = [diff(y.vel), 0]/Ts;
z.vel = [diff(z.pos), 0]/Ts;
z.acc = [diff(z.vel), 0]/Ts;

   if max(x.vel) > x.Vmax,
plot(x.pos)
plot(x.vel)
error('x-axis: vmax');
end;
if max(x.acc) > x.Amax,
plot(x.acc)
error('x-axis: amax')
end;
if max(y.vel) > y.Vmax,
```

```
plot(y.vel);
error('y-axis: vmax')
end;
if max(y.acc) > y.Amax,
plot(x.acc);
error('y-axis: amax')
end;
if max(z.vel) > z.Vmax,
plot(z.acc);
error('z-axis: vmax')
end;
if max(z.acc) > y.Amax,
plot(z.acc);
error('z-axis: amax')
end;
duration = length(x.pos)*Ts;
entries = length(x.pos);
if entries > 64000,
entries
duration
error('max entries exceeded')
end;

   xx = [x.pos' x.vel' x.acc'];
save('coils_x_table.txt', '-ascii', '-double', 'xx');
yy = [y.pos' y.vel' y.acc']; save('coils_y_table.txt', '-ascii', '-double', 'yy');
zz = [z.pos' z.vel' z.acc']; save('coils_z_table.txt', '-ascii', '-double', 'zz');

   surf(postX, postY, postZ);
hold on
plot3(x.pos, y.pos, z.pos,'Color','red','LineWidth',2);
xlabel(' itx rm-axis (m)')
ylabel(' ity rm-axis (m)')
zlabel(' itz rm-axis (m)')
xlabel(' bfx-axis (m)')
ylabel(' bfy-axis (m)')
zlabel(' bfz-axis (m)')
axis equal
axis equal
hold off
view([0 90])
figure(1)
```

```
view([0 0])

   figure
plot(x.vel)
title('vel')
figure
plot(x.acc)
title('acc')
   figure
comet3(x.pos, y.pos, z.pos);
```

A14 Matlab code to generate the bondhead trajectory for a DSLL coil

```
function coils

   answer=questdlg('Select the coil?', 'Choice', 'Inner', 'Outer', 'Inner');
switch answer
case 'Inner'

   Corrfac2= 0.98
Diameter = 1050e-6;
Windings = 6;
vTime = 4;
DistPerWinding = 100e-6/Corrfac2;
Rotationangle = pi/2;

   vXEndPos = 1260e-6;
vYEndPos = 0e-6;
vZStartPos = 350e-6;
vZSearchPos = 150e-6;

   padSizeX = 300e-6;
padSizeY = 600e-6;
padPostDistanceBlankY = 00e-6;

   corrFactorZup = 0.99;
```

```
    circleOffset = 4.7/4*pi/2;

    corrFactorEnd = 3550;

    postDiameter = 650e-6
postHeight = 1000e-6;

    case 'Outer'
Corrfac2= 1
Diameter = 2950e-6;
Windings = 2
vTime = 1.8;
DistPerWinding = 450e-6/Corrfac2;
Rotationangle = pi/2;

    vXEndPos = 1460e-6;
vYEndPos = 0e-6;
vZStartPos = 200e-6;
vZSearchPos = 230e-6;

    padSizeX = 300e-6;
padSizeY = 600e-6;
padPostDistanceBlankY = 00e-6;

    corrFactorZup = 0.99;

    circleOffset = pi/2;

    corrFactorEnd = 3050;

    postDiameter = 2600e-6;
postHeight = 1000e-6;
end

    [postX,postY,postZ] = cylinder;
postX = postX * postDiameter/2;
postX = postX + vXEndPos/2;
postY = postY * postDiameter/2;
postY = postY + padPostDistanceBlankY;
postZ = postZ * postHeight;
```

```
    x.Vmax = 0.95;
x.Amax = 71.1;
x.Rmax = 67028;
y.Vmax = 0.95;
y.Amax = 71.1;
y.Rmax = 67028;
z.Vmax = 1880;
z.Amax = 533.0;
z.Rmax = 502714;

    Ts = 164.5e-6;
f = Windings/(Corrfac2*vTime);
vRampTime = 0.04;
vRampTicks = round(vRampTime/Ts);
vRampUp = -(1/(vRampTicks^2))*([0:vRampTicks-1] - (vRampTicks))^2 + 1;
vRampDown = fliplr(vRampUp);
vRampCurve = cumsum(vRampUp);
vDiff = round(vRampCurve(end));

    t = [vRampUp, ones(1,round(vTime*Corrfac2/Ts-2*vDiff-corrFactorEnd*vTime*Corrfac2/Windings)),
vRampDown];
t = cumsum(t*Ts);
time = 0:Ts:(length(t)-1)*Ts;

    x.pos = Diameter/2 * (-1)*sin(2*pi*f*t+circleOffset);
x.pos = x.pos - x.pos(1);
x.pos = [x.pos(1) x.pos];
x.pos = x.pos + vXEndPos/2 - sin(circleOffset)*Diameter/2;

    y.pos = Diameter/2 * (-1)*cos(2*pi*f*t+circleOffset);
y.pos = y.pos - y.pos(1);
y.pos = [y.pos(1) y.pos];
y.pos = y.pos + padPostDistanceBlankY - (cos(circleOffset)*Diameter/2);

    DistanceZ = Windings*DistPerWinding;
zUpVmax = DistanceZ/vTime(end)*corrFactorZup;

    para.xstart = 0.0;
para.xend = DistanceZ;
para.vmax = zUpVmax;
para.amax = z.Amax;
para.rmax = z.Rmax;
```

```
para.drf = 1.0;

   seg = StandardMotionAlgo(para); [tZ, z.jerk, z.acc, z.vel, z.pos] = Movement(seg)
   if length(z.pos) < min(length(x.pos), length(y.pos)) error('z-axis: move too short')
end;

   z.pos = z.pos(1:end-5);

   zonly = length(z.pos) - length(x.pos);
x.pos = [x.pos, ones(1, zonly)*x.pos(end)];
y.pos = [y.pos, ones(1, zonly)*y.pos(end)];

   vPos(1) = 0;
vPos(2) = x.pos(1);
vPara(1) = x.Rmax/3000;
vPara(2) = x.Amax/300;
vPara(3) = x.Vmax;
vPara(4) = Ts; [acc, vel, pos] = intrtab(GetRedRuckTable(vPos, vPara), Ts); xstart.acc = acc';
xstart.vel = vel';
xstart.pos = pos';

   vPos(1) = x.pos(end);
vPos(2) = vXEndPos;
vPara(1) = x.Rmax/1000;
vPara(2) = x.Amax/10;
vPara(3) = x.Vmax;
vPara(4) = Ts; [acc, vel, pos] = intrtab(GetRedRuckTable(vPos, vPara), Ts);
xend.acc = acc';
xend.vel = vel';
xend.pos = pos' + x.pos(end);

   vPos(1) = 0;
vPos(2) = y.pos(1);
vPara(1) = y.Rmax/3000;
vPara(2) = y.Amax/300;
vPara(3) = y.Vmax;
vPara(4) = Ts; [acc, vel, pos] = intrtab(GetRedRuckTable(vPos, vPara), Ts); ystart.acc = acc';
ystart.vel = vel';
ystart.pos = pos';

   vPos(1) = y.pos(end);
vPos(2) = vYEndPos;
```

```
vPara(1) = y.Rmax/1000;
vPara(2) = y.Amax/10;
vPara(3) = y.Vmax;
vPara(4) = Ts; [acc, vel, pos] = intrtab(GetRedRuckTable(vPos, vPara), Ts); yend.acc = acc';
yend.vel = vel';
yend.pos = pos' + y.pos(end);

   vPos(1) = 0;
vPos(2) = vZStartPos;
vPara(1) = z.Rmax/1000;
vPara(2) = z.Amax/10;
vPara(3) = z.Vmax;
vPara(4) = Ts; [acc, vel, pos] = intrtab(GetRedRuckTable(vPos, vPara), Ts); zstart.acc = acc';
zstart.vel = vel';
zstart.pos = pos';
z.pos = z.pos + zstart.pos(end);

   vPos(1) = z.pos(end);
vPos(2) = vZSearchPos;
vPara(1) = z.Rmax/3000;
vPara(2) = z.Amax/30;
vPara(3) = z.Vmax;
vPara(4) = Ts; [acc, vel, pos] = intrtab(GetRedRuckTable(vPos, vPara), Ts); zsearch.acc = acc';
zsearch.vel = vel';
zsearch.pos = pos' + z.pos(end);

   xyWait = length(xstart.pos) - length(ystart.pos);
if xyWait < 0
x.begin = [zeros(1,length(zstart.pos)), xstart.pos,
ones(1,abs(xyWait)) * xstart.pos(end)];
y.begin = [zeros(1,length(zstart.pos)), ystart.pos];
else
x.begin = [zeros(1,length(zstart.pos)), xstart.pos];
y.begin = [zeros(1,length(zstart.pos)), ystart.pos,
ones(1,abs(xyWait)) * ystart.pos(end)];
end

   x.posSize = length(x.begin);
z.posSize = length(zstart.pos);
zWait = x.posSize - z.posSize;
if zWait > 0
z.begin = [zstart.pos, ones(1,zWait) * zstart.pos(end)];
```

```
else
z.begin = zstart.pos;
end
   x.pos = [x.begin x.pos xend.pos];
y.pos = [y.begin y.pos yend.pos];

   z.pos = [z.begin z.pos];
endHeight = z.pos(end)
x.posSize = length(x.pos);
y.posSize = length(y.pos);
z.posSize = length(z.pos);
z.pos = [z.pos, ones(1,max(x.posSize-z.posSize,y.posSize-z.posSize)) * z.pos(end), zsearch.pos];

   x.pos = [x.pos, ones(1, length(z.pos)-length(x.pos))*x.pos(end)];
y.pos = [y.pos, ones(1, length(z.pos)-length(y.pos))*y.pos(end)];

   x.vel = [diff(x.pos), 0]/Ts;
x.acc = [diff(x.vel), 0]/Ts;
y.vel = [diff(y.pos), 0]/Ts;
y.acc = [diff(y.vel), 0]/Ts;
z.vel = [diff(z.pos), 0]/Ts;
z.acc = [diff(z.vel), 0]/Ts;

   if max(x.vel) > x.Vmax,
plot(x.pos)
plot(x.vel)
error('x-axis: vmax');
end;
if max(x.acc) > x.Amax,
plot(x.acc)
error('x-axis: amax')
end;
if max(y.vel) > y.Vmax,
plot(y.vel);
error('y-axis: vmax')
end;
if max(y.acc) > y.Amax,
plot(x.acc);
error('y-axis: amax')
end;
if max(z.vel) > z.Vmax,
plot(z.acc);
```

```
error('z-axis: vmax')
end;
if max(z.acc) > y.Amax,
plot(z.acc);
error('z-axis: amax')
end;
duration = length(x.pos)*Ts;
entries = length(x.pos);
if entries > 63999,
entries
duration
error('max entries exceeded')
end;

   xx = [x.pos' x.vel' x.acc'];
save('coilsxtable.txt', '-ascii', '-double', 'xx');
yy = [y.pos' y.vel' y.acc'];
save('coilsytable.txt', '-ascii', '-double', 'yy');
zz = [z.pos' z.vel' z.acc'];
save('coilstable.txt', '-ascii', '-double', 'zz');

   figure surf(postX, postY, postZ);
hold on
plot3(x.pos, y.pos, z.pos,'Color','red','LineWidth',2);
xlabel(' itx rm-axis (m)')
ylabel(' ity rm-axis (m)')
zlabel(' itz rm-axis (m)')
xlabel(' bfx-axis (m)')
ylabel(' bfy-axis (m)')
zlabel(' bfz-axis (m)')
axis equal
axis equal
hold off
view([0 90])
figure(1)
```

A15 Wire bonder parameters for copper wire

The Table A.2 lists the process parameters used to wind the micro-coils around SU-8 posts.

Table A.2: Wirebonder parameters

Pyrex wafer (525 μm)				
Wedge Bond				
Bond mode	Engineering			
	Impact segment 1	Impact segment 2	Bond segment 1	Bond segment 2
Duration segment	2 ms	2 ms	2 ms	2 ms
Force end	600 mN	600 mN	700 mN	450 mN
Ultrasonic Power	0 %	0 %	0%	35 %
Ultrasonic rise time	0.7 ms	0.7 ms	2 ms	3 ms
Control Mode	Force	Force	Force	Force
Slow impact factor		0.5		
Scrub Distance		- 5 μm	- 8 μm	0 μm
Scrub angle		0°	0°	
Number of scrubs		0	0	0

Process Temperature	
Heater Temperature	150° C
Nitrogen flow rate	
Flow rate	47 l/min

Free air ball	
EFO mode	Manual
Electrode to wire distance	500 μm
Pre-spark voltage	4500 V
Spark segments	1
EFO mode current	110.15 mA
EFO time	0.5500 ms
Tail length	500 μm

Ball Bond	
Bond mode	Standard
Impact force	800 mN
Bond force	300 mN
Ultrasonic power	90%
Bond time	30 ms
Bond force dwell time	0 ms
Ultrasonic rise time	1 ms
Ultrasonic rapid decay	off
Scrub	off

Looping	
Loop mode	Advanced loop
Loop type	Quality arc
Loop shape	coils

Bibliography

[1] F. Bloch, W. W. Hansen, and M. Packard, "Nuclear induction," *Phys. Rev.*, vol. 69, pp. 127–127, Feb 1946.

[2] E. M. Purcell, H. C. Torrey, and R. V. Pound, "Resonance absorption by nuclear magnetic moments in a solid," *Phys. Rev.*, vol. 69, pp. 37–38, Jan 1946.

[3] M. E. Lacey, R. Subramanian, D. L. Olson, A. G. Webb, and J. V. Sweedler, "High-resolution NMR spectroscopy of sample volumes from 1 nl to 10 μl," *Chemical Reviews*, vol. 99, no. 10, pp. 3133–3152, 1999.

[4] D. Hoult and R. Richards, "The signal-to-noise ratio of the nuclear magnetic resonance experiment," *Journal of Magnetic Resonance*, vol. 24, no. 1, pp. 71 – 85, 1976.

[5] A. Samoson, T. Tuherm, J. Past, A. Reinhold, T. Anupõld, and I. Heinmaa, *New Horizons for Magic-Angle Spinning NMR*, pp. 15–31. Berlin, Heidelberg: Springer Berlin Heidelberg, 2005.

[6] A. P. M. Kentgens, J. Bart, P. J. M. van Bentum, A. Brinkmann, E. R. H. van Eck, J. G. E. Gardeniers, J. W. G. Janssen, P. Knijn, S. Vasa, and M. H. W. Verkuijlen, "High-resolution liquid- and solid-state nuclear magnetic resonance of nanoliter sample volumes using microcoil detectors," *The Journal of Chemical Physics*, vol. 128, no. 5, p. 052202, 2008.

[7] A. Webb, D. Olson, T. Peck, J. Sweedler, and R. Magin, "Development of a solenoidal nanoliter-volume RF coil for NMR," *Bulletin of Magnetic Resonance*, vol. 17, no. 1, pp. 214–215, 1995.

[8] A. Webb, "Radiofrequency microcoils in magnetic resonance," *Progress in Nuclear Magnetic Resonance Spectroscopy*, vol. 31, no. 1, pp. 1–42, 1997.

[9] H. Janssen, A. Brinkmann, E. R. H. van Eck, P. J. M. van Bentum, and A. P. M. Kentgens, "Microcoil high-resolution magic angle spinning NMR spectroscopy," *Journal of the American Chemical Society*, vol. 128, no. 27, pp. 8722–8723, 2006.

[10] D. Sakellariou, G. L. Goff, and J.-F. Jacquinot, "High-resolution, high-sensitivity NMR of nanolitre anisotropic samples by coil spinning," *Nature*, vol. 447, pp. 694–697, June 2007.

[11] V. Badilita, B. Fassbender, K. Kratt, A. Wong, C. Bonhomme, D. Sakellariou, J. G. Korvink, and U. Wallrabe, "Microfabricated inserts for magic angle coil spinning (MACS) wireless NMR spectroscopy," *PLoS ONE*, vol. 7, p. e42848, 08 2012.

[12] A. Abragam, *The Principles of Nuclear Magnetism.* Clarendon Press, Oxford, 1961.

[13] M. H. Levitt, *Spin dynamics: basics of nuclear magnetic resonance.* New York, USA: John Wiley & Sons, 2001.

[14] J. Keeler, *Understanding NMR spectroscopy.* John Wiley & Sons, 2011.

[15] J. Mispelter, M. Lupu, and A. Briguet, *NMR Probeheads for Biophysical and Biomedical Experiments.* Imperial College Press, 2006.

[16] E. R. Andrew, A. Bradbury, and R. G. Eades, "Nuclear magnetic resonance spectra from a crystal rotated at high speed," *Nature*, vol. 182, pp. 1659–1659, Dec. 1958.

[17] I. J. Lowe, "Free induction decays of rotating solids," *Phys. Rev. Lett.*, vol. 2, pp. 285–287, Apr 1959.

[18] E. D. Ostroff and J. S. Waugh, "Multiple spin echoes and spin locking in solids," *Phys. Rev. Lett.*, vol. 16, pp. 1097–1098, Jun 1966.

[19] P. Mansfield and D. Ware, "Nuclear resonance line narrowing in solids by repeated short pulse RF irradiation," *Physics Letters*, vol. 22, no. 2, pp. 133–135, 1966.

[20] B. Gerstein, R. Pembleton, R. Wilson, and L. Ryan, "High resolution NMR in randomly oriented solids with homonuclear dipolar broadening: combined multiple pulse NMR and magic angle spinning," *The Journal of Chemical Physics*, vol. 66, no. 1, pp. 361–362, 1977.

[21] A. Pines, M. G. Gibby, and J. S. Waugh, "Proton-enhanced nuclear induction spectroscopy. a method for high resolution NMR of dilute spins in solids," *The Journal of Chemical Physics*, vol. 56, no. 4, pp. 1776–1777, 1972.

[22] A. Pines, M. G. Gibby, and J. S. Waugh, "Proton-enhanced NMR of dilute spins in solids," *The Journal of Chemical Physics*, vol. 59, no. 2, pp. 569–590, 1973.

[23] S. R. Hartmann and E. L. Hahn, "Nuclear double resonance in the rotating frame," *Phys. Rev.*, vol. 128, pp. 2042–2053, Dec 1962.

[24] J. Schaefer and E. Stejskal, "Carbon-13 nuclear magnetic resonance of polymers spinning at the magic angle," *Journal of the American Chemical Society*, vol. 98, no. 4, pp. 1031–1032, 1976.

[25] A. McDermott, F. Creuzet, A. Kolbert, and R. Griffin, "High-resolution magic-angle-spinning NMR spectra of protons in deuterated solids," *Journal of Magnetic Resonance (1969)*, vol. 98, no. 2, pp. 408 – 413, 1992.

[26] M. Maricq and J. S. Waugh, "NMR in rotating solids," *The Journal of Chemical Physics*, vol. 70, no. 7, pp. 3300–3316, 1979.

[27] J. Herzfeld and A. E. Berger, "Sideband intensities in NMR spectra of samples spinning at the magic angle," *The Journal of Chemical Physics*, vol. 73, no. 12, pp. 6021–6030, 1980.

[28] T. Polenova, R. Gupta, and A. Goldbourt, "Magic angle spinning NMR spectroscopy: a versatile technique for structural and dynamic analysis of solid-phase systems," *Analytical Chemistry*, pp. 5458–5469, 2015.

[29] U. Haeberlen and J. S. Waugh, "Coherent averaging effects in magnetic resonance," *Phys. Rev.*, vol. 175, pp. 453–467, Nov 1968.

[30] A. Böckmann, M. Ernst, and B. H. Meier, "Spinning proteins, the faster, the better?," *Journal of Magnetic Resonance*, vol. 253, pp. 71 – 79, 2015. Special Issue: Recent Achievements and New Directions in Biomolecular Solid State NMR.

[31] A. Samoson, T. Tuherm, J. Past, A. Reinhold, T. Anupõld, and I. Heinmaa, "100+ kHz MAS NMR," in *EUROMAR 2012, in: Magnetic Resonance Conference; 1–5 July: University College. Dublin, Ireland*, p. 247, July 2012.

[32] Q. Y. Yue, M. Malon, C. Martineau, F. Taulelle, and Y. Nishiyama, "Rapid measurement of multidimensional ^1H solid-state NMR spectra at ultra-fast MAS frequencies," *Journal of Magnetic Resonance*, vol. 239, no. Supplement C, pp. 75 – 80, 2014.

[33] S. Penzel, A. Oss, M.-L. Org, A. Samoson, A. Böckmann, M. Ernst, and B. H. Meier, "Spinning faster: protein NMR at MAS frequencies up to 126 kHz," *Journal of Biomolecular NMR*, vol. 73, pp. 19–29, Feb 2019.

[34] Y.-L. Lin, Y.-S. Cheng, C.-I. Ho, Z.-H. Guo, S.-J. Huang, M.-L. Org, A. Oss, A. Samoson, and J. C. C. Chan, "Preparation of fibril nuclei of beta-amyloid peptides in reverse micelles," *Chem. Commun.*, vol. 54, pp. 10459–10462, 2018.

[35] A. Samoson, "H-MAS," *Journal of Magnetic Resonance*, vol. 306, pp. 167 – 172, 2019.

[36] J. R. Lewandowski, J.-N. Dumez, U. Akbey, S. Lange, L. Emsley, and H. Oschkinat, "Enhanced resolution and coherence lifetimes in the solid-state NMR spectroscopy of perdeuterated proteins under ultrafast magic-angle spinning," *The Journal of Physical Chemistry Letters*, vol. 2, no. 17, pp. 2205–2211, 2011.

[37] A. Lesage, "Recent advances in solid-state NMR spectroscopy of spin I = 1/2 nuclei," *Phys. Chem. Chem. Phys.*, vol. 11, pp. 6876–6891, 2009.

[38] S. E. Ashbrook, "Recent advances in solid-state NMR spectroscopy of quadrupolar nuclei," *Phys. Chem. Chem. Phys.*, vol. 11, pp. 6892–6905, 2009.

[39] E. Kundla, A. Samoson, and E. Lippmaa, "High-resolution NMR of quadrupolar nuclei in rotating solids," *Chemical Physics Letters*, vol. 83, no. 2, pp. 229 – 232, 1981.

[40] A. Samoson and A. Pines, "Double rotor for solid-state NMR," *Review of Scientific Instruments*, vol. 60, no. 10, pp. 3239–3241, 1989.

[41] Y. Wu, B. Sun, A. Pines, A. Samoson, and E. Lippmaa, "NMR experiments with a new double rotor," *Journal of Magnetic Resonance (1969)*, vol. 89, no. 2, pp. 297 – 309, 1990.

[42] K. Mueller, B. Sun, G. Chingas, J. Zwanziger, T. Terao, and A. Pines, "Dynamic-angle spinning of quadrupolar nuclei," *Journal of Magnetic Resonance (1969)*, vol. 86, no. 3, pp. 470 – 487, 1990.

[43] L. Frydman and J. S. Harwood, "Isotropic spectra of half-integer quadrupolar spins from bidimensional magic-angle spinning NMR," *Journal of the American Chemical Society*, vol. 117, no. 19, pp. 5367–5368, 1995.

[44] Z. Gan, "Isotropic NMR spectra of half-integer quadrupolar nuclei using satellite transitions and magic-angle spinning," *Journal of the American Chemical Society*, vol. 122, no. 13, pp. 3242 – 3243, 2000.

[45] A. Samoson, *Extended magic-angle spinning. In: The encyclopedia of nuclear magnetic resonance*, vol. 9. Advances in NMR. John Wiley & Sons, 2002.

[46] S. S. Adhikari, U. Wallrabe, V. Badilita, and J. G. Korvink, "Capacitor re-design overcomes the rotation rate limit of MACS resonators," *Concepts in Magnetic Resonance Part B: Magnetic Resonance Engineering*, vol. 47B, no. 4, p. e21362, 2018.

[47] Bruker, "Bruker supplies NMR spectrometers for protein research," 2021.

[48] A. W. Overhauser, "Polarization of nuclei in metals," *Phys. Rev.*, vol. 92, pp. 411–415, Oct 1953.

[49] T. Carver and C. Slichter, "Polarization of nuclear spins in metals," *Physical Review*, vol. 92, no. 1, pp. 212–213, 1953.

[50] A. Abragam and M. Goldman, "Principles of dynamic nuclear polarisation," *Reports on Progress in Physics*, vol. 41, pp. 395–467, mar 1978.

[51] M. Afeworki, R. A. McKay, and J. Schaefer, "Selective observation of the interface of heterogeneous polycarbonate/polystyrene blends by dynamic nuclear polarization carbon-13 NMR spectroscopy," *Macromolecules*, vol. 25, no. 16, pp. 4084–4091, 1992.

[52] R. Wind, F. Anthonio, M. Duijvestijn, J. Smidt, J. Trommel, and G. de Vette, "Experimental setup for enhanced ^{13}C NMR spectroscopy in solids using dynamic nuclear polarization," *Journal of Magnetic Resonance (1969)*, vol. 52, no. 3, pp. 424 – 434, 1983.

[53] D. Singel, H. Seidel, R. Kendrick, and C. Yannoni, "A spectrometer for EPR, DNP, and multinuclear high-resolution NMR," *Journal of Magnetic Resonance (1969)*, vol. 81, no. 1, pp. 145 – 161, 1989.

[54] L. R. Becerra, G. J. Gerfen, R. J. Temkin, D. J. Singel, and R. G. Griffin, "Dynamic nuclear polarization with a cyclotron resonance maser at 5 T," *Physical Review Letters*, vol. 71, no. 21, p. 3561, 1993.

[55] K. Kreischer, C. Farrar, R. Griffin, R. Temkin, and J. Vieregg, "The development of a 250 GHz cw gyrotron for EPR and NMR spectroscopy," in *Proceedings of the 24th International Conference on Infrared and Millimeter Waves, UC Davis, Monterey, CA*, 1999.

[56] A. C. Torrezan, S.-T. Han, M. A. Shapiro, J. R. Sirigiri, and R. J. Temkin, "CW operation of a tunable 330/460 GHz gyrotron for enhanced nuclear magnetic resonance," in *2008 33rd International Conference on Infrared, Millimeter and Terahertz Waves*, pp. 1–2, IEEE, 2008.

[57] A. C. Torrezan, S.-T. Han, I. Mastovsky, M. A. Shapiro, J. R. Sirigiri, R. J. Temkin, A. B. Barnes, and R. G. Griffin, "Continuous-wave operation of a frequency-tunable 460-GHz second-harmonic gyrotron for enhanced nuclear magnetic resonance," *IEEE Transactions on Plasma Science*, vol. 38, no. 6, pp. 1150–1159, 2010.

[58] T. Maly, G. T. Debelouchina, V. S. Bajaj, K.-N. Hu, C.-G. Joo, M. L. Mak–Jurkauskas, J. R. Sirigiri, P. C. A. van der Wel, J. Herzfeld, R. J. Temkin, and R. G. Griffin, "Dynamic nuclear polarization at high magnetic fields," *The Journal of Chemical Physics*, vol. 128, no. 5, p. 052211, 2008.

[59] A. B. Barnes, G. De Paëpe, P. C. A. van der Wel, K.-N. Hu, C.-G. Joo, V. S. Bajaj, M. L. Mak-Jurkauskas, J. R. Sirigiri, J. Herzfeld, R. J. Temkin, and R. G. Griffin, "High-field dynamic nuclear polarization for solid and solution biological NMR," *Applied Magnetic Resonance*, vol. 34, pp. 237–263, Aug 2008.

[60] G. T. Debelouchina, M. J. Bayro, P. C. A. van der Wel, M. A. Caporini, A. B. Barnes, M. Rosay, W. E. Maas, and R. G. Griffin, "Dynamic nuclear polarization-enhanced solid-state NMR spectroscopy of GNNQQNY nanocrystals and amyloid fibrils," *Phys. Chem. Chem. Phys.*, vol. 12, pp. 5911–5919, 2010.

[61] K.-N. Hu, H.-h. Yu, T. M. Swager, and R. G. Griffin, "Dynamic nuclear polarization with biradicals," *Journal of the American Chemical Society*, vol. 126, no. 35, pp. 10844–10845, 2004.

[62] C. Song, K.-N. Hu, C.-G. Joo, T. M. Swager, and R. G. Griffin, "TOTAPOL: a biradical polarizing agent for dynamic nuclear polarization experiments in aqueous media," *Journal of the American Chemical Society*, vol. 128, no. 35, pp. 11385–11390, 2006.

[63] C. Sauvée, M. Rosay, G. Casano, F. Aussenac, R. T. Weber, O. Ouari, and P. Tordo, "Highly efficient, water-soluble polarizing agents for dynamic nuclear polarization at high frequency," *Angewandte Chemie International Edition*, vol. 52, no. 41, pp. 10858–10861, 2013.

[64] G. Mathies, M. A. Caporini, V. K. Michaelis, Y. Liu, K.-N. Hu, D. Mance, J. L. Zweier, M. Rosay, M. Baldus, and R. G. Griffin, "Efficient dynamic nuclear polarization at 800 MHz/527 GHz with trityl-nitroxide biradicals," *Angewandte Chemie International Edition*, vol. 54, no. 40, pp. 11770–11774, 2015.

[65] P. Chen, B. J. Albert, C. Gao, N. Alaniva, L. E. Price, F. J. Scott, E. P. Saliba, E. L. Sesti, P. T. Judge, E. W. Fisher, *et al.*, "Magic angle spinning spheres," *Science advances*, vol. 4, no. 9, p. eaau1540, 2018.

[66] P.-H. Chen, C. Gao, and A. B. Barnes, "Perspectives on microwave coupling into cylindrical and spherical rotors with dielectric lenses for magic angle spinning dynamic nuclear polarization," *Journal of Magnetic Resonance*, vol. 308, p. 106518, 2019.

[67] P.-H. Chen, C. Gao, L. E. Price, M. A. Urban, T. M. O. Popp, and A. B. Barnes, "Two millimeter diameter spherical rotors spinning at 68 kHz for MAS NMR," *Journal of Magnetic Resonance*, vol. 8-9, p. 100015, 2021.

[68] J. Natterer and J. Bargon, "Parahydrogen induced polarization," *Progress in Nuclear Magnetic Resonance Spectroscopy*, vol. 31, no. 4, pp. 293 – 315, 1997.

[69] C. Bowers and D. Weitekamp, "Transformation of symmetrization order to nuclear-spin magnetization by chemical reaction and nuclear magnetic resonance," *Physical Review Letters*, vol. 57, no. 21, pp. 2645–2648, 1986.

[70] T. Eisenschmid, R. Kirss, P. Deutsch, S. Hommeltoft, R. Eisenberg, J. Bargon, R. Lawler, and A. Balch, "Para hydrogen induced polarization in hydrogenation reactions," *Journal of the American Chemical Society*, vol. 109, no. 26, pp. 8089–8091, 1987.

[71] C. Bowers and D. Weitekamp, "Parahydrogen and synthesis allow dramatically enhanced nuclear alignment," *Journal of the American Chemical Society*, vol. 109, no. 18, pp. 5541–5542, 1987.

[72] M. G. Pravica and D. P. Weitekamp, "Net NMR alignment by adiabatic transport of parahydrogen addition products to high magnetic field," *Chemical Physics Letters*, vol. 145, no. 4, pp. 255 – 258, 1988.

[73] S. B. Duckett and R. E. Mewis, "Application of para hydrogen induced polarization techniques in NMR spectroscopy and imaging," *Accounts of chemical research*, vol. 45, no. 8, pp. 1247–1257, 2012.

[74] R. Adams, J. Aguilar, K. Atkinson, M. Cowley, P. Elliott, S. Duckett, G. Green, I. Khazal, J. Lopez-Serrano, and D. Williamson, "Reversible interactions with para-hydrogen enhance NMR sensitivity by polarization transfer," *Science*, vol. 323, no. 5922, pp. 1708–1711, 2009.

[75] L. Bordonali, N. Nordin, E. Fuhrer, N. MacKinnon, and J. G. Korvink, "Parahydrogen based NMR hyperpolarisation goes micro: an alveolus for small molecule chemosensing," *Lab Chip*, vol. 19, pp. 503–512, 2019.

[76] J. Eills, W. Hale, M. Sharma, M. Rossetto, M. H. Levitt, and M. Utz, "High-resolution nuclear magnetic resonance spectroscopy with picomole sensitivity by hyperpolarization on a chip," *Journal of the American Chemical Society*, vol. 141, no. 25, pp. 9955–9963, 2019.

[77] A. Grünberg, X. Yeping, H. Breitzke, and G. Buntkowsky, "Solid-state NMR characterization of wilkinson's catalyst immobilized in mesoporous SBA-3 silica," *Chemistry – A European Journal*, vol. 16, no. 23, pp. 6993–6998, 2010.

[78] T. Gutmann, T. Ratajczyk, Y. Xu, H. Breitzke, A. Grünberg, S. Dillenberger, U. Bommerich, T. Trantzschel, J. Bernarding, and G. Buntkowsky, "Understanding the leaching properties of heterogenized catalysts: A combined solid-state and PHIP NMR study," *Solid State Nuclear Magnetic Resonance*, vol. 38, no. 4, pp. 90 – 96, 2010.

[79] T. Room, S. Appelt, R. Seydoux, E. Hahn, A. Pines, and E. Hahn, "Enhancement of surface NMR by laser-polarized noble gases," *Physical Review B - Condensed Matter and Materials Physics*, vol. 55, no. 17, pp. 11604–11610, 1997. cited By 68.

[80] T. G. Walker and W. Happer, "Spin-exchange optical pumping of noble-gas nuclei," *Rev. Mod. Phys.*, vol. 69, pp. 629–642, Apr 1997.

[81] G. Navon, Y. Song, T. Room, S. Appelt, R. E. Taylor, and A. Pines, "Enhancement of solution NMR and MRI with laser-polarized Xenon," *Science*, vol. 271, no. 5257, pp. 1848–1851, 1996.

[82] D. Raftery, E. MacNamara, G. Fisher, C. V. Rice, and J. Smith, "Optical pumping and magic angle spinning: Sensitivity and resolution enhancement for surface NMR obtained with laser-polarized xenon," *Journal of the American Chemical Society*, vol. 119, no. 37, pp. 8746–8747, 1997.

[83] E. Brunner, R. Seydoux, M. Haake, A. Pines, and J. Reimer, "Surface NMR using laser-polarized ^{129}Xe under magic angle spinning conditions," *Journal of Magnetic Resonance*, vol. 130, no. 1, pp. 145 – 148, 1998.

[84] J. P. King, P. J. Coles, and J. A. Reimer, "Optical polarization of ^{13}C nuclei in diamond through nitrogen vacancy centers," *Phys. Rev. B*, vol. 81, p. 073201, Feb 2010.

[85] T. Staudacher, F. Shi, S. Pezzagna, J. Meijer, J. Du, C. A. Meriles, F. Reinhard, and J. Wrachtrup, "Nuclear magnetic resonance spectroscopy on a 5 nm^3 sample volume," *Science*, vol. 339, no. 6119, pp. 561–563, 2013.

[86] H. J. Mamin, M. Kim, M. H. Sherwood, C. T. Rettner, K. Ohno, D. D. Awschalom, and D. Rugar, "Nanoscale nuclear magnetic resonance with a nitrogen-vacancy spin sensor," *Science*, vol. 339, no. 6119, pp. 557–560, 2013.

[87] R. Schirhagl, K. Chang, M. Loretz, and C. L. Degen, "Nitrogen-vacancy centers in diamond: Nanoscale sensors for physics and biology," *Annual Review of Physical Chemistry*, vol. 65, no. 1, pp. 83–105, 2014.

[88] M. Loretz, S. Pezzagna, J. Meijer, and C. L. Degen, "Nanoscale nuclear magnetic resonance with a 1.9-nm-deep nitrogen-vacancy sensor," *Applied Physics Letters*, vol. 104, no. 3, p. 033102, 2014.

[89] J. A. Sidles, "Noninductive detection of single proton magnetic resonance," *Applied Physics Letters*, vol. 58, no. 24, pp. 2854–2856, 1991.

[90] Y. S. Greenberg, "Application of superconducting quantum interference devices to nuclear magnetic resonance," *Rev. Mod. Phys.*, vol. 70, pp. 175–222, Jan 1998.

[91] I. M. Savukov and M. V. Romalis, "NMR detection with an atomic magnetometer," *Phys. Rev. Lett.*, vol. 94, p. 123001, Mar 2005.

[92] D. Hoult, "The NMR receiver: a description and analysis of design," *Progress in Nuclear Magnetic Resonance Spectroscopy*, vol. 12, no. 1, pp. 41–77, 1978.

[93] D. L. Olson, T. L. Peck, A. G. Webb, R. L. Magin, and J. V. Sweedler, "High-resolution microcoil ^1H-NMR for mass-limited, nanoliter-volume samples," *Science*, vol. 270, no. 5244, pp. 1967–1970, 1995.

[94] D. L. Olson, M. E. Lacey, and J. V. Sweedler, "High-resolution microcoil NMR for analysis of mass-limited, nanoliter samples," *Analytical chemistry*, vol. 70, no. 3, pp. 645–650, 1998.

[95] D. L. Olson, M. E. Lacey, and J. V. Sweedler, "The nanoliter niche," *Analytical chemistry (Washington, DC)*, vol. 70, no. 7, pp. 257A–264A, 1998.

[96] R. Black, T. Early, P. Roemer, O. Mueller, A. Mogro-Campero, L. Turner, and G. Johnson, "A high-temperature superconducting receiver for nuclear magnetic resonance microscopy," *Science*, vol. 259, no. 5096, pp. 793–795, 1993.

[97] H. Hill, "Improved sensitivity of NMR spectroscopy probes by use of high-temperature superconductive detection coils," *Applied Superconductivity, IEEE Transactions on*, vol. 7, pp. 3750–3755, June 1997.

[98] C. Koo, R. F. Godley, M. P. McDougall, S. M. Wright, and A. Han, "A microfluidically cryocooled spiral microcoil with inductive coupling for MR microscopy," *IEEE Transactions on Biomedical Engineering*, vol. 61, pp. 76–84, Jan 2014.

[99] K. Takeda, "Microcoils and microsamples in solid-state NMR," *Solid State Nuclear Magnetic Resonance*, vol. 47-48, pp. 1 – 9, 2012.

[100] K. Yamauchi, J. Janssen, and A. Kentgens, "Implementing solenoid microcoils for wide-line solid-state NMR," *Journal of Magnetic Resonance*, vol. 167, no. 1, pp. 87 – 96, 2004.

[101] E. W. Hagaman, J. Jiao, and T. Moore, "The generation of intense radiofrequency fields in μcoils," *Journal of Magnetic Resonance*, vol. 193, no. 1, pp. 150 – 152, 2008.

[102] T. Peck, R. Magin, and P. Lauterbur, "Design and analysis of microcoils for NMR microscopy," *Journal of Magnetic Resonance, Series B*, vol. 108, no. 2, pp. 114 – 124, 1995.

[103] L. Fuks, F. Huang, C. Carter, W. Edelstein, and P. Roemer, "Susceptibility, lineshape, and shimming in high-resolution NMR," *Journal of Magnetic Resonance (1969)*, vol. 100, no. 2, pp. 229–242, 1992.

[104] R. Kc, Y. N. Gowda, D. Djukovic, I. D. Henry, G. H. Park, and D. Raftery, "Susceptibility-matched plugs for microcoil NMR probes," *Journal of Magnetic Resonance*, vol. 205, no. 1, pp. 63–68, 2010.

[105] W. G. Clark, "Pulsed nuclear resonance apparatus," *Review of Scientific Instruments*, vol. 35, no. 3, pp. 316–333, 1964.

[106] R. M. Fratila and A. H. Velders, "Small-volume nuclear magnetic resonance spectroscopy," *Annual Review of Analytical Chemistry*, vol. 4, no. 1, pp. 227–249, 2011. PMID: 21391818.

[107] A. Webb, "Radiofrequency microcoils for magnetic resonance imaging and spectroscopy," *Journal of Magnetic Resonance*, vol. 229, pp. 55–66, 2013. Frontiers of In Vivo and Materials MRI Research.

[108] J. Korvink, V. Badilita, D. Mager, O. Gruschke, N. Spengler, S. Sundar Adhikari Parenky, U. Wallrabe, and M. Meissner, *Innovative Coil Fabrication Techniques for Miniaturized Magnetic Resonance Detectors*, ch. 5, pp. 109–141. John Wiley and Sons, Ltd, 2018.

[109] J. A. Rogers, R. J. Jackman, G. M. Whitesides, D. L. Olson, and J. V. Sweedler, "Using microcontact printing to fabricate microcoils on capillaries for high resolution proton nuclear magnetic resonance on nanoliter volumes," *Applied physics letters*, vol. 70, no. 18, pp. 2464–2466, 1997.

[110] V. Badilita, K. Kratt, N. Baxan, M. Mohmmadzadeh, T. Burger, H. Weber, D. v. Elverfeldt, J. Hennig, J. G. Korvink, and U. Wallrabe, "On-chip three dimensional microcoils for MRI at the microscale," *Lab Chip*, vol. 10, pp. 1387–1390, 2010.

[111] K. R. Minard and R. A. Wind, "Solenoidal microcoil design—part I: Optimizing RF homogeneity and coil dimensions," *Concepts in Magnetic Resonance: An Educational Journal*, vol. 13, no. 2, pp. 128–142, 2001.

[112] K. R. Minard and R. A. Wind, "Solenoidal microcoil design—part II: Optimizing winding parameters for maximum signal-to-noise performance," *Concepts in Magnetic Resonance*, vol. 13, no. 3, pp. 190–210, 2001.

[113] C. Massin, G. Boero, F. Vincent, J. Abenhaim, P.-A. Besse, and R. Popovic, "High-Q factor RF planar microcoils for micro-scale NMR spectroscopy," *Sensors and Actuators A: Physical*, vol. 97, pp. 280–288, 2002.

[114] H. Ryan, S.-H. Song, A. Zass, J. Korvink, and M. Utz, "Contactless NMR spectroscopy on a chip," *Analytical Chemistry*, vol. 84, no. 8, pp. 3696–3702, 2012.

[115] H. Davoodi, N. Nordin, H. Munakata, J. G. Korvink, N. MacKinnon, and V. Badilita, "Untuned broadband spiral micro-coils achieve sensitive multi-nuclear NMR TX/RX from microfluidic samples," *Scientific reports*, vol. 11, no. 1, pp. 1–12, 2021.

[116] S. Eroglu, B. Gimi, B. Roman, G. Friedman, and R. L. Magin, "NMR spiral surface microcoils: design, fabrication, and imaging," *Concepts in Magnetic Resonance Part B: Magnetic Resonance Engineering: An Educational Journal*, vol. 17, no. 1, pp. 1–10, 2003.

[117] P. Van Bentum, J. Janssen, A. Kentgens, J. Bart, and J. G. Gardeniers, "Stripline probes for nuclear magnetic resonance," *Journal of magnetic resonance*, vol. 189, no. 1, pp. 104–113, 2007.

[118] J. Bart, J. Janssen, P. Van Bentum, A. Kentgens, and J. G. Gardeniers, "Optimization of stripline-based microfluidic chips for high-resolution NMR," *Journal of magnetic resonance*, vol. 201, no. 2, pp. 175–185, 2009.

[119] G. Finch, A. Yilmaz, and M. Utz, "An optimised detector for in-situ high-resolution NMR in microfluidic devices," *Journal of Magnetic Resonance*, vol. 262, pp. 73 – 80, 2016.

[120] Y. Maguire, I. L. Chuang, S. Zhang, and N. Gershenfeld, "Ultra-small-sample molecular structure detection using microslot waveguide nuclear spin resonance," *Proceedings of the National Academy of Sciences*, vol. 104, no. 22, pp. 9198–9203, 2007.

[121] H. G. Krojanski, J. Lambert, Y. Gerikalan, D. Suter, and R. Hergenröder, "Microslot NMR probe for metabolomics studies," *Analytical chemistry*, vol. 80, no. 22, pp. 8668–8672, 2008.

[122] K. Ehrmann, N. Saillen, F. Vincent, M. Stettler, M. Jordan, F. M. Wurm, P.-A. Besse, and R. Popovic, "Microfabricated solenoids and Helmholtz coils for NMR spectroscopy of mammalian cells," *Lab on a Chip*, vol. 7, no. 3, pp. 373–380, 2007.

[123] S. Leidich, M. Braun, T. Gessner, and T. Riemer, "Silicon cylinder spiral coil for nuclear magnetic resonance spectroscopy of nanoliter samples," *Concepts in Magnetic Resonance Part B: Magnetic Resonance Engineering: An Educational Journal*, vol. 35, no. 1, pp. 11–22, 2009.

[124] N. Spengler, J. Hoefflin, A. Moazenzadeh, D. Mager, N. MacKinnon, V. Badilita, U. Wallrabe, and J. G. Korvink, "Heteronuclear Micro-Helmholtz coil facilitates µm-range spatial and sub-Hz spectral resolution NMR of nL-volume samples on customisable microfluidic chips," *PLOS ONE*, vol. 11, 01 2016.

[125] V. Malba, R. Maxwell, L. B. Evans, A. F. Bernhardt, M. Cosman, and K. Yan, "Laser-lathe lithography—a novel method for manufacturing nuclear magnetic resonance microcoils," *Biomedical Microdevices*, vol. 5, no. 1, pp. 21–27, 2003.

[126] O. Nassar, D. Mager, and J. G. Korvink, "Wireless double micro-resonator for orientation free tracking of MR-catheter during interventional MRI," *IEEE Journal of Electromagnetics, RF and Microwaves in Medicine and Biology*, vol. 5, no. 1, pp. 78–83, 2020.

[127] O. Nassar, M. Jouda, M. Rapp, D. Mager, J. G. Korvink, and N. MacKinnon, "Integrated impedance sensing of liquid sample plug flow enables automated high throughput NMR spectroscopy," *Microsystems & Nanoengineering*, vol. 7, no. 1, pp. 1–17, 2021.

[128] N. Spengler, P. T. While, M. V. Meissner, U. Wallrabe, and J. G. Korvink, "Magnetic lenz lenses improve the limit-of-detection in nuclear magnetic resonance," *PLOS ONE*, vol. 12, pp. 1–17, 08 2017.

[129] N. Wang, M. Meissner, N. MacKinnon, V. Luchnikov, D. Mager, and J. Korvink, "Fast prototyping of microtubes with embedded sensing elements made possible with an inkjet printing and rolling process," *Journal of Micromechanics and Microengineering*, vol. 28, no. 2, p. 025003, 2017.

[130] J. A. Lehmann-Horn, J.-F. Jacquinot, J. C. Ginefri, C. Bonhomme, and D. Sakellariou, "Monolithic MACS micro resonators," *Journal of Magnetic Resonance*, vol. 271, no. Supplement C, pp. 46 – 51, 2016.

[131] Y. Nishiyama, Y. Endo, T. Nemoto, A.-K. Bouzier-Sore, and A. Wong, "High-resolution NMR-based metabolic detection of microgram biopsies using a 1 mm HRμMAS probe," *Analyst*, vol. 140, no. 24, pp. 8097–8100, 2015.

[132] Z. Tošner, A. Purea, J. O. Struppe, S. Wegner, F. Engelke, S. J. Glaser, and B. Reif, "Radiofrequency fields in MAS solid state NMR probes," *Journal of Magnetic Resonance*, vol. 284, pp. 20–32, 2017.

[133] D. Hoult, "A flux enhancer for obtaining large signals from small samples," in *Proceedings of the 5th Annual Meeting of ISMRM, Vancouver, BC, Canada*, p. 1518, 1997.

[134] F. E. Terman, *Electronic and radio engineering*. McGraw-Hill, 1955.

[135] C. Lucas-Torres and A. Wong, "Current developments in µMAS NMR analysis for metabolomics," *Metabolites*, vol. 9, no. 2, p. 29, 2019.

[136] M. Utz and R. Monazami, "Nuclear magnetic resonance in microfluidic environments using inductively coupled radiofrequency resonators," *Journal of Magnetic Resonance*, vol. 198, no. 1, pp. 132 – 136, 2009.

[137] G. Carret, T. Berthelot, and P. Berthault, "Inductive coupling and flow for increased NMR sensitivity.," *Analytical chemistry*, vol. 90 19, pp. 11169–11173, 2018.

[138] J. A. Tang and A. Jerschow, "Practical aspects of liquid-state NMR with inductively coupled solenoid coils," *Magnetic Resonance in Chemistry*, vol. 48, no. 10, pp. 763–770, 2010.

[139] J.-C. Ginefri, A. Rubin, M. Tatoulian, M. Woytasik, F. Boumezbeur, B. Djemaï, M. Poirier-Quinot, F. Lethimonnier, L. Darrasse, and E. Dufour-Gergam, "Implanted, inductively-coupled, radiofrequency coils fabricated on flexible polymeric material: Application to in vivo rat brain MRI at 7 T," *Journal of Magnetic Resonance*, vol. 224, pp. 61–70, 2012.

[140] R. Kamberger, K. Göbel-Guéniot, J. Gerlach, O. Gruschke, J. Hennig, P. LeVan, C. Haas, and J. Korvink, "Improved method for MR microscopy of brain tissue cultured with the interface method combined with Lenz lenses," *Magnetic resonance imaging*, vol. 52, pp. 24–32, 2018.

[141] D. D. Traficante, "Impedance: what it is, and why it must be matched," *Concepts in Magnetic Resonance*, vol. 1, no. 2, pp. 73–92, 1989.

[142] W. Froncisz, A. Jesmanowicz, and J. S. Hyde, "Inductive (flux linkage) coupling to local coils in magnetic resonance imaging and spectroscopy," *Journal of Magnetic Resonance (1969)*, vol. 66, no. 1, pp. 135 – 143, 1986.

[143] P. L. Kuhns, M. J. Lizak, S.-H. Lee, and M. S. Conradi, "Inductive coupling and tuning in NMR probes; applications," *Journal of Magnetic Resonance (1969)*, vol. 78, no. 1, pp. 69 – 76, 1988.

[144] T. Wang, L. Ciobanu, X. Zhang, and A. Webb, "Inductively coupled RF coil design for simultaneous microimaging of multiple samples," *Concepts in Magnetic Resonance Part B: Magnetic Resonance Engineering: An Educational Journal*, vol. 33, no. 4, pp. 236–243, 2008.

[145] M. Bilgen, "Inductively-overcoupled coil design for high resolution magnetic resonance imaging," *BioMedical Engineering OnLine*, vol. 5, pp. 3 – 3, 2006.

[146] D. I. Hoult and B. Tomanek, "Use of mutually inductive coupling in probe design," *Concepts in Magnetic Resonance*, vol. 15, pp. 262–285, 2002.

[147] J.-F. Jacquinot and D. Sakellariou, "NMR signal detection using inductive coupling: Applications to rotating microcoils," *Concepts in Magnetic Resonance Part A*, vol. 38A, no. 2, pp. 33–51, 2011.

[148] S. S. Adhikari, L. Zhao, T. Dickmeis, J. G. Korvink, and V. Badilita, "Inductively coupled magic angle spinning microresonators benchmarked for high-resolution single embryo metabolomic profiling," *Analyst*, vol. 144, pp. 7192–7199, 2019.

[149] A. Wong, B. Jimenez, X. Li, E. Holmes, J. K. Nicholson, J. C. Lindon, and D. Sakellariou, "Evaluation of high resolution magic-angle coil spinning NMR spectroscopy for metabolic profiling of nanoliter tissue biopsies," *Analytical Chemistry*, vol. 84, no. 8, pp. 3843–3848, 2012. PMID: 22449140.

[150] A. Wong, X. Li, and D. Sakellariou, "Refined magic-angle coil spinning resonator for nanoliter NMR spectroscopy: Enhanced spectral resolution," *Analytical Chemistry*, vol. 85, no. 4, pp. 2021–2026, 2013. PMID: 23343461.

[151] A. Wong, X. Li, L. Molin, F. Solari, B. Elena-Herrmann, and D. Sakellariou, "μhigh resolution-magic-angle spinning NMR spectroscopy for metabolic phenotyping of caenorhabditis elegans," *Analytical Chemistry*, vol. 86, no. 12, pp. 6064–6070, 2014. PMID: 24897622.

[152] M. Inukai and K. Takeda, "Double-resonance magic angle coil spinning," *Journal of Magnetic Resonance*, vol. 202, no. 2, pp. 274 – 278, 2010.

[153] A. Wong, C. Boutin, and P. M. Aguiar, "^1H high resolution magic-angle coil spinning (HR-MACS) μNMR metabolic profiling of whole saccharomyces cervisiae cells: a demonstrative study," *Frontiers in Chemistry*, vol. 2, p. 38, 2014.

[154] P. M. Aguiar, J.-F. Jacquinot, and D. Sakellariou, "Experimental and numerical examination of eddy (Foucault) currents in rotating micro-coils: Generation of heat and its impact on sample temperature," *Journal of Magnetic Resonance*, vol. 200, no. 1, pp. 6 – 14, 2009.

[155] P. M. Aguiar, J.-F. Jacquinot, and D. Sakellariou, "A convenient, high-sensitivity approach to multiple-resonance NMR at nanolitre volumes with inductively-coupled micro-coils," *Chem. Commun.*, vol. 47, pp. 2119–2121, 2011.

[156] K. Kratt, V. Badilita, T. Burger, J. G. Korvink, and U. Wallrabe, "A fully MEMS-compatible process for 3D high aspect ratio micro coils obtained with an automatic wire bonder," *Journal of Micromechanics and Microengineering*, vol. 20, no. 1, p. 015021, 2010.

[157] K. Kratt, V. Badilita, T. Burger, J. Mohr, M. Börner, J. G. Korvink, and U. Wallrabe, "High aspect ratio PMMA posts and characterization method for micro coils manufactured with an automatic wire bonder," *Sensors and actuators A: Physical*, vol. 156, no. 2, pp. 328–333, 2009.

[158] H. H. Gatzen, V. Saile, and J. Leuthold, *Micro and Nano Fabrication: Tools and Processes*. New York, USA: Springer Verlag, 2015.

[159] S. S. Adhikari, "Low-cost microfabricated micro-detectors for magic angle coil spinning (MACS) NMR spectroscopy," Master's thesis, University of Freiburg, June 2014.

[160] V. Badilita, S. S. Adhikari, U. MacKinnon, N.and Wallrabe, and J. Korvink, "Disposable ^{1}H NMR detectors for food quality monitoring: Application to butter and citrus juice discrimination," in *Chem Biol Microsyst Soc.*, pp. 1710–1712, October 2014.

[161] H. Davoodi, M. Jouda, J. G. Korvink, N. MacKinnon, and V. Badilita, "Broadband and multi-resonant sensors for NMR," *Progress in Nuclear Magnetic Resonance Spectroscopy*, vol. 112-113, pp. 34 – 54, 2019.

[162] H. A. C. Tilmans, W. D. Raedt, and E. Beyne, "MEMS for wireless communications: from RF-MEMS components to RF-MEMS-SiP ," *Journal of Micromechanics and Microengineering*, vol. 13, pp. S139–S163, jun 2003.

[163] N. M. Nguyen and R. G. Meyer, "Si IC-compatible inductors and LC passive filters," *IEEE Journal of Solid-State Circuits*, vol. 25, pp. 1028–1031, Aug 1990.

[164] Y.-K. Yoon, J.-W. Park, and M. Allen, "Polymer-core conductor approaches for RF MEMS," *Microelectromechanical Systems, Journal of*, vol. 14, pp. 886 – 894, 11 2005.

[165] R. C. Meier, J. Hoefflin, V. Badilita, U. Wallrabe, and J. G. Korvink, "Microfluidic integration of wirebonded microcoils for on-chip applications in nuclear magnetic resonance," *Journal of Micromechanics and Microengineering*, vol. 24, no. 4, p. 045021, 2014.

[166] Exxelia group (Temex ceramics)„ *Microwave components Product catalogue 157*, 07 2015.

[167] Z. Lu, K. Poletkin, B. den Hartogh, U. Wallrabe, and V. Badilita, "3D micro-machined inductive contactless suspension: Testing and modeling," *Sensors and Actuators A: Physical*, vol. 220, pp. 134 – 143, 2014.

[168] H. Wang, W. Li, and Z. Feng, "A compact and high-performance eddy-current sensor based on meander-spiral coil," *IEEE Transactions on Magnetics*, vol. 51, pp. 1–6, Sept 2015.

[169] M. Z. Baharom, M. Z. Nuawi, G. Priyandoko, and S. M. Harris, "Eddy current braking experiment using brake disc from aluminium series of A16061 and A17075," *IOP Conference Series: Materials Science and Engineering*, vol. 36, no. 1, p. 012005, 2012.

[170] N. Ghalichechian and K. Sertel, "Permittivity and loss characterization of SU-8 films for mmW and Terahertz applications," *IEEE Antennas and Wireless Propagation Letters*, vol. 14, pp. 723–726, 2015.

[171] G. Aubert, J.-F. Jacquinot, and D. Sakellariou, "Eddy current effects in plain and hollow cylinders spinning inside homogeneous magnetic fields: Application to magnetic resonance," *The Journal of Chemical Physics*, vol. 137, no. 15, p. 154201, 2012.

[172] C. Ammann, P. Meier, and A. Merbach, "A simple multinuclear NMR thermometer," *Journal of Magnetic Resonance*, vol. 46, no. 2, pp. 319 – 321, 1982.

[173] J. H. Klootwijk, K. B. Jinesh, W. Dekkers, J. F. Verhoeven, F. C. van den Heuvel, H.-D. Kim, D. Blin, M. A. Verheijen, R. G. R. Weemaes, M. Kaiser, J. J. M. Ruigrok, and F. Roozeboom, "Ultrahigh capacitance density for multiple ALD-grown MIM capacitor stacks in 3-D silicon," *IEEE Electron Device Letters*, vol. 29, no. 7, pp. 740–742, 2008.

[174] M. K. Matters-Kammerer, K. B. Jinesh, T. G. S. M. Rijks, F. Roozeboom, and J. H. Klootwijk, "Characterization and modeling of atomic layer deposited high-density trench capacitors in silicon," *IEEE Transactions on Semiconductor Manufacturing*, vol. 25, no. 2, pp. 247–254, 2012.

[175] D. Dietz, Y. Celik, A. Goehlich, and H. Vogt, "ALD-based 3D-capacitors for harsh environments," in *2016 12th Conference on Ph.D. Research in Microelectronics and Electronics (PRIME)*, pp. 1–4, 2016.

[176] Knowles„ *Non-magnetic Datasheet, Issue 5*, 12 2015.

[177] J. F. Schenck, "The role of magnetic susceptibility in magnetic resonance imaging: MRI magnetic compatibility of the first and second kinds," *Medical physics*, vol. 23, no. 6, pp. 815–850, 1996.

[178] T. Barbara, "Cylindrical demagnetization fields and microprobe design in high-resolution NMR," *Journal of Magnetic Resonance, Series A*, vol. 109, no. 2, pp. 265–269, 1994.

[179] M. C. Wapler, J. Leupold, I. Dragonu, D. von Elverfeld, M. Zaitsev, and U. Wallrabe, "Magnetic properties of materials for MR engineering, micro-MR and beyond," *Journal of Magnetic Resonance*, vol. 242, no. 0, pp. 233 – 242, 2014.

[180] H. Shinohara, H. Goto, T. Kasahara, and J. Mizuno, "Fabrication of a polymer high-aspect-ratio pillar array using UV imprinting," *Micromachines*, vol. 4, pp. 157–167, 04 2013.

[181] R. Kamberger, A. Moazenzadeh, J. Korvink, and O. Gruschke, "Hollow microcoils made possible with external support structures manufactured with a two-solvent process," *Journal of Micromechanics and Microengineering*, vol. 26, no. 6, p. 065002, 2016.

[182] H. Lorenz, M. Despont, N. Fahrni, N. LaBianca, P. Renaud, and P. Vettiger, "SU-8: a low-cost negative resist for MEMS," *Journal of Micromechanics and Microengineering*, vol. 7, no. 3, p. 121, 1997.

[183] A. del Campo and C. Greiner, "SU-8: a photoresist for high-aspect-ratio and 3D submicron lithography," *Journal of Micromechanics and Microengineering*, vol. 17, no. 6, p. R81, 2007.

[184] C.-H. Lin, G.-B. Lee, B.-W. Chang, and G.-L. Chang, "A new fabrication process for ultra-thick microfluidic microstructures utilizing SU-8 photoresist," *Journal of Micromechanics and Microengineering*, vol. 12, no. 5, p. 590, 2002.

[185] J. D. Williams and W. Wang, "Study on the postbaking process and the effects on UV lithography of high aspect ratio SU-8 microstructures," *Journal of Micro/Nanolithography, MEMS, and MOEMS*, vol. 3, no. 4, pp. 563 – 568, 2004.

[186] W.-J. Kang, E. Rabe, S. Kopetz, and A. Neyer, "Novel exposure methods based on reflection and refraction effects in the field of SU-8 lithography," *Journal of Micromechanics and Microengineering*, vol. 16, pp. 821–831, mar 2006.

[187] Microchemicals GmbH„ *Technical datasheet AZ 1500 series*, 1 2017.

[188] Microchemicals GmbH„ *Technical datasheet AZ 4500 series*, 1 2017.

[189] Microchemicals GmbH„ *Technical datasheet AZ 40XT*, 1 2017.

[190] V. Badilita, R. C. Meier, N. Spengler, U. Wallrabe, M. Utz, and J. G. Korvink, "Microscale nuclear magnetic resonance: a tool for soft matter research," *Soft Matter*, vol. 8, pp. 10583–10597, 2012.

[191] W. P. Aue, E. Bartholdi, and R. R. Ernst, "Two-dimensional spectroscopy. application to nuclear magnetic resonance," *The Journal of Chemical Physics*, vol. 64, no. 5, pp. 2229–2246, 1976.

[192] G. J. Lieschke and P. D. Currie, "Animal models of human disease: zebrafish swim into view," *Nature Reviews Genetics*, vol. 8, no. 5, p. 353, 2007.

[193] V. E. Prince, R. M. Anderson, and G. Dalgin, "Zebrafish pancreas development and regeneration: Fishing for diabetes therapies," in *Current topics in developmental biology*, vol. 124, pp. 235–276, Elsevier, 2017.

[194] G. Wang, S. K. Rajpurohit, F. Delaspre, S. L. Walker, D. T. White, A. Ceasrine, R. Kuruvilla, R.-j. Li, J. S. Shim, J. O. Liu, *et al.*, "First quantitative high-throughput screen in zebrafish identifies novel pathways for increasing pancreatic β-cell mass," *Elife*, vol. 4, p. e08261, 2015.

[195] S. H. Lam, Y. L. Wu, V. B. Vega, L. D. Miller, J. Spitsbergen, Y. Tong, H. Zhan, K. R. Govindarajan, S. Lee, S. Mathavan, *et al.*, "Conservation of gene expression signatures between zebrafish and human liver tumors and tumor progression," *Nature biotechnology*, vol. 24, no. 1, p. 73, 2006.

[196] M. Qi, M. C. Philip, N. Yang, and J. V. Sweedler, "Single cell neurometabolomics," *ACS chemical neuroscience*, vol. 9, no. 1, pp. 40–50, 2017.

[197] P. Gut, S. Reischauer, D. Y. Stainier, and R. Arnaout, "Little fish, big data: zebrafish as a model for cardiovascular and metabolic disease," *Physiological reviews*, vol. 97, no. 3, pp. 889–938, 2017.

[198] P.-Y. Lam and R. T. Peterson, "Developing zebrafish disease models for in vivo small molecule screens," *Current Opinion in Chemical Biology*, vol. 50, pp. 37 – 44, 2019. Next Generation Therapeutics.

[199] A. Ordas, R.-J. Raterink, F. Cunningham, H. J. Jansen, M. I. Wiweger, S. Jong-Raadsen, S. Bos, R. H. Bates, D. Barros, A. H. Meijer, *et al.*, "Testing tuberculosis drug efficacy in a zebrafish high-throughput translational medicine screen," *Antimicrobial agents and chemotherapy*, vol. 59, no. 2, pp. 753–762, 2015.

[200] C. A. MacRae and R. T. Peterson, "Zebrafish as tools for drug discovery," *Nature reviews Drug discovery*, vol. 14, no. 10, p. 721, 2015.

[201] K. A. Horzmann and J. L. Freeman, "Making Waves: New Developments in Toxicology With the Zebrafish," *Toxicological Sciences*, vol. 163, pp. 5–12, 02 2018.

[202] T. Dickmeis, Y. Feng, M. C. Mione, N. Ninov, M. Santoro, H. P. Spaink, and P. Gut, "Nano-sampling and reporter tools to study metabolic regulation in zebrafish," *Frontiers in Cell and Developmental Biology*, vol. 7, p. 15, 2019.

[203] J. P. Berry, U. Roy, A. Jaja-Chimedza, K. Sanchez, J. Matysik, and A. Alia, "High-resolution magic angle spinning nuclear magnetic resonance of intact zebrafish embryos detects metabolic changes following exposure to teratogenic polymethoxyalkenes from algae," *Zebrafish*, vol. 13, no. 5, pp. 456–465, 2016.

[204] U. Roy, L. Conklin, J. Schiller, J. Matysik, J. P. Berry, and A. Alia, "Metabolic profiling of zebrafish (Danio rerio) embryos by NMR spectroscopy reveals multifaceted toxicity of β-methylamino-L-alanine (BMAA)," *Scientific Reports*, vol. 7, p. 17305, dec 2017.

[205] J. L. Markley, M. E. Anderson, Q. Cui, H. R. Eghbalnia, I. A. Lewis, A. D. Hegeman, J. Li, C. F. Schulte, M. R. Sussman, W. M. Westler, *et al.*, "New bioinformatics resources for metabolomics," in *Biocomputing 2007*, pp. 157–168, World Scientific, 2007.

[206] M. T. Akhtar, M. Y. Mushtaq, R. Verpoorte, M. K. Richardson, and Y. H. Choi, "Zebrafish as a model for systems medicine R&D: rethinking the metabolic effects of carrier solvents and culture buffers determined by ^1H NMR metabolomics," *Omics: a journal of integrative biology*, vol. 20, no. 1, pp. 42–52, 2016.

[207] M. Ohring, *Reliability and Failure of Electronic Materials and Devices.* San Diego, USA: Academic Press., 1998.

[208] D. C. Montgomery, *Introduction to Statistical Quality Control.* New York, USA: John Wiley & Sons, 2004.

[209] C. Lucas-Torres, G. Huber, A. Ichikawa, Y. Nishiyama, and A. Wong, "HR-μMAS NMR-based metabolomics: localized metabolic profiling of a garlic clove with μg tissues," *Analytical chemistry*, vol. 90, no. 22, pp. 13736–13743, 2018.

[210] M. Nishiyama, C. Lucas-Torres, R. Piao, Y. Yanagisawa, Y. Nishiyama, and A. Wong, "Supplemental shimming for HR-μMAS NMR spectroscopy," *Applied Magnetic Resonance*, vol. 50, no. 11, pp. 1305–1313, 2019.

[211] Y. L. Mobarhan, B. Fortier-McGill, R. Soong, W. E. Maas, M. Fey, M. Monette, H. J. Stronks, S. Schmidt, H. Heumann, W. Norwood, and A. J. Simpson, "Comprehensive multiphase NMR applied to a living organism," *Chem. Sci.*, vol. 7, pp. 4856–4866, 2016.

[212] J. O. Brauckmann, J. W. G. H. Janssen, and A. P. M. Kentgens, "High resolution triple resonance micro magic angle spinning NMR spectroscopy of nanoliter sample volumes," *Phys. Chem. Chem. Phys.*, vol. 18, pp. 4902–4910, 2016.

[213] K. R. Thulborn and J. J. H. Ackerman, "Absolute molar concentrations by NMR in inhomogeneous B_1. A scheme for analysis of in vivo metabolites," *Journal of Magnetic Resonance (1969)*, vol. 55, no. 3, pp. 357–371, 1983.

[214] P.-G. Henry, I. Tkáč, and R. Gruetter, "^{1}H-localized broadband ^{13}C NMR spectroscopy of the rat brain in vivo at 9.4 T," *Magnetic Resonance in Medicine*, vol. 50, pp. 684–692, oct 2003.

[215] Y. J. Jiang, R. J. Pugmire, and D. M. Grant, "An efficient double-tuned $^{13}C/^{1}H$ probe circuit for CP/MAS NMR and its importance in linewidths," *Journal of Magnetic Resonance (1969)*, vol. 71, no. 3, pp. 485–494, 1987.

[216] M. A. Eastman, P. J. Grandinetti, Y. K. Lee, and A. Pines, "Double-tuned hopping-coil probe for dynamic-angle-spinning NMR," *Journal of Magnetic Resonance (1969)*, vol. 98, no. 2, pp. 333–341, 1992.

[217] R. Subramanian and A. G. Webb, "Design of solenoidal microcoils for high-resolution ^{13}C NMR spectroscopy.," *Analytical chemistry*, vol. 70, no. 13, pp. 2454–8, 1998.

[218] S. Amari, A. Müfit Uluğ, J. Bornemann, P. C. M. Van Zijl, P. B. Barker, A. M. Ulug, J. Bornemann, P. C. M. Van Zijl, and P. B. Barker, "Multiple tuning of birdcage resonators," *Magnetic Resonance in Medicine*, vol. 37, pp. 243–251, feb 1997.

[219] P. Cao, X. Zhang, I. Park, C. Najac, S. J. Nelson, S. Ronen, and P. E. Z. Larson, "^{1}H-^{13}C independently tuned radiofrequency surface coil applied for in vivo hyperpolarized MRI," *Magnetic Resonance in Medicine*, vol. 76, no. 5, pp. 1612–1620, 2016.

[220] Y. Otake, Y. Soutome, K. Hirata, H. Ochi, and Y. Bito, "Double-tuned radiofrequency coil for ^{19}F and ^{1}H Imaging," *Magnetic Resonance in Medical Sciences*, vol. 13, no. 3, pp. 199–205, 2014.

[221] N. V. Reo, C. S. Ewy, B. A. Siegfried, and J. J. H. Ackerman, "High-field ^{13}C NMR spectroscopy of tissue in Vivo. A double-resonance surface-coil probe," *Journal of Magnetic Resonance (1969)*, vol. 58, no. 1, pp. 76–84, 1984.

[222] M. Meyerspeer, E. S. Roig, R. Gruetter, and A. W. Magill, "An improved trap design for decoupling multinuclear RF coils," *Magnetic Resonance in Medicine*, vol. 72, no. 2, pp. 584–590, 2014.

[223] I. J. Lowe and M. Engelsberg, "A fast recovery pulsed nuclear magnetic resonance sample probe using a delay line," *Review of Scientific Instruments*, vol. 45, no. 5, pp. 631–639, 1974.

[224] I. J. Lowe and D. W. Whitson, "Homogeneous RF field delay line probe for pulsed nuclear magnetic resonance," *Review of Scientific Instruments*, vol. 48, no. 3, pp. 268–274, 1977.

[225] H. T. Stokes, T. A. Case, D. C. Ailion, and C. H. Wang, "NMR observations of molecular motions and Zeeman-quadrupole cross relaxation in 1,2-difluorotetrachloroethanea," *The Journal of Chemical Physics*, vol. 70, no. 8, p. 3563, 1979.

[226] A. Kubo and S. Ichikawa, "Ultra-broadband NMR probe: Numerical and experimental study of transmission line NMR probe," *Journal of Magnetic Resonance*, vol. 162, no. 2, pp. 284–299, 2003.

[227] D. Murphree, S. B. Cahn, D. Rahmlow, and D. DeMille, "An easily constructed, tuning free, ultra-broadband probe for NMR," *Journal of Magnetic Resonance*, vol. 188, no. 1, pp. 160–167, 2007.

[228] R. M. Fratila, V. M. Gomez, S. Sýkora, and A. H. Velders, "Multinuclear nanoliter one-dimensional and two-dimensional NMR spectroscopy with a single non-resonant microcoil.," *Nature communications*, vol. 5, p. 3025, 2014.

[229] J. Schoenmaker, K. R. Pirota, and J. C. Teixeira, "Magnetic flux amplification by Lenz lenses," *Review of Scientific Instruments*, vol. 84, no. 8, p. 085120, 2013.

[230] M. Jouda, R. Kamberger, J. Leupold, N. Spengler, J. Hennig, O. Gruschke, and J. G. Korvink, "A comparison of Lenz lenses and LC resonators for NMR signal enhancement," *Concepts in Magnetic Resonance Part B: Magnetic Resonance Engineering*, vol. 47B, no. 3, p. e21357, 2017.

[231] T. Meier, N. Wang, D. Mager, J. G. Korvink, S. Petitgirard, and L. Dubrovinsky, "Magnetic flux tailoring through Lenz lenses for ultrasmall samples: A new pathway to high-pressure nuclear magnetic resonance," *Science Advances*, vol. 3, no. 12, 2017.

[232] T. Meier, S. Khandarkhaeva, S. Petitgirard, T. Körber, A. Lauerer, E. Rössler, and L. Dubrovinsky, "NMR at pressures up to 90 GPa," *Journal of Magnetic Resonance*, vol. 292, pp. 44 – 47, 2018.

[233] T. Meier, S. Petitgirard, S. Khandarkhaeva, and L. Dubrovinsky, "Observation of nuclear quantum effects and hydrogen bond symmetrisation in high pressure ice," *Nature Communications*, vol. 9, p. 2766, 2018.

[234] P. von Witzendorff, A. Bordin, O. Suttmann, R. S. Patel, J. Bovatsek, and L. Overmeyer, "Laser ablation of borosilicate glass with high power shaped UV nanosecond laser pulses," in *Laser Applications in Microelectronic and Optoelectronic Manufacturing (LAMOM) XXI*, vol. 9735, pp. 89 – 98, International Society for Optics and Photonics, SPIE, 2016.

[235] H. Shin and D. Kim, "Cutting thin glass by femtosecond laser ablation," *Optics and Laser Technology*, vol. 102, pp. 1–11, 2018.

[236] J. G. Korvink, N. MacKinnon, V. Badilita, and M. Jouda, ""Small is beautiful" in NMR," *Journal of Magnetic Resonance*, vol. 306, pp. 112–117, 2019.

[237] A. Wong, "A roadmap to high-resolution standard microcoil MAS NMR spectroscopy for metabolomics," *NMR in Biomedicine*, vol. n/a, no. n/a, p. e4683, 2022.

[238] O. Beckonert, H. C. Keun, T. M. Ebbels, J. Bundy, E. Holmes, J. C. Lindon, and J. K. Nicholson, "Metabolic profiling, metabolomic and metabonomic procedures for NMR spectroscopy of urine, plasma, serum and tissue extracts," *Nature protocols*, vol. 2, no. 11, p. 2692, 2007.

[239] A.-H. Emwas, R. Roy, R. T. McKay, L. Tenori, E. Saccenti, G. N. Gowda, D. Raftery, F. Alahmari, L. Jaremko, M. Jaremko, *et al.*, "NMR spectroscopy for metabolomics research," *Metabolites*, vol. 9, no. 7, p. 123, 2019.

[240] J. C. Lindon, O. P. Beckonert, E. Holmes, and J. K. Nicholson, "High-resolution magic angle spinning NMR spectroscopy: Application to biomedical studies," *Progress in Nuclear Magnetic Resonance Spectroscopy*, vol. 55, no. 2, pp. 79–100, 2009.

[241] O. Beckonert, M. Coen, H. C. Keun, Y. Wang, T. Ebbels, E. Holmes, J. C. Lindon, and J. K. Nicholson, "High-resolution magic-angle-spinning NMR spectroscopy for metabolic profiling of intact tissues," *Nature protocols*, vol. 5, no. 6, pp. 1019–1032, 2010.

[242] Y.-T. Cheng, M. Jouda, and J. Korvink, "Sample-centred shimming enables independent parallel NMR detection," *Scientific reports*, vol. 12, no. 1, pp. 1–9, 2022.

[243] S. Van Meerten, P. J. M. van Bentum, and A. P. Kentgens, "Shim-on-chip design for microfluidic NMR detectors," *Analytical chemistry*, vol. 90, no. 17, pp. 10134–10138, 2018.

[244] C. Lucas-Torres, T. Bernard, G. Huber, P. Berthault, Y. Nishiyama, P. S. Kandiyal, B. Elena-Herrmann, L. Molin, F. Solari, A.-K. Bouzier-Sore, and A. Wong, "General guidelines for sample preparation strategies in HR-μMAS NMR-based metabolomics of microscopic specimens," *Metabolites*, vol. 10, no. 2, 2020.

[245] M. Westerfield, *THE ZEBRAFISH BOOK. A guide for the laboratory use of zebrafish Danio* (Brachydanio) rerio.* University of Oregon Press,Eugene., 5 ed., 2007.

[246] C. Nusslein-Volhard, *Zebrafish, A Practical Approach.*, vol. 261. Oxford University Press, Oxford., 2002.

[247] P. Choudhary, "Automated setup for RF measurements of microcoils," Master's thesis, Karlsruhe university of applied sciences, Nov. 2016.

Publications

[SA1] S. S. Adhikari, U. Wallrabe, V. Badilita, and J. G. Korvink, "Capacitor re-design overcomes the rotation rate limit of MACS resonators," *Concepts in Magnetic Resonance Part B: Magnetic Resonance Engineering*, vol. 47B, no. 4, p. e21362, 2018.

[SA2] S. S. Adhikari, L. Zhao, T. Dickmeis, J. G. Korvink, and V. Badilita, "Inductively coupled magic angle spinning microresonators benchmarked for high-resolution single embryo metabolomic profiling," *Analyst*, vol. 144, pp. 7192–7199, 2019.

[SA3] M. I. Beyaz, H. C. Baelhadj, S. Habibiabad, S. S. Adhikari, H. Davoodi, and V. Badilita, "A non-resonant kinetic energy harvester for bioimplantable applications," *Micromachines*, vol. 9, no. 5, p. 217, 2018.

[SA4] H. C. Baelhadj, S. S. Adhikari, H. Davoodi, V. Badilita, and M. İ. Beyaz, "A sub-cm^3 energy harvester for in-vivo biosensors," *Microelectronic Engineering*, vol. 226, p. 111288, 2020.

[SA5] J. Korvink, V. Badilita, D. Mager, O. Gruschke, N. Spengler, S. Sundar Adhikari Parenky, U. Wallrabe, and M. Meissner, *Innovative Coil Fabrication Techniques for Miniaturized Magnetic Resonance Detectors*, ch. 5, pp. 109–141. John Wiley & Sons, Ltd, 2018.

Acknowledgement

I would like to express my gratitude to Prof. Dr. Jan G. Korvink for giving me the opportunity to be a part of his research group and pursue this challenging yet stimulating project. His close supervision, constructive feedback, guidance and valuable insights during the course of my stay has made an invaluable contribution to my professional life.

I am also grateful to Prof. Dr. Gisela Guthausen for agreeing to be the second referee for my thesis and for taking time out of her busy schedule to evaluate my work.

I would also like to acknowledge the contribution of Prof. Dr. Ulrike Wallrabe during my doctoral studies and will be forever grateful for her valuable suggestions and for facilitating the use of her wirebonding lab.

I am forever indebted to Dr. Vlad Badilita for his guidance, belief and tons of patience throughout the span of this work. I would like to deeply appreciate his motivational words during the depths of despair and encouragement during crest of euphoria and would like to acknowledge his profound influence on my personal and professional life.

Dr. Hossein Davoodi was one of my office mates and we spent a lot of time bouncing ideas of each other. I am thankful to him for tolerating my endless technical questions and for a great friendship. I was fortunate to have Dr. Nurdiana Nordin, Mohammad Abdo and Albina Julius as my other office mates and grateful to them for the collegial atmosphere in the office. I will always remember the jovial times we spent together.

I will be forever grateful to Dr. Li Zhao for his assistance at a crucial juncture of my project and providing me deep insights into solid-state NMR measurement techniques. I would like to sincerely acknowledge Dr. Ali Moazenzadeh, Dr. Mazin Jouda and Dr. Neil MacKinnon for their support with the wirebonder, RF Lab and NMR spectrometer respectively. I would also like to take this opportunity appreciate the support from Dr. Ronald Kampmann, Dr. Nils Spengler, Dr. Oliver Gruschke, Dr. Omar Nassar, Dr. Sebastain Kiss, Dr. Markus Meissner, Dr. Erwin Fuhrer, Dr. Asa Asadollahbaik, Sagar Wadhwa and others from the Korvink research group and rest of the IMT PhD colleagues for creating a conducive atmosphere for research and numerous BBQ evenings. Special mention to Dr. Patrick Doll and Dr. Pascal Meyer for their support with the wafer polishing equipment. Special thanks to Dr. Erwin Fuhrer, Dr. Swati Sharma and Diana for the extremely competitive badminton games. I had a lot of fun. I would also like to thank my master student, Pratik Choudhary, for his invaluable contribution to my work.

This work would not have been possible without the immense support of the cleanroom staff at IMT. Dr. Uwe Köhler, Dr. Richard Thelen, Heike Fornasier, Florian Rupp, Marco Heiler, Stefan Hengsbach and Thomas Heneka for troubleshooting issues during sensor fabrication. My special thanks goes to Late Giuseppe Papagno and Barbara Matthis for agreeing to my

endless requests for wafer dicing and electroplating respectively. Special mention to my colleagues from Microworks GmbH, Thomas Beckenbach and Konstantin Kaiser for their assistance in the cleanroom. I am also extremely grateful to Gerda Flohr and Dagmar Felkel for help with administrative work.

I would also like to mention the external collaborators, Prof. Mustafa Beyaz and Hacene Baelhadj from Antalya university for the fruitful collaboration.

I would like to acknowledge the funding from the ERC (European reasearch council) and the KNMF (Karlsruhe Nano Micro Facility) infrastructure facility at KIT who made this project possible. Special thanks to the Zebrafish facility (EZRC) at KIT and Dr. Thomas Dickmeis for facilitating zebrafish samples for my experiments.

My lifelong friends and peers from NITK, Rai mama, Nittu, Don, Pod, Biker Bunny, Ganna, Kamina, Chikku, Ravi, PC, Thulla, Azeem, Suppandi, Kamath, Umili and Udupa have been a constant source of encouragement. I had the pleasure of living with amazing flatmates in Karlsruhe. Friedi, Ellen, Sabrina, Simone, Shahrzad and Doro, thank you from the bottom of my heart. My friends in Germany, Marion, Sarai, Naser, Moritz, Claudia, Matthias, Frallet, Peng were a constant source of support and fun activities.

Last but not the least, my heartfelt thanks goes to my parents, my brother and my cousins for their continuous support and faith, and helping me be a better version of myself, personally and professionally.